Fluid-structure interaction with the application to the non-linear aeroelastic phenomena

UNIVERSITAT
POLITÈCNICA
DE VALÈNCIA

Andrés Cremades Botella

Supervisor: Dr. D. Antonio José Torregrosa Huguet
Dr. D. Pedro Manuel Quintero Igeño

Departamento de Máquinas y Motores Térmicos
Instituto Universitario CMT
Universitat Politècnica de València

This dissertation is submitted for the degree of
Doctor of Philosophy

October 2023

We were taught to think big, but the bigger thing happened when we took care of the smaller details.

Acknowledgements

I would like to thank all the people that have been at my side since I started this thesis in 2019. I will not lie if I say it has not been an easy way. We have been living in a complex period that required a big amount of patience and mental resilience. For this reason, I really want to start this section acknowledging the help that all my family (my grandma, my aunts and uncles, and my cousins), provided me, specially my parents and my brother, who specially supported me in 2020 when we had to leave the office and work from home due to the COVID-19 pandemic.

I would also like to thank the support and confidence provided by my thesis directors, Tono Torregrosa and Pedro Quintero, who had been helping me every day during this process. They know how hard it has been and all the effort we had to pay until we achieved publishing the first results of this research. In addition, I want to valuate the contribution of Antonio Gil who embrace me in his office and acted as a third supervisor most of the time of the thesis. I want to mention also all the researchers with who I had the pleasure to share the office, Andrea Mares, Pau Raga... I had invaluable learning from all of you.

Moreover, my best wishes to Ricardo Vinuesa who accept me in the Royal Institute of Technology of Stockholm and treated me like one of his doctoral students. Ricardo, thanks also for trusting me in the new projects that we will be conducting in the following years. Regarding my time in KTH I would like to mention the help that all my office mates provided to me, specially Fran and Pol who became great friends. Also to Roberto Navarro, who came to Stockholm in the same months and always cared for me.

I also want to thank all the researchers that collaborated with me at some point of the research, Andrés, Luismi, Martin, Moritz and Sergio, who spent tones of time helping me writing our last work. Also to the team of accoustics and aerodynamics of the Hong Kong University of Science and Technology for providing us the geometry of the resistant membrane wing model.

This acknowledgement is also for the team of Horus UPV, which I helped to create as a master student. I have spent a lot of hours working with these students, teaching them and learning from their work. You really deserve all the success that you are achieving. Special mention to those with who I had a closer relationship, Joan Albert, Javi, Fede, Alex, Manu,

Sevilla, Andrés... I would need all the page for writing all your names. I am really proud of all of you and I hope you still having a lot of success in the future. I would also love to mention Sergio García-Nieto for trusting me and the team in doing such a piece of work.

I would also like to thank all the colleges from CMT that became family during this time: Marcos, Andrés, Brayan (and Anthony I will include you in this list), Álvaro, Adi, Frank, Javi, Vitor, Ale, Rodri... so many names to mention. I wish you all a great future. And I hope we can work together in the future.

To my friends of Aspe, Luiso, Carmona, Manus, Jose Manueles, V.J., Mili, that have always been so close despite the distance. The friend in Valencia that were in my side most of the time, Mar, Luis, Martyna, Geles, Alberto, Joja, Pablo, Mara, Diego, Alicia... All the friends that cared from me all over the world, Álvaro, Sinfo, Pau, Cara, Salva, María, Sofía, Peter, Christian, Martin, Adin, Tommy, June... Thank you all.

I would also like to thank the roller skating community, specially in Valencia and Stockholm, for welcoming and teaching me an extraordinary sport. Thanks to Nerea for introducing me to the group, to all my ”instructors“ and friends, Miguel, Word, Luciana, Andrea, Nat, Paul, Gwen, Belén, Stefano, Kike, Guille, Roman, Jennifer, David, Rikard... You really changed my life guys.

Finally, to Lucía, thank you for being part of my life. Everything has been easier since I share my time with you.

To conclude this acknowledgments, I would like to thank all the researcher, programmers, engineers, scientist, companies and people who decided to give disinterestedly their work to the community.

Abstract

The complex environmental situation and the legal requirements for decreasing pollutant emissions and fuel consumption have increased the interest in reducing the empty weight and drag of vehicles and developing renewable energy sources. Due to the former, the aviation industry has proposed new designs integrating high strength-to-weight ratios, such as composite materials and higher aspect ratio wings. These increases in aspect ratio have also been applied to wind energy generation. The rotors of wind turbines are increasing their diameters in recent years: a clear example is the massive off-shore facilities. Using larger and lightweight structures increases the effects of the aerodynamic loads on structural deformation. Structural dynamics are strongly connected to the air-structure interaction. This phenomenon, called aeroelasticity, combines the effect of the external aerodynamic loads, the inertial forces, and the internal elastic stress of the structure. The complex combination of all the previous effects may damp the vibrations of the structure, or on the contrary, they could increase their amplitude, resulting in an unstable phenomenon.

The simulation of the aeroelastic phenomena can be performed using different approaches. The well-known finite element analysis is the most extended methodology for solving solid elastic equations. Regarding fluid conservation equations, computational fluid dynamics is the principal tool for resolving general aerodynamic problems. The aeroelastic simulations can be calculated by combining the previous algorithms. Nevertheless, the computational cost of these methodologies is excessive for a general engineering case. Therefore, new methodologies are required.

This work focuses on developing aeroelastic reduced-order models that compute the coupled phenomena without substantial accuracy losses. Initially, the complete three-dimensional structure is reduced to an equivalent section that reproduces the structure. The equivalent structural section is coupled with two aerodynamic models. The first one uses the forces calculated with aeroelastic computational fluid dynamics. Then, a surrogate model based on artificial neural networks is combined with the equivalent section. Both models show accurate agreement compared to the complete three-dimensional simulations in predicting unstable velocity. However, the three-dimensional aerodynamic effects, load distribution, orthotropic materials, and structural couplings cannot be considered.

In order to solve the previous limitations, a reduced-order model based on a beam element solver is proposed. The algorithm is designed to consider a general orthotropic material and different typologies of aeroelastic problems. Initially, the software is proven to simulate accurately a squared cross-section composite material beam. The results are validated with the complete three-dimensional simulations, demonstrating the capabilities of the tool for predicting the instabilities and the effects of the fiber orientations. Then, the algorithm is used for simulating a wind turbine blade, and the algorithm results are used to improve the operation range of the blades without weight penalties. Finally, a resistant membrane wing is simulated, obtaining high accuracy in the prediction of the flutter velocity compared with the complete coupled simulation. In addition, the only limitation of the model is the prediction of the membrane distortion.

The work presents a set of reduced-order models that allow for reducing the computational cost of the aeroelastic simulations by orders of magnitude. In addition, a decision pattern is provided for selecting the appropriate algorithm for the interest problem.

Resumen

El interés en reducir el peso y resistencia aerodinámica de vehículos y en desarrollar fuentes de energía renovables se ha incrementado debido a la compleja situación ambiental y los requerimientos legales para reducir las emisiones de contaminantes y el consumo de combustibles. La industria aeronáutica ha propuesto nuevos diseños que integren conceptos como alas de alto alargamiento y materiales con elevada resistencia específica, como los materiales compuestos. Por su parte, conceptos similares se emplean en la generación de energía eólica. El radio de las palas de las turbinas eólicas se incrementa paulatinamente, siendo un ejemplo muy claro las grandes instalaciones off-shore. El uso de estructuras más alargadas y ligeras provoca mayor deformación debida a las cargas aerodinámicas. Este fenómeno se conoce como aeroelasticidad y combina los efectos de las cargas aerodinámicas, los efectos inerciales y las tensiones internas de la estructura. La combinación de las cargas anteriores provoca fenómenos de amortiguamiento de las vibraciones, o por el contrario, inestabilidades aeroelásticas.

Diferentes metodologías pueden ser empleadas para simular los fenómenos aeroelásticos. La metodología más extendida para la simulación de las ecuaciones elásticas del sólido es la conocida como análisis de elementos finitos. Respecto a las ecuaciones de conservación del fluido, la mecánica de fluidos computacional es la herramienta de resolución para un problema arbitrario. La combinación de las metodologías anteriores puede ser empleada para el cálculo de fenómenos aeroelásticos. Sin embargo, el coste computacional de estas simulaciones es inasumible en la mayoría de casos de aplicación. Se requiere una metodología nueva capaz de reducir el coste de cálculo.

Este trabajo se centra en el desarrollo de modelos de orden reducido que permitan resolver el problema acoplado sin pérdidas sustanciales de precisión. En primer lugar, la estructura tridimensional se reduce a una sección equivalente que reproduzca la física del sólido original. La sección equivalente se acopla con dos modelos aerodinámicos. El primero emplea las fuerzas aerodinámicas obtenidas mediante simulaciones de mecánica de fluidos computacional. Posteriormente se utiliza un modelo reducido basado en redes neuronales. Ambos modelos presentan elevada precisión respecto a las simulaciones tridimensionales. Sin embargo, algunos efectos como los efectos aerodinámicos tridimensionales, las distribu-

ciones de carga aerodinámica, la presencia de materiales ortotrópicos y los acoplamientos estructurales no pueden ser simulados.

Con el objetivo de resolver los limitantes del modelo anterior, se propone un segundo modelo de orden reducido. En este caso se trata de un algoritmo basado en elementos de viga. El algoritmo se diseña para ser capaz de incluir el cálculo de materiales ortotrópicos y diferentes tipos de problemas aeroelásticos. Inicialmente, se emplea el software para determinar su precisión en el cálculo de una viga de material compuesto y sección rectangular. Estos resultados se validan con las simulaciones tridimensionales. De este modo se demuestra la capacidad de la herramienta computacional para predecir las inestabilidades y los efectos de acoplamiento estructural provocados por la orientación de las fibras. Posteriormente, el algoritmo se emplea en la simulación de turbinas eólicas, mejorando los rangos de operación de las palas sin que ello suponga una penalización desde el punto de vista del peso de la misma. Finalmente, un ala basada en una estructura de membrana resistente es simulada. El cálculo obtiene una gran precisión en la predicción de la velocidad de flameo respecto a la simulación acoplada, siendo la única limitación del modelo la predicción de la distorsión de la membrana.

El trabajo presente un conjunto de modelos de orden reducido que permiten disminuir el coste computacional de las simulaciones aeroelásticas en órdenes de magnitud. También, se proporcionan directrices para la selección del modelo reducido apropiado para los casos de interés.

Resum

L'interès a reduir el pes i la resistència aerodinàmica dels vehicles i a desenvolupar fonts d'energia renovables s'ha incrementat a causa de la complexa situació ambiental i els requeriments legals per a reduir les emissions de contaminants i el consum de combustibles. La indústria aeronàutica ha proposat nous dissenys que integren conceptes com ales d'alt allargament i materials amb elevada resistència específica, com ara els materials compostos. Per la seua banda, conceptes similars es fan servir en la generació d'energia eòlica. El radi de les pales de les turbines eòliques s'incrementa progresivament, sent un exemple molt clar les grans instal·lacions off-shore. L'ús d'estructures més allargades i lleugeres provoca més deformació deguda a les càrregues aerodinàmiques. Aquest fenomen es coneix com a aeroelasticitat i combina els efectes de les càrregues aerodinàmiques, els efectes inercials i les tensions internes de l'estructura. La combinació de les càrregues anteriors provoca fenòmens d'esmorteïment de les vibracions, o per contra, inestabilitats aeroelàstiques.

Diferents metodologies poden ser emprades per simular els fenòmens aeroelàstics. La metodologia més estesa per a la simulació de les equacions elàstiques del sòlid és la coneguda com a anàlisi d'elements finits. Pel que fa a les equacions de conservació del fluid, la mecànica de fluids computacional és l'eina de resolució per a un problema arbitrari. La combinació de les metodologies anteriors pot ser emprada per al càlcul de fenòmens aeroelàstics. Tot i això, el cost computacional d'aquestes simulacions és inassumible en la majoria de casos d'aplicació. Cal una metodologia nova capaç de reduir el cost de càlcul.

Aquest treball se centra en el desenvolupament de models d'ordre reduït que permeten resoldre el problema acoblat sense pèrdues substancials de precisió. En primer lloc, l'estructura tridimensional es reduix a una secció equivalent que reproduixca la física del sòlid original. La secció equivalent s'acobla amb dos models aerodinàmics. El primer empra les forces aerodinàmiques obtingudes mitjançant simulacions de mecànica de fluids computacional. Posteriorment es fa servir un model reduït basat en xarxes neuronals. Tots dos models presenten elevada precisió respecte a les simulacions tridimensionals. No obstant això, alguns efectes com ara els efectes aerodinàmics tridimensionals, les distribucions de càrrega aerodinàmica, la presència de materials ortotròpics i els acoblaments estructurals no poden ser simulats.

Amb l'objectiu de resoldre els limitants del model anterior, es proposa un segon model dordre reduït. En aquest cas és un algorisme basat en elements de biga. L'algorisme es dissenya per ser capaç d'incloure el càlcul de materials ortotròpics i diferents tipus de problemes aeroelàstics. Inicialment, s'empra el programari per determinar-ne la precisió en el càlcul d'una biga de material compost i secció rectangular. Aquests resultats es validen amb les simulacions tridimensionals. D'aquesta manera, es demostra la capacitat de l'eina computacional per predir les inestabilitats i els efectes d'acoblament estructural provocats per l'orientació de les fibres. Posteriorment, l'algorisme s'empra en la simulació de turbines eòliques, millorant els rangs d'operació de les pales sense que això suposi una penalització des del punt de vista del pes. Finalment, una ala basada en una estructura de membrana resistent és simulada. El càlcul obté una gran precisió en la predicció de la velocitat de flameig respecte a la simulació acoblada, i l'única limitació del model és la predicció de la distorsió de la membrana.

El treball presenta un conjunt de models reduïts que permeten disminuir el cost computacional de les simulacions aeroelàstiques en ordres de magnitud. També es proporcionen directrius per a la selecció del model reduït adequat per als casos d'interès.

List of publications

The following papers form the basis of this thesis:

- Gil, A. and Tiseira, A. and Quintero, P. and Cremades, A. Prediction of the non-linear aeroelastic behavior of a cantilever flat plate and equivalent 2D model, *Aerospace Science and Technology*, 113: 106685, 2021 [1].
- Torregrosa, A.J. and García-Cuevas, L.M. and Quintero, P. and Cremades, A. On the application of artificial neural network for the development of a nonlinear aeroelastic model, *Aerospace Science and Technology*, 115: 106845, 2021 [2].
- Torregrosa, A.J. and Gil, A. and Quintero, P. and Cremades, A. A reduced order model based on artificial neural networks for nonlinear aeroelastic phenomena and application to composite material beams, *Composite Structures*, 295: 115845, 2022 [3].
- Torregrosa, A.J. and Gil, A. and Quintero, P. and Cremades, A. On the effects of orthotropic materials in flutter protection of wind turbine flexible blades, *Journal of Wind Engineering and Industrial Aerodynamics*, 227: 105055, 2022 [4].
- Torregrosa, A.J. and Gil, A. and Quintero, P. and Cremades, A. Multifi

  delity approach to the numerical aeroelastic simulation of flexible membrane wings, *preprint submitted to Aerospace Science and Technology* [5].

Division of work between authors

The publications have been done in collaboration with other researchers, being the author signatures of articles [1–5] in order of seniority. The respondent performed all the calculations, developed the models and post-process the results presented in this document.

Side project publications

The following is a list of side project publications in which the author of this thesis has been involved during the researches leading to the present work. Although not directly present in this document, they have provided a deeper insight in artificial intelligence, deep neural networks and fluid mechanics.

- Cremades, Andres and Hoyas, Sergio and Quintero, Pedro and Lellep, Martin and Linkmann, Moritz and Vinuesa, Ricardo. Explaining wall-bounded turbulence through deep learning, *arXiv preprint arXiv:2302.01250*, 2023 [6].

Funding

This thesis have been funded by Spanish Ministry of Science, Innovation and University through the University Faculty Training (FPU) program with reference FPU19/02201.

Code repository

Link to the code repository. Contact: a.cremades.phd@gmail.com

References

[1] A. Gil, A. Tiseira, P. Quintero, and A. Cremades. Prediction of the non-linear aeroelastic behavior of a cantilever flat plate and equivalent 2d model. *Aerospace Science and Technology*, 113:106685, 2021.

[2] AJ Torregrosa, LM García-Cuevas, P Quintero, and A Cremades. On the application of artificial neural network for the development of a nonlinear aeroelastic model. *Aerospace Science and Technology*, 115: 106845, 2021.

[3] AJ Torregrosa, A Gil, P Quintero, and A Cremades. A reduced order model based on artificial neural networks for nonlinear aeroelastic phenomena and application to composite material beams. *Composite Structures*, 295:115845, 2022.

[4] AJ Torregrosa, A Gil, P Quintero, and A Cremades. On the effects of orthotropic materials in flutter protection of wind turbine flexible blades. *Journal of Wind Engineering and Industrial Aerodynamics*, 227: 105055, 2022.

[5] AJ Torregrosa, A Gil, P Quintero, and A Cremades. Multi
delity approach to the numerical aeroelastic simulation of flexible membrane wings. *preprint submited to Aerospace Science and Technology*, 2023.

[6] Andres Cremades, Sergio Hoyas, Pedro Quintero, Martin Lellep, Moritz Linkmann, and Ricardo Vinuesa. Explaining wall-bounded turbulence through deep learning. *arXiv preprint arXiv:2302.01250*, 2023.

Table of contents

List of figures

List of tables

Nomenclature

α	Angle of attack
α_{thex}	Expansion coefficient of the material
α_g	Geometric angle of attack
α_i	Induced angle of attack
α_{lim}	Gradient limiter
α_{eff}	Effective angle of attack
$\alpha_{L=0}$	Zero lift angle of attack
$\bar{\alpha}$	Frequency domain angle of attack.
$\bar{\mathbf{Q}}$	Rotated reduced constitutive matrix
$\bar{F_L}$	Frequency lift force
$\bar{F_{La}}$	Added mass term of the frequency lift force
$\bar{F_{Lc}}$	Circulatory term of the frequency lift force
$\bar{M_L}$	Frequency pitching moment
$\bar{M_{La}}$	Added mass term of the frequency pitching moment
$\bar{M_{Lc}}$	Circulatory term of the frequency pitching moment
$\bar{v}$	Frequency domain plunge of the airfoil.
β	Perimeter of the closed-section
β_f	Gradient factor of the cell

Ψ Vector of the area terms in the multi-cell cross-section

Θ Vector of amplitudes of the twist angle

θ Rotation vector

$\Delta\alpha$ Variation of the angle of attack

Δt Time step

ΔT_{ps} Variation of temperature creating the prestress in the resistant membrane

δx Cell size

$\delta \mathscr{W}$ Virtual work of the system.

δ_R Integration of the perimeter of the cell

δ_{ij} Kronecker delta

$\dot{m}_f$ Mass flow

ε Normal strain

ε_0 Prestress applied to the resistant membrane

$\varepsilon_{\text{RMSprop}}$ Smoothing term of the RMSProp

ε_i Normal strain in the i direction.

$\varepsilon_{m_{x_i}}$ Normal strain on the mean fiber of the wall in the direction i.

Γ Moment due to high order effects

γ Tangential strain

Γ_i Vortex intensity of each horseshoe ring in the wing

Γ_v Vortex intensity

γ_{ij} Tangential strain in the i and j directions.

$\gamma_{m_{x_i x_j}}$ Tangential strain on the mean fiber of the wall in the directions i and j.

Γ_{zz} High order stress on the thin walls of the structure

λ Eigenvalues of the system

$(\nabla\zeta)_{r,i}$ Reconstrunction gradients on the face i

$\langle\alpha\rangle$ Mean angle of attack

$\langle\mathbf{v}\rangle$ Averaged velocity vector

$\langle p\rangle$ Averaged pressure

χ^e Shape function of the element

$\langle\tau\rangle$ Mean shear stress tensor

τ_v Viscous stress tensor

$\mathbf{A}$ Cross-section stiffness matrix

$\mathbf{a}$ Area vector

$\mathbf{A}_{\text{aero}}$ Aerodynamic terms depending on the displacement

$\mathbf{A}_{\text{sys}}$ System matrix

$\mathbf{A}_{\theta,\theta}$ Twist aerodynamic influence matrix in the twist equation

$\mathbf{A}_{\theta,w}$ Plunge aerodynamic influence matrix in the twist equation

$\mathbf{A}_{v,\theta}$ Twist aerodynamic influence matrix in the plunge equation

$\mathbf{A}_{v,v}$ Plunge aerodynamic influence matrix in the plunge equation

$\mathbf{b}$ Volumetric force

$\mathbf{B}_{\text{aero}}$ Aerodynamic terms depending on the velocity

$\mathbf{B}_M$ Matrix relating the strain with the displacements on the nodes.

$\mathbf{C}$ Constitutive matrix

$\mathbf{C}_M$ Constitutive matrix on the element.

$\mathbf{d_s}$ Vector connecting the centroids

$\mathbf{D}$ Strain tensor

$\mathbf{D}_{\text{aero}}$ Aerodynamic terms depending on the acceleration

$\mathbf{D}_M$ Strain on the nodes.

$\mathbf{F_{nc}}$ Non-conservative forces

$\mathbf{f}$ Vector of shape functions of the twist angle

$\mathbf{F}^G$ Global force vector

$\mathbf{f}_{\text{mod}}$ Structural frequency vector

$\mathbf{F}_{\text{sys}}$ System forces vector

$\mathbf{f}_M$ Nodal load on the element.

$\mathbf{f}_M^{\text{ext}}$ External loads of the element.

$\mathbf{f}_M^{\text{int}}$ Internal loads of the element.

$\mathbf{g}$ Vector of shape functions of the vertical displacement

$\mathbf{H}$ Matrix of the areas of the multi-cell cross-section

$\mathbf{Ks}^*$, $\mathbf{Ks}$ Stiffness matrix relating forces and strains

$\mathbf{K}$ Stiffness matrix of the system

$\mathbf{K}^e$ Stiffness matrix of the element nodes

$\mathbf{K}^G$ Global stiffness matrix

$\mathbf{K}_\theta$ Stiffness matrix for the torsional motion

$\mathbf{K}_p^G$ Global stiffness permutation matrix

$\mathbf{K}_v$ Stiffness matrix for the flexural motion

$\mathbf{L}_{LU}$ Unit lower triangular matrix

$\mathbf{M}$ Mass matrix of the system

$\mathbf{M}^e$ Mass matrix of the element nodes

$\mathbf{M}_\theta$ Mass matrix for the torsional motion

$\mathbf{M}_s$ Mass matrix of the cross-section

$\mathbf{M}_v$ Mass matrix for the flexural motion

$\mathbf{P}_i$ Stiffness matrix relating forces and a set of strains

$\mathbf{Q_f}$	Generalized forces
$\mathbf{Q}$	Reduced constitutive matrix
$\mathbf{q}$	Degrees of freedom vector
$\mathbf{q}^G$	Global displacement vector
$\mathbf{q}_{\text{eig}}$	Eigenvector of the dynamic system
$\mathbf{q}_f$	Curve distributed load on the element.
$\mathbf{q}_N^e$	Generalized displacement vector of the element nodes
$\mathbf{R}$	Matrix to convert engineering strain to tensor strain
$\mathbf{r}$	Vector from the cross-section reference point to a point of its wall
$\mathbf{R}_T$	Reynolds stress tensor
$\mathbf{S}$	Stress tensor
$\mathbf{S}_A$	Inverse of the matrix of the areas of the multi-cell cross-section
$\mathbf{S}_M$	Stress tensor on the element.
$\mathbf{T}$	Rotation matrix
$\mathbf{t}$	External tension on the element.
$\mathbf{u}$	Displacement vector
$\mathbf{U}_{LU}$	Unit upper triangular matrix
$\mathbf{u}_M$	Vector of the nodal displacements.
$\mathbf{u}_{oi}$	Additional vectors to the nodal quantities.
$\mathbf{V}$	Vector of amplitudes of the vertical displacement
$\mathbf{v}$	Velocity vector of the fluid
$\mathbf{v}'$	Fluctuating velocity vector
$\mathbf{x}$	Position vector
$\mathscr{T}$	Kinetic energy

$\mathscr{U}$	Elastic energy
$\mathscr{F}$	Activation function of the neuron
$\mathscr{L}$	Loss function
μ	Dynamic viscosity
μ_T	Turbulent eddy viscosity
μ_v	Volumetric viscosity or secondary viscosity
$\nabla\zeta_f$	Gradient of the transport variable on the face
ν	Kinematic viscosity
ν_T	Kinematic eddy viscosity
ν_t	Exponential average of squares of gradients
ν_{ij}	Poisson coefficient in the i and j direction
Ω	Rotation velocity
ω	Specific dissipation rate per unit of turbulent kinetic energy
ω_θ	Torsional natural frequency
Ω_A	Area of the closed-section
ω_f	Angular frequency
$\overline{\theta}$	Amplitude of the twist angle
$\overline{v}$	Amplitude of the vertical displacement
$\phi(s)$	Wagner's function
ϕ	Rotation in the x direction
ϕ_i	Induced angle
Ψ	Double of the area-perimeter ratio of the closed-section
ψ	Rotation in the y direction
ρ_∞	Free stream density

ρ_f Density of the fluid

ρ_s Density of the material

σ Normal stress

σ_f Sigmoid function on the LSTM neuron

τ Tangential stress

τ_w Shear stress

Error Error of the mesh

Error_r Function independent of the grid spacing

Re Reynolds number

θ Rotation in the y direction (twist angle)

θ_g Geometrical twist of the blade

θ_k Bias of the neuron k

$\tilde{C}_t$ Cell input activation vector

υ_t Initial learning ratio

φ Polar coordinate of the span position

ξ Nondimensional position of the geometric torsion axis of the blade cross-section

ξ_{RMSProp} Hyperparameter of the RMSProp

ξ_i Internal coordinate of the element.

ξ_{ea} Frequency domain plunge of the airfoil.

ξ_{iM} Internal coordinate of the element node M.

ζ Generic transport variable

$_f$ Face diffusivity

$\zeta_{f,i}$ Transport property in the face of cell i

a Rotor-disk normal induced velocity ratio

a' Rotor-disk tangential induced velocity ratio

a_d Nondimensional distance from the aerodynamic reference point to the location of the torsional stiffness.

A_f Area of the face

A_n Coefficients of the vortex intensity series

a_w Rotor-disk normal induced velocity ratio in the wake

A_{ij}, B_{ij}, D_{ij}, F_{ij}, H_{ij} Stiffness coefficients

AE Aerodynamic efficiency

b Bias of the LSTM neuron

B_ω Bi-moment

c Chord of the airfoil

$C(\kappa)$ Theodorsen's transfer function

c_d Drag coefficient of the airfoil

C_L Three-dimensional lift coefficient

c_l Airfoil lift coefficient

c_l^{dyn} Dynamic lift force coefficient

c_l^{st} Steady lift force coefficient

C_M Three-dimensional moment coefficient

c_m Airfoil aerodynamic pitching moment

c_m^{dyn} Dynamic pitching moment coefficient

c_m^{st} Steady pitching moment coefficient

c_n Normal force coefficient of the blade

C_P Power coefficient

c_p Pressure coefficient of the airfoil

C_t Cell state of the LSTM neuron

c_w Power coefficient of the airfoil

$c_{d,2D-min}$ Minimum drag coefficient

$c_{l,\text{inviscid}}$ Inviscid aerodynamic lift coefficient

c_{l_0} Initial aerodynamic lift force

c_{l_α} Aerodynamic lift force derivative with respect to the angle of attack

$c_{l_\theta^{(n)}}$ Derivative of the lift coefficient respect to the n derivative of the twist

$c_{l_v^{(n)}}$ Derivative of the lift coefficient respect to the n derivative of the vertical displacement

$c_{m,\text{inviscid}}$ Inviscid aerodynamic moment coefficient

c_{m_0} Initial aerodynamic pitching moment

c_{m_α} Aerodynamic pitching moment derivative with respect to the angle of attack

$c_{m_\theta^{(n)}}$ Derivative of the moment coefficient respect to the n derivative of the twist

$c_{m_v^{(n)}}$ Derivative of the moment coefficient respect to the n derivative of the vertical displacement

$c_{x,3D}$ Three-dimensional aerodynamic coefficient

$c_{x,\text{inviscid}}$ Inviscid aerodynamic coefficient

D_f Diffusive term

$d_{i,j}$ Extrapolation coefficients

E Elastic modulus

e Internal energy of the fluid

E_i Elastic modulus in i direction

F Tip loss function

f Solution of the CFD calculation

f_{Exact} Exact solution of the CFD calculation

F_i Forces in the i direction

f_i Solution of the CFD calculation in the mesh i.

F_L Lift force

F_N Disk normal force

F_s Safety factor

f_t Forget gate of the LSTM neuron

F_w Warping function

$f_{h=0}$ Value of the CFD calculation at zero grid spacing

f_i Extrapolated function

G Shear elastic modulus

g_i Function independent of the grid spacing

Gr_t Gradient at a time t

h Thickness of the cross-section wall

H_1 Constant of the Richardson's extrapolation

h_g Grid spacing

h_i Hidden layer neuron i

H_M Proportional constant of the node M of the shape function.

h_t Internal state of the LSTM neuron

I_θ Moment of inertia of the cross-section

i_i Input layer neuron i

I_s Cross-section inertia

i_t Input gate of the LSTM neuron

I_x Second moment of area of the cross-section

I_{2D} Cross-section equivalent inertia

J	Torsion constant
J_v	Bessel function of the first kind of real order v and complex argument
k	Turbulent kinetic energy
k^*	Nonlinear torsion stiffness of the beam
K_θ	Torsional stiffness
k_f	Conductivity of the fluid
K_h	Linear stiffness of the cross-section
k_θ	Cross-section equivalent twist stiffness
k_v	Cross-section equivalent plunge stiffness
L	Length of the beam, semi-span of the wing or beam element.
l_{ref}	Reference length
L_{ij}	Stress couples on the thin walls of the structure
m	Mass of the cross-section
m_0, m_1, m_2	Mass coefficients of the cross-section
M_i	Moment in the i direction
m_s	Cross-section mass
m_{2D}	Cross-section equivalent mass
n	Position in the wall-normal direction
N_b	Number of blades
N_{ij}	Forces on the thin walls of the structure, if $i = j$ they are called membrane forces, other wise are transverse shear
o_i	Output layer neuron i
o_t	Output gate of the LSTM neuron
p	Pressure

p_c	Order of convergence
p_f	Exponent term of the flutter solution
Q	Rotor torque
Q_s	Energy source
R	Radius of the blade
r	Radial position
r_g	Grid refinement ratio
r_n	Normal distance to a point of the cross-section wall
r_t	Tangential distance to a point of the cross-section wall
s	Position in the wall-tangential direction
S_θ	Mass unbalance
s_i	Spatial discretization of the cell i from the centroid to the face
s_k	Internal value of the neuron k
s_t	Nondimensional time
T	Temperature
t	Time
u	Displacement in the x direction
u_0	Displacement of the cross-section reference point in the x direction
u_τ	Friction velocity
u_{m_i}	Displacements on the mean fiber of the wall in the direction i.
v	Displacement in the y direction (vertical displacement of the cross-section)
v_0	Displacement of the cross-section reference point in the y direction
V_∞	Free stream velocity
V_D	Divergence velocity

V_F	Flutter velocity
V_i	Volume of the element i
v_i	Induced velocity normal to the wing/blade plane
v_p	Vertical displacement of a point of the cross-section
v_{ref}	Reference velocity
V_{rel}	Total velocity relative to the cross-section of the blade
v_{it}	Rotor-disk Tangential induced velocity
W	Weights of the LSTM neuron
w	Displacement in the z direction
w^j	Direction of the RMSProp
w_0	Displacement of the cross-section reference point in the z direction
w_a	Velocity of the aerodynamic center
w_f^0	Factor that ponderates the Gauss and the least squares methods
w_f^{lsq}	Factor that ponderates the least squares methods
w_f^G	Factor that ponderates the Gauss
w_j	Weight j of the neuron
W_M	Warping of the cross-section
x	Position in the x direction
x_c	Chord-wise coordinate of the cross-section
x_e	Cross-section element x position.
x_f	Position of the face
x_i	Position of the centroid i
x_t	Input of the LSTM neuron

y Position in the y direction

y^+ Nondimensional wall-distance

y_{true} Real value of the output of the network

y_e Cross-section element y position.

y_j Input j of the neuron

y_k Output of the network

Y_v Bessel function of the second kind of real order v and complex argument

z Position in the z direction (span-wise coordinate)

z_0 Position in the span wise direction

Acronyms / Abbreviations

AI Artificial Intelligence

ANN Artificial Neural Network

BEM Beam element momentum

CFD Computational fluid dynamics

CFL Courant-Friedrich-Lewy number

CNN Convolutional neural network

CSD/CFD Computational solid dynamics/computational fluid dynamics

DNS Direct numerical simulation

FEA Finite element analysis

FEM Finite element method

FFN Feed forward network

FIV Flow induced vibrations

FSI Fluid structure interaction

GCI Grid convergence index

LCO Limit cycle oscillation

LES Large eddy simulation

LLT Lifting line theory

LSTM Long-short term memory

MAV Micro air vehicle

ML Machine learning

MSE Mean squared error

PDE Partial differential equation

POD Proper orthogonal decomposition

RANS Reynolds-averaged Navier-Stokes

RE Richardson's extrapolation

ReLU Rectified linear unit

RMSProp Root Mean Square Propagation

ROM Reduced order model

SHAP Shappley additive explanations

SST Shear stress transport

TWB Thin-walled beam

URANs Unsteady Reynolds averaged Navier–Stokes

VIV Vortex induced vibrations

VLM Vortex lattice method

Chapter 1

Introduction

1.1 Importance of aeroelasticity for an efficient world

The current climate emergency is increasing efforts to reduce greenhouse gas emissions. Reducing the structural weight and aerodynamic drag of vehicles is directly related to lowering energy spending. The International Energy Agency quantified that the total energy consumption related to transport is responsible for 30% of the global, being in 2021 responsible for 37% of the global CO_2 emissions from end-use sectors [1]. In this sense, according to the work of Graham et al. [2], the future concepts of low-emission aircraft are related to the increase in the wings aspect ratio to reduce the induced drag generated by the wing-tip vortex and the all-composite structure to decrease the empty weight of the aircraft.

Indeed, concerning the former, Hicken and Zingg [3] and Abbas et al. [4] stated that the induced aerodynamic drag supposes to be around 40% of the total drag of an airplane during a cruise flight. This fact explains the interest in designing wings with a high aspect ratio. Nevertheless, the aerodynamic benefit of increasing the aspect ratio produces inherent structural design issues due to the higher flexibility and stress on the root of the wing [5].

Regarding weight reduction, the inclusion of composite materials is expected to produce, in elements in which all the metal materials could be replaced, such as the wings, a reduction of 35% by 2030. However, the decrease in the frame weight of the whole aircraft is lower. According to Greitzer et al. [6], the weight alleviation of the complete structure is estimated at 30%. Figure 1.1 shows the midterm estimation of the aircraft weight reduction. In addition, the H3.X structural concept developed by NASA for cleaner aviation is also illustrated.

The previous design trends, which push towards lighter and more efficient structures, produce, as a consequence, the interaction between fields of study that were considered isolated in the past [7]. This fact is, for instance, increasing the interest in combining the aeroelastic phenomena with the flight dynamics of the aircraft.

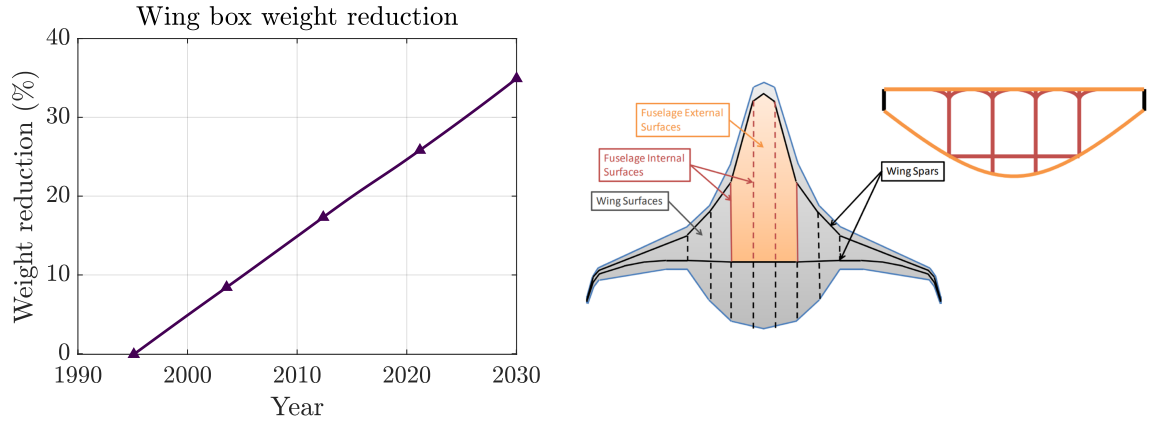

Fig. 1.1 **Weight reduction of the aircraft frame and schematic representation of the H3.X concept.** (Left) weight reduction estimation and (right) structure concept of the aircraft and detail of the fuselage cross-section. Data and image taken from [6].

In combination with lighter transport, the environmental challenge requires increasing clean energy production [8]. The evolution of renewable energy has been rising over the years [9]. This trend can be observed in the IEA data analysis [1]. Figure 1.2 (left) illustrates the global energy supply by source. Two main conclusions may be extracted from this figure: global energy consumption has been rising over the years, and the presence of renewable sources is progressively growing. Indeed, wind and solar energy production are the sources with a higher expected increase in the following years. In fact, in Figure 1.2 (right), it can be observed that in the Net Zero Scenario, the wind energy is expected to grow approximately 300% of its current supply energy. Photovoltaic energy is also expected to increase production by 600% 2021 levels by 2030.

In order to achieve the expected increase in wind energy production, a new generation of offshore wind farms will be required [10]. These facilities are increasing the diameter of the wind turbine blades to increase energy production. According to Yao et al. [11], in the last 40 years, the radius of the wind turbines has increased from 8 m to 111 m. Figure 1.3 shows the evolution of blade diameter as the power generation has increased. As occurred with the aircraft wings, increasing the radius of the blades generates higher deflections [12]. As a consequence, wind-induced vibrations, which are related to the interaction between the structure and the surrounding flow [13], might rise with time under strong winds, leading to destructive effects such as stall-induced vibrations [14] or flutter [15]. Due to this reason, aeroelastic effects are becoming crucial in their structural design.

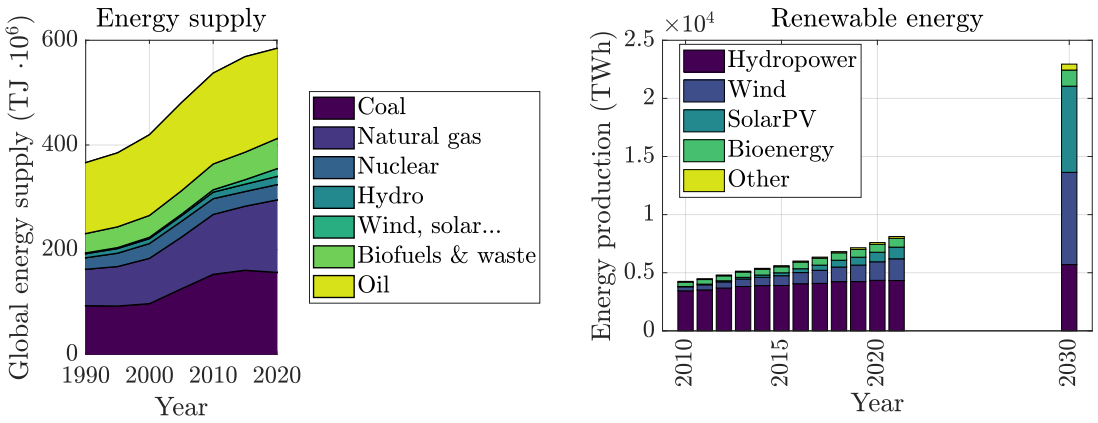

Fig. 1.2 **Woldwide energy consumption by source.** (Left) worldwide evolution of the energy supply by source and (right) renewable energy evolution and expectation in the Net Zero Scenario. Data extracted from the International Energy Agency [1].

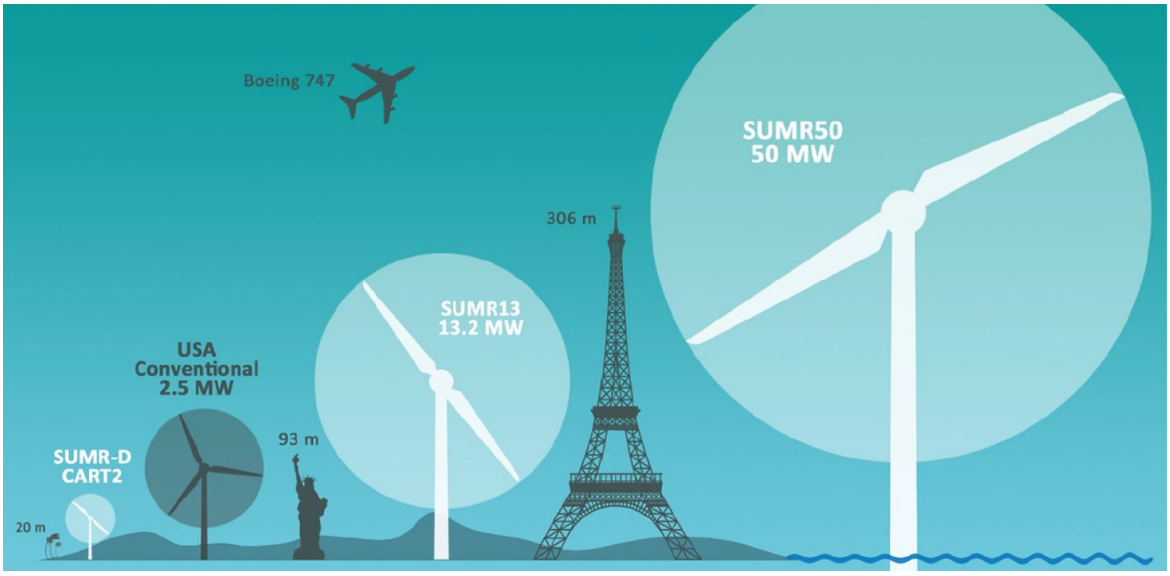

Fig. 1.3 **Evolution of the rotor diameter with the generated power.** Image taken from [11].

Regarding the solar panel facilities, similar effects are observed. Therefore, engineers are challenged to efficiently design the supports of the photovoltaic cells. Typically, the loads have been applied as an equivalent static [16]. This methodology is generally conservative and practical for the solar panel industry. Nevertheless, dynamic effects such as damping or resonance are avoided. Therefore, to perform an efficient design, many authors have developed models for the complex aerodynamic loads acting on the solar arrays [17–19].

Improving the aeroelastic capabilities of the structures requires higher stiffness. Nonetheless, this increase in stiffness is usually related to a thicker cross-section wall, which results

in a rise in weight. Another solution is substituting traditional materials with advanced composite materials [20–22]. These materials present a high stiffness-to-weight ratio, which results in lighter structures [23]. This property, combined with their specific resistance, has spread the use of composite laminates in applications in which the diversity and severity of the loads require high-performance materials, such as aerospace [24], automotive [25], naval [26], energy [27, 28] or civil [29, 30] industries.

Additionally, composite materials allow novel designs which improve the whole behavior of the structure [31–33]. Composites are orthotropic, and thus their mechanical properties depend on the orientation of the plies [34]. A specific configuration of the layup may present bending-twisting couplings, which could damp or amplify the vibrations [35]. An optimum layup configuration might take profit from the mechanical coupling using it for improving the structural performance while maintaining the original weight [36]. From the aeroelastic point of view, these effects are of interest as they can be used as a passive control or actuator for the elastic structure. Stanford et al. [37] studied two opposed effects. The first coupling is called wash-in or positive coupling. The aerodynamic forces lift the structure while the surface increases its angle of attack. This phenomenon generates the augmentation of flight loads. The opposite effect is the wash-out, known as negative coupling. The angle of attack is reduced when the aerodynamic surface is lifting. Both phenomena are desired to improve the aeroelastic limits of the structure. Wash-in helps in flutter alleviation while wash-out protects against divergence [38]. Both effects are illustrated in Figure 1.4.

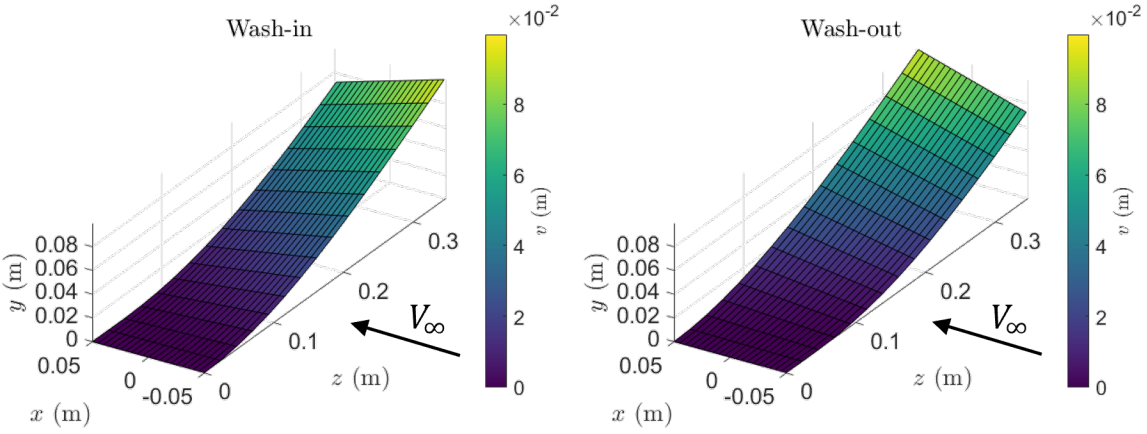

Fig. 1.4 **Aeroelastic structural coupling phenomena.** (Left) Wash-in effect and (right) wash-out effect.

1.2 Motivation and objectives

As introduced in the previous section, understanding and predicting aeroelastic phenomena are critical points in designing future efficient structures required to overcome the complex environmental situation of humanity. The technological development and the aerodynamic optimization of the aerodynamic surfaces require higher aspect ratios, thus, more flexible structures. These structures exhibit larger deformation, and their aeroelastic analysis becomes critical for their integrity.

The previous ideas evidence the necessity of an accurate fluid-structure interaction analysis. The analysis requires experimental or numerical methodologies. The former is based on manufacturing a model of the structure to be tested and presents scaling complexities, mainly from the structural point of view. In fact, Ricciardi et al. [39] stated that scaling the components cannot achieve structural similitude. In other words, the materials used for the scaling might have different properties, and the manufacturing techniques might change. Therefore, the experimental analysis of the structures typically requires modifying and optimizing the internal components. Numerical simulations can overcome the previous limitations as the real structure can be simulated under operation conditions. However, regarding these numerical methodologies, the computational cost associated with the simulation of the complete three-dimensional problem is prohibitive in the initial stages of the design process of many projects [40]. For these reasons, the necessity of developing lower computational cost tools is becoming of paramount importance. In the last decades, many authors have proposed various aeroelastic models. The simpler ones are based on equivalent airfoils. These models have been widely used for theoretical explanations of the phenomena [41], but the procedures to convert a real structure into an equivalent section still need to be clarified. In addition to these simpler structures, the beam model methodology has been widely used in the literature [42]. Nevertheless, an aeroelastic reduced order model for the calculation of the nonlinear problem is required for many engineering applications [43, 44], and the existing solvers are mainly based on potential aerodynamics [45].

This work focuses on developing a set of reduced-order models (ROMs) for the aeroelastic simulation of a general problem, including nonlinear operation points. Their complexity and level of simplification classify the models. In addition to this primary objective, the following points are achieved during the work:

- Showing a methodology for calculating fluid-structure interaction simulations joining the finite element analysis capabilities and the computational fluid dynamics. The capabilities of the proprietary software Star CCM+ for the aeroelastic simulation were

demonstrated even for complex cases of application involving orthotropic materials, multi-body structures and nonlinear prestressed flexible membranes.

- Developing a methodology for reducing a general three-dimensional structure into an equivalent section with a rigid motion. This motion is dominated by mass and stiffness properties derived from the initial structure characteristics. Although the equivalent sections have been traditionally used for theoretical cases, this work proposes modifying the theory to represent general structures no matter their boundary conditions.

- Use artificial neural networks to calculate complex aerodynamic loads under transient effects. The methodology for training the network and comparing different structures is shown. The neural networks are trained to calculate a novel aerodynamic surrogate model.

- Developing a beam element solver for general orthotropic materials. The solver can reproduce the stiffness and mass of the structure, including the higher-order model and the structural couplings. The structural model for orthotropic thin-walled cross-section beams presented in the work of Librescu and Song [46] is joined in an in-home solver with a set of existing aerodynamic models such as Prandtl Lifting Line Theory, Blade Element Momentum theory and Theodorsen transient coefficients and the previous solvers based on artificial neural networks.

- Application of the previous beam element solver to a general aeroelastic solver. The solver is coupled with aerodynamic models, which can describe different problems: wings, rotating blades, and transient situations. Moreover, the solver may be applied to resolve complex frames as semi-monocoque structures.

1.3 Structure of the work

This document presents the information that covers the previous items. In order to introduce it, the first chapter, Chapter 2, is dedicated to describing the fundamentals of fluid-structure interaction. The equations underlying the solid and fluid behavior are presented, and then the aeroelastic problem is introduced.

In the following chapter, Chapter 3, the methodology of the work is described. Firstly, the well-known numerical methods used to resolve the partial differential equations of the solid and the fluid are presented, showing the strategies for coupling both solvers. Then the reduced order models are derived. The different aerodynamic theories are explained, the

solvers based on neural networks presented, and the structural models derived. Finally, the beam element solver for a general aeroelastic problem is developed. In this section, all the algorithms and the configuration of the simulations are shown.

In Chapter 4, the results of the work are presented. The reduced order models are applied to a set of fundamental and engineering problems in order to validate their accuracy. The chapter starts by studying an isotropic flat plate under aerodynamic loads. Firstly, the structure is reduced to a mass-spring system, and the aerodynamic loads are calculated using a computational fluid dynamics solver. Then, the aerodynamic solver is substituted by a surrogate model based on artificial neural networks. These results are followed by using a beam element solver, previously validated against the literature, for calculating the previous geometry, but in this case, using a laminated layup. Finally, the solver is used in two engineering problems. The first is a wind turbine blade, improving its structure y rotating the fibers. The second one is a semi-monocoque membrane-resistant wing. In this case, the deviations of the results due to the shell behavior of the skin are evaluated, as well as the effect of prestressing the membrane.

Finally, Chapter 5 presents the global discussion of the previous results. In addition, the future steps for completing this work are enumerated.

References

[1] International Energy Agency. Key world energy statistics, https://www.iea.org/reports/key-world-energy-statistics-2020, accessed 20-nov-2022. IEA, Paris, 2020.

[2] William Richard Graham, Cesare Alan Hall, and M Vera Morales. The potential of future aircraft technology for noise and pollutant emissions reduction. *Transport policy*, 34:36–51, 2014.

[3] Jason E Hicken and David W Zingg. Induced-drag minimization of nonplanar geometries based on the euler equations. *AIAA journal*, 48(11):2564–2575, 2010.

[4] A Abbas, J De Vicente, and E Valero. Aerodynamic technologies to improve aircraft performance. *Aerospace science and technology*, 28(1):100–132, 2013.

[5] Frederico Afonso, José Vale, Éder Oliveira, Fernando Lau, and Afzal Suleman. A review on non-linear aeroelasticity of high aspect-ratio wings. *Progress in Aerospace Sciences*, 89:40–57, 2017.

[6] Edward M Greitzer, PA Bonnefoy, E DelaRosaBlanco, CS Dorbian, M Drela, DK Hall, RJ Hansman, JI Hileman, RH Liebeck, J Lovegren, et al. N+ 3 aircraft concept designs and trade studies. Technical report, 2010.

[7] R Bombardieri, R Cavallaro, R Castellanos, and F Auricchio. On the dynamic fluid–structure stability response of an innovative airplane configuration. *Journal of Fluids and Structures*, 105:103347, 2021.

[8] Ibrahim Dincer. Renewable energy and sustainable development: a crucial review. *Renewable and sustainable energy reviews*, 4(2):157–175, 2000.

[9] Salvatore Ruggiero and Heikki Lehkonen. Renewable energy growth and the financial performance of electric utilities: A panel data study. *Journal of Cleaner Production*, 142:3676–3688, 2017.

[10] Rehana Perveen, Nand Kishor, and Soumya R Mohanty. Off-shore wind farm development: Present status and challenges. *Renewable and Sustainable Energy Reviews*, 29:780–792, 2014.

[11] S. Yao, M. Chetan, D. T. Griffith, A. S. Escalera Mendoza, M. S. Selig, D. Martin, Sepideh Kianbakh, Kathryn Johnson, and E. Loth. Aero-structural design and optimization of 50 MW wind turbine with over 250-m blades. *Wind Engineering*, 46:273–295, 2021.

[12] Zhanwei Li, Binrong Wen, Xingjian Dong, Zhike Peng, Yegao Qu, and Wenming Zhang. Aerodynamic and aeroelastic characteristics offlexible wind turbine bladesunder periodic unsteady inflows. *Journal of Wind Engineering & Industrial Aerodynamics*, 197:104057, 2020.

[13] M.H. Hansen. Aeroelastic Instability Problems for Wind Turbines. *Wind Energy*, 10:551–577, 2007.

[14] Morten H Hansen. Improved modal dynamics of wind turbines to avoid stall-induced vibrations. *Wind Energy: An International Journal for Progress and Applications in Wind Power Conversion Technology*, 6(2):179–195, 2003.

[15] L. Sanches, T. A. Guimaraes, and F. D. Marques. Aeroelastic tailoring of nonlinear typical section using the method of multiple scales to predict post-flutter stable LCOs. *Aerospace Science and Technology*, 90: 157–168, 2019.

[16] Andreas Schellenberg, Joe Maffei, Karl Telleen, and Rob Ward. Structural analysis and application of wind loads to solar arrays. *Journal of Wind Engineering and Industrial Aerodynamics*, 123:261–272, 2013. ISSN 0167-6105. doi: https://doi.org/10.1016/j.jweia.2013.06.011.

[17] Matthew T.L. Browne, Zachary J. Taylor, Sihan Li, and Scott Gamble. A wind load design method for ground-mounted multi-row solar arrays based on a compilation of wind tunnel experiments. *Journal of Wind Engineering and Industrial Aerodynamics*, 205:104294, 2020. ISSN 0167-6105. doi: https://doi.org/10.1016/j.jweia.2020.104294.

[18] Onur Yemenici and Muhammed Osman Aksoy. An experimental and numerical study of wind effects on a ground-mounted solar panel at different panel tilt angles and wind directions. *Journal of Wind Engineering and Industrial Aerodynamics*, 213:104630, 2021. ISSN 0167-6105. doi: https://doi.org/10.1016/j.jweia.2021.104630.

[19] Aly Mousaad Aly and Girma Bitsuamlak. Aerodynamics of ground-mounted solar panels: Test model scale effects. *Journal of Wind Engineering and Industrial Aerodynamics*, 123:250–260, 2013. ISSN 0167-6105. doi: https://doi.org/10.1016/j.jweia.2013.07.007.

[20] Robert M Jones. *Mechanics of composite materials*. CRC press, 2018.

[21] Trevor William Clyne and Derek Hull. *An introduction to composite materials*. Cambridge university press, 2019.

[22] Rachid Hsissou, Rajaa Seghiri, Zakaria Benzekri, Miloudi Hilali, Mohamed Rafik, and Ahmed Elharfi. Polymer composite materials: A comprehensive review. *Composite structures*, 262:113640, 2021.

[23] Guo Dong Goh, Vishwesh Dikshit, Arun Prasanth Nagalingam, Guo Liang Goh, Shweta Agarwala, Swee Leong Sing, Jun Wei, and Wai Yee Yeong. Characterization of mechanical properties and fracture mode of additively manufactured carbon fiber and glass fiber reinforced thermoplastics. *Materials & Design*, 137:79–89, 2018.

[24] A. D. Shaw, I. Dayyani, and M. I. Friswell. Optimisation of composite corrugated skins for buckling in morphing aircraft. *Composite Structures*, 119:227–237, 2015.

[25] Trevor Sabiston, Bin LiJidong Kang, David Wilkinson, and Carlos Engler-Pinto. Accounting for the microstructure in the prediction of the fatigue lifeof injection moulded composites for automotive applications. *Composite Structures*, 255:112898, 2021.

[26] A. Gargano, K. Pingkarawat, M. Blacklock, V. Pickerd, and A.P. Mouritz. Comparative assessment of the explosive blast performance of carbonand glass fibre-polymer composites used in naval ship structures. *Composite Structures*, 171:306–316, 2017.

[27] Roham Rafiee, Mojtaba Tahani, and Mohsen Moradi. Simulation of aeroelastic behavior in a composite wind turbine blade. *Journal of Wind Engineering & Industrial Aerodynamics*, 151:60–69, 2016.

[28] Lin Wang, Robin Quant, and Athanasios Kolios. Fluid structure interaction modelling of horizontal-axis wind turbine blades based on cfd and fea. *Journal of Wind Engineering & Industrial Aerodynamics*, 158: 11–25, 2016.

[29] Carlos Pascual Agullo. *Translucent load-bearing GFRP envelopes for daylighting and solar cell integration in buliding construction.* PhD thesis, EPFL, Laussane, 2014.

[30] Carlos Pascual, Julia de Castro, Andreas Schueler, and Thomas Keller. Integration of dye solar cells in load-bearing translucent glass fiber-reinforced polymer laminates. *Journal of Composite Materials*, 51: 939–953, 2016.

[31] VC Sherrer, TJ Hertz, and MH Shirk. Wind tunnel demonstration of aeroelastic tailoring applied to forward swept wings. *Journal of Aircraft*, 18(11):976–983, 1981.

[32] Terrence Weisshaar, Changho Nam, and Alicia Batista-Rodriguez. Aeroelastic tailoring for improved uav performance. In *39th AIAA/ASME/ASCE/AHS/ASC Structures, Structural Dynamics, and Materials Conference and Exhibit*, page 1757, 1998.

[33] Bret K Stanford and Christine V Jutte. Comparison of curvilinear stiffeners and tow steered composites for aeroelastic tailoring of aircraft wings. *Computers & Structures*, 183:48–60, 2017.

[34] Zhi-Guang Song and Feng-Ming Li. Active aeroelastic flutter analysis and vibration control of supersonic composite laminated plate. *Composite Structures*, 94(2):702–713, 2012.

[35] G.A. Geroghiades and J.R. Banerjee. Flutter modes of composite wings exhibiting wash-in and wash-out. 38th Structures, Structural Dynamics and Materials Conference, 1997.

[36] AJ Torregrosa, A Gil, P Quintero, and A Cremades. On the effects of orthotropic materials in flutter protection of wind turbine flexible blades. *Journal of Wind Engineering and Industrial Aerodynamics*, 227:105055, 2022.

[37] Bret K. Stanford, Christine V. Jutte, and K. Chauncey Wu. Aeroelastic benefits of tow steering for composite plates. *Composite Structures*, 118:416–422, 2014.

[38] Terrence A Weisshaar and Rosemary J Ryan. Control of aeroelastic instabilities through stiffness cross-coupling. *Journal of Aircraft*, 23(2):148–155, 1986.

[39] Anthony P Ricciardi, Robert A Canfield, Mayuresh J Patil, and Ned Lindsley. Nonlinear aeroelastic scaled-model design. *Journal of Aircraft*, 53(1):20–32, 2016.

[40] Roland Feil, Tobias Pflumm, Pietro Bortolotti, and Marco Morandini. A cross-sectional aeroelastic analysis and structural optimization tool for slender composite strictures. *Composite structures*, 253: 112755, 2020.

[41] Earl H Dowell, RH Scanlan, F Sisto, HC Curtiss Jr, and H Saunders. A modern course in aeroelasticity. 1981.

[42] Lin Wang, Xiongwei Liu, and Athanasios Kolios. State of the art in the aeroelasticity of wind turbine blades: Aeroelastic modelling. *Renewable and Sustainable Energy Reviews*, 64:195–210, 2016.

[43] M Vahdati, AI Sayma, JG Marshall, and M Imregun. Mechanisms and prediction methods for fan blade stall flutter. *Journal of Propulsion and Power*, 17(5):1100–1108, 2001.

[44] Norizham Abdul Razak, Thomas Andrianne, and Grigorios Dimitriadis. Flutter and stall flutter of a rectangular wing in a wind tunnel. *AIAA journal*, 49(10):2258–2271, 2011.

[45] Alfonso Del Carre and Rafael Palacios. Efficient time-domain simulations in nonlinear aeroelasticity. In *AIAA Scitech 2019 Forum*, page 2038, 2019.

[46] Liviu Librescu and Ohseop Song. *Thin-Walled Composite Beams. Theory and Application*. Springer, 2006.

Chapter 2

Fundamentals of fluid-structure interaction

2.1 Introduction to the fluid-structure interaction

A flow passing around a solid surface generates a velocity field, which produces pressure and shear stress distributions, resulting in loads on the surface. These loads exert stress and strain on the solid, which as a consequence, is deformed [1].

Depending on the flow conditions, the material properties, and the solid geometry, two different scenarios are presented: rigid and elastic structures. On the one hand, the solid could be assumed as a rigid body in the case of small deformations of the structure. In this case, only the structural integrity of the components (internal stress and strain) is analyzed. Some examples are the wall of a combustion chamber [2–4], the propeller of a centrifugal compressor [5–7], super-tall buildings [8, 9] or valves [10]. On the other hand, when the structure is flexible enough, the former deformation is noticeable, modifying the flow field and leading to a coupled phenomenon (fluid-structure interaction). Analyzing the interaction between the solid and the fluid is required for predicting the flying capabilities of aircraft [11–13], the structural integrity of wind turbine blades [14–16] or the evolution of blood flows inside veins and hearts [17–19].

Fluid-structure interaction (FSI) analysis is a multidisciplinary field that addresses a wide range of problems of different natures. Current research has been developed in the FSI area for reducing the structural weight and improving endurance and efficiency of aircraft [20], increasing the diameter of future offshore wind farms [21], or protecting solar panels from damaging wing [22]. Depending on the nature and the purpose of the system under study, the fluid-structure interaction may be classified into four main groups, see Figure 2.1.

- **Vortex-induced vibration (VIV)**: a vibration of a solid as a response to the vortex shedding that the flow is generating. This vibration has a characteristic frequency similar to the vortex frequency. This phenomenon has a direct application in energy generation, for example, the design of bladeless wind turbines [23].
- **Flow-induced vibration (FIV)**: a fully turbulent flow around the solid produces an unsteady load in a wide range of frequencies. Consequently, the structure exhibits a vibration in a wide frequency range with an essential contribution of its natural frequencies. This phenomenon is related to flow-induced noise generation. For instance, FIV is a significant problem in the thermocouple well in the fast-breeder reactor at Monju in Japan, which presents a drag direction vibration [24].
- **Aeroelasticity**: this field focuses on the interaction between the airflow and the structural response. Aeroelasticity mainly deals with the destructive unstable phenomena that may appear in the structural system [25]. The aeroelastic analysis might focus on static problems such as divergence [26] or control reversal [27], or on dynamic problems: flutter [28], stall flutter [29] and buffeting [30] as an example.
- **Other important FSI phenomena**: for instance, the flow inside flexible pipes. The sudden closing of a valve could lead to a water hammer and, thus, to the destruction of the pipe.

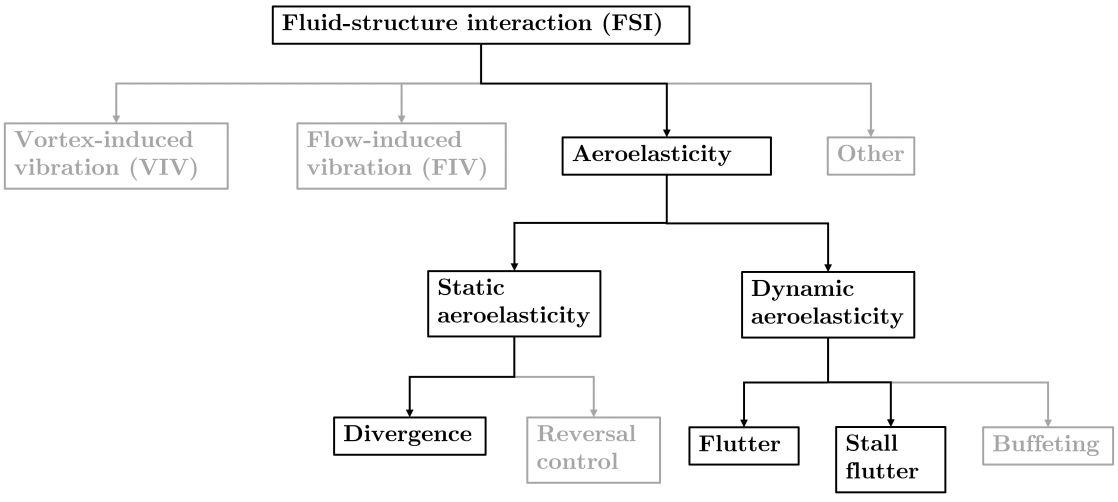

Fig. 2.1 **Classification of fluid structure interaction phenomena.** The dark line highlights the phenomena studied in the present work.

Fluid-structure interaction phenomena can be analyzed from an experimental or a computational point of view. This work focuses on the numerical approach to fluid conservation and the solid elastic equations applied to aeroelastic problems. This methodology shows how to calculate a three-dimensional solution to the problem and also presents low computational cost theories and algorithms for simulating the phenomena. In the following sections, a first approach to the solid and the fluid equations is provided. In addition, the aeroelastic phenomena and their instabilities are presented.

2.2 Fundamentals of elasticity

The theory of elasticity deals with the relationship between the loads applied to a structure and its resulting deformation [31–34]. The elastic analysis of a solid provides information about the internal stress and strain of the material, and thus, it allows the prediction of possible failures of the components.

Assuming a solid under a loading state, normal and tangential stress distributions appear in the material. Stress is defined as the force applied per unit area. The stress tensor, **S**, in an infinitesimal portion of the solid is defined in Equation (2.1). The normal stress is denoted by σ_{ij}, the tangential by τ_{ij}, and the orthogonal directions of the generic reference frame by 1, 2, and 3.

$$\mathbf{S} = \begin{bmatrix} \sigma_{11} & \tau_{12} & \tau_{13} \\ \tau_{12} & \sigma_{22} & \tau_{23} \\ \tau_{13} & \tau_{23} & \sigma_{33} \end{bmatrix} \tag{2.1}$$

Applying Newton's second law to an infinitesimal portion of the solid determines the mechanics of the static system, Equation (2.2). In the equation, vector **b** denotes the volumetric forces, **u** the displacement vector, and ρ_s the solid density.

$$\left.\begin{array}{l} \frac{\partial \sigma_{11}}{\partial x_1} + \frac{\partial \tau_{12}}{\partial x_2} + \frac{\partial \tau_{13}}{\partial x_3} + b_1 = \rho_s \ddot{u}_1 \\ \frac{\partial \tau_{12}}{\partial x_1} + \frac{\partial \sigma_{22}}{\partial x_2} + \frac{\partial \tau_{23}}{\partial x_3} + b_2 = \rho_s \ddot{u}_2 \\ \frac{\partial \tau_{13}}{\partial x_1} + \frac{\partial \tau_{23}}{\partial x_2} + \frac{\partial \sigma_{33}}{\partial x_3} + b_3 = \rho_s \ddot{u}_3 \end{array}\right\} \rightarrow \Delta \mathbf{S} + \mathbf{b} = \rho_s \ddot{\mathbf{u}} \tag{2.2}$$

As the solid is elastic, the stress also produces deformations. If the strains are small enough, the physical behavior of the material can be approximated by a linear or Hookean relationship [35]. This relationship is called the constitutive equation, and the matrix **C** is the constitutive matrix. Equation (2.3) shows the Hookean relationship between stress and strain (**D**) tensors and the general definition of the constitutive matrix.

$$\mathbf{S}_{ij} = \mathbf{C}_{ijkl}\mathbf{D}_{kl} \rightarrow \mathbf{C} = \begin{bmatrix} C_{1111} & C_{1122} & C_{1133} & C_{1123} & C_{1113} & C_{1112} \\ & C_{2222} & C_{2233} & C_{2223} & C_{2213} & C_{2212} \\ & & C_{3333} & C_{3323} & C_{3313} & C_{3312} \\ & & & C_{2323} & C_{2313} & C_{2312} \\ & Sym. & & & C_{1313} & C_{1312} \\ & & & & & C_{1212} \end{bmatrix} \tag{2.3}$$

The strain tensor is defined similarly as the stress tensor, Equation (2.4). The normal strain is defined by ε_{ii} and the tangential as γ_{ij}.

$$\mathbf{D} = \begin{bmatrix} \varepsilon_{11} & \gamma_{12} & \gamma_{13} \\ \gamma_{12} & \varepsilon_{22} & \gamma_{23} \\ \gamma_{13} & \gamma_{23} & \varepsilon_{33} \end{bmatrix} \text{ being, } \begin{cases} \varepsilon_{ii} = \frac{\partial u_i}{\partial x_i} \\ \gamma_{ij} = \frac{\partial u_i}{\partial x_j} + \frac{\partial u_j}{\partial x_i} \end{cases} \tag{2.4}$$

Depending on the type of material, the constitutive matrix adopts a different shape. For instance, when the material presents three planes of symmetry (orthotropic material), the terms $C_{1123} = C_{1113} = C_{1112} = C_{2223} = C_{2213} = C_{2212} = C_{3323} = C_{3313} = C_{3312} = C_{2313} = C_{2312} = C_{1312} = 0$. This property is expected in the case of unidirectional fiber reinforced plastics, for example, carbon fiber reinforced polymer (CFRP). The constitutive matrix of the orthotropic material is presented in Equation (2.5).

$$\mathbf{S}_{ij} = \mathbf{C}_{ijkl}\mathbf{D}_{kl} \rightarrow \mathbf{C} = \begin{bmatrix} C_{1111} & C_{1122} & C_{1133} & 0 & 0 & 0 \\ & C_{2222} & C_{2233} & 0 & 0 & 0 \\ & & C_{3333} & 0 & 0 & 0 \\ & & & C_{2323} & 0 & 0 \\ & Sym. & & & C_{1313} & 0 \\ & & & & & C_{1212} \end{bmatrix} \tag{2.5}$$

Therefore, orthotropic material requires nine independent elastic parameters to be defined. Other materials, for instance, metallic materials, present symmetry in every direction. They are called isotropic materials. For these materials, the following conditions are meet: $C_{1111} = C_{2222} = C_{3333}$, $C_{1122} = C_{1133} = C_{2233}$ and $C_{1212} = C_{3131} = C_{2323} = (C_{1111} - C_{1122})/2$. Their constitutive matrix could be expressed as in Equation (2.6).

$$\mathbf{S}_{ij} = \mathbf{C}_{ijkl}\mathbf{D}_{kl} \rightarrow \mathbf{C} = \begin{bmatrix} C_{1111} & C_{1122} & C_{1122} & 0 & 0 & 0 \\ & C_{1111} & C_{1122} & 0 & 0 & 0 \\ & & C_{1111} & 0 & 0 & 0 \\ & & & \frac{C_{1111}-C_{1122}}{2} & 0 & 0 \\ & Sym. & & & \frac{C_{1111}-C_{1122}}{2} & 0 \\ & & & & & \frac{C_{1111}-C_{1122}}{2} \end{bmatrix} \tag{2.6}$$

Two independent variables are sufficient to define the constitutive relationships regarding the isotropic material.

2.3 Fundamentals of fluid mechanics

Fluid mechanics studies the behavior of liquids and gases in motion [36–38]. This motion can be described for a single phase compressible flow employing the conservation equations: mass, Equation (2.7); momentum, Equation (2.8) and energy, Equation (2.9).

$$\frac{\partial \rho_f}{\partial t} + \nabla\left(\rho_f \mathbf{v}\right) \tag{2.7}$$

$$\frac{\partial \rho_f \mathbf{v}}{\partial t} + \mathbf{v}\nabla\left(\rho_f \mathbf{v}\right) = -\nabla p + \nabla\tau_v + \rho_f \mathbf{b} \tag{2.8}$$

$$\frac{\partial \rho_f \left(e + \frac{1}{2}\mathbf{v}^T\mathbf{v}\right)}{\partial t} + \nabla\left(\rho_f\left(e + \frac{1}{2}\mathbf{v}^T\mathbf{v}\right)\mathbf{v}\right) = -\nabla\left(\mathbf{v}p + \tau_v\mathbf{v} + k_f\nabla T\right)) + \rho_f\mathbf{b}^T\mathbf{v} + Q_s \tag{2.9}$$

In the equations, the fluid velocity vector is denoted by $\mathbf{v}$, the fluid density ρ_f, and its pressure by p. The viscous effects are included in the equations using the stress tensor, τ_v, whose terms are defined in Equation (2.10) for a Newtonian fluid. The variable $\mathbf{b}$ expresses the volumetric forces on the flow. Relative to the energetic terms, the temperature is expressed by T, the internal energy by a function of the temperature and the pressure $e = e(T, p)$, the conductivity by k_f, and the energy sources by Q. The previous variables depend on the time t and space $\mathbf{x}$.

$$\tau_{v_{ij}} = \mu\left(\frac{\partial v_i}{\partial x_j} + \frac{\partial v_j}{\partial x_i}\right) + \left(\mu_v - \frac{2}{3}\mu\right)\frac{\partial v_k}{\partial x_k}\delta_{ij} \tag{2.10}$$

Here, μ is the dynamic viscosity, μ_v is the volumetric viscosity or secondary viscosity and δ_{ij} is the Kronecker delta.

However, although the conservation equations have been known since the nineteenth century, their analytic solution can only be obtained for elementary flows, as pointed out by Osborn Reynolds 140 years ago [39]. The turbulent behavior of the fluid is associated with the well-known Reynolds number, $\mathrm{Re} = \frac{v_{\mathrm{ref}} l_{\mathrm{ref}} \rho_f}{\mu}$, being v_{ref} the reference velocity and l_{ref} the reference length. The Reynolds number determines the ratio between the inertial and viscous forces acting on the fluid. When the viscous effects are dominant, the flow presents a low Reynolds number (laminar flow), and the turbulent effects are negligible. Laminar flows are essential for applications such as lubrication. However, for almost all the flows of practical interest, the inertial effects are principal, and the Reynolds number is high, requiring the resolution of the turbulent conservation equations. Turbulence is a multi-scale phenomenon in time and space. The energy is transferred from the largest to the smallest scales, where it is dissipated in a process called energy cascade [40].

This multi-scale energy transfer supposes the main challenge for the numerical solution of the conservation equations. Calculating all the scales requires an extremely fine discretization of the domain, which is still computationally unaffordable for practical applications. The complete simulation of the conservation equations is called direct numerical simulation (DNS). With the development of computational power and more efficient numerical algorithms, many authors have been able to simulate fundamental examples of wall-bounded flows [41].

In order to reduce the computational power required for the DNS, many authors have studied turbulent flows and developed mathematical models. These models are a standard tool in computational fluid dynamics (CFD) for industrial applications and may model totally or partially the turbulent scales. The former are called Reynolds-averaged Navier-Stokes (RANS) [42]. For the latter, large eddy simulation (LES), only the smallest scales are modeled [43].

2.4 Introduction to the aeroelastic phenomena: instabilities

Aeroelasticity is the discipline that analyzes the interaction between the inertial effects on the solid, the elastic behavior of the structure, and the aerodynamic loads acting on the solid surface. The relationship between the previous forces was pointed by Collar [44] in the so-called Collar's triangle, Figure 2.2. This diagram relates inertial, elastic, and aerodynamic effects indicating the disciplines resulting from their combination:

- Rigid-body aerodynamics (flight dynamics and control). This field results in the interaction of inertial and aerodynamic forces.
- Structural vibrations (structural response to dynamic loads). It depends on the inertial and elastic forces.
- Static aeroelasticity (elastic and aerodynamic forces). The implications of aeroelastic phenomena are related to structural design and aerodynamic optimization.
- Dynamic aeroelasticity (elastic, inertial, and aerodynamic forces). Protection of the structure against flow-induced vibrations.

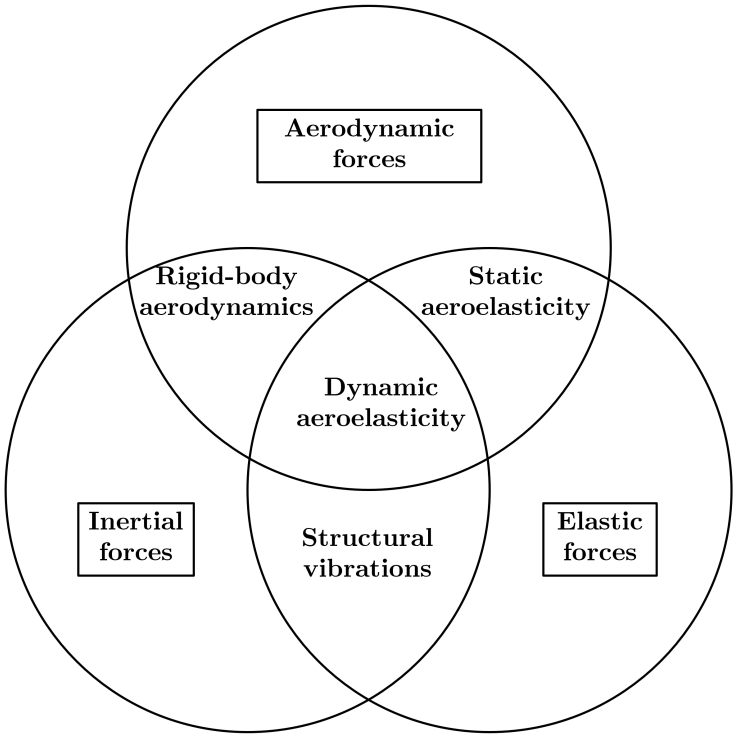

Fig. 2.2 **Collar's diagram.** Relationship between inertial, elastic and aerodynamic forces and the fields of study resulting from their combination.

Note that, although in the previous classification, the aeroelastic problem and the control problem have been dissociated, the advances in materials, the weight reduction in the aircraft structure, and the advances in control techniques have required the combination of both fields in a discipline called aeroservoelasticity [45–47].

The aeroelastic formulation is derived from the general dynamic equation of the undamped solid (spring-mass system). This equation is obtained from the Lagrange equation:

$$\frac{d}{dt}\left(\frac{\partial \mathscr{T}}{\partial \dot{\mathbf{q}}}\right) + \frac{\partial \mathscr{U}}{\partial \mathbf{q}} = \mathbf{F_{nc}} \tag{2.11}$$

where $\mathscr{T}$ is the kinetic energy of the system, $\mathscr{U}$ is the elastic energy, $\mathbf{q}$ is a vector containing the degrees of freedom of the system and $\mathbf{F_{nc}}$ is the non-conservative forces vector. The general dynamic equation of the system is described below:

$$\mathbf{M}\ddot{\mathbf{q}} + \mathbf{K}\mathbf{q} = \mathbf{F_{nc}}, \tag{2.12}$$

being $\mathbf{M}$ the mass matrix and $\mathbf{K}$ the stiffness matrix of the system. In the general case of the aeroelastic problem, the mass and stiffness matrix and the non-conservative force present a nonlinear term and must be updated at every time step. Nevertheless, the structure might be considered linear for simplicity and cost efficiency, and the aerodynamic model might be simplified for many applications.

Concerning the aeroelastic phenomena, the aerodynamic non-conservative forces depend on the deformation state of the structure, the frequency of the motion, and the aerodynamic performance of the cross-section. These nonlinear loads are complicated to model. Complex phenomena such as boundary layer detachment, vortex shedding, and transient effects must be considered for correctly modeling the loads. In addition, the aerodynamic forces are coupled with the motion. As a consequence, the aerodynamic effects might damp or amplify the vibrations. There is a particular interest in determining the amplifying events or unstable conditions. The following sections describe, for simplified case studies, the primary instabilities studied in the present work: divergence, flutter, and stall flutter.

2.4.1 Static instability: divergence

Divergence is related to an abrupt twist increase due to an elevated free stream velocity. A typical section of the structure is defined for analyzing this static instability. This simplified section is a flat plate airfoil immersed in a flow field with velocity V_∞. The cross-section twist θ is restricted by a torsional stiffness K_θ.

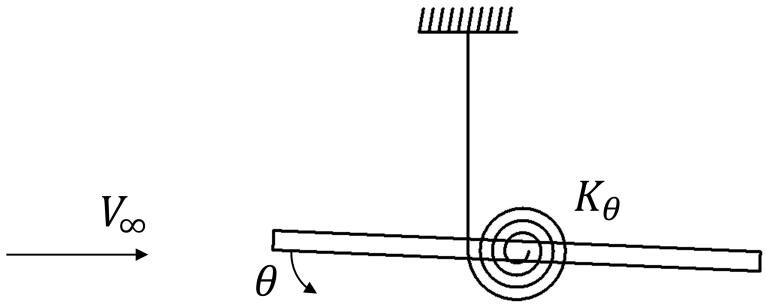

Fig. 2.3 **Typical section of the static aeroelasticity.** The scheme shows a typical airfoil under a free stream condition V_∞. The twist of the airfoil, θ is limited by a torsional stiffness, K_θ.

The dynamic system, Equation (2.12), is simplified for describing only a torsional degree of freedom under steady conditions. This equation is written as follows:

$$-\frac{1}{2}\rho_\infty V_\infty^2 c^2 c_m = K_\theta \theta, \tag{2.13}$$

where c is the chord of the airfoil, and c_m is the aerodynamic pitching moment. The pitching moment is defined, for a simplified linear aerodynamic model, as a function of the angle of attack:

$$c_m = c_{m_0} + c_{m_\alpha}\alpha + a_d\left(c_{l_0} + c_{l_\alpha}\alpha\right), \tag{2.14}$$

being α the instantaneous angle of attack, and a_d the nondimensional distance from the aerodynamic reference point to the location of the torsional stiffness. In addition, c_{m_0} and c_{l_0} are the initial pitching moment and lift coefficient, and c_{m_α} and c_{l_α} are their derivatives with respect to the angle of attack. The instantaneous angle of attack is defined in the counter-wise direction of the instantaneous twist, θ:

$$\alpha = -\theta. \tag{2.15}$$

Substituting the aerodynamic coefficient in Equation 2.13, the value of the twist angle is obtained as follows:

$$\theta = \frac{c_{m_0} + a_d c_{l_0}}{c_{m_\alpha} + a_d c_{l_\alpha} - \frac{K_\theta}{\frac{1}{2}\rho_\infty V_\infty^2 c^2}}. \tag{2.16}$$

The value of the twist angle tends to infinity when the divergence velocity V_D is reached:

$$c_{m_\alpha} + a_d c_{l_\alpha} - \frac{K_\theta}{\frac{1}{2}\rho_\infty V_\infty^2 c^2} = 0 \rightarrow V_D = \sqrt{\frac{2K_\theta}{\rho_\infty c^2 \left(c_{m_\alpha} + a_d c_{l_\alpha}\right)}} \tag{2.17}$$

Notice that in the aerodynamic center, the slope of the pitching moment is null, $c_{m_\alpha} = 0$. Therefore, the divergence velocity is only feasible when the aerodynamic center is located ahead of the elastic axis of the airfoil. In addition, the previous solution has been obtained assuming a linear aerodynamic model. However, for a real airfoil, the aerodynamic behavior is nonlinear. Thus, the twisting angle cannot increase infinitely. Nevertheless, under divergence conditions, the structure presents abrupt deformations, which can lead to structural failure.

2.4.2 Linear dynamic instability: flutter

Flutter is another catastrophic aeroelastic effect that can lead to structural failure. This phenomenon is created by positive feedback between the structure deformation and the aerodynamic loads acting on the aerodynamic surface. Therefore, an amplified oscillatory motion is established in the structure. In order to illustrate the phenomenon, the simplest case of flutter, two degrees of freedom model, is defined in Figure 2.4.

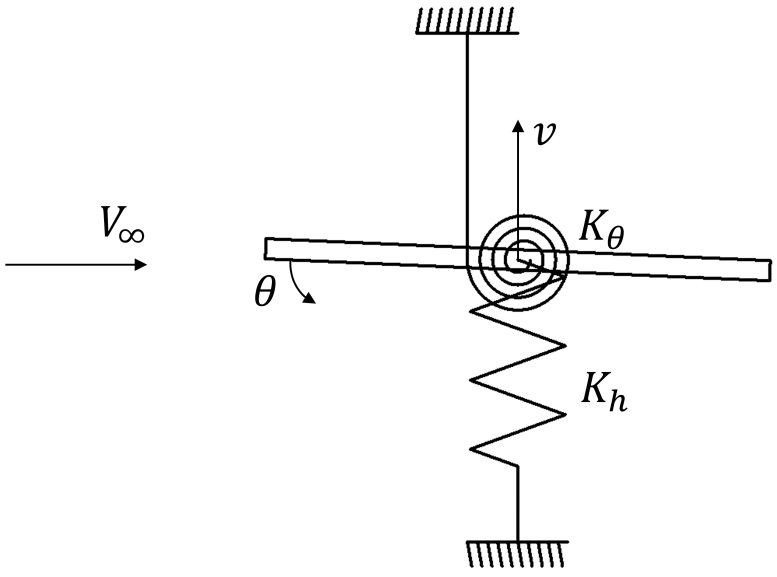

Fig. 2.4 **Typical section for the dynamic aeroelasticity.** The scheme shows a typical airfoil under a free stream condition V_∞. The twist of the airfoil, θ, is limited by a torsional stiffness, K_θ, and its deflection v is restricted by a linear stiffness K_h.

In this case, Equation 2.12 is modified to describe a plunging-pitching airfoil. The dynamic behavior of the two degrees of freedom section is defined in Equation 2.18.

$$\begin{bmatrix} I_\theta & S_\theta \\ S_\theta & m \end{bmatrix} \begin{Bmatrix} \theta \\ v \end{Bmatrix} = \begin{Bmatrix} -\frac{1}{2}\rho_\infty V_\infty^2 c^2 c_m \\ \frac{1}{2}\rho_\infty V_\infty^2 c c_l \end{Bmatrix} \tag{2.18}$$

Here, the section inertia is defined with I_θ, its mass with m, the mass unbalance with S_θ, the vertical displacement of the airfoil with v, and the lift coefficient with c_l. The mass constants are defined as follows:

$$I_\theta = \int \rho_s x_c^2 dx_c, \qquad S_\theta = -\int \rho_s x_c dx_c, \qquad m = \int \rho_s dx_c, \tag{2.19}$$

where x_c is the chord-wise coordinate of the cross-section. Assuming a linear steady aerodynamic model, a solution with an exponential shape is obtained:

$$\theta = \overline{\theta} e^{p_f t}, \qquad v = \overline{v} e^{p_f t}, \tag{2.20}$$

where the amplitude of the twist and deflection of the section are $\overline{\theta}$ and $\overline{v}$, respectively. Equation 2.18 can be expressed as follows for a linear steady aerodynamic model:

$$\begin{bmatrix} I_\theta p_f^2 + K_\theta - \frac{1}{2}\rho_\infty V_\infty^2 c^2 \left(c_{m_\alpha} + a_d c_{l_\alpha}\right) & S_\theta p_f^2 \\ S_\theta p_f^2 + \frac{1}{2}\rho_\infty V_\infty^2 c c_{l_\alpha} & m p_f^2 + K_h \end{bmatrix} \begin{Bmatrix} \bar{\theta} \\ \bar{v} \end{Bmatrix} e^{p_f t} = \begin{Bmatrix} -\frac{1}{2}\rho_\infty V_\infty^2 c^2 \left(c_{m_0} + a_d c_{l_0}\right) \\ \frac{1}{2}\rho_\infty V_\infty^2 c^2 c_{l_0} \end{Bmatrix} \tag{2.21}$$

The homogeneous solution of the previous equation is calculated, and the exponent factor p_f is obtained. The characteristics of this complex number determine the behavior of the system. The system is stable if the exponent p_f has a negative real part. Unstable conditions are reached when the real part of p_f becomes positive. In addition, the exponent imaginary part determines the oscillatory nature of the phenomenon. The real and imaginary parts of exponent p_f are expressed for the different free stream reduced velocities in the diagrams $Re(p_f) - V_\infty/\omega_\theta c$ and $Im(p_f) - V_\infty/\omega_\theta c$, being ω_θ the natural torsion vibration angular frequency.

Figure 2.5 presents an example of these diagrams. The diagram shows a simple case where flutter and divergence conditions are reached. The system presents a stable behavior for low free stream velocity, and neutral damped oscillations, $Re(p_f) = 0$. Flutter conditions are reached for a free stream velocity of $V_F = 2.96\omega_\theta c$. Note that the real part of some curves becomes positive while they still have a non-zero imaginary part (square marker). For higher

velocities, $V_D = 4.05\omega_\theta c$, their imaginary part gets a null value, producing a non-oscillatory behavior known as divergence (triangle marker).

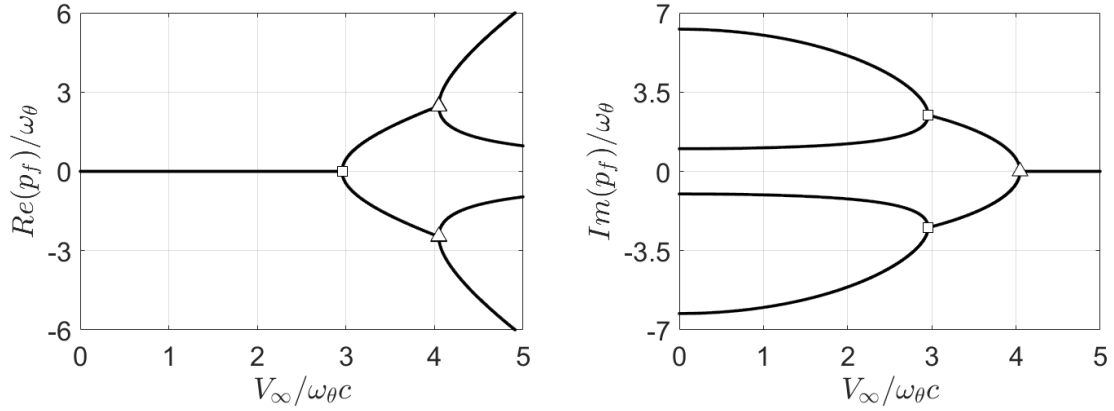

Fig. 2.5 **Flutter curves for a simple steady aerodynamics problem.** The curves indicate the real and the imaginary terms of the variable p_f. The squares indicate the flutter conditions, while the triangles show the divergence.

2.4.3 Nonlinear dynamic instability: stall flutter

The previous sections described linear aeroelastic instabilities, divergence, and flutter. Nevertheless, when the incidence of the cross-section of the structure is high enough, the flow around the suction side presents a partial or total separation from the surface which occurs periodically during the oscillation. During the oscillation, the low-velocity vortex is shed periodically from the separation point. This non-linearity in the aerodynamic forces may increase the amplitude of the vibrations producing the so-called stall flutter. This mechanism contrasts with the classical flutter in which the relationship and delay between aerodynamic and elastic forces dominate the phenomenon.

Stall flutter is of primary importance in the analysis of bluff bodies in which the separation of the boundary layer occurs for low-incidence angles. For instance, this phenomenon has been studied for a vast number of applications such as bridge decks [48], cables [49], and wings [50].

Different mechanisms are related to the stall flutter. When stall flutter occurs, two different behaviors can be obtained due to their aerodynamic behavior. Some systems present an amplitude that smoothly grows with time. This process is the so-called soft flutter. Soft flutter progressively increases the amplitude with time, leading to large oscillations or an equilibrium value.

In contrast to the previous mechanism, flutter may appear as a self-sustaining oscillation for some conditions where the amplitude immediately reaches large finite values. The structure is expected to grow beyond a critical vibratory amplitude. This phenomenon is called hard flutter.

References

[1] Pedro Manuel Quintero Igeño. *Characterization of Fluid Structure Interaction Mechanisms and its application to the vibroacoustic phenomena.* PhD thesis, June 2019.

[2] Olga V. Korotkaya. Substructure method for thermal-stress analysis of liquid-propellant rocket engine combustion chamber. *International Journal of Aerospace and Mechanical Engineering*, 8(4):739–742, 2014.

[3] Vladislav M Anisimov, Ivan A Zubrilin, and Mikhail Y Orlov. Investigation of thermal and stress states of the annular combustion chamber flame tube walls. In *Turbo Expo: Power for Land, Sea, and Air*, volume 49767, page V04BT04A021. American Society of Mechanical Engineers, 2016.

[4] Chaobin Hu and Xiaobing Zhang. A fluid-structure coupling method to obtain parameter distributions in a combustion chamber with moving boundaries. *Applied Thermal Engineering*, 141:1048–1054, 2018. ISSN 1359-4311.

[5] J. Pei, F.-K. Benra, and H. Dohmen. Application of different strategies of partitioned fluid-structure interaction simulation for a single-blade pump impeller. *Proceedings of the Institution of Mechanical Engineers, Part E: Journal of Precess Mechanical Engineering*, 226(4):297–308, 2012.

[6] Hyun-Su Kang and Youn-Jea Kim. Optimal design of impeller for centrifugal compressor under the influence of one-way flid-structure interaction. *Journal of Mechanical Science and Technology*, 30(9): 3953–3959, 2016.

[7] S. Huo, H. Huang, D. Huang, Z. Liu, and H. Chen. Modal characteristics and fluid-structure interaction vibration response of submerged impeller. *Journal of Vibration and Control*, 28(15-16):2020–2031, 2022.

[8] K. Wijesooriya, D. Mohotti, A. Amin, and K. Chauhan. An uncouple fluid structures interaction method in the assessment of structureal responses of tall buildings. *Structures*, 25:448–462, 2020.

[9] K. Wijesooriya, D. Mohotti, A. Amin, and K. Chauhan. Comparison between an uncoupled one-way and two-way fluid structure interaction simulation on a super-tall slender structure. *Engineering Structures*, 229:111636, 2021.

[10] H. Mazaheri, A.H. Nambdar, and A. Amiri. Behavior of a smart one-way micro-valve considering fluid-structure interaction. *Journal of Intelligent material Systems and Structures*, 29(20):3960–3971, 2018.

[11] M.J. de C. Henshaw, K.J. Badcock, G.A. Vio, C.B. Allen, J. Chamberlain, I. Kaynes, G. Dimitriadis, J.E. cooper, M.A. Woodgate, A.M. Rampurawala, D. Jones, C. Fenwick, A.L. Gaitonde, N.V. Taylor, D.S. Amor, T.A. Eccles, and C. J. Denley. Non-linear aeroelastic prediction for aircraft applications. *Progress in Aeroespace Sciences*, 43:65–137, 2007.

[12] Joseba Murua, Rafael Palacios, J. Michael, and R. Graham. Applications of the unsteady vortex-lattice method in aircraft aeroelasticity and flight dynamics. *Progress in Aeroespace Sciences*, 55:46–72, 2012.

[13] Rafic M. Ajaj, Muhammed S. Parancheerivilakkathil, Mohammadreza Amoozgar, Michael I. Friswell, and Wesley J. Cantwell. Recent developments in the aeroelasticity of morphing aircraft. *Progress in Aeroespace Sciences*, 120:100682, 2021.

[14] Martin Otto Laver Hansen, Jens Nørkær Sørensen, S Voutsinas, Niels Sørensen, and H Aa Madsen. State of the art in wind turbine aerodynamics and aeroelasticity. *Progress in aerospace sciences*, 42(4):285–330, 2006.

[15] Pinting Zhang and Shuhong Huang. Review of aeroelasticity for wind turbine: Current status, research forcus and future perspectives. *Frontiers in Energy*, 5:419–434, 2011.

[16] Lin Wang, Xiongwei Liu, and Athanasios Kolios. State of the art in the aeroelasticity of wind turbine blades: Aeroelastic modelling. *Renewable and Sustainable Energy Reviews*, 64:195–210, 2016.

[17] Luca Formaggia, Alexandra Moura, and Fabio Nobile. On the stability of the coupling of 3d and 1d fluid-structure interaction models for blood flow simulations. *ESAIM: Mathematical Modelling and Numerical Analysis*, 41(4):743–769, 2007.

[18] Boyang Su, Liang Zhong, Xi-Kun Wang, Jun-Mei Zhang, Ru San Tan, John Carson Allen, Soon Keat Tan, Sangho Kim, and Hwa Liang Leo. Numerical simulation of pationent-specific left ventricular model with both mitral and aortic valves by fsi approach. *Computer Methods and Programs in Biomedicine*, 113:474–482, 2014.

[19] Marco Fedele, Elena Faggiano, Luca Dedè, and Alfio Quarteroni. A patient-specific aortic valve model based on moving resistive immersed implicit surfaces. *Biomech Model Mechanobiol*, 16:1779–1803, 2017.

[20] Nhan T. Nguyen, Kevin Reynlds, Ting Eric, and Natalia Nguyen. Distributed Propulsion Aircraft with Aeroelastic Wing Shaping Control for Improved Aerodynamic Efficiency. *Journal of Aircraft*, pages 1–19, 2018.

[21] S. Yao, M. Chetan, D. T. Griffith, A. S. Escalera Mendoza, M. S. Selig, D. Martin, Sepideh Kianbakh, Kathryn Johnson, and E. Loth. Aero-structural design and optimization of 50 MW wind turbine with over 250-m blades. *Wind Engineering*, 46:273–295, 2021.

[22] Xu-Hui He, Hao Ding, Hai-Quan Jing, Fang Zhang, Xiao-Ping Wu, and Xiao-Jun Weng. Wind-induced vibration and its suppression of photovoltaic modules supported by suspension cables. *Journal of Wind Engineering & Industrial aerodynamics*, page 104275, 2020.

[23] A Chizfahm, E Azadi Yazdi, and M Eghtesad. Dynamic modeling of vortex induced vibration wind turbines. *Renewable Energy*, 121:632–643, 2018.

[24] Chapter 1 - introduction. In Shigehiko Kaneko, Tomomichi Nakamura, Fumio Inada, Minoru Kato, Kunihiko Ishihara, Takashi Nishihara, and Mikael A. Langthjem, editors, *Flow-induced Vibrations (Second Edition)*, pages 1–28. Academic Press, Oxford, second edition edition, 2014. ISBN 978-0-08-098347-9. doi: https://doi.org/10.1016/B978-0-08-098347-9.00001-1.

[25] Earl H Dowell, RH Scanlan, F Sisto, HC Curtiss Jr, and H Saunders. A modern course in aeroelasticity. 1981.

[26] Masaki Kameyama and Hisao Fukunaga. Optimum design of composite plate wings for aeroelastic characteristics using lamination parameters. *Computers & structures*, 85(3-4):213–224, 2007.

[27] George Platanitis and Thomas W Strganac. Suppression of control reversal using leading-and trailing-edge control surfaces. *Journal of guidance, control, and dynamics*, 28(3):452–460, 2005.

[28] Steven J Hollowell and John Dugundji. Aeroelastic flutter and divergence of stiffness coupled, graphite/epoxy cantilevered plates. *Journal of Aircraft*, 21(1):69–76, 1984.

[29] Peter Dunn and John Dugundji. Nonlinear stall flutter and divergence analysis of cantilevered graphite/epoxy wings. *AIAA journal*, 30(1):153–162, 1992.

[30] Xinzhong Chen, Masaru Matsumoto, and Ahsan Kareem. Time domain flutter and buffeting response analysis of bridges. *Journal of Engineering Mechanics*, 126(1):7–16, 2000.

[31] S. Timoshenko and J.N. Goodier. *Theory of Elasticity*. Engineering Societies Monographs, 1982.

[32] E.J. HEARN. Mechanics of materials 1 (third edition). Butterworth-Heinemann, Oxford, third edition edition, 1997. ISBN 978-0-7506-3265-2. doi: https://doi.org/10.1016/B978-075063265-2/50000-1.

[33] Jean P. Mercier, Gérald Zambelli, and Wilfried Kurz. *Chapter 6 - Elastic behaviour of solids*. Elsevier, Oxford, 2002. ISBN 978-2-84299-286-6. doi: https://doi.org/10.1016/B978-2-84299-286-6.50012-3.

[34] James R Barber. *Elasticity*. Springer, 2002.

[35] Gerald Wempner. *Mechanics of solids with applications to thin bodies*, volume 2. Springer Science & Business Media, 1982.

[36] Antonio Crespo Martínez. *Mecánica de fluidos*. S.A. Ediciones Paraninfo, 2006.

[37] John F Douglas, Janusz M Gasiorek, John A Swaffield, and Lynne B Jack. *Fluid mechanics*. Pearson education, 2005.

[38] Bruce Roy Munson, Theodore Hisao Okiishi, Wade W Huebsch, and Alric P Rothmayer. *Fluid mechanics*. Wiley Singapore, 2013.

[39] Osborne Reynolds. An experimental investigation of the circumstances which determine whether the motion of water shall be direct or sinuous, and of the law of resistance in parallel channels. *Philosophical Transactions of the Royal society of London*, 174:935–982, 1883.

[40] A. N. Kolmogorov. Local structure of turbulence in an incompressible fluid at very high Reynolds numbers. *Dokl. Akad. Nauk.*, SSSR (30):9–13, 1941.

[41] J. Kim, P. Moin, and R. Moser. Turbulence statistics in fully developed channels flows at low Reynolds numbers. *Journal of Fluid Mechanics*, 177:133–166, 1987.

[42] Osborne Reynolds. Iv. on the dynamical theory of incompressible viscous fluids and the determination of the criterion. *Philosophical transactions of the royal society of london.(a.)*, (186):123–164, 1895.

[43] Joseph Smagorinsky. General circulation experiments with the primitive equations: I. the basic experiment. *Monthly weather review*, 91(3):99–164, 1963.

[44] A Ro Collar. The expanding domain of aeroelasticity. *The Aeronautical Journal*, 50(428):613–636, 1946.

[45] Weiwei Zhang and Zhengyin Ye. Control law design for transonic aeroservoelasticity. *Aerospace Science and Technology*, 11(2-3):136–145, 2007.

[46] RM Botez. Morphing wing, uav and aircraft multidisciplinary studies at the laboratory of applied research in active controls, avionics and aeroservoelasticity larcase. *Aerospace Lab*, (14):1–11, 2018.

[47] Rauno Cavallaro and Rocco Bombardieri. Studies on lateral-directional coupled flight dynamics and aeroelasticity of a prandtlplane. In *AIAA Scitech 2019 Forum*, page 1118, 2019.

[48] YJ Ge, ZX Lin, FC Cao, JB Pang, and HF Xiang. Investigation and prevention of deck galloping oscillation with computational and experimental techniques. *Journal of Wind Engineering and Industrial Aerodynamics*, 90(12-15):2087–2098, 2002.

[49] John HG Macdonald and Guy L Larose. Two-degree-of-freedom inclined cable galloping—part 1: General formulation and solution for perfectly tuned system. *Journal of Wind Engineering and Industrial Aerodynamics*, 96(3):291–307, 2008.

[50] Norizham Abdul Razak, Thomas Andrianne, and Grigorios Dimitriadis. Flutter and stall flutter of a rectangular wing in a wind tunnel. *AIAA journal*, 49(10):2258–2271, 2011.

Chapter 3

Computational simulation of aeroelastic phenomena

3.1 Introduction to the computational simulation

In Chapter 2, the physics and the main equations of the fluid-solid interaction phenomena were presented. As previously explained, aeroelasticity is a complex physical problem that combines the aerodynamic effects of the flow with the inertial and elastic forces acting on the structure. The complexity of the phenomena requires the use of experimental tests or numerical simulations for its characterization.

From the numerical perspective, different tools and methodologies have been proposed to model the fluid-structure coupled problem. FSI simulations require the calculation of structural and fluid dynamic equations. Concerning the former, finite element analysis (FEA) has been widely used to obtain the internal stress and strain of the structure of any given geometry [1]. For instance, Kumari and Sinha [2] analyzed the carbon fiber reinforced fiber T-shape joint between the spar and the lower skin of a wing, and Kesel et al. [3] studied the mechanical aspects of insect wings using FEA. For the resolution of the fluid conservation equations, the most extended tool for generic aerodynamic analysis is the so-called computational fluid dynamics (CFD). The flow fields (velocity, pressure, temperature) are calculated using numerical algorithms in any possible laminar or turbulent flow geometry. In fact, Li et al. [4] demonstrated that different fidelity levels of CFD simulations could predict the experimental results regarding force and power in a wind turbine rotor. Other works, such as those performed by Palacios et al. [5], use the results of the CFD simulations for correcting the aerodynamic linear models. Both solvers have been coupled in order to resolve the FSI problem.

Two different methodologies could be used to couple the equations: classical and integrated [6, 7]. The classical methodology is based on combining the solid and the fluid equations in an uncoupled way. However, the integrated methodology solves both equations simultaneously. In order to account for the energy transfer required for simulating the aeroelastic physics, an integrated or partially-integrated solver is required [8, 9]. Partially-integrated algorithms have been applied to the aeroelastic problem for a wide range of applications. For example, Kaviani and Nejat [10], Dai et al. [11] calculated the aeroelastic behavior of horizontal axis wind turbines, and Nakata and Liu [12] simulated flexible insect wings. The coupled solution of the aeroelastic system is associated with an out-of-order computational cost. Thus, as previously mentioned, the fully coupled three-dimensional simulation of an elastic solid and a viscous flow is not affordable at the initial stages of the design process [13].

In order to reduce the complexity of the problem and, consequently, its computational cost, many authors have proposed simplifications on the fundamental equations of the solid and the fluid. From the structural perspective, the most common simplification is dimensional reduction. Thin-walled structures are simplified to a shell or membrane in many applications to reduce the computational cost associated with the simulation [14, 15]. Another common approach for slender structures is the use of beam models. Beam elements have been applied to isotropic and orthotropic materials. In fact, Carrera et al. [16] applied a unified formulation to obtain the vibrational state of a rotating blade, and Farsadi et al. [17] applied the Librescu composite thin-walled beam (TWB) theory [18] to the optimization of the aeroelastic response of a wing. Finally, some simple structures, such as the typical section presented in Figures 2.3 and 2.4, reduce the three-dimensional solid to a two-dimensional typical section restricted by a set of springs [19, 20]. These models have been traditionally used for solving aeroelastic phenomena (see the classical reference of Dowell et al. [21]). However, it requires that a single bending and torsion mode dominates the vibration of the structure. Thus, the typical section is unsuitable for simulating secondary vibration modes or structural coupling.

As presented in Chapter 2, the partial differential equations describing fluid motion present a high complexity for providing a numerical solution. The simulation of all the turbulent scales requires an unacceptable computational cost, and their use is restricted to simple cases [22, 23]. In addition, these simulations generate a large amount of data, becoming more common in the simulations running in the petabyte scale [24]. The practical limitations of the DNS have motivated the simplification of the turbulent equations. The advances in computation and algorithms are allowing for the use of high-fidelity methods (LES) in industry [25]. These methods are standard in predicting sound production as the

model can provide enough spatial and temporal accuracy [26]. However, although some works have applied the LES to the FSI simulations [27, 28], this high-fidelity resolution is still unaffordable for an industrial calculation. In order to reduce the computational cost, all the turbulence scales can be modeled (RANS models). Using RANS and unsteady RANS (URANS) CFD is a common practice for many applications [29, 30].

Although RANS models present an acceptable cost for the aerodynamic calculation resolution and can predict three-dimensional and nonlinear effects of the flow, many authors have used or implemented simplified methods. A common approach is the use of inviscid flows. For instance, Peng and Jinglong [31] and Banks et al. [32] solved the Euler and deformable body equations for simulating the FSI problem. To decrease the computational cost of the three-dimensional algorithms, surface methodologies such as the vortex-lattice method (VLM) or Prandtl lifting line theory (LLT) can be employed [33]. Jeon et al. [34] applied the VLM to wind turbines, while Murua et al. [35] joined the solver with a nonlinear beam model to solve the aeroelastic behavior of a flexible aircraft. Other authors, such as Spall et al. [36], utilized the LLT for calculating aerodynamic forces on sails. Aerodynamic reduced order models are also applied to obtain rotating blade loads, being the blade element momentum (BEM) theory widely applied to the calculation of propellers [37, 38] and wind turbines [39, 40].

In addition to the previous models, in the 1930s Theodorsen [41] derived the expressions of the unsteady aerodynamic coefficients of an oscillating airfoil. These effects were obtained for a potential flow, applying a Kutta condition [42] and Bessel functions [43]. Theodorsen theory provides a solution in the frequency domain, which has been employed for the aeroelastic calculation of rotor blades [44], bridge decks [45] or wing [46] flutter. Nevertheless, although this model works accurately for the linear aerodynamic range near stall, the results could be improvable. Therefore, Leishman and Beddoes [47] proposed the so-called Leishman-Beddoes (L-B) method for calculating the aerodynamics of the unsteady nonlinear airfoil. The L-B model is based on the thin airfoil theory. However, this theory includes semiempirical corrections to include inviscid stall effects. Its main use is related to rotating aerodynamics. For instance, Gupta and Leishman [48] calculated the effects of the dynamic stall in a rotating airfoil, and Hansen et al. [49] used a similar formulation for wind turbine aeroelasticity.

Despite the previous models, many authors have developed different Reduced Order Models (ROMs) to simplify the CFD simulations or to include complex nonlinear effects [50]. A significant amount of them is based on proper orthogonal decomposition (POD). These methods have been proven accurate in a wide range of problems: optimization of a compressor [51] or aeroelastic calculation of a wing [52]. Nevertheless, POD “ROMs

are only suitable for a frozen aeroelastic model configuration" [50]. This fact is due to the associated frequencies of the ROM, which are dependent upon the mass and stiffness distribution. Therefore, any change in the structure will lead to a different motion and eigenvalues of the flow field and, thus, to a different POD.

Artificial intelligence (AI) and artificial neural networks (ANN) have been demonstrated to predict a wide range of physical phenomena in recent years. A clear example is the work of Vinuesa and Brunton [53], where machine learning (ML) algorithms were used to accelerate DNS simulations. Moreover, some authors have applied ANN to solve aerodynamic [54] and aeroelastic problems. For instance, Wu and Kareem [55] modeled the hysteretic nonlinear behavior of bridge decks under aerodynamic loads. This work calculates the nonlinearities in the turbulent flow around the solid by splitting the aerodynamic coefficients into a static and a dynamic term. A problem with using ANNs is the need to train the model. Some authors, as Chen et al. [56], have calculated the aeroelastic behavior of the system using an ANN fed with experimental data. In other papers, as the work published by Abbas et al. [57] and Li et al. [58], the ANN is fitted using CFD results. In addition, the previous authors have presented models based on different architectures. Abbas et al. [57] used a feed forward network (FFN), while Li et al. [58] applied a long-short term memory (LSTM) network. Nevertheless, most of the studies do not compare the FFN, which only uses the information of the current time step, with the LSTM, which maintains the information of the previous time steps. Their applicability is determined by evaluating the convenience, precision, and limitations of each typology.

This chapter shows the main computational tools for simulating aeroelastic problems. First, the computational tools for simulating three-dimensional problems are presented. The work focuses on the coupled simulations between the FEA and the CFD. The mathematical formulation of both theories is presented, focusing on the models used for practical applications. Then, the ROMs developed along the work are described and derived. The structural and aerodynamic simplifications are presented, the AI framework is described, and the algorithms are detailed in the following sections.

3.2 Three-dimensional simulation of aeroelastic phenomena

3.2.1 Computational fluid dynamics: CFD

The complexity of the fluid conservation equations forbids the use of analytical solutions for the resolution of a general problem. This section describes the numerical tools and

algorithms used to resolve the CFD simulations. The total resolution of the conservation equations, Equations (2.7), (2.8) and (2.9), requires excessive computational resources. In order to simplify the equations, the turbulence transportation can be partially (LES) or totally modeled (RANS and URANS). This section focuses on describing the Reynolds averaged Navier–Stokes models.

In order to simplify the turbulent equations, the Reynolds decomposition is applied to the velocity vector. The velocity is divided into an average velocity vector $\langle \mathbf{v} \rangle$ and a fluctuating velocity vector $\mathbf{v}'$:

$$\mathbf{v} = \langle \mathbf{v} \rangle + \mathbf{v}' \tag{3.1}$$

The simplification is presented for an incompressible flow for the sake of brevity and because, along the work, the compressible effects of the air will not be analyzed. The velocity vector is substituted into the mass and momentum equations, Equations (2.7) and (2.8). The calculation of the mean of the mass equation for an incompressible flow results in the following expressions as the mean fluctuating flow field is null:

$$\nabla \langle \mathbf{v} \rangle = 0 \qquad \nabla \mathbf{v}' = 0. \tag{3.2}$$

The same operation is applied to the momentum equation:

$$\frac{\partial \rho_f \langle \mathbf{v} \rangle}{\partial t} + \langle \mathbf{v} \rangle \nabla \left(\rho_f \langle \mathbf{v} \rangle \right) = -\nabla \langle p \rangle + \nabla \langle \tau \rangle + \mathbf{R}_T + \rho_f \mathbf{b}, \tag{3.3}$$

where $\langle p \rangle$ is the mean pressure of the flow, $\langle \tau \rangle$ is the mean shear stress tensor and $\mathbf{R}_T$ the Reynolds stress tensor. In the equation the temporal variation is calculated by $\frac{\partial \rho_f \langle \mathbf{v} \rangle}{\partial t}$, the advection term $\langle \mathbf{v} \rangle \nabla \left(\rho_f \langle \mathbf{v} \rangle \right)$, the diffusive term $\nabla \langle \tau \rangle$, the source term $-\nabla \langle p \rangle + \rho_f \mathbf{b}$ and the turbulent term $\mathbf{R}_T$. The mean shear stress tensor of the diffusive term is calculated as follows:

$$\left\langle \tau_{ij} \right\rangle = \mu \left(\frac{\partial \langle v_i \rangle}{\partial x_j} + \frac{\partial \langle v_j \rangle}{\partial x_i} \right) \tag{3.4}$$

and the Reynolds stress tensor is defined as:

$$R_{T_{ij}} = -\frac{\partial \left\langle v_i' v_j' \right\rangle}{\partial x_j}. \tag{3.5}$$

The Reynolds stress tensor is directly related to the generation of drag [59], and the regions of the flow with a higher Reynolds stress have been demonstrated to be crucial for understanding

turbulent transport [60]. Including the Reynolds stress in the equations adds extra degrees of freedom. Therefore, additional equations are required to solve the system. These equations are called turbulence models. Some of the most popular are Spallar-Allmaras, $k-\varepsilon$, and $k-\omega$. These are eddy viscosity models and are based on the analogy between the molecular gradient-diffusion process and the turbulent motion:

$$\mathbf{R}_T = 2\mu_T \frac{1}{2}\left(\nabla\langle\mathbf{v}\rangle + \nabla\langle\mathbf{v}\rangle^T\right) - \frac{2}{3}\left(\mu_T \nabla\langle\mathbf{v}\rangle\right)\mathbf{I}, \tag{3.6}$$

where, μ_T is the turbulent eddy viscosity and $\mathbf{I}$ is the identity matrix. For the different turbulent models, the value of μ_T is derived from transport equations. Note that Equation (3.6) does not include the anisotropy of the model. For these reasons, some models include nonlinear constitutive relations.

The $k-\omega$ model with shear stress transport (SST) has been used in this work. This model comprises two equations that solve the turbulent kinetic energy k and the specific dissipation rate per unit of turbulent kinetic energy ω to determine the turbulent eddy viscosity [61]. The main advantages of the $k-\omega$ are the performance under adverse pressure gradients and the possibility of applying it to viscous-dominated regions. Nevertheless, the computations are sensitive to the values of ω in the free stream (values of the inlet of internal flow). Adding a non-conservative cross-diffusion term, Menter [62] addressed the sensitivity on the ω values, formulating the so-called shear stress transport (SST) model. The equations defining this model are presented below:

$$\frac{\partial k}{\partial t} + \mathbf{v}\nabla k = G_1 - G_2 k\omega + \nabla\left(\left(\nu + G_3\nu_T\right)\nabla k\right) \tag{3.7}$$

$$\frac{\partial \omega}{\partial t} + \mathbf{v}\nabla\omega = G_4 - G_5\omega^2 + \nabla\left(\left(\nu + G_6\nu_T\right)\nabla\omega\right) + G_7\frac{1}{\omega}\nabla k\nabla\omega, \tag{3.8}$$

where the variables G_1, G_2, G_3, G_4, G_5, G_6 and G_7 are closure parameters and auxiliary relations of the model and ν_T, is the kinematic eddy viscosity, which is a function of k and ω [62].

The PDE system must be converted into an algebraic equation system for the numerical simulation of the previous equations. In order to convert the system, the domain is discretized to a finite number of elements (mesh). The equations might be resolved using different mathematical schemes and algorithms. The methodology followed for generating the mesh and evaluating its adequacy will be presented in Section 3.2.1.

Segregated and coupled resolution of the equations

Throughout the work, two different approaches were used for calculating the conservation equations: segregated and coupled solvers. The segregated solver calculates the mass and momentum conservation equations sequentially. The solution of the equations is obtained iteratively for the velocity and the pressure. The most common segregated algorithms are SIMPLE and PISO. Figure 3.5 presents the workflow for both methods. Both algorithms share many steps. However, they present some differences. The PISO is faster in the short time-steps and becomes unstable in the long. The accuracy of the SIMPLE is reduced for long time steps, although it produces steady results. Therefore, in the present document, SIMPLE is used for the steady solution, while PISO is used for the transient solutions with greater temporal accuracy. The coupled solver calculates the conservation equations simultaneously as a vector of equations. The system of equations can be solved using explicit or implicit integration.

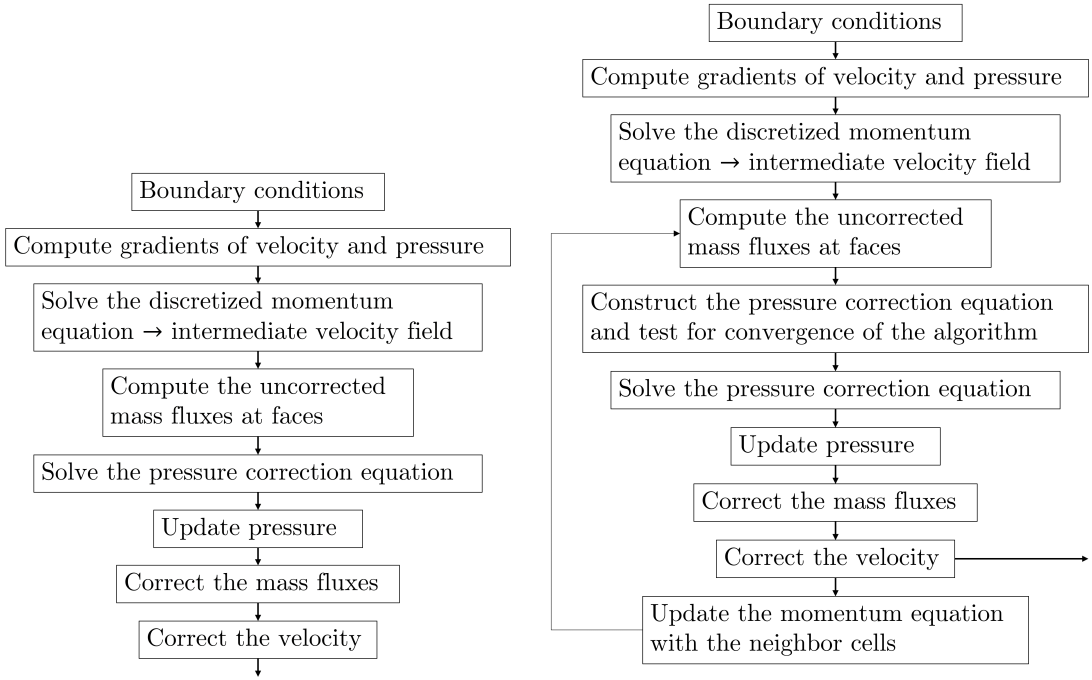

Fig. 3.1 **Algorithm of the segregated solvers.** SIMPLE algorithm (left) and PISO algorithm (right).

Numerical integration schemes of the advection term

Relative to the numerical simulation of the terms of the equation, the advection terms are integrated using a second-order upwind scheme. The convective flux is computed as:

$$\left(\dot{m}_f \zeta\right)_f = \begin{cases} \dot{m}_f \zeta_{f,0} & \text{for } \dot{m}_f \geq 0 \\ \dot{m}_f \zeta_{f,1} & \text{for } \dot{m}_f < 0 \end{cases}, \tag{3.9}$$

where ζ represents the transport of any property, $\dot{m}_f$ the mass flow, and the face values $\zeta_{f,0}$ and $\zeta_{f,1}$ are interpolated from the cell center values on the side faces:

$$\zeta_{f,0} = \zeta_0 + s_0 \left(\nabla\zeta\right)_{r,0}, \qquad \zeta_{f,1} = \zeta_1 + s_1 \left(\nabla\zeta\right)_{r,1} \tag{3.10}$$

being s_0 and s_1 the spatial discretization:

$$s_0 = x_f - x_0, \qquad s_1 = x_f - x_1. \tag{3.11}$$

The values of the reconstruction gradients ($\left(\nabla\zeta\right)_{r,0}$ and $\left(\nabla\zeta\right)_{r,1}$ are limited, so they do not exceed the maximum and minimum of the neighboring cell centroid values. A scale factor α_{lim} is defined. The Venkatakrishnan limiter has been used for the simulations of this work [63].

$$\left(\nabla\zeta\right)_{r,0} = \alpha_{\text{lim}} \nabla\zeta \tag{3.12}$$

Numerical integration schemes of the diffusive term

Relative to the numerical integration of the diffusive terms, the diffusive flow through an internal cell face of any flow variable is discretized as follows:

$$D_f = \left({}_d \nabla\zeta \mathbf{a}\right)_f, \tag{3.13}$$

being ${}_d$ the face diffusivity, $\nabla\zeta$ the gradient of the fluid property ζ and $\mathbf{a}$ the area vector. A second-order expression for an interior face gradient is used:

$$\nabla\zeta_f = \left(\zeta_1 - \zeta_0\right) \frac{\mathbf{a}}{\mathbf{a}\mathbf{d_s}} + \overline{\nabla\zeta} - \left(\overline{\nabla\zeta}\mathbf{d_s}\right) \frac{\mathbf{a}}{\mathbf{a}\mathbf{d_s}}, \tag{3.14}$$

where:

$$\mathbf{d_s} = \mathbf{x_1} - \mathbf{x_0}, \qquad \overline{\nabla\zeta} = \frac{\nabla\zeta_0 + \nabla\zeta_1}{2} \tag{3.15}$$

This formulation assumes that the centroids 0 and 1 lie on the opposite sides of the inner faces, and the area vector points out of cell 0. The angle between the vectors $\mathbf{a}$ and $\mathbf{d_s}$ is smaller than 90 degrees to avoid nonphysical solutions.

Numerical integration of the transient term

The resolution of the transient term requires the use of an additional discretization. The solution is divided into time steps, depending on the previous ones. The transient simulations calculated in this work use a second-order Euler implicit integration. This scheme uses the solution at the current $n+1$ and in the previous two n and $n-1$ time steps in a backward differentiation formula:

$$\frac{d}{dt}(\zeta V_i) = \left(\frac{3}{2}(\zeta V_i)_{n+1} - 2(\zeta V_i)_n + \frac{1}{2}(\zeta V_i)_{n-1}\right)\frac{1}{\Delta t} \tag{3.16}$$

where V_i is the volume of the element.

Computation of gradients

In the CFD simulation, a hybrid Gauss-least squares method is used. In this methodology, the gradient is computed as follows:

$$\nabla\zeta = \sum_f (\zeta_n - \zeta_0)\, w_f^0 \tag{3.17}$$

where w_f^0 is a weighted average of the Gauss and the least squares methods:

$$w_f^0 = \beta_f w_f^{\text{lsq}} + \left(1-\beta_f\right) w_f^G \tag{3.18}$$

The variable β_f is the gradient factor of the cell. The value of the factor w_f^{lsq} computed by the least squares method is calculated as:

$$w_f^{\text{lsq}} = \left(\sum_f \frac{\mathbf{d_s}\otimes\mathbf{d_s}}{\mathbf{d_s}^2}\right)^{-1}\frac{\mathbf{d_s}}{\mathbf{d_s}^2}, \tag{3.19}$$

being d_s the distance between the centroids of the cell 0 and the neighboring cell n through the face f. The value of the factor is also calculated using the Gauss method w_f^G:

$$w_f^G = \frac{A_f}{V_0+V_n}, \tag{3.20}$$

where A_f is the face area and V_0 and V_n the volumes of elements 0 and n respectively.

Methodology of the CFD simulation

Once the PDE system underlying the CFD software is explained, the fluid dynamics analysis methodology will be described. This procedure comprises the preprocessing of the cases. The

methodology for meshing the domain is described, the calculation error must be delimited, and the model requirements must be addressed.

The preprocessing of the CFD simulation requires the discretization of the domain. The meshes of the present work use polygonal elements [64] for the bi-dimensional simulations and polyhedral elements [65] for the three-dimensional cases. Generating these meshes requires a similar cost compared with the wide-used tetrahedral meshes. However, the number of elements may be five times fewer, leading to a lower computational cost of the calculation.

The meshes are refined near the zones of interest using a set of bodies of influence. Figure 3.2 shows an example of the polygonal mesh used to calculate airfoil aerodynamics. Similar procedures are followed for the three-dimensional analysis.

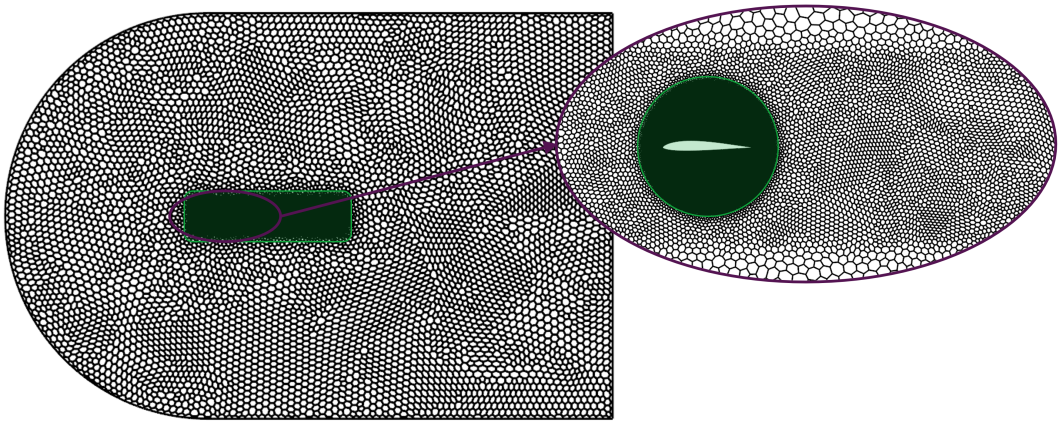

Fig. 3.2 **Refinement example based on bodies of influence of the CFD mesh.** Note that the green areas mark the bodies of influence of the mesh and its zoom on the interest section.

In addition, the numerical error of the simulation must be limited to a maximum value of the interest variables. This procedure, known as mesh independence analysis, is required to verify the validity of the numerical results. The mesh independence analysis is performed by duplicating the number of grid cells and checking the error to the finest mesh. In order to obtain the error concerning the real value, Richardson's extrapolation (RE) is applied [66]. The solution error is defined as the difference between the numerical and the exact solution:

$$\text{Error} = f(h_g) - f_{\text{Exact}} = H_1 h_{gc}^p + \text{H.O.T.}, \tag{3.21}$$

where H_1 is a constant, h_g the grid spacing and p_c the order of convergence. In the case of the CFD solver, the order of convergence is normally lower than the expected theoretical value. The previous equations can be expressed as follows:

$$\log(\text{Error}) = \log H_1 + p_c \log h_g. \tag{3.22}$$

The order of convergence p_c can be calculated from the simulation data. However, for a more straightforward definition, a constant grid refinement ratio r_g can be assumed:

$$p_c = \ln\left(\frac{f_3 - f_2}{f_2 - f_1}\right) / \ln r_g, \tag{3.23}$$

where the values of f_i are the solutions of the different meshes, being the number 1 the finest and 3 the coarsest. Then the RE is applied:

$$f = f_{h_g=0} + g_1 h_g + g_2 h_g^2 + g_3 h_g^3 + ..., \tag{3.24}$$

where g_i is a function independent of the grid spacing and $f_{h_g=0}$ is the continuum value at zero grid spacing. The value of $f_{h_g=0}$ is estimated as follows:

$$f_{h_g=0} \approx f_1 + \frac{f_1 - f_2}{r^2 - 1}. \tag{3.25}$$

The grid refinement ratio is calculated, assuming a finer grid spacing h_{g1} and h_{g2}, as:

$$r = \frac{h_{g2}}{h_{g1}} \tag{3.26}$$

Then a grid convergence index (GCI) is obtained. For calculating the GCI, three levels of refinement are required. The GCI of the finer mesh is defined as:

$$\text{GCI}_{\text{fine}} = \frac{F_s \text{Error}_r}{r_{g\,c}^p - 1} \tag{3.27}$$

being $\text{Error}_r = \frac{f_{i+1} - f_i}{f_i}$ the relative error. The value of the safety factor F_s is recommended to be $F_s = 3$ for comparing two grids and $F_s = 1.25$ for comparing three or more grids. For a coarser grid, the GCI is defined as follows:

$$\text{GCI}_{\text{coarse}} = \frac{F_s \text{Error}_r r_{g\,c}^p}{r_{g\,c}^p - 1} \tag{3.28}$$

Then, the results must be checked to be in the asymptotic range of convergence. This condition is satisfied when:

$$\mathrm{GCI}_{23} = \mathrm{GCI}_{12} r_{gc}^{p} \tag{3.29}$$

If this condition is satisfied, the value of the interest variable is determined to be f_1 with an error band of GCI_{12}.

In addition to spatial discretization is temporal discretization. The time-step definition is related to the Courant-Friedrich-Lewy number. This number is defined as a function of the time-step Δt, the cell velocity $\mathbf{v}$ and the cell size Δx:

$$\mathrm{CFL} = \frac{\Delta t \mathbf{v}}{\Delta x} \tag{3.30}$$

This time step must be low enough to simulate the flow field accurately. To check the adequacy of the time step, simulations with different values should be calculated, ensuring that the value of Δt is not affecting the results.

In addition, to meet the wall treatment of the turbulence model, an appropriate boundary layer discretization is required in CFD calculation. The correct application of the SST model requires a nondimensional wall distance of the first cell in the viscous sublayer ($y^+ < 5$) or in the logarithmic layer ($y^+ > 30$) using wall-treatment functions. The nondimensional wall distance is defined as $y^+ = \frac{y u_\tau}{\nu}$, being $u_\tau = \frac{\sqrt{\tau_w}}{\rho_f}$ the friction velocity and τ_w the shear stress.

3.2.2 Finite elements analisys: FEA

The finite element analysis is a common tool in resolving the elasticity equations presented in Chapter 2. The finite element method (FEM) is a robust algorithm for calculating the approximate solution of partial differential equations in continuous problems.

The method is based, similarly to the CFD solvers, on the discretization of the domain. The equations are solved for the values on the grid points. In order to solve the PDE, a set of shape functions is used for interpolating the result inside the elements. Then, the functions are integrated along the elements, reducing the order of the derivatives with integration by parts. These shape functions allow FEM to present a continuous solution. The PDE used in the structural analysis includes derivatives up to the second order. Therefore, the integral form presents first-order derivatives. For this reason, the shape functions must ensure continuity on the space coordinates. The shape functions are defined in the element normal coordinates. Along the work, hexahedral elements were used, Figure 3.3. The shape functions for a linear hexahedral element are defined below:

$$H_M(\xi_i) = \frac{1}{8}(1 + \xi_{iM}\xi_i), \text{ where } M = 1, ..., 8 \tag{3.31}$$

where the proportional constant corresponding to node M is denoted by H_M, the local coordinate of the element frame by ξ_i, and the coordinate of the node M by ξ_{iM}. Nevertheless, the linear elements cannot provide enough mode shapes to approximate shear and bending in solid mechanics. For this reason, to overcome this effect known as locking, and to avoid stiffening effects, these elements add three additional vectors $\mathbf{u}_{oi}$ to the nodal displacement $\mathbf{u}_M$:

$$\mathbf{u}(\xi_i) = H_M(\xi_i)\,\mathbf{u}_M + \mathbf{u}_{oi}\left(1-\xi_i^2\right), \text{ where } i = 1,2,3 \text{ and } M = 1,...,8. \tag{3.32}$$

In order to improve the accuracy of the numerical solver, quadratic elements could be used. In addition, for thin-walled structures, shell elements can be used. These elements allow a dimensional reduction and, thus, a decrease in the computational cost of the simulation. The mathematical simplification of the shell elements will be discussed later.

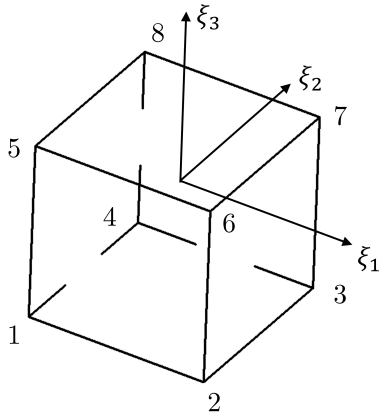

Fig. 3.3 **Visualization of the generic hexahedral element.** The variables ξ_1, ξ_2 and ξ_3 are the inner coordinates of the elements.

The shape functions are defined in the cell frame. Therefore, the shape functions must be transformed into the global frame to compute the solution in the global coordinates. Figure 3.4 shows the transformation from the element reference frame to the global reference frame.

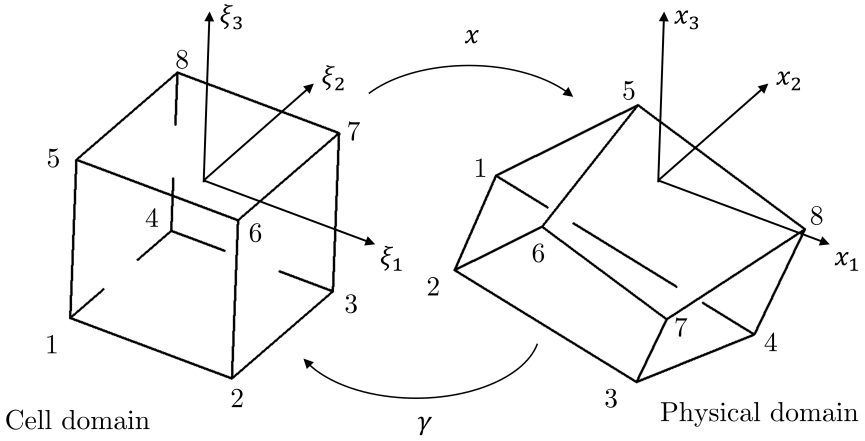

Fig. 3.4 **Transformation of the hexahedral element from the element reference frame to the global reference frame.** Note that the elements are defined in a local reference frame and assembled in a global reference frame.

The Green-Lagrange strain is then calculated from the displacement on the nodes:

$$\delta \mathbf{D}_M = \mathbf{B}_M \delta \mathbf{u}_M, \tag{3.33}$$

where $\mathbf{D}_M$ is the strain tensor, $\mathbf{u}_M$ the displacement vector and $\mathbf{B}_M$ the matrix that relates the strain and the displacement. This matrix is approximated as follows for infinitesimal displacements:

$$\mathbf{B}_M = \begin{bmatrix} \frac{\partial H_M}{\partial x_1} & 0 & 0 \\ 0 & \frac{\partial H_M}{\partial x_2} & 0 \\ 0 & 0 & \frac{\partial H_M}{\partial x_3} \\ \frac{\partial H_M}{\partial x_2} & \frac{\partial H_M}{\partial x_1} & 0 \\ 0 & \frac{\partial H_M}{\partial x_3} & \frac{\partial H_M}{\partial x_2} \\ \frac{\partial H_M}{\partial x_3} & 0 & \frac{\partial H_M}{\partial x_1} \end{bmatrix}, \tag{3.34}$$

where the derivatives of the shape function are calculated using the chain rule.

$$\frac{\partial H_M}{\partial \mathbf{x}} = \mathbf{J}^{-1} \frac{\partial H_M}{\partial \xi}, \text{ being } \mathbf{J} \text{ the jacobian: } \mathbf{J} = \begin{bmatrix} \frac{\partial x_1}{\partial \xi_1} & \frac{\partial x_1}{\partial \xi_2} & \frac{\partial x_1}{\partial \xi_3} \\ \frac{\partial x_2}{\partial \xi_1} & \frac{\partial x_2}{\partial \xi_2} & \frac{\partial x_2}{\partial \xi_3} \\ \frac{\partial x_3}{\partial \xi_1} & \frac{\partial x_3}{\partial \xi_2} & \frac{\partial x_3}{\partial \xi_3} \end{bmatrix} \tag{3.35}$$

The solution of the FEA is calculated to minimize the virtual work, $\delta\mathscr{W}$, of the system. The virtual work of an element is defined in Equation (3.36). This virtual work is produced by the internal loads, $\mathbf{f}_M^{\text{int}}$, the inertial terms, $\mathbf{M}$ and the external forces applied at a node M, $\mathbf{f}_M^{\text{ext}}$.

$$\delta\mathscr{W} = \delta\mathbf{u}_M^T \left[\int_{V_0} \mathbf{B}_M^T \mathbf{S}_M dV + \int_{V_0} H_M \mathbf{I} \rho_s H_M^T \ddot{\mathbf{u}}_M dV - \int_{V_0} H_M \mathbf{b} dV - \int_{S_0} H_M \mathbf{t} dS - \int_{l_0} H_M \mathbf{q}_f dl - \mathbf{f}_M \right] = 0. \tag{3.36}$$

The solution of the dynamic system follows Equation (2.12). The stiffness matrix is obtained from the internal forces.

$$\mathbf{K} = \frac{\partial \mathbf{f}_M^{\text{int}}}{\partial \mathbf{u}_M}, \text{ defining the internal force } \mathbf{f}_M^{\text{int}} \text{ as: } \mathbf{f}_M^{\text{int}} = \int_{V_0} \mathbf{B}_M^T \mathbf{S}_M dV \tag{3.37}$$

Note that the the element stress tensor $\mathbf{S}_M$ as stated in Chapter 2 may be related to the discrete strain tensor $\mathbf{D}_M$ by the constitutive matrix $\mathbf{C}_M$. In order to obtain the characteristics of the dynamic system, the stiffness matrix can be calculated using the constitutive relationships, and the mass matrix is obtained from the inertial term:

$$\mathbf{K} = \int_{V_0} \mathbf{B}_M^T \mathbf{C}_M \mathbf{B}_M dV, \qquad \mathbf{M} = \int_{V_0} H_M \mathbf{I} \rho_s H_M^T dV \tag{3.38}$$

In addition, the external loads acting in the discrete system are a result of the volumetric forces $\mathbf{b}$, surface tractions $\mathbf{t}$, line loads $\mathbf{q}$ and point forces $\mathbf{f}_M$:

$$\mathbf{f}_M^{\text{ext}} = \int_{V_0} H_M \mathbf{b} dV + \int_{S_0} H_M \mathbf{t} dS + \int_{l_0} H_M \mathbf{q}_f + \mathbf{f}_M \tag{3.39}$$

Notice that loads of the previous equations and the restrictions of the problem are applied through Dirichlet and Neumann boundary conditions.

Shell finite element method

The normal stress in the wall-normal direction can be assumed to be negligible for thin-walled structures. For this reason and to reduce the computational cost of the simulations, the shell FEM might be applied. Additionally, this theory assumes that the faces normal to the shell surface will remain undeformed. The kinematic relationships are modified in order to follow the previous assumptions:

$$u_1(x_1,x_2,x_3) = u_{m_1}(x_1,x_2) - x_3\frac{\partial u_{m_3}(x_1,x_2)}{\partial x_1} \tag{3.40}$$

$$u_2(x_1,x_2,x_3) = u_{m_2}(x_1,x_2) - x_3\frac{\partial u_{m_3}(x_1,x_2)}{\partial x_2} \tag{3.41}$$

$$u_3(x_1,x_2,x_3) = u_{m_3}(x_1,x_2) \tag{3.42}$$

Note that u_{m_1}, u_{m_2}, u_{m_3} are the displacements of the midplane, $\mathbf{u}_m$. Then, the deformations of the system are calculated similarly to Equation (3.33). Evaluating the terms of the strain tensor independently, the following expressions are obtained for the normal strains:

$$\varepsilon_{x_1} = \frac{\partial u_1}{\partial x_1} = \frac{\partial u_{m_1}}{\partial x_1} - x_3\frac{\partial^2 u_{m_3}}{\partial x_1^2} = \varepsilon_{m_{x_1}} - x_3\frac{\partial^2 u_{m_3}}{\partial x_1^2} \tag{3.43}$$

$$\varepsilon_{x_2} = \frac{\partial u_2}{\partial x_2} = \frac{\partial u_{m_2}}{\partial x_2} - x_3\frac{\partial^2 u_{m_3}}{\partial x_2^2} = \varepsilon_{m_{x_2}} - x_3\frac{\partial^2 u_{m_3}}{\partial x_2^2} \tag{3.44}$$

$$\varepsilon_{x_3} = \frac{\partial u_3}{\partial x_3} = 0 \tag{3.45}$$

and relative to the tangential strains:

$$\gamma_{x_1x_2} = \frac{\partial u_1}{\partial x_2} + \frac{\partial u_2}{\partial x_1} = \frac{\partial u_{m_1}}{\partial x_2} + \frac{\partial u_{m_2}}{\partial x_1} - 2x_3\frac{\partial^2 u_{m_3}}{\partial x_1 \partial x_2} = \gamma_{m_{x_1x_2}} - 2x_3\frac{\partial^2 u_{m_3}}{\partial x_1 \partial x_2} \tag{3.46}$$

$$\gamma_{x_2x_3} = \frac{\partial u_2}{\partial x_3} + \frac{\partial u_3}{\partial x_2} = -\frac{\partial u_3}{\partial x_2} + \frac{\partial u_3}{\partial x_2} = 0 \tag{3.47}$$

$$\gamma_{x_1x_3} = \frac{\partial u_1}{\partial x_3} + \frac{\partial u_3}{\partial x_1} = -\frac{\partial u_3}{\partial x_1} + \frac{\partial u_3}{\partial x_1} = 0 \tag{3.48}$$

In the previous equations, two different terms are obtained: the membrane, which depends on u_1 and u_2, and the bending, which depends on u_3. Therefore, the solution can be analyzed as two uncoupled problems, the membrane problem, a bi-dimensional elastic problem, and the bending problem.

Methodology of the FEA

As with the CFD methodology, the FEA requires converting the PDE system into an algebraic problem. Therefore, the domain must be discretized into a set of grid elements. The

solution of the system is calculated for the values of the displacement on the nodes and then interpolated with the shape functions inside the elements.

Along this work, most of the structures present thin walls. Therefore, the use of a shell FEM is preferred. Nevertheless, as the coupled FSI problem has been calculated in proprietary software which does not admit shell elements, both meshes have been used along the document.

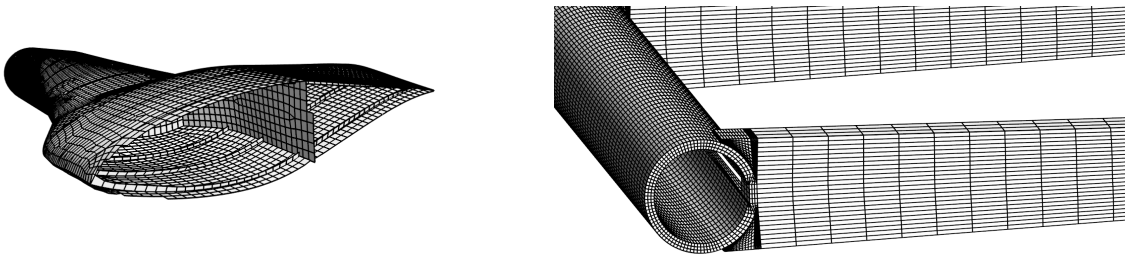

Fig. 3.5 **Examples of multielement FEM meshes.** (left) Shell element mesh of a wind turbine blade, (right) internal 3D mesh of the internal elements of the sail-type structure. Note that the different elements present a separated mesh which joints the neighboring element by a bonded contact.

When the finite element simulations are analyzed, their accuracy must be ensured. The accuracy of the FEM calculation is related to the order of the elements and the number of elements. In other words, a second-order element will improve the solution of the first-order element and substantially increase the number of elements. A mesh convergence analysis is performed before the calculation of the problem. In this procedure, the magnitude of interest, in the case of the aeroelastic analysis, the displacement, is analyzed through finer meshes until the number of elements is not affecting the results, in a similar process as explained for the CFD.

In addition, for multi-layer composite materials or multi-component problems, the elements are assembled using bonded contacts. The bonded contact restricts the movement of the bodies so they cannot separate, slide or rotate. In other words, the components act like a single solid. The contact is generated surface-to-surface in the case of the three-dimensional simulation and edge-to-surface in the case of the shell structure.

3.2.3 Fluid structure interaction: FSI

In order to couple the solid and the fluid solution, two different approaches can be followed: monolithic and segregated [67]. The former calculates the solid and the fluid equations using the same solver. This approach is coupled (integrated) and stable. It allows the use of higher-time steps. However, its main drawback is the necessity of dedicated software,

which requires high computational resources. The second approach uses different software for solving fluid and solid equations. Along the work, separated solvers are used to solve the equations. The segregated approach is also subdivided depending on the direction of the coupling.

On the one hand, the classical methodology (one-way coupling) calculates the solution of the fluid. Then it applies the pressure and friction loads to the structure without modifying the geometry. For example, using the steady pressure field around a wing to calculate the stress of the material. This method is the most straightforward way of coupling. Nevertheless, its interest in aeroelastic phenomena is limited to specific applications in which the motion of the solid is not affecting the fluid around it. The workflow of the one-way-coupling is presented in Figure 3.6.

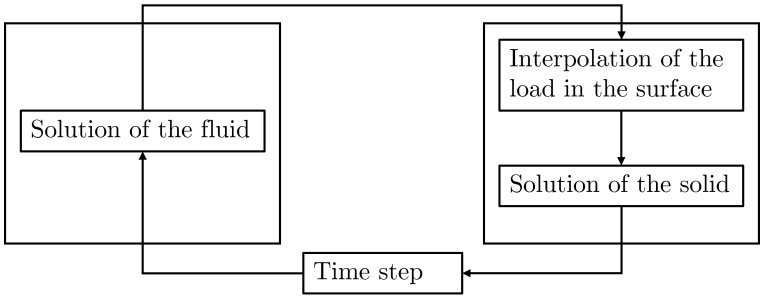

Fig. 3.6 **One-way workflow.** The solution of the fluid is solved and then the solid is calculated based on this solution without mesh deformation.

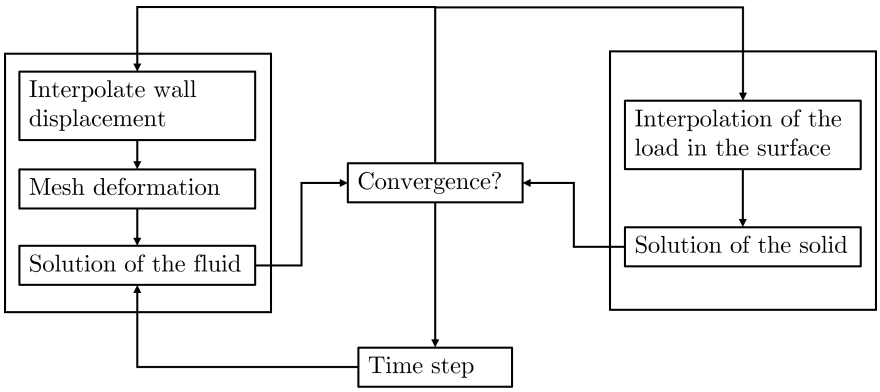

Fig. 3.7 **Two-way workflow.** A loop of convergence between the solid and the fluid is solved in each iteration. The fluid flow is calculated. Then the solid is deformed using the loads recalculated after the deformation. The reevaluations of the loop determine if the solver is implicit or explicit.

On the other hand, the partially-integrated methodology (two-way-coupling) uses the solution of the flow field to deform the structure. The geometry is modified, and the mesh is

updated to the displaced solid. Then, the flow field is recalculated for the next time step. If the coupling between the solid and the fluid only is updated in one inner iteration, they are explicitly coupled. However, if they are coupled in every internal iteration, they are implicitly coupled. Along the work, a partially-integrated algorithm of the CFD solver based on the finite volume method and the FEA for the structure was used. The forces are divided into a pressure and a shear component and mapped on the solid surface.

3.3 Reduced order models

The reduction of computational cost associated with the aeroelastic problem is obtained by simplifying the physical models of the solvers. The different aerodynamic and structural models used in the reduced-order models are presented in this section. Regarding the aerodynamic models, wing, and blade aerodynamics are explained. Their equations are derived from the first principles, and the final expressions are presented. Concerning the structure, two models are exposed. The first one reduces the complete three-dimensional solid to an equivalent section with rigid solid motion retained by a set of springs. The second one simplifies the structure into a beam model. Finally, the complete algorithm of the ROM is shown, describing the different functions and algorithms.

3.3.1 Aerodynamic models

The three-dimensional calculation of the aerodynamic loads acting on a structure requires a discretization in the order of 10M of elements. The computational cost of the CFD simulation is increased by the internal simulations resulting in coupling the physics. Therefore, the aeroelastic simulations are related to a high computational cost. When an airfoil is submerged in a flow field, a pressure imbalance is generated between its surfaces. As a result, an aerodynamic force is generated as a reaction to the flow deflection. A bi-dimensional airfoil simulation may be conducted to calculate this force. This simulation requires a low computational cost compared with a complete three-dimensional simulation. However, the prediction of loads of a single bi-dimensional airfoil does not match the real value of the aerodynamic forces. The pressure imbalance on the wing tip produces a flow in the spanwise direction, generating the so-called tip vortex. As a result, the effective local incidence of the cross-sections is reduced, and their aerodynamic efficiency is decreased. The induced drag is generated as a consequence of the generation of lift.

A three-dimensional characterization of this phenomenon requires the resolution of the three-dimensional flow around the structure. In this case, the complete conservation equation

system must be solved using CFD software. In order to simplify these calculations, the use of inviscid equations might be explored. Nevertheless, neglecting viscosity, and thus, turbulent flows, is only suitable for certain cases of study where the flow is slightly detached, and the aerodynamic lift is proportional to the angle of attack. Therefore, two steady models are proposed to consider these nonlinear effects. These models take the CFD-simulated bi-dimensional aerodynamic coefficients and correct their values by accounting for the three-dimensional effects. The finite wings aerodynamics is corrected using the Prandlt lifting line theory (LLT) [68], while the rotating aerodynamics is calculated using the beam element momentum theory (BEM) [69, 70].

In addition, a flexible structure imparts pitching and plunging motion on the cross-section of the beams. As a consequence of the motion of an airfoil, its wake and, thus, its aerodynamic forces are modified. The classical theory proposed by Theodorsen [41] calculates these transient effects by developing the potential theory.

The previous theories are combined in the document in order to simulate the steady and transient effects of the aerodynamic sections. This section presents the theoretical background of the aerodynamic submodels of the ROMs. Then, the models are used in practical applications for obtaining the results of the aeroelastic simulations of the structures.

Modeling of finite wings

The wing-tip effects were previously mentioned: in the case of a finite wing flying inside a free stream, the pressure difference between the pressure and the suction surfaces produces a vortex that extends downstream from the wing-tip. This vortex produces an additional velocity component that moves counter wise the lift force. This phenomenon, known as downwash, reduces the effective angle of attack of the sections at the same time as it induces drag. In other words, lift generation is directly related to drag production. The three-dimensional aerodynamic effects of a finite wing can be observed in Figure 3.8.

In order to simulate the three-dimensional effects of a wing, the tip vortex is included in the model by using the Prandtl finite wing lifting line theory (LLT). The methodology of the LLT method is based on the potential aerodynamics theory, which assumes an inviscid irrotational flow. This theory is based on the Kutta-Joukowski theorem, which assumes that the aerodynamic lift force F_L is proportional to the strength of the vortex that generates it, Γ_v.

$$F_L = \rho_\infty V_\infty \Gamma_v, \tag{3.49}$$

where ρ_∞ is the free stream density and V_∞ the free stream velocity. The theory substitutes the finite wing with bound vortices from tip to tip. The vortex filaments are assumed to

continue downstream. Due to Helmholtz's theorem, the vortex filament cannot end inside the fluid. Therefore, the vortex continues as two free vortices extending downstream (horseshoe vortex). Figure 3.9 presents the horseshoe definition of the wing. As can be observed in the figure, the tip effects of the wing produce that the intensity of the vortices near the tip is smaller than in the symmetry plane. This fact is related to the downwash velocity and the lower lift production in the tips.

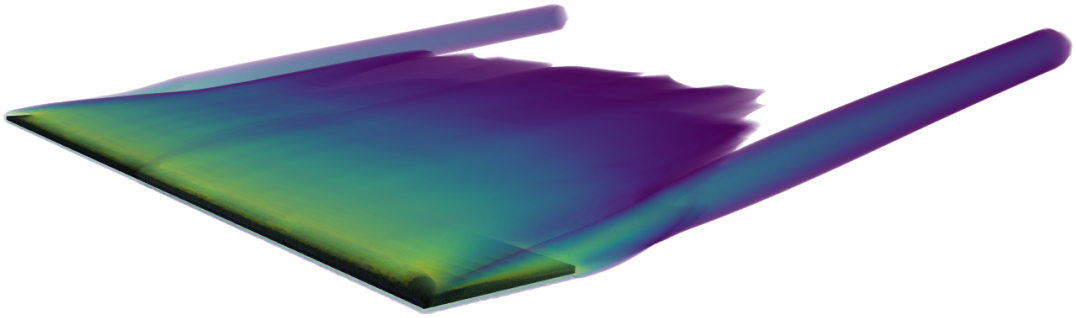

Fig. 3.8 **Visualization of the vorticity on a wing.** The figure shows the vorticity field around a squared cross-section airfoil wing. The vorticity has been calculated through a RANS simulation.

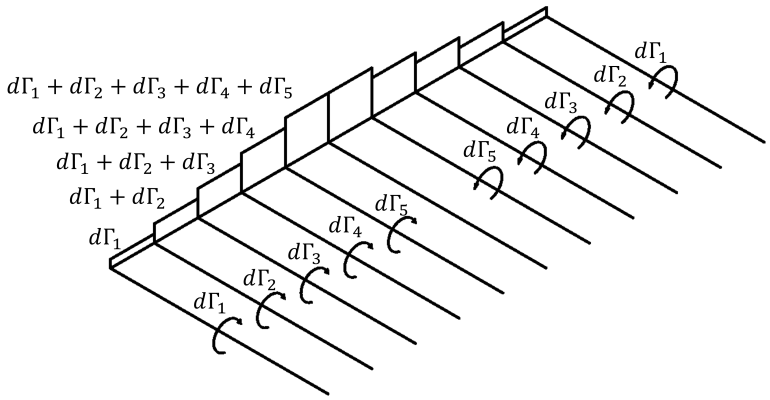

Fig. 3.9 **Horseshoe distribution of the finite wing.** Note that the horseshoe vortices extend downstream from the wing. The intensity of the vortex near the tip is smaller than in the symmetry plane. The vortex intensity line density of the vortex in the i horseshoe is expressed with Γ_i.

For any position in the spanwise direction, z_0, of the wing, the trailing vortices dz induce a velocity v_i whose magnitude is defined by the Biot-Savart law:

$$dv_i = -\frac{\frac{d\Gamma_v}{dz}dz}{4\pi(z_0 - z)}, \tag{3.50}$$

where $\frac{d\Gamma_v}{dz}$ is the variation of the vortex intensity along the spanwise direction, z_0 is the position in which the downwash velocity is calculated, and z the spanwise coordinate of the affecting vortex. Then, the induced velocity and angle of attack, α_i, at point z_0 are calculated by integrating the previous equation along the total wing span L.

$$v_i(z_0) = -\frac{1}{4\pi}\int_{-L_w}^{L_w}\frac{\frac{d\Gamma_v}{dz}}{z_0 - z}dz, \;\; \alpha_i(z_0) = tan^{-1}\left(\frac{v_i(z_0)}{V_\infty}\right) \approx \frac{v_i(z_0)}{V_\infty}. \tag{3.51}$$

The aerodynamic lift coefficient is calculated equating the lift slope, $c_{l\alpha}$, and the effective angle of attack, α_{eff}, with the Kutta-Jukowski principle for the horseshoe distribution:

$$c_l(z_0) = c_{l\alpha}(\alpha_{eff}(z_0) - \alpha_{L=0}), \;\; c_l(z_0) = \frac{2\Gamma_v(z_0)}{V_\infty c(z_0)}, \tag{3.52}$$

where the parameter $\alpha_{L=0}$ expresses the zero lift angle of attack and c is the chord of the airfoil. The effective angle of attack is calculated from the following equation:

$$\alpha_{eff}(z_0) = \alpha_g(z_0) - \alpha_i. \tag{3.53}$$

The effective angle of attack is the superposition of the geometric angle of attack α_g and the induced angle of attack. Combining the expressions in Equations (3.51), (3.52) and (3.53), the value of the geometric angle of attack is calculated below:

$$\alpha_g(z_0) = \frac{2\Gamma_v(z_0)}{c_{l\alpha}V_\infty c(z_0)} + \alpha_{L=0}(z_0) + \frac{1}{2c_{l\alpha}V_\infty}\int_{-L}^{L}\frac{\frac{d\Gamma_v}{dz}}{z_0 - z}dz \tag{3.54}$$

In a general lift distribution, the spanwise coordinate must be transformed, relating the spanwise coordinate with the angle φ:

$$z = -L\cos\varphi, \tag{3.55}$$

then, the intensity of the vortices is expressed as a sum of sins:

$$\Gamma_v(\theta) = 4LV_\infty\sum_{n=1}^{N}A_n\sin(n\varphi) \tag{3.56}$$

The lifting line problem is solved by calculating the A_n terms of Equation (3.56). Substituting the value of the vortex intensity in Equation (3.54), the system of equations can be solved for the N span points φ_0, Equation (3.57).

$$\alpha_g(\varphi_0) = \frac{8L}{c_{l\alpha}c(\varphi_0)} \sum_{n=1}^{N} A_n \sin(n\varphi_0) + \alpha_{L=0}(\varphi_0) + \frac{2\pi}{c_{l\alpha}} \sum_{n=1}^{N} nA_n \frac{\sin(n\varphi_0)}{\sin(\varphi_0)} \tag{3.57}$$

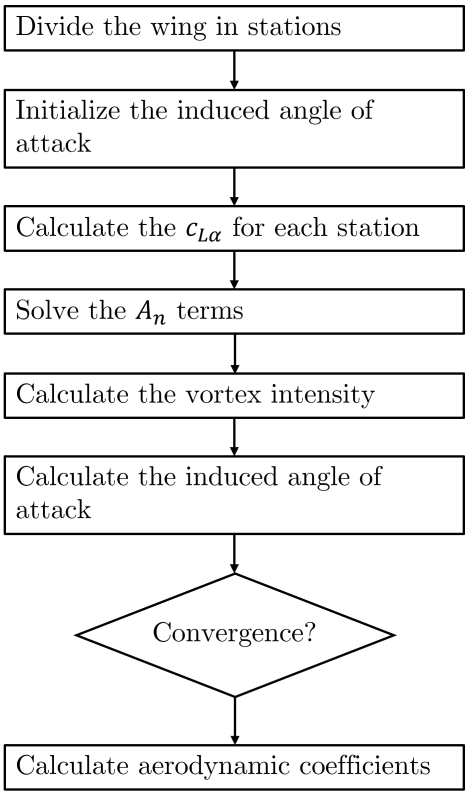

Fig. 3.10 **Workflow of the nonlinear LLT.** The nonlinear LLT is an iterative method that takes the aerodynamic information from the airfoil curves.

The previous equations have been derived for a potential flow. Thus, it is only suitable for linear aerodynamics and cannot simulate the nonlinear effects of the flow. A nonlinear LLT algorithm is applied to obtain the aerodynamic forces in the present work. This procedure takes the nonlinear aerodynamic coefficients from a bi-dimensional simulation. This iterative procedure is presented in Figure 3.10. The first stage of the method requires dividing the wing into a set of N sections in which the coefficients A_n are calculated. Then, the induced angle of attack is initialized. The iterative process starts by calculating the lift slope at the operating point of each stage. This step includes the nonlinear information in the calculations. Then,

the A_n terms and, thus, the vortex intensity are calculated. From this point, the corresponding downwash velocity and the induced angle of attack are trivial. If the error in the induced angle of attack does not match the required accuracy, the lift slope is reevaluated, and the process is repeated. Once the convergence of the method is ensured, the aerodynamic coefficients are calculated.

Modeling of rotating blades

The three-dimensional aerodynamic effects of the rotating blades are calculated using the blade element momentum theory (BEM). The BEM theory assumes that the blade can be considered as a finite number of independent stream tubes. The solver can account for the nonlinear aerodynamics of the airfoil and the induced velocity produced by the rotation and includes a model to simulate the stall delay of the rotating blade. A visualization of the complex aerodynamics of a rotating propeller is presented in Figure 3.11.

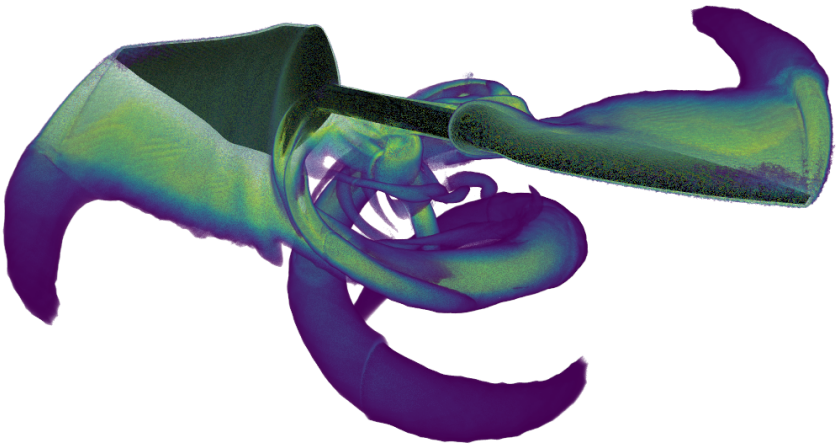

Fig. 3.11 **Visualization of the vorticity of the DA4022 propeller.** The blade is rotated immersed in a rotor plane-normal free stream. The flow is calculated using a RANS simulation.

The BEM theory assumes that the spanwise flow is negligible and the flow is axisymmetric. It is based on combining the blade element theory and the momentum conservation equation for obtaining the induced velocity. In other words, the total axial force obtained by integrating the airfoil loads equals the global axial force estimated by the momentum equation. The induced velocity is calculated from the previous relationship. BEM theory calculates the aerodynamic coefficients of the blade along its radial coordinate. Therefore, this methodology allows us to calculate the thrust produced and the power generated or consumed by the blades and can account for the effects of the rotation velocity. BEM analysis

requires determining the aerodynamic conditions in every single section of the blade. Figure 3.12 shows the schematic representation of the airfoil and the velocity components.

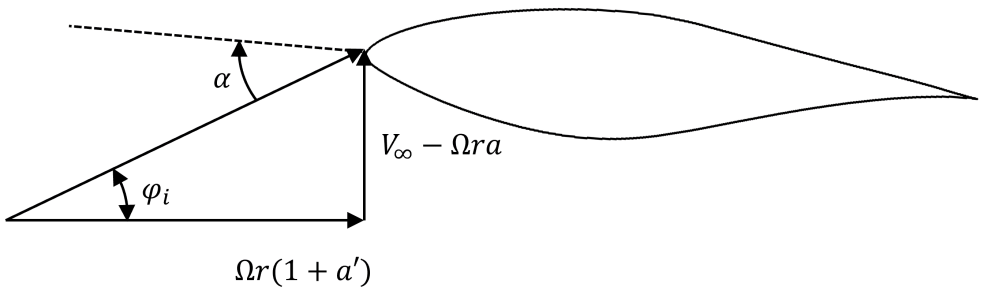

Fig. 3.12 **Schematic section of the blade.** The figure shows the velocity decomposition of a single-blade section. The parameter α is the angle of attack, V_∞ the free stream velocity, Ω the rotation velocity, r the radial position, a the disk-normal induced velocity ratio, and a' the tangential induced velocity ratio.

From the beam element perspective, the axial force F_N and the torque Q generated by an infinitesimal blade portion are obtained from their aerodynamic coefficients:

$$dF_N = \frac{N_b}{2}\rho_\infty V_{\text{rel}}^2 \left(c_l \cos(\varphi_i) + c_d \sin(\varphi_i)\right) c dr \tag{3.58}$$

$$dQ = \frac{N_b}{2}\rho_\infty V_{\text{rel}}^2 \left(c_l \sin(\varphi_i) - c_d \cos(\varphi_i)\right) c r dr, \tag{3.59}$$

where N_b is the number of blades, V_{rel} the airfoil relative velocity, r the radial position of the airfoil, c_d and c_l are the drag and lift coefficients respectively and φ_i is the induced angle. Equation (3.60) presents relative velocity and induced angle definitions.

$$V_{\text{rel}} = \sqrt{\left(V_\infty - (\Omega R a)\right)^2 + \left(\Omega r (1 + a')\right)^2}, \;\; \tan(\varphi_i) = \frac{V_\infty}{\Omega R}\frac{1-a}{1+a'}, \tag{3.60}$$

being a and a' the induced velocity factors in the disk normal and tangential directions. For wind turbines the induced velocity factors are defined as $a = \frac{v_i}{\Omega R}$ and $a' = \frac{v_{it}}{\Omega R}$. The normal and tangential induced velocities are denoted by v_i and v_{it}. For propellers, the factors are $a = -\frac{v_i}{\Omega R}$ and $a' \approx 0$. The induced velocities are calculated using the momentum theory. The value of the induced velocities in the normal disk direction is obtained by combining Equation (3.58) with the momentum theory, Equation (3.61). In contrast, the value in the disk tangential direction is calculated by combining Equations (3.59) and (3.62). The expressions

of the momentum theory force and torque are modified to include the induction factor on the plane of the rotor where the thrust coefficient is dependent [71].

$$dF_N = \begin{cases} \rho_\infty V_\infty^2 2a_w(1-a)\pi r F dr & a < \frac{1}{3} \\ \rho_\infty V_\infty^2 2a_w \pi r \left(1 - \frac{a}{2}(5-3a)\right) F dr & a \geq \frac{1}{3} \end{cases} \tag{3.61}$$

$$dQ = 4a'(1-a)\rho V_\infty \pi r^3 \Omega dr. \tag{3.62}$$

Here, the parameter a_w is the induced velocity in the wake. This parameter is related to the induced velocity in the rotor plane by Equation 3.63:

$$a = \frac{a_w}{2}\left(1 - \frac{a_w^2(1-a)}{4\left(\frac{R\Omega}{V_\infty}\right)^2 (a_w - a)}\right) \tag{3.63}$$

In equation 3.61, the tip-loss effects are included using the function F. This correction depends on the number of blades, the relative wind angle, and the position of the blade:

$$F = \left(\frac{2}{\pi}\right)\cos^{-1}\left[exp\left(-\left\{\frac{N_b(1-r/R)}{2(1-r/R)\sin(\varphi_i)}\right\}\right)\right] \tag{3.64}$$

In addition, the three-dimensional behavior of the blade generates extra lift and reduces drag compared to the two-dimensional airfoil. These effects have been corrected using equation (3.65) from Chaviaropoulos and Hansen [72].

$$c_{x,3D} = c_{x,2D} + 2.2(c/r)\cos^4(\theta)\Delta c_x \tag{3.65}$$

Here, $X = l, d, m$ references the lift, drag, and moment coefficients. The parameter Δc_x is calculated with Equation (3.66).

$$\Delta c_l = c_{l,\text{inviscid}} - c_{l,2D};\ \Delta c_d = c_{d,2D} - c_{d,2D-\min};\ \Delta c_m = c_{m,\text{inviscid}} - c_{m,2D} \tag{3.66}$$

Modeling of pitching and plunging airfoils

The aerodynamic forces acting on an airfoil are divided into quasi-steady and dynamic forces. The former is a consequence of the relative position of the airfoil in the flow. On the other side, the dynamic forces depend on the effects of the wake. When an airfoil moves perpendicular to the free flow, the fluid field is altered, modifying the aerodynamic loads and, according to the Kutta-Jokowski theorem, the circulation around the airfoil. For this reason, a vortex is generated in the trailing edge counter wise the airfoil vortex to maintain

the circulation constant, creating a circulation distribution in the wake. This evolution can be observed in Figure 3.13.

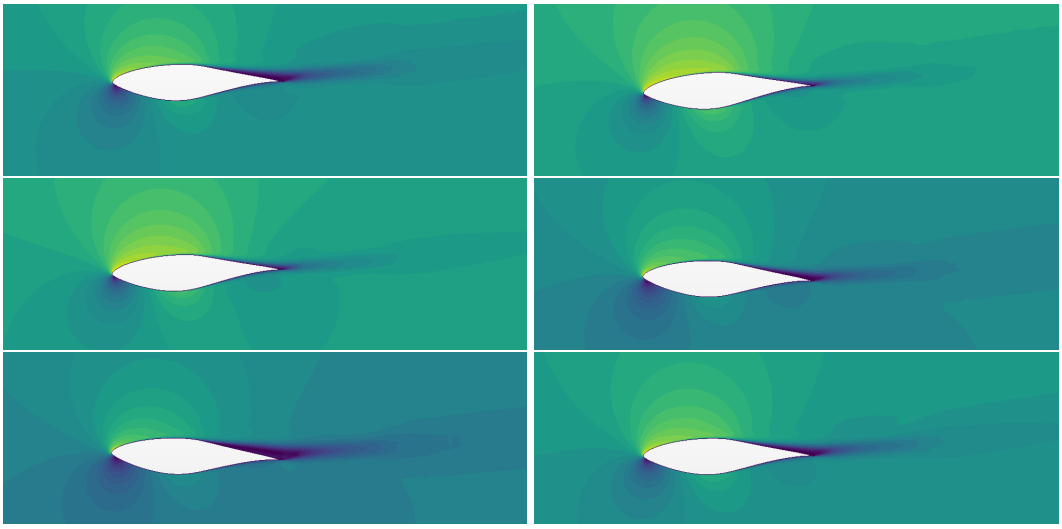

Fig. 3.13 **Visualization of the velocity field evolution of a pitching plunging airfoil.** The fields are calculated for an S809 airfoil with a pitching movement centered in 8 deg of incidence, an amplitude of 2.5 deg, and a plunging movement with an amplitude $0.1c$. The period of the pitching motion is 40% of the plunging oscillation. The temporal distance between the images is 20% of the pitching period. Results were obtained using a 2D URANS simulation.

Modeling the aerodynamic forces of pitching and plunging airfoils requires accounting for the quasi-steady effects and, for rapid maneuvers, the added-mass terms, which are included in the Theodorsen [41] model. For the former, the aerodynamic loads are multiplied by a frequency domain function called Theodorsen's transfer function. The expression of the aerodynamic lift is provided in Equation (3.67).

$$\begin{aligned} \hat{F}_L = \hat{F}_{La} + \hat{F}_{Lc}, \;\; \hat{F}_{La} &= \pi\rho_\infty \left(\frac{c}{2}\right)^2 \left[-\omega_f^2 \hat{v} + i\omega_f V_{\text{rel}} \hat{\alpha} + \frac{c}{2}\xi_{ea}\omega_f^2 \hat{\alpha}\right], \\ \hat{F}_{Lc} &= c_{l_\alpha}\rho_\infty V_{\text{rel}} \frac{c}{2} C(\kappa) \left[i\omega_f \hat{v} + V_{\text{rel}}\hat{\alpha} + \frac{c}{2}\left(\frac{1}{2} - \xi_{ea}\right) i\omega_f \hat{\alpha}\right], \end{aligned} \tag{3.67}$$

where $\hat{F}_{La}$ is the added-mass term of the lift and $\hat{F}_{Lc}$ the circulatory lift. The angular frequency of the aerodynamic force is denoted by ω_f and the nondimensional distance from the half chord to the elastic axis by ξ_{ea}. The symbol $\hat{}$ on the force, vertical displacement v, and angle of attack α denote that the frequency domain defines the magnitudes. Concerning

the pitching moment, a similar expression is used. The pitch moment, M_p is divided into a circulatory moment M_{pc} and an added mass moment M_{pa}:

$$\begin{aligned} \hat{M}_p &= \hat{M}_{pa} + \hat{M}_{pc}, \\ \hat{M}_{pa} &= \pi\rho_\infty \left(\frac{c}{2}\right)^2 \left[-\omega^2\, \xi_{ea}\frac{c}{2}\hat{h} - i\omega V_{\text{rel}} \left(\frac{1}{2} - \xi_{ea}\right)\hat{\alpha} + \left(\frac{c}{2}\right)^2 \left(\frac{1}{8} + \xi_{ea}^2\right)\omega^2\hat{\alpha}\right], \\ \hat{M}_{pc} &= c_{l_\alpha}\rho_\infty V_{\text{rel}} \left(\frac{c}{2}\right)^2 \left(\frac{1}{2} + \xi_{ea}\right) C(\kappa) \left[i\omega\hat{h} + V_{\text{rel}}\hat{\alpha} + \frac{c}{2}\left(\frac{1}{2} - \xi_{ea}\right) i\omega\hat{\alpha}\right], \end{aligned} \tag{3.68}$$

The circulatory terms of both loads are dependent on Theodorsen's transfer function, $C(\kappa)$. This function is defined using a combination of Bessel functions as follows:

$$C(\kappa) = \frac{J_1(\kappa) - iY_1(\kappa)}{(J_1(\kappa) - iY_1(\kappa)) + i\,(J_0(\kappa) - iY_0(\kappa))} \tag{3.69}$$

being J_v the Bessel function of the first kind of real order v and complex argument and Y_v the Bessel function of the second kind of real order v and complex argument. These functions are defined as follows:

$$J_v(\kappa) = \sum_{m=0}^{\infty} \frac{(-1)^m}{m!(m+v)!}\left(\frac{x}{2}\right)^{2m+v} \qquad \text{and} \qquad J_{-v}(\kappa) = (-1)^v J_v(\kappa) \tag{3.70}$$

$$Y_v(\kappa) = \frac{J_v(\kappa)\cos(v\pi) - J_{-v}(\kappa)}{\sin(v\pi)} \tag{3.71}$$

The previous equations have been provided in the frequency domain. However, the solution to the transient problem requires integration over time. In order to convert from frequency to time, an inverse Fourier transformation is required. The computational cost of this transformation becomes high as it requires storing all the previous time steps and the information in both domains. Due to this reason, the Duhamel transformation is performed to calculate the dynamic load as a superposition of impulses, Equation (3.72). The complex function $C(k)$ is simplified using Wagner's function $\phi(s)$.

$$\begin{aligned} L(t) = \pi\rho_\infty \left(\frac{c}{2}\right)^2 \left(-\frac{d^2v}{dt^2} - V_\infty\frac{d\theta}{dt} + \frac{c}{2}\xi_{ea}\frac{d^2\theta}{dt^2}\right) \\ -2\pi\rho_\infty V_\infty \frac{c}{2}\left(w_a(0)\phi(s_t) + \int_0^{s_t}\frac{dw_a}{d\sigma}(\sigma)\phi(s_t-\sigma)d\sigma\right) \end{aligned} \tag{3.72}$$

The vertical velocity in the aerodynamic center, w_a, the nondimensional time, s_t, and Wagner's function, $\phi(s_t)$, are defined by equation 3.73.

$$w_a = \frac{dv}{dt} + V_\infty \theta + \frac{c}{2}\left(\frac{1}{2} - a\right)\frac{d\theta}{dt} \; ; \; s_t = \frac{2tV_\infty}{c} \; ; \; \phi(s_t) = 1 - 0.165e^{-0.0455s_t} - 0.355e^{-0.3s_t} \tag{3.73}$$

3.3.2 Artificial Neural Networks for nonlinear flow predictions

Artificial neural networks (ANN) are computational models constituted by a set of unitary entities, which are interconnected, called neurons. The neurons take a set of inputs to generate the output. The output of a neuron can be used as input in the following layer of the network. These multilayer structures are known as deep neural networks (DNNs). Due to their complexity and the difficulty of understanding the physical meaning of each internal parameter of the network, the ANN may be used as a black box to fit the model to a specific physical phenomenon, constructing a surrogate model which works as a nonlinear regression.

The coefficients of the ANN can be fitted against (the network can learn from, in ANN parlance) training data. Inside a neuron, the normalized input parameters are multiplied by a set of weights, the fitting parameters of the ANN. The weights are fitted by a training process in which the error, usually called loss of the system, is reduced. The structure of a typical generic ANN may be observed in Figure 3.14. This structure comprises an input layer, which includes the physical magnitudes, a hidden layer, and an output layer that gives the ANN results. Each layer is connected by a set of neurons, which can be classified depending on its internal structure. In the current work, two typologies are presented and tested to simulate dynamic nonlinear aerodynamics: feed-forward (FNN) and long short-term memory (LSTM) networks.

A training process is required to fit the internal parameters of the neural network. This procedure takes the following steps:

1. A batch of time steps (input variables and results) is taken from the data set.
2. A backpropagation algorithm calculates partial derivatives over weights and biases.
3. A single step of an optimization algorithm is used to compute a new set of weights, advancing to a new epoch.

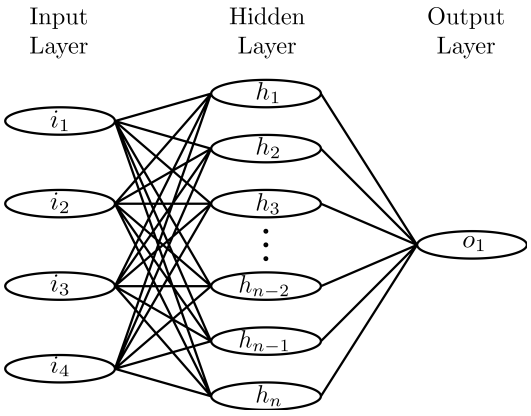

Fig. 3.14 **Generic typical ANN.** The architecture of the network presents an input (i_i), a hidden (h_i) and an output (o_i) layer.

Feed forward

Feed-forward neural networks calculate the results of the neuron taking only into account the input variables of a specific time step. The basic unit of a feed-forward network is presented in Figure 3.15.

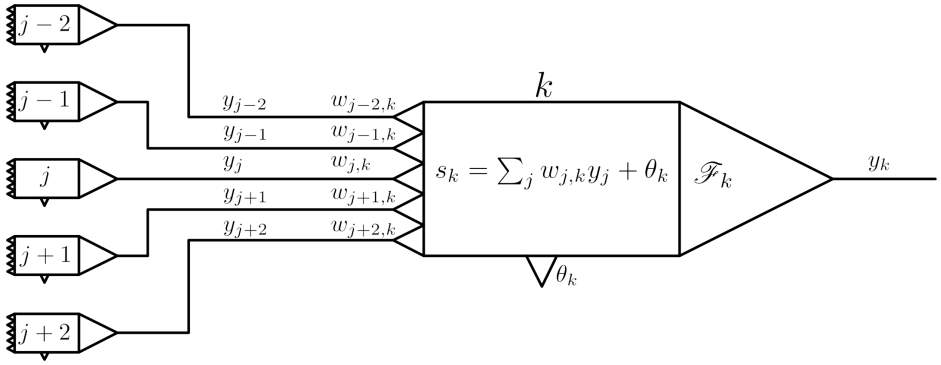

Fig. 3.15 **Artificial feed-forward network.** The internal architecture of the neuron show the input parameters y_j, the weights w_j, the bias θ_k, the activation function $\mathscr{F}$ and the output y_k.

Inside the artificial neuron, the input variables are multiplied by a set of weights $w_{j,k}$ and an additional bias θ_k is added, as follows:

$$s_k = \sum_j w_{j,k} y_j + \theta_k \tag{3.74}$$

After variable s_k is calculated, it must be evaluated in an activation function. The activation function is a non-decreasing function with a threshold value. The most commonly used activation functions include step, rectified linear unit (ReLU), and sigmoid. These functions

are represented in Figure 3.16. Equation (3.75) presents the formulation of the whole neuron after multiplying the results by the activation function. The choice of activation function depends on the specific requirements of the model and the problem being solved. For example, the use of step functions is of high utility in classification problems where the neuron must be activated or deactivated. The ReLU function is the most used activation function, mainly used for CNNs. These functions are widely used due to the low computational cost and the reduction of the vanishing gradients problem. The sigmoid is used for continuous outputs between 0 and 1.

$$y_k = \mathscr{F}(s_k) = \mathscr{F}\left(\sum_j w_{j,k} y_j + \theta_k\right) \tag{3.75}$$

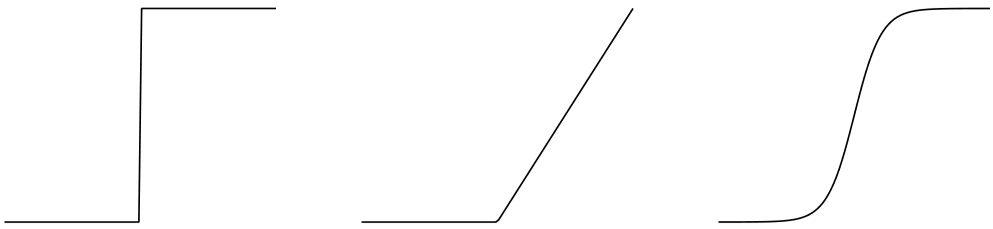

Fig. 3.16 **Activation functions of the neural networks.** (Left) step function, (center) rectified linear unit function (ReLU), (right) sigmoid function.

After the neural network is built, the values of the weights are set through a supervised training process in which an objective function, loss function, must be optimized [73]. The mean squared error is selected as the loss function, $\mathscr{L}$:

$$\mathscr{L} = MSE = \frac{1}{n}\sum_{i=1}^{n}(y_{\text{true}} - y_k)^2 \tag{3.76}$$

where n is the number of data, y_{true} is the output real value and y_k the output predicted value. The loss function can be expressed as a function of the weights and biases:

$$\mathscr{L} = \mathscr{L}(w_1, w_2, ..., w_n, \theta_1, \theta_2, ..., \theta_n) \tag{3.77}$$

As the activation functions are continuous in the whole domain, the derivatives of the loss function concerning the weights and biases may be calculated using the backpropagation method as follows for the whole domain of the problem:

$$\frac{\partial \mathscr{L}}{\partial w_n} = \frac{\partial \mathscr{L}}{\partial y_k}\frac{\partial y_k}{\partial w_n} = w_n f'(w_1 y_1 + w_2 y_2 + ... + w_n, \theta_1, \theta_2, ..., \theta_n) \tag{3.78}$$

$$\frac{\partial \mathscr{L}}{\partial \theta_n} = \frac{\partial \mathscr{L}}{\partial y_k}\frac{\partial y_k}{\partial \theta_n} = \theta_n f'\left(w_1 y_1 + w_2 y_2 + ... + w_n, \theta_1, \theta_2, ..., \theta_n\right) \tag{3.79}$$

The derivative is applied to the complete artificial neural network. Assuming the nomenclature of Figure 3.14, the derivative of the output variable, o_1, for the input variable weight of the first layer of neurons, $w_{i,n}$, can be expressed as:

$$\frac{\partial \mathscr{L}}{\partial w_{i,n}} = \frac{\partial \mathscr{L}}{\partial o_1}\frac{\partial o_1}{\partial h_n}\frac{\partial h_n}{\partial w_{i,n}} \tag{3.80}$$

where h_n is the hidden layer value. The same procedure can be applied to the second layer of neurons. Then, the derivative concerning the input weight of the second layer, $w_{h,n}$, is calculated as:

$$\frac{\partial \mathscr{L}}{\partial w_{h,n}} = \frac{\partial \mathscr{L}}{\partial o_1}\frac{\partial o_1}{\partial w_{h,n}} \tag{3.81}$$

Different optimization algorithms may be used to obtain the value of the weights: Stochastic Gradient Descent (SGD), Adam, Root Mean Square Propagation (RMSProp)... In the current work, the RMSProp algorithm was applied. This formulation automatically fits the learning ratio of the artificial neural network in order to reduce the computing time. RMSProp is a gradient-based algorithm that uses Equations 3.82, 3.83 and 3.84.

$$\upsilon_t = \xi_{\text{RMSProp}}\upsilon_{t-1} + (1 - \xi_{\text{RMSProp}})Gr_t^2 \tag{3.82}$$

$$\Delta w_t^j = -\frac{\eta}{\sqrt{\upsilon_t + \varepsilon_{\text{RMSprop}}}}Gr_t \tag{3.83}$$

$$w_{t+1}^j = w_t^j + \Delta w_t \tag{3.84}$$

where η is the initial learning ratio, using a default value of 0.001 [74], υ_t is the exponential average of squares of gradients, and Gr_t is the gradient at a time t along the direction w^j. The hyperparameter ξ_{RMSProp} has a recommended value of 0.9, and $\varepsilon_{\text{RMSprop}}$ is a smoothing term to avoid the division by zero, usually in the order of 10^{-8}.

Long-short term memory: LSTM

Another type of network is the recursive neural network (RNN). The cells of this structure contain internal loops, which can store information, making the data persistent inside the network. These schemes are of high interest in predictions based on the evolution of past information. A clear example of use is natural language.

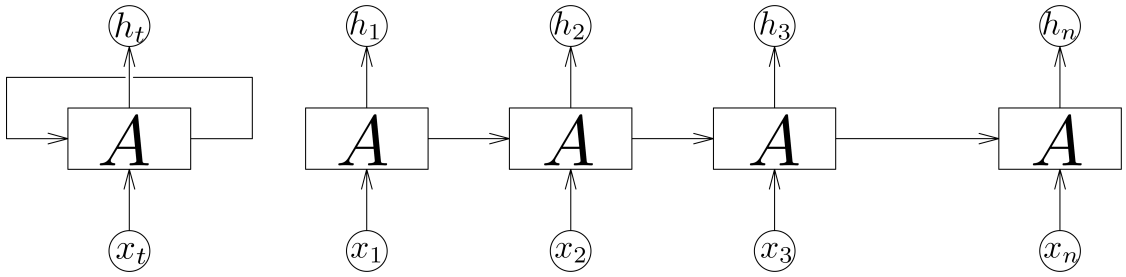

Fig. 3.17 **Recurrent neural cell generic structure.** (Left) simplified cell, (right) extended cell structure.

One of the main types of recursive neural networks is long short-term memory (LSTM). Its structure was proposed by Hochreiter and Schmidhuber [75] to overcome the problems of vanishing gradients and gradient explosion, which appeared in RNN. The LSTM comes from an improved method of back-propagating the error: constant error backpropagation. The LSTM network keeps the error at a more constant level, allowing to increase in the number of epochs of the training process [76]. LSTM networks can learn from long-term and short-term information. Thus, they can consider the effect of the aerodynamic cycle.

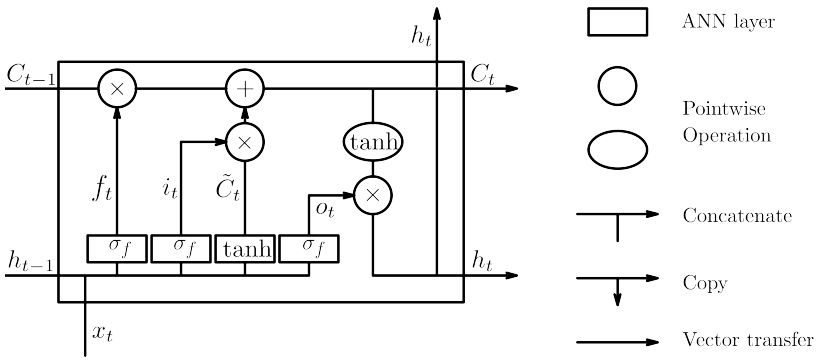

Fig. 3.18 **LSTM cell generic structure.** The schematic representation shows the input gate, the forget gate, the output gate, and the internal state of the neuron.

The internal structure of an LSTM network is presented in Figure 3.18. The following equations govern the LSTM neuron:

$$C_t = f_t \times C_{t-1} + i_t \times \tilde{C}_t \tag{3.85}$$

$$f_t = \sigma_f \left(W_f \cdot [h_{t-1}, x_t] + b_f \right) \tag{3.86}$$

$$\tilde{C}_t = \tanh \left(W_c \cdot [h_{t-1}, x_t] + b_c \right) \tag{3.87}$$

$$i_t = \sigma_f \left(W_i \cdot [h_{t-1}, x_t] + b_i \right) \tag{3.88}$$

$$h_t = o_t \times \tanh(C_t) \tag{3.89}$$

$$o_t = \sigma_f(W_o \cdot [h_{t-1}, x_t] + b_o) \tag{3.90}$$

where C_t is the cell state in the time t, f_t is the result of the forget gate, i_t and C_t add information to the cell state (input gate), and o_t is the result of the output gate and h_t is the internal state of the cell. The weights of the LSTM neuron must be adjusted using a training process with an optimization algorithm.

Finally, it is essential to consider that the batch of data used in an LSTM network must be continuous and ordered in time. However, in FFN networks, the order of the dataset might be random without affecting the solution.

Application of the artificial neural network to model transient nonlinear aerodynamic coefficients

The aerodynamic lift and pitching moment coefficients depend on the flow conditions and the airfoil position relative to the stream. Therefore, the coefficients are a function of the angle of attack and its derivatives, which, at the same time, depend on the structure vibration.

In the work of Wu and Kareem [55], the aerodynamic coefficients were expressed as the sum of a steady and a transient term. Following this idea, the aerodynamic coefficients are modeled as steady coefficients c_m^{st} and c_l^{st}, which are a function of the angle of attack α of the structure and its position $\mathbf{x}$, in case it is interacting with other bodies, and the dynamic coefficients, c_m^{dyn} and c_l^{dyn}, which depend on the mean angle of attack $\langle\alpha\rangle$, its amplitude $\Delta\alpha$, its velocity $\dot{\alpha}$ and its acceleration $\ddot{\alpha}$. Equations (3.91) and (3.92) show the definition of the aerodynamic coefficients.

$$c_m = c_m^{\text{st}}(\alpha, \mathbf{x}) + c_m^{\text{dyn}}(\langle\alpha\rangle, \Delta\alpha, \dot{\alpha}, \ddot{\alpha}) \tag{3.91}$$

$$c_l = c_l^{\text{st}}(\alpha, \mathbf{x}) + c_l^{\text{dyn}}(\langle\alpha\rangle, \Delta\alpha, \dot{\alpha}, \ddot{\alpha}) \tag{3.92}$$

On the one hand, the steady coefficients are straightforward to calculate. They can be obtained experimentally from a bi-dimensional rigid body test or numerically using computational fluid mechanics or potential aerodynamics. Along this work, these coefficients were calculated from bi-dimensional RANS simulations. On the other hand, the dynamic coefficients are predicted using a neural network. These ANNs are trained using a batch of bi-dimensional RANS simulations of a pitching airfoil. The simplified architecture of the aerodynamic neural network is presented in Figure 3.19. The amplitude and frequency of the oscillations are chosen in order to contain the working conditions of interest.

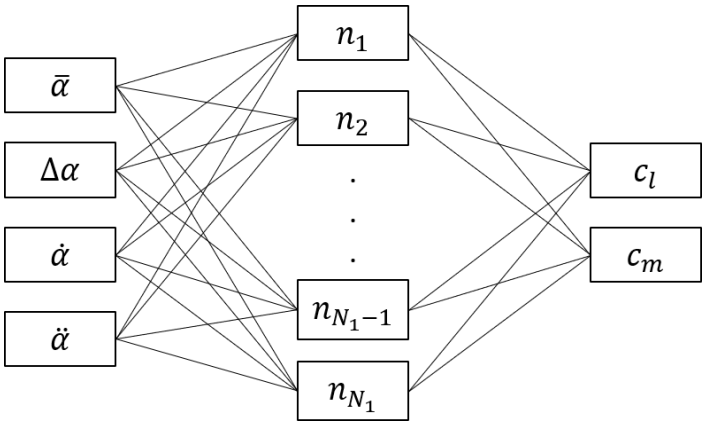

Fig. 3.19 **Schematic architecture of the aerodynamic ANN.** The inputs and outputs and hidden layers of the neural network are presented.

3.3.3 Structural models

The reduction of the computational cost in the aeroelastic phenomena also requires the simplification of the structural calculations. This section describes the models used in the dissertation for decreasing the computational cost associated. Two different approaches are described in the document. Both simplifications are related to dimensional reduction and simplify the three-dimensional structure into a rigid solid motion and a one-dimensional problem.

The first model is a 0D structure. An equivalent set of masses and springs is proposed. This methodology has been widely used since the traditional references [21]. This section presents a methodology for including the effects of boundary conditions on the solution, and the mathematical background is derived.

However, the previous approach can only include one mode of vibration of the solution. Therefore, the aeroelastic effects of secondary twisting or plunging modes should be addressed. In addition, the methodology could be more straightforward in those structures in which there is a coupling between the torsion and the bending movements. In order to overcome the previous problems, a beam model for the general orthotropic material is presented. This methodology calculates the cross-section characteristic using the theory derived by Librescu and Song [77] and then applies a beam element integration to solve the structure.

Equivalent mass-spring system

This section derives the methodology for reducing an arbitrary three-dimensional beam to an equivalent bi-dimensional section. Due to the aerodynamic and mechanical characteristics

of the thin airfoil cross-section, only two degrees of freedom are selected, the torsion angle and the vertical displacement. In addition, the out-of-plane motions of the cross-section are assumed negligible and are not included in the problem.

The Lagrange equation, Equation (2.11) governs the system. For slender structures, a beam-type behavior is expected. The structure can be reduced to an equivalent section whose motion is dominated by bending and torsion deformations. Therefore, as this equivalent section system presents two degrees of freedom, the reader is referred to Figure 2.4 for a visual representation of the section.

In order to describe the beam motion, the displacement of the section may be expressed as a summation of the vibration modes weighted by their influence on the problem. The degrees of freedom are expressed as follows:

$$\theta(z,t) = \Theta(t)\mathbf{f}(z) = \sum_{n=1}^{\infty} (\Theta_i(t) \cdot f_i(z)) \qquad v(z,t) = \mathbf{V}(t)\mathbf{g}(z) = \sum_{n=1}^{\infty} (V_i(t) \cdot g_i(z)) \tag{3.93}$$

where z is the beam-wise direction, t is the time, $v(z,t)$ is the vertical displacement of the cross-section, $\theta(z,t)$ its twist, $f_i(z)$ and $g_i(z)$ are the associated eigenfunctions for torsion and bending, respectively [78] and $\Theta_i(t)$ and $V_i(t)$ are the amplitudes associated with each of them. Both functions must comply with the boundary conditions of the structure, which, for the case of a clamped-free plate, are $\theta(0,t) = \theta'(0,t) = 0$; $v(0,t) = v'(0,t) = 0$ and $v''(L,t) = 0$. In Equation (3.93), the modal shapes contain all the spatial information, while the temporal dependency is contained in their weighting terms. Figure 3.20 shows these functions for the flexural and torsional motion of a beam structure with one end fixed and the other end free.

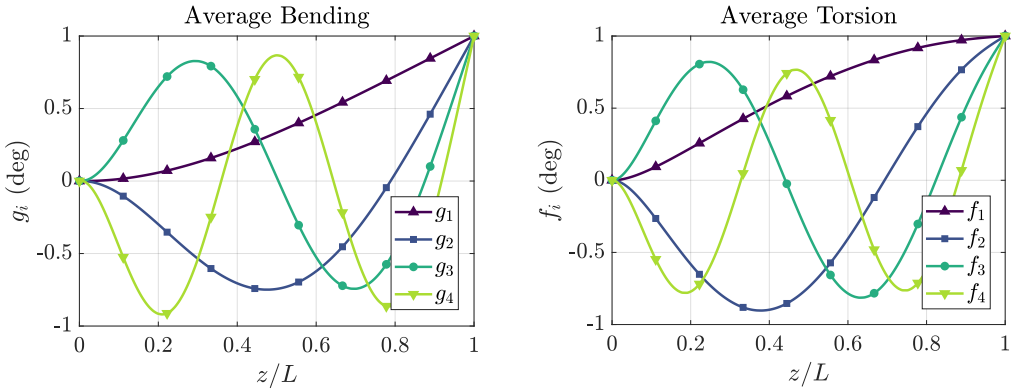

Fig. 3.20 **Modal shape functions of the beam.** Four first vibration modes normalized with the value in the free end of the beam. Bending modes (left) and torsion modes (right).

The motion of the plate is supposed to be a combination of torsional and flexural modes. Assuming a thin airfoil, the vertical displacement and velocity of any point located over the cross-section (v_p) can be calculated as a function of the chordwise coordinate x as follows, assuming small deformations and linearizing the equations:

$$v_p = -x\sum_0^\infty \Theta_i(t)\cdot f_i(z) + \sum_0^\infty V_i(t)\cdot g_i(z) \qquad \dot{v}_p = -x\sum_0^\infty \dot{\Theta}(t)\cdot f_i(z) + \sum_0^\infty \dot{V}(t)\cdot g_i(z) \quad (3.94)$$

With these assumptions, kinetic, $\mathscr{T}$, and potential, $\mathscr{U}$, energies of the plate could be expressed following Equation 3.95:

$$\mathscr{T} = \frac{1}{2}\iiint \rho_s \dot{v}_p^2 dV \qquad U = \frac{1}{2}\int GJ\left(\frac{d\,\theta}{dz}\right)^2 dz + \frac{1}{2}\int EI_x\left(\frac{d^2\,v}{dz^2}\right)^2 dz \qquad (3.95)$$

where E is the elastic modulus, G is the shear modulus of the material, J is the torsion constant of the section, and I_x is the second moment of area of the section. Therefore, the left-hand term of the Lagrange equations can be written when a bounded number of N eigenfunctions are considered and separating the contribution of the flexural and torsional motion, as in Equation (3.96):

$$\frac{d}{dt}\frac{\partial \mathscr{T}}{\partial \dot{\Theta}} = I_s L \mathbf{M}_\theta \ddot{\Theta} \qquad \frac{d}{dt}\frac{\partial \mathscr{T}}{\partial \dot{\mathbf{W}}} = m_s L \mathbf{M}_v \ddot{\mathbf{V}} \qquad \frac{\partial \mathscr{U}}{\partial \Theta} = \frac{GJ}{L}\mathbf{K}_\theta \Theta \qquad \frac{\partial \mathscr{U}}{\partial \mathbf{V}} = \frac{EI}{L^3}\mathbf{K}_v \mathbf{V} \quad (3.96)$$

where $\mathbf{M}_\theta$ and $\mathbf{M_v}$ are the mass matrices for the torsional and flexural motions, respectively, I_s the cross-section inertia, m_s the cross-section mass and $\mathbf{K}_\theta$ and $\mathbf{K_v}$ are the stiffness matrices for the torsional and flexural motions. Their components can be calculated as stated in Equations 3.97 and 3.98. Note that if eigenfunctions are taken forming an orthogonal base, the off-diagonal terms will be zero:

$$M_\theta^{ij} = \int_0^1 f_i\left(\frac{z}{L}\right) f_j\left(\frac{z}{L}\right) d\left(\frac{z}{L}\right) \qquad M_v^{ij} = \int_0^1 g_i\left(\frac{z}{L}\right) g_j\left(\frac{z}{L}\right) d\left(\frac{z}{L}\right) \qquad (3.97)$$

$$K_\theta^{ij} = \int_0^1 f_i'\left(\frac{z}{L}\right) f_j'\left(\frac{z}{L}\right) d\left(\frac{z}{L}\right) \qquad K_v^{ij} = \int_0^1 g_i''\left(\frac{z}{L}\right) g_j''\left(\frac{z}{L}\right) d\left(\frac{z}{L}\right) \qquad (3.98)$$

Finally, it is necessary to obtain the generalized forces. The virtual work, $\delta\mathscr{W}$, generated at an arbitrary section will combine the virtual displacement produced by the vertical force

(lift) and the virtual torsion produced by the aerodynamic moment. In consequence, Equation 3.99 can be stated:

$$\begin{aligned}\frac{d(\delta\mathscr{W})}{dz} &= \frac{1}{2}\rho_\infty V_\infty^2 c c_l \cdot \delta v + \frac{1}{2}\rho_\infty V_\infty^2 c^2 c_m \cdot \delta\theta \\ &= \frac{1}{2}\rho_\infty V_\infty^2 c c_l \cdot \sum_1^\infty (\delta V_i g_i) + \frac{1}{2}\rho_\infty V_\infty^2 c^2 c_m \cdot \sum_1^\infty (\delta\Theta_i f_i)\end{aligned} \tag{3.99}$$

where c_l and c_m are the aerodynamic coefficients for lift and moment, respectively. Next, two different assumptions will be made to obtain an equivalent 2D model by integrating Equation (3.99).

- The aerodynamic coefficients, c_l and c_m, are a function only of the local angle of attack and its derivatives of each one of the sections, i.e., the effects of three-dimensionality of the aerodynamics can be neglected as a first approach.
- The aerodynamic force coefficients can be linearized around the rigid angle of attack. The linear term of the series will be supposed to be constant for the whole span of the plate. This assumption is only valid when the difference between the pitching angle in the tip and the root is low.

With the previous assumptions, the aerodynamic coefficients of Equation (3.99) can be written in a general way as:

$$c_l = c_l(v_0,\theta_0) + c_{l_\theta}\theta + \frac{c_{l_v}}{c}v + \frac{c\cdot c_{l\dot\theta}}{V_\infty}\dot\theta + \frac{c_{l\dot v}}{V_\infty}\dot v + \sum_{n=2}^{N}\frac{c^n\cdot c_{l\theta^{(n)}}}{V_\infty^n}\theta^{(n)} + \sum_{n=2}^{N}\frac{c^{n-1}\cdot c_{lv^{(n)}}}{V_\infty^n}v^{(n)}, \tag{3.100}$$

being $\theta^{(n)} = \frac{\partial^n\theta}{\partial t^n}$ and $v^{(n)} = \frac{\partial^n v}{\partial t^n}$. As a consequence, it will be possible to establish the value of the generalized forces as follows:

$$\mathbf{Q}_{f_\Theta} = \mathbf{Q}_{f_\Theta,0} + \frac{1}{2}\rho_\infty V_\infty^2 c^2 L\mathbf{A}_{\theta,\mathbf{v}}\sum_0^\infty \frac{c_{m_v^{(n)}}c^{n-1}}{V_\infty^n}\mathbf{V}^{(n)} + \frac{1}{2}\rho_\infty V_\infty^2 c^2 L\mathbf{A}_{\theta,\theta}\sum_0^\infty \frac{c_{m_\theta^{(n)}}c^n}{V_\infty^n}\Theta^{(n)} \tag{3.101}$$

$$\mathbf{Q}_{f_\mathbf{V}} = \mathbf{Q}_{f_\mathbf{V},0} + \frac{1}{2}\rho_\infty V_\infty^2 c L\mathbf{A}_{\mathbf{v},\mathbf{v}}\sum_0^\infty \frac{c_{l_v^{(n)}}c^{n-1}}{V_\infty^n}\mathbf{V}^{(n)} + \frac{1}{2}\rho_\infty V_\infty^2 c L\mathbf{A}_{\mathbf{v},\theta}\sum_0^\infty \frac{c_{l_\theta^{(n)}}c^n}{V_\infty^n}\Theta^{(n)} \tag{3.102}$$

where $\mathbf{A}_{\theta,\theta}$, $\mathbf{A}_{\mathbf{w},\theta}$, $\mathbf{A}_{\theta,\mathbf{w}}$ and $\mathbf{A}_{\mathbf{w},\mathbf{w}}$ are the aerodynamic influence matrices, whose components are given by:

$$\begin{aligned} A^{ij}_{\theta,v} = \int_0^1 f_i\left(\frac{z}{L}\right)\cdot g_j\left(\frac{z}{L}\right) d\left(\frac{z}{L}\right) \quad A^{ij}_{\theta,\theta} = \int_0^1 f_i\left(\frac{z}{L}\right)\cdot f_j\left(\frac{z}{L}\right) d\left(\frac{z}{L}\right) \\ A^{ij}_{v,v} = \int_0^1 g_i\left(\frac{z}{L}\right)\cdot g_j\left(\frac{z}{L}\right) d\left(\frac{z}{L}\right) \end{aligned} \tag{3.103}$$

Note how, as torsion and flexion eigenfunctions are not necessarily orthogonal between them, matrices $\mathbf{A}_{\theta,\mathbf{v}}$ and $\mathbf{A}_{\mathbf{v},\theta}$ could contain non-zero values in the diagonal. However, when $i \neq j$, $\frac{A^{ij}_{\theta,v}}{A^{ii}_{\theta,v}} < 1$, indicating that cross terms contribute to a lesser extent to the resulting motion. Figure 3.21 presents the value of the $\mathbf{A}_{ij}$ matrices for a squared cross-section clamped beam.

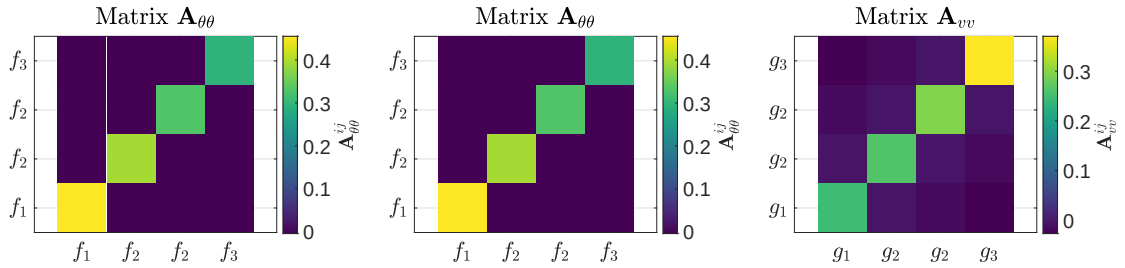

Fig. 3.21 **Aerodynamic influence matrices.** The color of the squares represents the value of each element for a 4×4 matrix. Results for a squared cross-section clamped beam.

Additionally, for values of the velocity below or around the divergence, as the series need to be convergent, it should be possible to assume that $\frac{V_i}{V_{i+1}} > 1$, allowing, then, to neglect the terms with a crossed contribution between low and high order modes. Therefore, it will be possible to establish a set of equations as follows:

$$\begin{aligned} I_s L M^{ii}_{\theta}\ddot{\Theta}_i + \frac{GJ}{L}K^{ii}_{\theta}\Theta_i = \\ \frac{1}{2}\rho_\infty V_\infty^2 c^2 L\left(A^{ii}_{\theta,v}\sum_{n=0}^{\infty}\frac{c_{m_v^{(n)}}V_\infty^n}{c^{n-1}}V_i^{(n)} + A^{ii}_{\theta,\theta}\sum_{n=0}^{\infty}\frac{c_{m_v^{(n)}}V_\infty^n}{c^n}\Theta_i^{(n)}\right) \end{aligned} \tag{3.104}$$

$$\begin{aligned} m_s L M^{ii}_{v}\ddot{V}_i + \frac{EI}{L^3}K^{ii}_{v}V_i = \\ \frac{1}{2}\rho_\infty V_\infty^2 c L\left(A^{ii}_{v,v}\sum_{n=0}^{\infty}\frac{c_{l_v^{(n)}}V_\infty^n}{c^{n-1}}V_i^{(n)} + A^{ii}_{v,\theta}\sum_{n=0}^{\infty}\frac{c_{l_v^{(n)}}V_\infty^n}{c^n}\Theta_i^{(n)}\right) \end{aligned} \tag{3.105}$$

On the other hand, the equations governing the motion of an aeroelastic characteristic section can be expressed by assuming a single relevant bending and torsion mode as:

$$I_s\ddot{\Theta}_1 + k_\theta\Theta_1 = \frac{1}{2}\rho_\infty V_\infty^2 c^2 L\left(A^{ii}_{\theta,v}\sum_{n=0}^{\infty}\frac{c_{m_v^{(n)}}V_\infty^n}{c^{n-1}}{V_1}^{(n)} + A^{ii}_{\theta,\theta}\sum_{n=0}^{\infty}\frac{c_{m_v^{(n)}}V_\infty^n}{c^n}{\Theta_1}^{(n)}\right) \tag{3.106}$$

$$m_s\ddot{V}_1 + k_v V_1 = \frac{1}{2}\rho_\infty V_\infty^2 c L\left(A^{ii}_{v,v}\sum_{n=0}^{\infty}\frac{c_{l_v^{(n)}}V_\infty^n}{c^{n-1}}{V_1}^{(n)} + A^{ii}_{v,\theta}\sum_{n=0}^{\infty}\frac{c_{l_v^{(n)}}V_\infty^n}{c^n}{\Theta_1}^{(n)}\right) \tag{3.107}$$

In consequence, an inspection of the equations would lead to the next deduction: a 2D CFD rigid body airfoil is capable of accurately representing the first mode of the 3D plate motion when the 2D properties of the airfoil are taken to be:

$$I_{2D} = I_s\frac{M^\theta_{11}}{A^\theta_{11}} \qquad k_\theta = \frac{GJ}{L^2}\frac{K^\theta_{11}}{A^\theta_{11}} \qquad m_{2D} = m_s\frac{M^v_{11}}{A^{\theta,v}_{11}} \qquad k_v = \frac{EI}{L^4}\frac{K^v_{11}}{A^{\theta,v}_{11}} \tag{3.108}$$

Therefore, dimensionally, it can be deduced that, for a given geometry, the aeroelastic response can be considered to be a function of the following non-dimensional parameters:

$$F_{2D}\left(\mathrm{Re},\mathrm{Ma},\frac{I_{2D}}{\frac{1}{2}\rho_\infty c^4},\frac{k_\theta}{\frac{1}{2}\rho_\infty V_\infty^2 c^2},\frac{m_{2D}}{\frac{1}{2}\rho_\infty c^2},\frac{k_v}{\frac{1}{2}\rho_\infty V_\infty^2},\frac{tV_\infty}{c},\frac{v_1}{c},\theta_1\right) = 0 \tag{3.109}$$

With this selection of parameters, it will be possible to reduce the complex 3D model to an equivalent 2D. The characteristic parameter of the analysis is the non-dimensional torsion stiffness $k^* = \frac{k_\theta}{\frac{1}{2}\rho_\infty V_\infty^2 c^2}$.

Orthotropic material thin-wall cross-section beam model

The development of reduced order models implies the simplification of the structure. In the previous section, a mass-spring system was explained. Nevertheless, this equivalent section cannot include the effects of second-order modes, the use of orthotropic materials, and the application of distributed loads. In addition, the coupling between torsion and bending is not straightforward for an equivalent section. In order to overcome these problems, this section describes a beam model based on Librescu and Song [77] theory, which can account for the previous effects.

In the first place, the characteristics of the cross-section are calculated. In order to calculate the internal elastic energy, a nonshearable linear model based on 5 degrees of

freedom is used. The model describes the behavior of thin-walled orthotropic materials structures. The displacements and rotation on a beam element are presented in Figure 3.22.

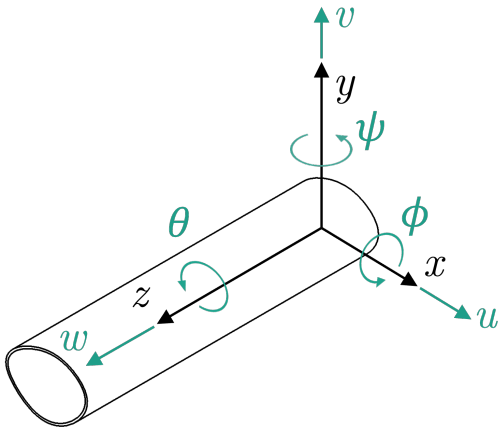

Fig. 3.22 **Displacements and rotations on a generic beam element.** The displacements are defined by the vector $\mathbf{u} = [u, v, w]$ and the rotations by $\theta = [\phi, \psi, \theta]$.

In order to derive the section stiffness and mass properties, the following assumptions must be applied:

- The longitudinal displacement of the section w is much smaller than the transverse displacements u and v.
- The normal stress in the thickness direction is negligible $\sigma_{nn} \approx 0$.
- The section is rigid $\varepsilon_{xx} = \varepsilon_{yy} = \varepsilon_{xy} = 0$.
- Warping of the section is included in the calculations.
- Shear strains are uniform in the section.

Thus, the displacement of a generic point of the section is defined in Equations 3.110, 3.111 and 3.112.

$$u = u_0 - \left(y - n\frac{dx}{ds}\right)\sin(\theta) - \left(x + n\frac{dy}{ds}\right)(1 - \cos(\theta)) \tag{3.110}$$

$$v = v_0 + \left(x + n\frac{dy}{ds}\right)\sin(\theta) - \left(y - n\frac{dx}{ds}\right)(1 - \cos(\theta)) \tag{3.111}$$

$$w = w_0 - \left(x + n\frac{dy}{ds}\right)\psi + \left(y - n\frac{dx}{ds}\right)\phi - (F_w(s) + nr_t(s))\frac{\partial\theta}{\partial z} \tag{3.112}$$

In the previous equations, subscript 0 indicates the reference point of the section, $F_w(s)$ and $nr_t(s)$ are the first and second warping functions, being r_t the tangential distance to an arbitrary point of the mean fiber of the wall. The cross-section coordinates are visualized in Figure 3.23. The wall reference frame comprises the wall-tangential coordinate s, the beam span-wise coordinate z, and the wall-normal coordinate n.

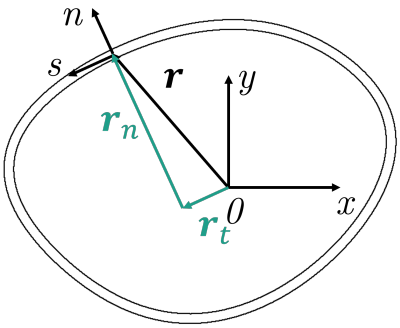

Fig. 3.23 **Visualization of the cross-section coordinates.** The global reference frame is the $x-y-z$ while the wall reference frame is $s-z-n$. The distance from the reference point 0 to a point in the wall is called **r**.

The warping function describes the movement of the cross-section out of its plane as an effect of the rotation. These functions are defined in Equation (3.113).

$$F_w(s) = \int_0^s (r_n(s) - \Psi)\, ds;\ \Psi = \frac{\oint \frac{r_n(s)ds}{h(s)}}{\frac{ds}{h(s)}} \rightarrow \text{if} h(s) = cte \rightarrow \Psi = \frac{2\Omega_A}{\beta} \tag{3.113}$$

being $h(s)$ the thickness of the wall, Ω_A the closed area of the section (null in the case of open cross-section), β its perimeter, and $r_n(s)$ the normal distance to an arbitrary point of the mean fiber of the wall. The normal and the tangential distance to a point in the cross-section wall are defined as follows:

$$r_t(s) = x\frac{dx}{ds} + y\frac{dy}{ds} \tag{3.114}$$

$$r_n(s) = y\frac{dx}{ds} - x\frac{dy}{ds} \tag{3.115}$$

A displacement field is generated when the loads are applied to the structure walls. This displacement field is the cause of the strain along the structure. These strains are calculated through the Green-Lagrange tensor, Equations (3.116), (3.117), and (3.118).

$$\varepsilon_{zz} = \frac{\partial w}{\partial z} + \frac{1}{2}\left[\left(\frac{\partial u}{\partial z}\right)^2 + \left(\frac{\partial v}{\partial z}\right)^2\right], \tag{3.116}$$

$$\gamma_{sz} = \gamma_{xz}\frac{dx}{ds} + \gamma_{yz}\frac{dy}{ds} + \Psi\frac{\partial \phi}{\partial z} + 2n\frac{\partial \phi}{\partial z}, \tag{3.117}$$

$$\gamma_{nz} = \gamma_{xz}\frac{dy}{ds} - \gamma_{yz}\frac{dx}{ds}. \tag{3.118}$$

In the previous equations, the tangential deformations γ_{xz} and γ_{yz} are defined as a function of the rotation of the section. The relationship between the displacement derivatives, the rotation, and the tangential deformation is provided in Figure 3.24.

$$\gamma_{xz} = -\psi + \frac{\partial u_0}{\partial z}\cos(\theta) + \frac{\partial v_0}{\partial z}\sin(\theta) \tag{3.119}$$

$$\gamma_{yz} = \phi + \frac{\partial v_0}{\partial z}\cos(\theta) - \frac{\partial u_0}{\partial z}\sin(\theta) \tag{3.120}$$

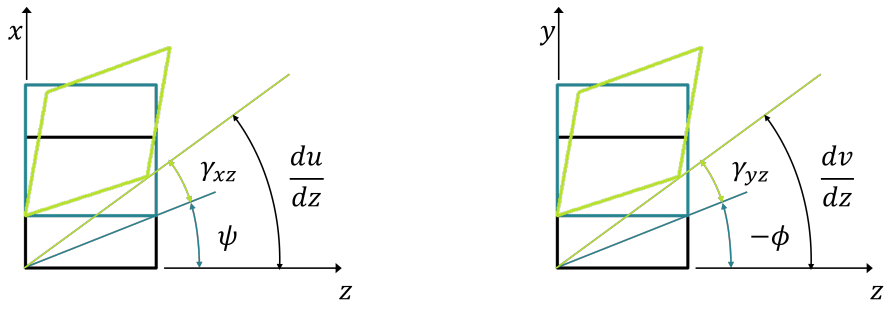

Fig. 3.24 **Angular deformation diagrams.** (Left) tangential deformation in the z-x plane and (right) in the y-z plane.

Equations (3.110), (3.111), (3.112),(3.119) and (3.120) are substituted into Equations (3.116), (3.117) and (3.118). An expression of the strains as a function of the n coordinate is obtained, Equations (3.121).

$$\varepsilon_{zz} = \varepsilon^0_{zz} + n\varepsilon^1_{zz} + n^2\varepsilon^2_{zz}, \qquad \gamma_{sz} = \gamma^0_{sz} + \gamma^{(t)}_{sz} = \gamma^0_{sz} + (\Psi + 2n)\,W_M, \qquad \gamma_{nz} = \gamma^0_{nz} \tag{3.121}$$

where W_M is the warping of the section, and its value is equivalent to $\frac{\partial \theta}{\partial z}$.

Previously, in Section 2.2, the constitutive equations of a generic orthotropic material were presented. Particularizing Equation (2.5) for thin-walled cross-section beams, the stress

in the lamina normal direction may be assumed negligible to the other directions. Thus, $\sigma_{33} = 0$, leading to a reduced constitutive matrix, $\mathbf{Q}$, Equation 3.122, where $\mathbf{T}$ is the rotation matrix between the systems and $\mathbf{R}$ converts from engineering strain to tensor strain.

$$\mathbf{Q} = \begin{bmatrix} Q_{1111} & Q_{1122} & 0 & 0 & 0 \\ & Q_{2222} & 0 & 0 & 0 \\ & & Q_{2323} & 0 & 0 \\ & Sym. & & Q_{1313} & 0 \\ & & & & Q_{1212} \end{bmatrix} \tag{3.122}$$

The values of the indexes of the Equation (3.122) are defined in Equations (3.123) and (3.124).

$$Q_{1111} = \frac{E_1}{1 - \nu_{12}\nu_{21}} \; ; \; Q_{1122} = \frac{E_1\nu_{21}}{1 - \nu_{12}\nu_{21}} = \frac{E_2\nu_{12}}{1 - \nu_{12}\nu_{21}} \; ; \; Q_{2222} = \frac{E_2}{1 - \nu_{12}\nu_{21}} \tag{3.123}$$

$$Q_{1212} = G_{12} \; ; \; Q_{2323} = G_{23} \; ; \; Q_{1313} = G_{13} \tag{3.124}$$

The previous constitutive matrix has been presented in the material coordinate system. Nevertheless, the material might be rotated with respect to the local coordinate system of the shell. The matrix must be rotated in these cases as indicated in Equation (3.125).

$$\bar{\mathbf{Q}} = \mathbf{T}^{-1}\mathbf{Q}\mathbf{R}\mathbf{T}\mathbf{R}^{-1} = \begin{bmatrix} \bar{Q}_{1111} & \bar{Q}_{1122} & 0 & 0 & \bar{Q}_{1112} \\ & \bar{Q}_{2222} & 0 & 0 & \bar{Q}_{2212} \\ & & \bar{Q}_{2323} & \bar{Q}_{2313} & 0 \\ & Sym. & & \bar{Q}_{1313} & 0 \\ & & & & \bar{Q}_{1212} \end{bmatrix} \tag{3.125}$$

A bi-dimensional constitutive equation is derived by focusing on the constitutive relationships of the shell or lamina. Section 3.2.2 introduced this idea of separating the membrane problem from the bending problem in the shell-type structures. A similar idea is presented for the 1D beam. The membrane forces are calculated as follows for a lamina of M plies:

$$N_{ss} = \sum_{k=1}^{M} \int_{h_{k-1}}^{h_k} \sigma_{ss} dn, \qquad N_{zz} = \sum_{k=1}^{M} \int_{h_{k-1}}^{h_k} \sigma_{zz} dn, \qquad N_{sz} = \sum_{k=1}^{M} \int_{h_{k-1}}^{h_k} \sigma_{sz} dn. \tag{3.126}$$

In addition, the transverse shear stresses are also defined:

$$N_{zn} = \sum_{k=1}^{M} \int_{h_{k-1}}^{h_k} \sigma_{zn} dn, \qquad N_{sn} = \sum_{k=1}^{M} \int_{h_{k-1}}^{h_k} \sigma_{sn} dn \tag{3.127}$$

The stress couples or the bending loads are multiplied by the normal distance to the mean fiber:

$$L_{ss} = \sum_{k=1}^{M} \int_{h_{k-1}}^{h_k} \sigma_{ss} n dn, \qquad L_{zz} = \sum_{k=1}^{M} \int_{h_{k-1}}^{h_k} \sigma_{zz} n dn, \qquad L_{sz} = \sum_{k=1}^{M} \int_{h_{k-1}}^{h_k} \sigma_{sz} n dn \tag{3.128}$$

Finally, the high-order stresses are defined:

$$\Gamma_{zz} = \sum_{k=1}^{M} \int_{h_{k-1}}^{h_k} \sigma_{zz} n^2 dn \tag{3.129}$$

Substituting the constitutive relationships on the laminate equations, the membrane stress, transverse shear stress, coupled stress and high order stress are expressed as follows in Equations (3.130), (3.131), (3.132) and (3.133).

$$\left\{ \begin{array}{c} N_{ss} \\ N_{zz} \\ N_{sz} \end{array} \right\} = \sum_{k=1}^{M} \int_{n_{k-1}}^{n_k} \left\{ \begin{array}{l} \bar{Q}_{1111}\varepsilon_{ss} + \bar{Q}_{1122}\varepsilon_{zz} + \bar{Q}_{1112}\gamma_{sz} \\ \bar{Q}_{1122}\varepsilon_{ss} + \bar{Q}_{2222}\varepsilon_{zz} + \bar{Q}_{2212}\gamma_{sz} \\ \bar{Q}_{1211}\varepsilon_{ss} + \bar{Q}_{1222}\varepsilon_{zz} + \bar{Q}_{1212}\gamma_{sz} \end{array} \right\}_k dn \tag{3.130}$$

$$\left\{ \begin{array}{c} N_{zn} \\ N_{sn} \end{array} \right\} = \sum_{k=1}^{M} \int_{n_{k-1}}^{n_k} \left\{ \begin{array}{l} \bar{Q}_{2323}\gamma_{zn} + \bar{Q}_{2313}\gamma_{sn} \\ \bar{Q}_{2313}\gamma_{zn} + \bar{Q}_{1313}\gamma_{sn} \end{array} \right\}_k dn \tag{3.131}$$

$$\left\{ \begin{array}{c} L_{zz} \\ L_{sz} \end{array} \right\} = \sum_{k=1}^{M} \int_{n_{k-1}}^{n_k} \left\{ \begin{array}{l} \bar{Q}_{1122}\varepsilon_{ss} + \bar{Q}_{2222}\varepsilon_{zz} + \bar{Q}_{2212}\gamma_{sz} \\ \bar{Q}_{1211}\varepsilon_{ss} + \bar{Q}_{1222}\varepsilon_{zz} + \bar{Q}_{1212}\gamma_{sz} \end{array} \right\}_k ndn \tag{3.132}$$

$$\Gamma_{zz} = \sum_{k=1}^{M} \int_{h_{k-1}}^{h_k} \left(\bar{Q}_{1122}\varepsilon_{ss} + \bar{Q}_{2222}\varepsilon_{zz} + \bar{Q}_{2212}\gamma_{sz}\right) n^2 dn \tag{3.133}$$

Then, the stiffness coefficients are defined. Stretching, bending-stretching, and higher order coefficients are expressed as:

$$(A_{ij}, B_{ij}, D_{ij}, F_{ij}, H_{ij}) = \sum_{k=1}^{M} \int_{h_{k-1}}^{h_k} \bar{\mathrm{Q}}_{ij}^{(k)} (1, n, n^2, n^3, n^4) dn \tag{3.134}$$

The forces and moments acting on the mean fiber of the walls can be calculated as a function of the strains by applying the previous stiffness coefficients. Equations 3.135 to 3.138, are obtained assuming $\varepsilon_{ss} = \varepsilon_{ss}^0$ and $\gamma_{sn} = \gamma_{sn}^0$ and using the constitutive relationships.

$$\left\{\begin{array}{c} N_{zz} \\ L_{zz} \\ \Gamma_{zz} \\ N_{sz} \\ L_{sz} \end{array}\right\} = \left[\begin{array}{ccccc} A_{22} & B_{22} & D_{22} & A_{26} & B_{26} \\ B_{22} & D_{22} & F_{22} & B_{26} & D_{26} \\ D_{22} & F_{22} & H_{22} & D_{26} & F_{26} \\ A_{26} & B_{26} & D_{26} & A_{66} & B_{66} \\ B_{26} & D_{26} & F_{26} & B_{66} & D_{66} \end{array}\right] \left\{\begin{array}{c} \varepsilon^0_{zz} \\ \varepsilon^1_{zz} \\ \varepsilon^2_{zz} \\ \gamma^0_{sz} + \Psi W_M \\ 2W_M \end{array}\right\} + \left[\begin{array}{c} A_{12} \\ B_{12} \\ D_{12} \\ A_{16} \\ B_{16} \end{array}\right] \left\{ \varepsilon^0_{ss} \right\} \tag{3.135}$$

$$\left\{\begin{array}{c} N_{zz} \\ L_{zz} \\ \Gamma_{zz} \\ N_{sz} \\ L_{sz} \end{array}\right\} = \mathbf{P}_1 \left\{\begin{array}{c} \varepsilon^0_{zz} \\ \varepsilon^1_{zz} \\ \varepsilon^2_{zz} \\ \gamma^0_{sz} + \Psi W_M \\ 2W_M \end{array}\right\} + \mathbf{P}_2 \left\{ \varepsilon^0_{ss} \right\} \tag{3.136}$$

$$\left\{\begin{array}{c} N_{ss} \\ L_{ss} \end{array}\right\} = \mathbf{P}_2^T \left\{\begin{array}{c} \varepsilon^0_{zz} \\ \varepsilon^1_{zz} \\ \varepsilon^2_{zz} \\ \gamma^0_{sz} + \Psi \\ 2W_M \end{array}\right\} + \left[A_{11} \right] \left\{ \varepsilon^0_{ss} \right\} = \mathbf{P}_2^T \left\{\begin{array}{c} \varepsilon^0_{zz} \\ \varepsilon^1_{zz} \\ \varepsilon^2_{zz} \\ \gamma^0_{sz} + \Psi W_M \\ 2W_M \end{array}\right\} + \mathbf{P}_3 \left\{ \varepsilon^0_{ss} \right\} \tag{3.137}$$

$$N_{zn} = A_{44}\gamma^0_{zn} + A_{45}\gamma^0_{sn}, \;\; N_{sn} = A_{45}\gamma^0_{zn} + A_{55}\gamma^0_{sn} \tag{3.138}$$

The previous system of equations is simplified by considering a beam model. In other words, the membrane and coupling stresses in the tangential direction N_{ss} and L_{ss} are considered negligible. Then the value of ε^0_{ss} can be calculated:

$$\left\{ \varepsilon^0_{ss} \right\} = -\mathbf{P}_3^{-1}\mathbf{P}_2^T \left\{\begin{array}{c} \varepsilon^0_{zz} \\ \varepsilon^1_{zz} \\ \varepsilon^2_{zz} \\ \gamma^0_{sz} + \Psi W_M \\ 2W_M \end{array}\right\}, \tag{3.139}$$

and substituting Equation (3.139) in Equation (3.135), the final stiffness matrix relating the loads with the strains is obtained:

$$\left\{\begin{array}{c} N_{zz} \\ L_{zz} \\ \Gamma_{zz} \\ N_{sz} \\ L_{sz} \end{array}\right\} = \mathbf{Ks}^* \left\{\begin{array}{c} \varepsilon^0_{zz} \\ \varepsilon^1_{zz} \\ \varepsilon^2_{zz} \\ \gamma^0_{sz} + \Psi W_M \\ 2W_M \end{array}\right\} \rightarrow \mathbf{Ks}^* = \mathbf{P}_1 - \mathbf{P}_2\mathbf{P}_3^{-1}\mathbf{P}_2^T \tag{3.140}$$

The system is simplified, collapsing the terms of the warping:

$$\left\{\begin{array}{c} N_{zz} \\ L_{zz} \\ \Gamma_{zz} \\ N_{sz} \\ L_{sz} \end{array}\right\} = \mathbf{Ks} \left\{\begin{array}{c} \varepsilon^0_{zz} \\ \varepsilon^1_{zz} \\ \varepsilon^2_{zz} \\ \gamma^0_{sz} \\ W_M \end{array}\right\} \tag{3.141}$$

$$N_{nz} = \left(A_{44} - \frac{A_{45}^2}{A_{55}}\right)\gamma^0_{zn} \tag{3.142}$$

The terms of the matrix **Ks** are calculated as a function of the stiffness quantities A_{ij}, B_{ij}, and D_{ij}. Their expressions are provided in Table 3.1.

Table 3.1 **Stiffness coefficients relating forces and strains.** The coefficients are calculated from the layup stiffness quantities.

$Ks_{11} = A_{22} - \frac{A_{12}^2}{A_{11}}$	$Ks_{12} = Ks_{21} = B_{22} - \frac{A_{12}B_{12}}{A_{11}}$
$Ks_{13} = Ks_{31} = D_{22} - \frac{A_{12}D_{12}}{A_{11}}$	$Ks_{14} = Ks_{41} = A_{26} - \frac{A_{12}A_{16}}{A_{11}}$
$Ks_{15} = Ks_{51} = \left(A_{26} - \frac{A_{12}A_{16}}{A_{11}}\right)\Psi + 2\left(B_{26} - \frac{A_{12}B_{16}}{A_{11}}\right)$	$Ks_{22} = D_{22} - \frac{B_{12}^2}{A_{11}}$
$Ks_{23} = Ks_{32} = F_{22} - \frac{B_{12}D_{12}}{A_{11}}$	$Ks_{24} = Ks_{42} = B_{26} - \frac{A_{16}B_{12}}{A_{11}}$
$Ks_{25} = Ks_{52} = \left(B_{26} - \frac{B_{12}A_{16}}{A_{11}}\right)\Psi + 2\left(D_{26} - \frac{B_{12}B_{16}}{A_{11}}\right)$	$Ks_{33} = H_{22} - \frac{D_{12}^2}{A_{11}}$
$Ks_{35} = Ks_{53} = \left(D_{26} - \frac{D_{12}A_{16}}{A_{11}}\right)\Psi + 2\left(F_{26} - \frac{B_{16}D_{12}}{A_{11}}\right)$	$Ks_{34} = Ks_{43} = D_{26} - \frac{A_{16}D_{12}}{A_{11}}$
$Ks_{45} = Ks_{54} = \left(A_{66} - \frac{A_{16}^2}{A_{11}}\right)\Psi + 2\left(B_{66} - \frac{A_{16}B_{16}}{A_{11}}\right)$	$Ks_{44} = A_{66} - \frac{A_{16}^2}{A_{11}}$
$Ks_{55} = \left(B_{66} - \frac{A_{16}B_{16}}{A_{11}}\right)\Psi + 2\left(D_{66} - \frac{B_{16}^2}{A_{11}}\right)$	

In order to solve the system, the potential energy, $\mathscr{U}$, of the deformation must be calculated. This energy is the product of the stress and the strain integrated along the volume of the solid:

$$\mathscr{U} = \frac{1}{2}\int_0^L \oint_c \sum_{k=1}^{M} \int_{h(k)} \left[\sigma_{zz}\varepsilon_{zz} + \tau_{sz}\gamma_{sz} + \sigma_{nz}\gamma_{nz}\right]_k dndsdz$$

$$= \frac{1}{2}\int_0^L \oint_c \sum_{k=1}^{M} \int_{h(k)} \left[\sigma_{zz}\left(\varepsilon_{zz}^0 + n\varepsilon_{zz}^1 + n^2\varepsilon_{zz}^2\right) + \tau_{sz}\left(\gamma_{sz}^0 + \Psi + 2nW_M\right) + \sigma_{nz}\left(\gamma_{nz}^0\right)\right]_k dndsdz \tag{3.143}$$

The loads are integrated along the wall-normal direction. Equation 3.143 can be expressed as follows:

$$\mathscr{U} = \frac{1}{2}\int_0^L \oint_c \left[N_{zz}\varepsilon_{zz}^0 + L_{zz}\varepsilon_{zz}^1 + \Gamma_{zz}\varepsilon_{zz}^2 + N_{sz}\left(\gamma_{sz}^0 + \Psi\right) + L_{sz}2W_M + N_{zn}\gamma_{nz}^0\right] dsdz \tag{3.144}$$

The system must be expressed regarding the beam model loads and displacements. The beam model loads are defined as a function of the membrane, coupled, and high-order stresses. The forces F_x and F_y are the transversal forces, F_z is the axial force, M_x, M_y are the bending moments, M_z the Saint-Venant twisting moment, B_ω is the bi-moment and Γ_z is the moment due to high order effects.

$$F_x(z,t) = \int_C \left(N_{sz}\frac{dx}{ds} + N_{zn}\frac{dy}{ds}\right) ds, \quad F_y(z,t) = \int_C \left(N_{sz}\frac{dy}{ds} - N_{zn}\frac{dy}{ds}\right) ds \tag{3.145}$$

$$F_z(z,t) = \int_C N_{zz} ds, \quad M_z(z,t) = \int_C \left(N_{sz}\Psi + 2L_{sz}\right) ds \tag{3.146}$$

$$M_y(z,t) = \int_C \left(-xN_{zz} - L_{zz}\frac{dy}{ds}\right) ds, \quad M_x(z,t) = \int_C \left(yN_{zz} + L_{zz}\frac{dx}{ds}\right) ds, \tag{3.147}$$

$$B_\omega(z,t) = \int_C \left(F_w(s)N_{zz} - r_t(s)L_{zz}\right) ds \tag{3.148}$$

$$\Gamma_z(z,t) = \int_C \left(N_{zz}\left((x-x_P)^2 + (y-y_P)^2\right) + 2L_{zz}r_n + \Gamma_{zz}\right) ds, \tag{3.149}$$

The terms ε^0, ε^1, and ε^2 of the strain may be expressed as a function of the beam displacements. For the sake of brevity, the intermediate steps are omitted. The resulting expression for the potential energy is:

$$\mathscr{U} = \frac{1}{2}\int_0^L \left[T_z \left(\frac{\partial w_0}{\partial z} + \frac{1}{2}\left(\frac{\partial u_0}{\partial z}\right)^2 + \frac{1}{2}\left(\frac{\partial v_0}{\partial z}\right)^2 \right) + Q_y \left(\phi + \frac{\partial v_0}{\partial z} cos\theta - \frac{\partial u_0}{\partial z} sin\theta \right) \right.$$
$$+Q_x \left(-\psi + \frac{\partial u_0}{\partial z} cos\theta + \frac{\partial v_0}{\partial z} sin\theta \right) + M_y \left(-\frac{\partial \psi}{\partial z} - \frac{\partial u_0}{\partial z}\frac{\partial \theta}{\partial z}\sin\theta + \frac{\partial v_0}{\partial z}\frac{\partial \theta}{\partial z}\cos\theta \right)$$
$$\left. +M_x \left(\frac{\partial \phi}{\partial z} - \frac{\partial u_0}{\partial z}\frac{\partial \theta}{\partial z}\cos\theta - \frac{\partial v_0}{\partial z}\frac{\partial \theta}{\partial z}\sin\theta \right) + M_z \frac{\partial \theta}{\partial z} - B_w \frac{\partial^2 \theta}{\partial z^2} + \frac{1}{2}\Lambda_z \left(\frac{\partial \theta}{\partial z}\right)^2 \right] dz \tag{3.150}$$

Then, the system is linearized. Small displacements of the structure are assumed. Therefore, the deformation energy is simplified to:

$$\mathscr{U} = \frac{1}{2}\int_0^L \left[T_z \frac{\partial w_0}{\partial z} + Q_y \left(\phi + \frac{\partial v_0}{\partial z} \right) + Q_x \left(-\psi + \frac{\partial u_0}{\partial z} \right) + M_y \left(-\frac{\partial \psi}{\partial z} \right) \right.$$
$$\left. +M_x \frac{\partial \phi}{\partial z} + M_z \frac{\partial \theta}{\partial z} - B_w \frac{\partial^2 \theta}{\partial z^2} \right] dz \tag{3.151}$$

The previous integral can be expressed in a matrix form:

$$\mathscr{U} = \frac{1}{2}\int_0^L \mathbf{q}^T \mathbf{Q}_f dz = \frac{1}{2}\int_0^L \mathbf{q}^T \mathbf{A}\mathbf{q} dz. \tag{3.152}$$

In Equation 3.152, the energy is calculated as the product of the generalized load vector $\mathbf{Q}_f$ and the generalized displacement vector $\mathbf{q}$. The displacement vector is defined as:

$$\mathbf{q} = \left[\begin{array}{ccccccc} \frac{\partial w_0}{\partial z}, & \phi + \frac{\partial v_0}{\partial z}, & -\psi + \frac{\partial u_0}{\partial z}, & -\frac{\partial \psi}{\partial z}, & \frac{\partial \phi}{\partial z}, & \frac{\partial \theta}{\partial z}, & \frac{\partial^2 \theta}{\partial z^2} \end{array} \right]^T \tag{3.153}$$

The previous vector is simplified for a nonshearable beam. In this particular application, the bending moments are related to the displacement derivatives: $\phi = -\frac{\partial v_0}{\partial z}$ and $\psi = \frac{\partial u_0}{\partial z}$.

$$\mathbf{q} = \left[\begin{array}{ccccc} \frac{\partial w_0}{\partial z}, & -\frac{\partial^2 u_0}{\partial z^2}, & -\frac{\partial^2 v_0}{\partial z^2}, & \frac{\partial \theta}{\partial z}, & \frac{\partial^2 \theta}{\partial z^2} \end{array} \right]^T \tag{3.154}$$

The relationship between the generalized forces and displacements is the cross-section stiffness matrix $\mathbf{A}$:

$$\mathbf{Q}_f = \mathbf{A}\mathbf{q} = \begin{bmatrix} a_{11} & a_{12} & a_{13} & a_{14} & a_{15} \\ & a_{22} & a_{23} & a_{24} & a_{25} \\ & & a_{33} & a_{34} & a_{35} \\ & sym. & & a_{44} & a_{45} \\ & & & & a_{55} \end{bmatrix} \mathbf{q} \tag{3.155}$$

The coefficients of this matrix are calculated as a function of the geometrical properties of the section. Table 3.2 shows the values of the matrix elements.

Table 3.2 **Elements of the cross-section stiffness matrix.** The stiffness properties of the cross-section are reduced to a matrix accounting for the elastic and geometrical characteristics.

$a_{11} = \int K_{11} ds$	$a_{12} = a_{21} = \int \left(K_{11} x + K_{12} \frac{dy}{ds} \right) ds$
$a_{13} = a_{31} = \int \left(K_{11} y - K_{12} \frac{dx}{ds} \right) ds$	$a_{14} = a_{41} = \int \left(K_{11} F_w - K_{12} r_t \right) ds$
$a_{15} = a_{51} = \int K_{15} ds$	$a_{22} = \int \left(K_{11} x^2 + 2 x K_{12} \frac{dy}{ds} + K_{22} \left(\frac{dy}{ds} \right)^2 \right) ds$
$a_{23} = a_{32} = \int \left(K_{11} xy - x K_{12} \frac{dx}{ds} + y K_{12} \frac{dy}{ds} - K_{22} \frac{dx}{ds} \frac{dy}{ds} \right) ds$	
$a_{24} = \int \left(K_{11} x F_w - K_{12} x r_t + F_w K_{12} \frac{dy}{ds} - K_{22} r_t \frac{dy}{ds} \right) ds$	
$a_{25} = a_{52} = \int \left(K_{15} x + K_{25} \frac{dy}{ds} \right) ds$	$a_{33} = \int \left(K_{11} y^2 - 2 y K_{12} \frac{dx}{ds} + K_{22} \left(\frac{dx}{ds} \right)^2 \right) ds$
$a_{34} = a_{43} = \int \left(K_{11} y F_w - K_{12} y r_t - F_w K_{12} \frac{dx}{ds} + K_{22} r_t \frac{dx}{ds} \right) ds$	
$a_{35} = a_{53} = \int \left(y K_{15} - K_{25} \frac{dx}{ds} \right) ds$	$a_{44} = \int \left(K_{11} F_w^2 - 2 K_{12} F_w r_t + K_{22} r_t^2 \right) ds$
$a_{45} = a_{54} = \int \left(K_{15} F_w - K_{25} r_t \right) ds$	$a_{55} = \int \left(\Psi K_{45} \right) ds + 2 \int K_{55} ds$

Obtaining the stiffness matrix stated in Equation (2.12), the potential energy must be derived concerning the degrees of freedom of the problem Lagrange equation (2.11). The potential energy of Equation (3.152) depends on the displacements of vector $\mathbf{q}$. However, these degrees of freedom are continuous in space. Therefore, in order to calculate the entire beam, a 1D finite element method is applied. The solution on the element nodes, $\mathbf{q}_N^e$, is obtained assuming a shape function vector χ^e.

$$\mathscr{U} = \frac{1}{2} \left(\mathbf{q}_N^e \right)^T \int_0^L \chi^e \mathbf{A} \left(\chi^e \right)^T dz \mathbf{q}_N^e = \frac{1}{2} \left(\mathbf{q}_N^e \right)^T \mathbf{K}^e \mathbf{q}_N^e \tag{3.156}$$

Equation (3.156) shows the definition of the local stiffness matrix of the beam element, $\mathbf{K}^e$. This matrix is calculated below for the local coordinate system and then is rotated to the global reference frame. The model assumes polynomial shape functions. The order of the function is related to the displacement that it describes.

Describing the aeroelastic behavior of the whole system requires the accurate modeling of the inertial forces and the kinetic energy. The kinetic energy T is calculated as:

$$\mathscr{T} = \frac{1}{2}\int_0^L \dot{\mathbf{q}}^T \mathbf{M}_s \dot{\mathbf{q}} dz. \tag{3.157}$$

being the matrix $\mathbf{M}_s$ the section mass matrix. In order to calculate the values of the matrix, the kinetic energy is expressed as a function of the density of the material and the velocity of each point of the section:

$$\mathscr{T} = \frac{1}{2}\int_0^L \oint_c \sum_{k=1}^{M} \int_{h(k)} \left[(\rho_s)_k \left(\dot{u}^2 + \dot{v}^2 + \dot{w}^2\right)\right] dndsdz. \tag{3.158}$$

Applying Hamilton's functional to the previous equation and integrating through the beam wall thickness and the mid-line of the cross-section, the mass matrix is obtained. Note that for the kinetic energy, seven degrees of freedom vector is used:

$$\dot{\mathbf{q}} = \begin{bmatrix} \dot{u}_0, & \dot{v}_0, & \dot{w}_0, & \dot{\phi}, & \dot{\psi}, & \dot{\theta} & \frac{\partial \dot{\theta}}{\partial z} \end{bmatrix}^T \tag{3.159}$$

The cross-section mass matrix is defined for the seven degrees of freedom vector. The matrix definition is:

$$\mathbf{M}_s = \begin{bmatrix} m_{11} & 0 & 0 & 0 & 0 & m_{16} & 0 \\ & m_{22} & 0 & 0 & 0 & m_{26} & 0 \\ & & m_{33} & m_{34} & m_{35} & 0 & m_{37} \\ & & & m_{44} & m_{45} & 0 & m_{47} \\ & & sym. & & m_{55} & 0 & m_{57} \\ & & & & & m_{66} & 0 \\ & & & & & & m_{77} \end{bmatrix}, \tag{3.160}$$

where the elements of the matrix are provided in Table 3.3.

The mass terms m_0, m_1, and m_2 in the previous integrals are the results of integrating the density along the normal coordinates of the different layup plies of the structure:

$$m_0 = \sum_{k=1}^{M} \int_{h(k)} \left(\rho_s^{(k)}\right) dn, \quad m_1 = \sum_{k=1}^{M} \int_{h(k)} \left(\rho_s^{(k)}\right) ndn, \quad m_2 = \sum_{k=1}^{M} \int_{h(k)} \left(\rho_s^{(k)}\right) n^2 dn \tag{3.161}$$

Then, the nonshearable conditions are imposed, and the solution of the displacements is calculated from the solutions of the nodes using the same polynomial shape functions presented before. In this case, $\mathbf{M}^e$ is the mass matrix of the beam element.

$$\mathscr{T} = \frac{1}{2}\left(\dot{\mathbf{q}}_N^e\right)^T \int_0^L \boldsymbol{\chi}^e \mathbf{M}_s^e \left(\boldsymbol{\chi}^e\right)^T dz \dot{\mathbf{q}}_N^e = \frac{1}{2}\left(\dot{\mathbf{q}}_N^e\right)^T \mathbf{M}^e \dot{\mathbf{q}}_N^e \tag{3.162}$$

Table 3.3 **Elements of the cross-section mass matrix.** The mass matrix is obtained as a function of the cross-section geometry and the density of the materials.

$m_{11} = \oint_c m_0 ds$	$m_{22} = \oint_c m_0 ds$
$m_{33} = \oint_c m_0 ds$	$m_{16} = -\oint_c m_0 y ds + \oint_c m_1 \frac{dx}{ds} ds$
$m_{34} = \oint_c m_0 y ds - \oint_c m_1 \frac{dx}{ds} ds$	$m_{26} = \oint_c m_0 x ds + \oint_c m_1 \frac{dy}{ds} ds$
$m_{35} = -\oint_c m_0 x ds - \oint_c m_1 \frac{dy}{ds} ds$	$m_{77} = \oint_c m_0 F_w^2 ds + \oint_c m_2 r_t^2 ds - 2\oint_c m_1 F_w r_t ds$
$m_{44} = \oint_c m_0 y^2 ds + \oint_c m_2 \left(\frac{dx}{ds}\right)^2 ds - 2\oint_c m_1 y \frac{dx}{ds} ds$	
$m_{55} = \oint_c m_0 x^2 ds + \oint_c m_2 \left(\frac{dy}{ds}\right)^2 ds + 2\oint_c m_1 x \frac{dy}{ds} ds$	
$m_{66} = \oint_c m_0 \left(y^2 + x^2\right) ds + \oint_c m_2 \left(\left(\frac{dx}{ds}\right)^2 + \left(\frac{dy}{ds}\right)^2\right) ds + 2\oint_c m_1 \left(x\frac{dy}{ds} - y\frac{dx}{ds}\right) ds$	
$m_{37} = -\oint_c m_0 F_w ds + \oint m_1 r_t ds$	$m_{45} = -\oint_c m_0 xy ds + \oint_c m_2 \frac{dx}{ds}\frac{dy}{ds} ds + \oint m_1 \left(y\frac{dy}{ds} - x\frac{dx}{ds}\right) ds$
$m_{57} = -\oint_c m_0 x F_w ds + \oint_c m_2 r_t \frac{dy}{ds} ds - \oint_c m_1 \left(F_w \frac{dy}{ds} - x r_t\right) ds$	
$m_{47} = -\oint_c m_0 y F_w ds - \oint_c m_2 r_t \frac{dx}{ds} ds + \oint_c m_1 \left(F_w \frac{dx}{ds} + y r_t\right) ds$	

3.3.4 Reduced order model for generic aeroelastic phenomena

In the previous sections, different aerodynamic and structural problems were presented. However, a complete aeroelastic model for general beam structures is still required. This section explains the aeroelastic algorithm developed for simulating the coupled phenomena. The code is based on the finite beam element method introduced in Section 3.3.3. The cross-section characteristics are calculated and integrated into the local reference frame along the beam element. Then, the matrices are rotated and assembled using the mesh connectivity in the global reference frame. Once the structural system has been obtained, the boundary conditions are applied to the nodes: connections between nodes, fixed displacements on the nodes, or external loads, among others. In the case of aeroelastic coupling, the aerodynamic loads are calculated for each time step using the sub-models presented in Section 3.3.1.

A diagram of the main solver is presented in Figure 3.25. The algorithm is divided into different sub-blocks. In the initialization sub-block, the problem is defined. The mesh of the geometry is provided for the beam, and the different cross-sections, material properties, and boundary conditions are defined. The mass, Equation (3.160), and stiffness, Equation (3.155), matrices of the cross-section are obtained from its geometry and the material. Then, the finite beam element method is applied to the elements of the mesh in order to calculate

the local and global mass and stiffness matrices. Then, if the solver requires the application or calculation of external forces and moments, the load generation functions are included in the problem. For the problems with aeroelastic coupling, this module is called at every time step to recalculate the aerodynamic loads. After the boundary conditions are applied, the solver is selected for the specific problem. A different solver is used depending on the nature of the problem: steady, transient, or modal. Finally, the results are post-processed in order to export or plot them.

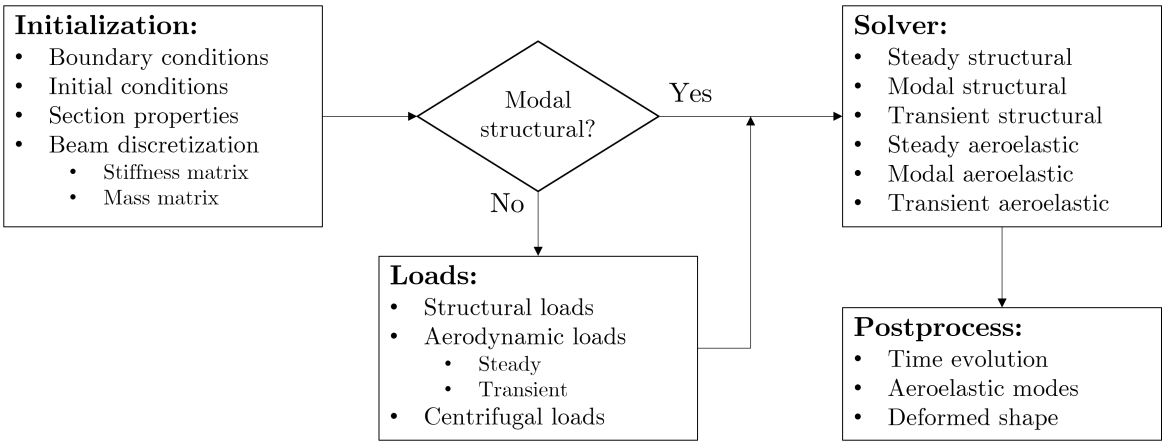

Fig. 3.25 **Main algorithm of the solver.** The solver is divided into a set of blocks. Initialization, the problem is defined, and the mass and stiffness matrices are calculated. Load calculation where the external forces and moments are applied. Solver, which applies the numerical schemes to obtain the displacements of the structure. Post-process to plot, store and export the results.

Initialization block: case configuration

In order to define the domain of the problem, a set of text files are provided to the code. The main text file contains the information on the case. The data contained in this file is presented in Figure 3.26.

When the calculation is initialized, the first step is deciding the type of problem. Each one is associated with a different solver. The mathematical definition of the numerical schemes will be presented later in the solver section. Then the mesh must be defined with an auxiliary file. This file provides the connectivity matrix, the grid points associated with the cross-sections, and the node sets that define the boundary conditions.

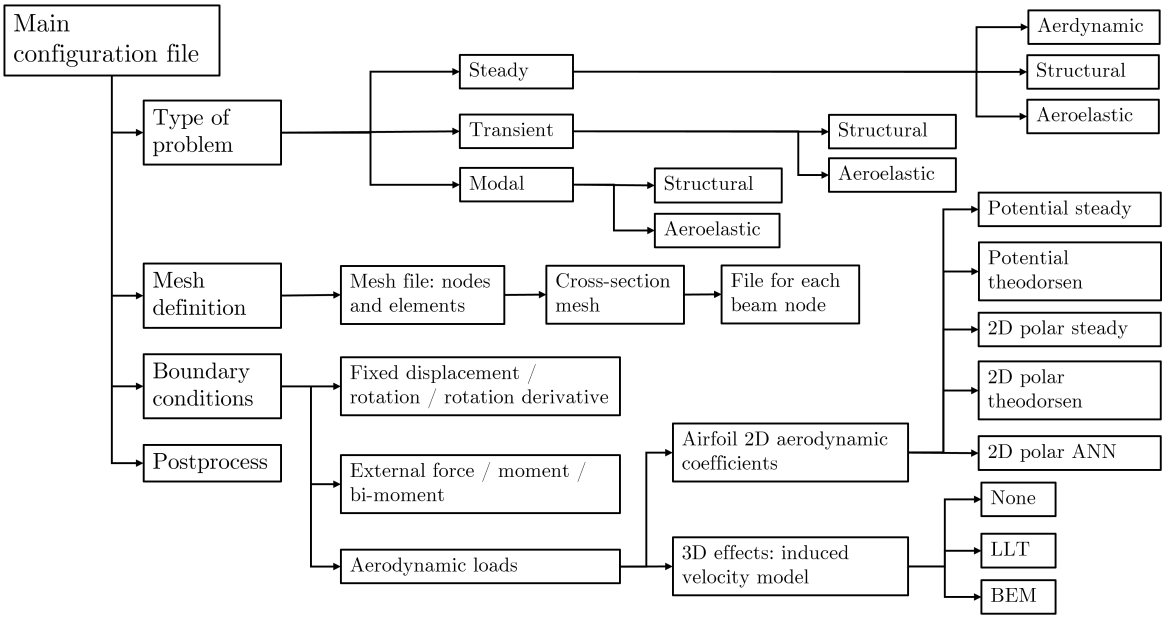

Fig. 3.26 **Main file information.** The configuration main file provides the information about the solver used, the mesh, the boundary conditions and the post-processing options.

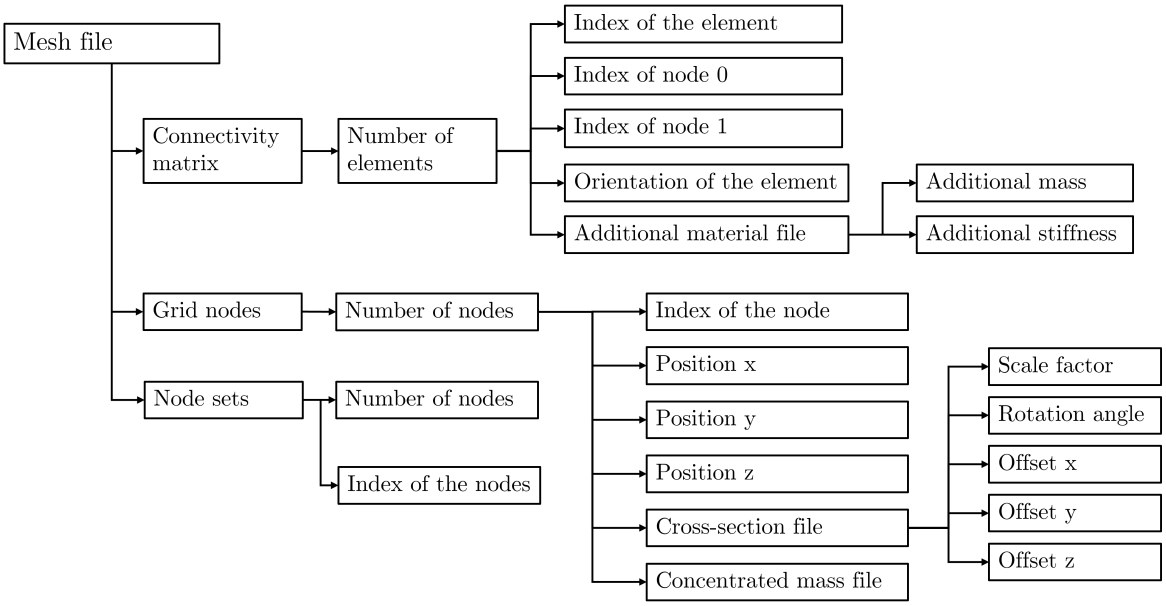

Fig. 3.27 **Mesh file information.** The connectivity matrix and the grid points are provided. Each grid point is associated with a cross-section file which is modified by a scale factor, a rotation angle, and an offset for its coordinates. In addition, sets of nodes are provided.

The elements are defined in the connectivity matrix. The number of elements, index, nodes, and orientation are provided. Moreover, the code allows the inclusion of extra

distributed mass and stiffness. The information relative to the cross-section is also provided. Each cross-section grid point is followed by the file defining its geometry, a scaling factor to increase or decrease its size, a rotation angle for creating a geometrical twist, and an offset in the cross-section origin of coordinates. Additional concentrated mass can be added to the cross-section. The diagram showing the information of the mesh file is provided in Figure 3.27.

Then, the information on the cross-section is provided in a similar file. As was defined in the beam mesh, a connectivity matrix is again provided, as well as the positions of the grid points of the cross-section.

The elements defined in the connectivity matrix also include all the information about the section walls associated with them. For a simple isotropic wall, its thickness and material are provided. However, the solver also allows the use of layups. The layup defines the material, orientation, and thickness of each ply.

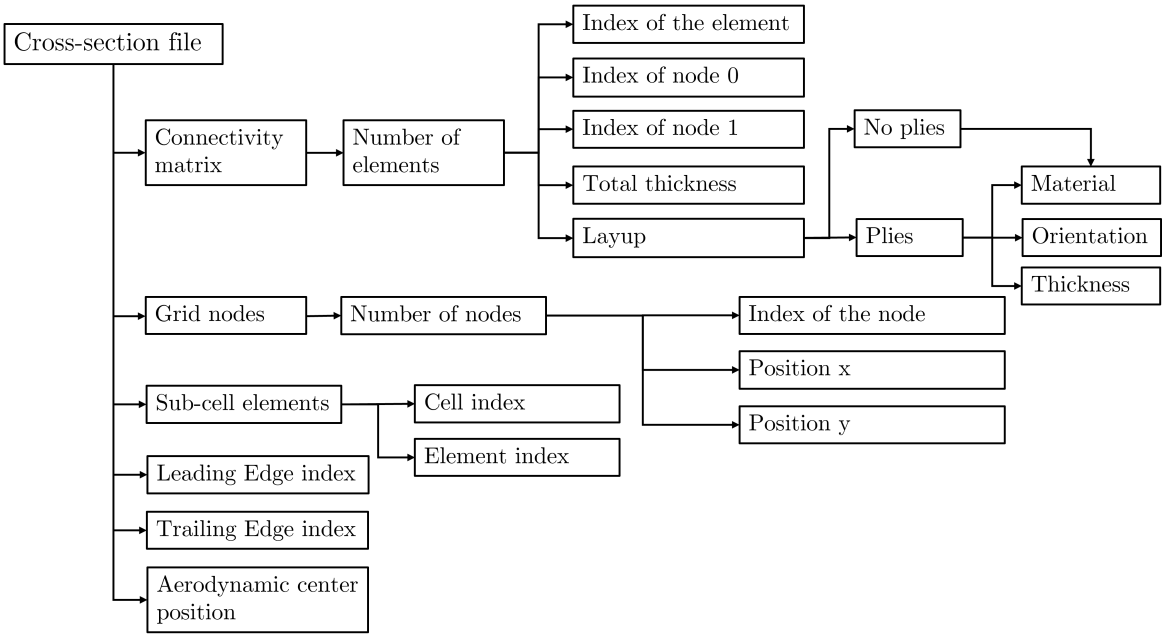

Fig. 3.28 **Cross-section file information.** The connectivity matrix, the grid points, and the cell matrix are provided. The elements of the section are related to the physical wall. They contain information about the thickness and the layup (orientation, thickness, and material) of the plies. In addition, the leading and trailing edge nodes are highlighted, and the aerodynamic center of the aerodynamic polar is provided.

In the beam theory, a different set of equations is used in the torsion of open-walled and closed-walled structures. Due to this reason, the typology of the cross-section is selected. The open-walled sections do not require additional information. Nevertheless, in the case of the

closed sections, an extra matrix must be provided. This matrix defines the cells composing the section. Each element is related to a closed cell or, in some structures, to a branch coming out of the cell. This information is also provided in the section file.

In order to calculate the aerodynamic coefficients of the cross-sections, the aerodynamic center of the polar is also defined, as well as the trailing and leading edges of the airfoil. The information regarding the section file is provided in Figure 3.28.

The constitutive matrix is calculated for a generic orthotropic material. Nevertheless, the algorithm allows the definition of orthotropic and isotropic materials. The material is defined in a separate file that accounts for the type of material. Then, the elastic modulus E, the shear modulus G, and the density ρ_s must be provided for the isotropic case. For the orthotropic material, the elastic modulus in the principal directions E_{11}, E_{22} and E_{33}, the shear modulus between the directions G_{12} and G_{23}, their Poisson coefficients ν_{12} and ν_{23} and the density ρ_s are defined. Note that 1 is the fiber direction, 2 is the shell-tangential fiber-normal direction, and 3 is the shell-normal direction. The schematic diagram of the material file is provided in Figure 3.29.

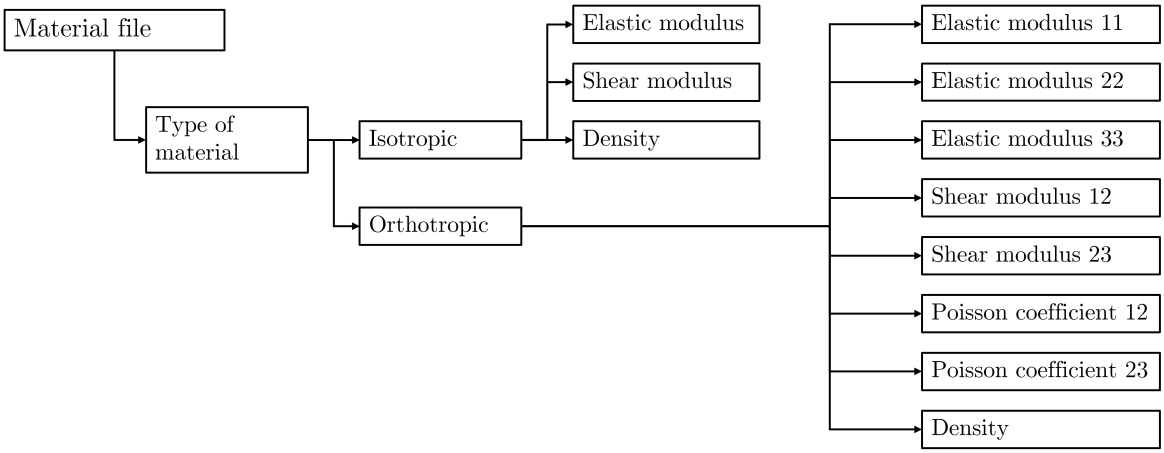

Fig. 3.29 **Material file information.** The code supports isotropic and orthotropic materials.

In addition, in Figure 3.27, additional mass and stiffness were included in the element definition, and additional mass could be provided to the grid points. The corresponding information is also provided through extra files. In the case of the distributed material, information about the material properties must be provided, including its cross-section area, inertia, crossed inertia, torsion constant, and the position of its center. For the concentrated mass, the total mass of the body and its inertia concerning the reference point of the cross-section are provided. The schematic diagram is provided in Figure 3.30.

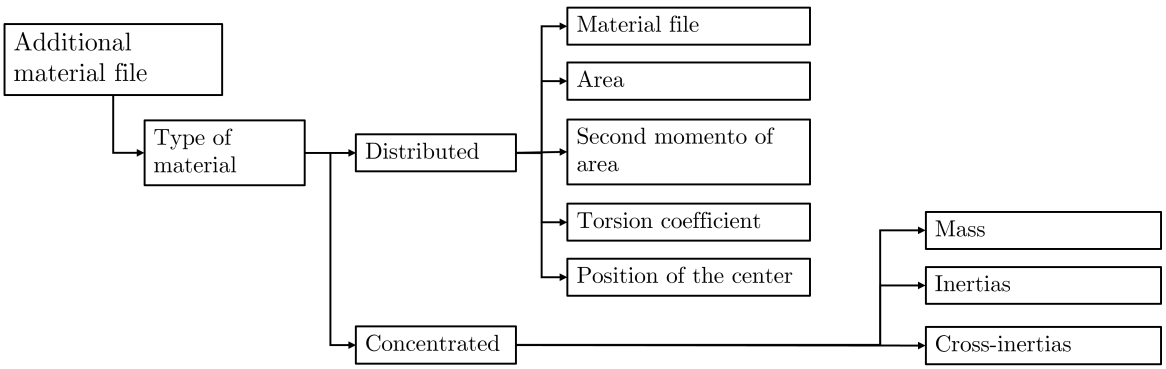

Fig. 3.30 **Additional material file information.** File for distributed or concentrated material.

Table 3.4 **Example of aerodynamic polar file.** The independent variables are defined with IV while c_l, c_d and c_m are the aerodynamic coefficients.

IV^1	IV^2	c_l	c_d	c_m
IV_1^1	IV_1^2	$c_{l_{11}}$	$c_{d_{11}}$	$c_{m_{11}}$
IV_1^1	IV_2^2	$c_{l_{12}}$	$c_{d_{12}}$	$c_{m_{12}}$
$\vdots$	$\vdots$	$\vdots$	$\vdots$	$\vdots$
IV_1^1	IV_N^2	$c_{l_{1N}}$	$c_{d_{1N}}$	$c_{m_{1N}}$
IV_2^1	IV_1^2	$c_{l_{21}}$	$c_{d_{21}}$	$c_{m_{21}}$
IV_2^1	IV_2^2	$c_{l_{22}}$	$c_{d_{22}}$	$c_{m_{22}}$
$\vdots$	$\vdots$	$\vdots$	$\vdots$	$\vdots$
IV_2^1	IV_N^2	$c_{l_{2N}}$	$c_{d_{2N}}$	$c_{m_{2N}}$
$\vdots$	$\vdots$	$\vdots$	$\vdots$	$\vdots$
IV_M^1	IV_1^2	$c_{l_{M1}}$	$c_{d_{M1}}$	$c_{m_{M1}}$
IV_M^1	IV_2^2	$c_{l_{M2}}$	$c_{d_{M2}}$	$c_{m_{M2}}$
$\vdots$	$\vdots$	$\vdots$	$\vdots$	$\vdots$
IV_M^1	IV_N^2	$c_{l_{MN}}$	$c_{d_{MN}}$	$c_{m_{MN}}$

Finally, the remaining information files are associated with the aerodynamic loads. If the bi-dimensional polar-based aerodynamic model has been selected, the lift, drag, and pitching moment coefficients must be provided to the code by a table. The table contains the independent and dependent variables of aerodynamics. For the independent variables, different parameters may be used. The typical variables are the angle of attack and Reynolds number. However, in some cases where the airfoil is close to a wall, the distance to the wall could be used as an independent parameter. The dependent parameters are the aerodynamic forces and moment. Table 3.4 provides an example of aerodynamic polar. In addition, for

those cases in which the *2D polar ANN* model is activated, the ANN is provided with a file containing the coefficients of the neural network after training.

Initialization block: structural model, 2D mass and stiffness matrices

The structural model is calculated after the configuration files are loaded into the algorithm. The calculation starts by obtaining the $\mathbf{A}$ and $\mathbf{M}_s$ matrices. Their values are computed by numerically integrating coefficients of Tables 3.2 and 3.3 for each cross-section element of the beam. Table 3.5 provides the numerical value of these coefficients. The geometrical values of the section element position x_e and y_e are calculated from its center of gravity. In addition, the orientations of the panel $\left(\frac{dx}{ds}\right)_e$ and $\left(\frac{dx}{ds}\right)_e$ are calculated from its end points. These parameters can be visualized in Figure 3.31.

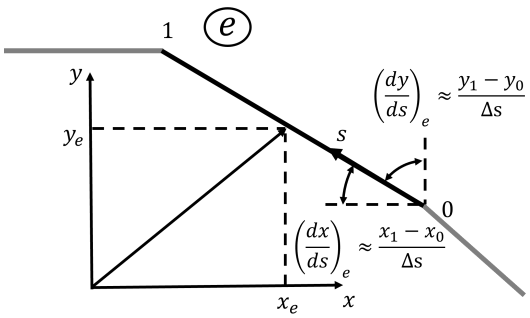

Fig. 3.31 **Geometrical parameters of a single element.** The position x_e and y_e of the element are referred to its center of gravity. The angles that the element is forming with the global axis are quantified by $\left(\frac{dx}{ds}\right)_e$ and $\left(\frac{dy}{ds}\right)_e$.

The stiffness, K_{ij}, and mass terms, m_i, are calculated by numerically integrating the material properties along the wall-normal coordinate. The stiffness terms are a function of the stiffness coefficients in the element:

$$(A_{ij}, B_{ij}, D_{ij}, F_{ij}, H_{ij})_e = \sum_{k=1}^{M} \left(\bar{\mathrm{Q}}_{ij}^{(k)}\right)_e \left(\Delta n, \frac{n_k^2 - n_{k-1}^2}{2}, \frac{n_k^3 - n_{k-1}^3}{3}, \frac{n_k^4 - n_{k-1}^4}{4}, \frac{n_k^5 - n_{k-1}^5}{5}\right), \tag{3.163}$$

being $\left(\bar{\mathrm{Q}}_{ij}^{(k)}\right)_e$ the constitutive relationship of the material with the corresponding orientation in the cross-section wall, n_k the initial and n_{k-1} the final wall-normal position of the ply. For the mass term:

$$(m_0, m_1, m_2) = \sum_{k=1}^{M} \left(\rho_s^{(k)}\right)_e \left(\Delta n, \frac{n_k^2 - n_{k-1}^2}{2}, \frac{n_k^3 - n_{k-1}^3}{3}\right), \tag{3.164}$$

where $\left(\rho_s^{(k)}\right)_e$ is the density of each ply. Calculating the warping function F_w and the cell area term Ψ in the case of close-section beams is not straightforward, and its explanation is provided below.

Table 3.5 **Elements of the cross-section stiffness matrix.** Numerical integration of the elements.

$a_{11} = \sum_e (K_{11})_e \Delta s_e$	$a_{12} = \sum_e \left((K_{11})_e x_e + (K_{12})_e \left(\frac{dy}{ds}\right)_e \right) \Delta s_e$
$a_{13} = \sum_e \left((K_{11})_e y_e - (K_{12})_e \left(\frac{dx}{ds}\right)_e \right) \Delta s_e$	$a_{14} = \sum_e \left((K_{11})_e (F_w)_e - (K_{12})_e (r_t)_e \right) \Delta s_e$
$a_{15} = \sum_e (K_{15})_e \Delta s_e$	$a_{25} = \sum_e (\left(K_{15})_e x_e + (K_{25})_e \left(\frac{dy}{ds}\right)_e \right) \Delta s_e$
$a_{22} = \sum_e \left((K_{11})_e x_e^2 + 2 x_e (K_{12})_e \left(\frac{dy}{ds}\right)_e + (K_{22})_e \left(\frac{dy}{ds}\right)_e^2 \right) \Delta s_e$	
$a_{23} = \sum_e \left((K_{11})_e x_e y_e - x_e (K_{12})_e \left(\frac{dx}{ds}\right)_e + y_e (K_{12})_e \left(\frac{dy}{ds}\right)_e - (K_{22})_e \left(\frac{dx}{ds}\right)_e \left(\frac{dy}{ds}\right)_e \right) \Delta s_e$	
$a_{24} = \sum_e \left((K_{11})_e x_e (F_w)_e - (K_{12})_e x_e (r_t)_e + (F_w)_e (K_{12})_e \left(\frac{dy}{ds}\right)_e - (K_{22})_e (r_t)_e \left(\frac{dy}{ds}\right)_e \right) \Delta s_e$	
$a_{33} = \sum_e \left((K_{11})_e y_e^2 - 2 y_e (K_{12})_e \left(\frac{dx}{ds}\right)_e + (K_{22})_e \left(\frac{dx}{ds}\right)_e^2 \right) \Delta s_e$	
$a_{34} = \sum_e \left((K_{11})_e y_e (F_w)_e - (K_{12})_e y_e (r_t)_e - (F_w)_e (K_{12})_e \left(\frac{dx}{ds}\right)_e + (K_{22})_e (r_t)_e \left(\frac{dx}{ds}\right)_e \right) \Delta s_e$	
$a_{35} = \sum_e \left(y_e (K_{15})_e - (K_{25})_e \left(\frac{dx}{ds}\right)_e \right) \Delta s_e$	$a_{45} = \sum_e \left((K_{15})_e (F_w)_e - (K_{25})_e (r_t)_e \right) \Delta s_e$
$a_{44} = \Delta s_e \left((K_{11})_e (F_w)_e^2 - 2 (K_{12})_e (F_w)_e (r_t)_e + (K_{22})_e (r_t)_e^2 \right) \Delta s_e$	
$a_{55} = \sum_e \left(\Psi_e (K_{45})_e \right) \Delta s_e + 2 \sum_e (K_{55})_e \Delta s_e$	
$m_{11} = \sum_e (m_0)_e \Delta s_e$	$m_{22} = \sum_e (m_0)_e \Delta s_e$
$m_{33} = \sum_e (m_0)_e \Delta s_e$	$m_{16} = -\sum_e (m_0)_e y_e \Delta s_e + \sum_e (m_1)_e \left(\frac{dx}{ds}\right)_e \Delta s_e$
$m_{34} = \sum_e (m_0)_e y_e \Delta s_e - \sum_e (m_1)_e \left(\frac{dx}{ds}\right)_e \Delta s_e$	$m_{26} = \sum_e (m_0)_e x_e \Delta s_e + \sum_e (m_1)_e \left(\frac{dy}{ds}\right) \Delta s_e$
$m_{35} = -\sum_e (m_0)_e x_e ds - \sum_e (m_1)_e \left(\frac{dy}{ds}\right)_e \Delta s_e$	$m_{37} = -\sum_e (m_0)_e (F_w)_e \Delta s_e + \sum_e (m_1)_e (r_t)_e \Delta s_e$
$m_{77} = \sum_e (m_0)_e (F_w)_e^2 \Delta s_e + \sum_e (m_2)_e (r_t)_e^2 \Delta s_e - 2 \sum_e (m_1)_e (F_w)_e (r_t)_e \Delta s_e$	
$m_{44} = \sum_e (m_0)_e y_e^2 \Delta s_e + \sum_e (m_2)_e \left(\frac{dx}{ds}\right)_e^2 \Delta s_e - 2 \sum_e (m_1)_e y_e \left(\frac{dx}{ds}\right)_e \Delta s_e$	
$m_{55} = \sum_e (m_0)_e x_e^2 \Delta s_e + \sum_e (m_2)_e \left(\frac{dy}{ds}\right)_e^2 \Delta s_e + 2 \sum_e (m_1)_e x_e \left(\frac{dy}{ds}\right)_e \Delta s_e$	
$m_{66} = \sum_e (m_0)_e \left(y_e^2 + x_e^2 \right) \Delta s_e + \sum_e (m_2)_e \left(\left(\frac{dx}{ds}\right)_e^2 + \left(\frac{dy}{ds}\right)_e^2 \right) \Delta s_e$ $+ 2 \sum_e (m_1)_e \left(x_e \left(\frac{dy}{ds}\right)_e - y_e \left(\frac{dx}{ds}\right)_e \right) \Delta s_e$	
$m_{45} = -\sum_e (m_0)_e x_e y_e \Delta s_e + \sum_e (m_2)_e \left(\frac{dx}{ds}\right)_e \left(\frac{dy}{ds}\right)_e \Delta s_e + \sum_e (m_1)_e \left(y_e \left(\frac{dy}{ds}\right)_e - x_e \left(\frac{dx}{ds}\right)_e \right) \Delta s_e$	
$m_{57} = -\sum_e m_0 x F_w ds + \oint_c m_2 r_t \frac{dy}{ds} ds - \oint_c m_1 \left(F_w \frac{dy}{ds} - x r_t \right) ds$	
$m_{47} = -\sum_e (m_0)_e y_e (F_w)_e \Delta s_e - \sum_e (m_2)_e (r_t)_e \left(\frac{dx}{ds}\right)_e \Delta s_e + \sum_e (m_1)_e \left((F_w)_e \left(\frac{dx}{ds}\right)_e + y_e (r_t)_e \right) \Delta s_e$	

Initialization block: structural model, warping function

For calculating the warping function F_w and the area term Ψ, the definitions of Equation (3.113) are used. For the generic case of a multicell cross-section, the calculation of the area term is slightly more complex. Indeed, a different value is calculated for each one of the walls of the cell. Assuming a generic multicell section, Figure 3.32, the relationship between the tangential deformation and the derivative of the twist angle is defined as:

$$\gamma_{sz} = \Psi \frac{\partial \theta}{\partial z}, \text{ being } \left\{ \begin{array}{c} \vdots \\ \gamma_{sz}^{R-1} \\ \gamma_{sz}^{R-1,R} \\ \gamma_{sz}^{R} \\ \gamma_{sz}^{R,R+1} \\ \gamma_{sz}^{R+1} \\ \vdots \end{array} \right\} = \left\{ \begin{array}{c} \vdots \\ \psi^{R-1} \\ \psi^{R-1,R} \\ \psi^{R} \\ \psi^{R+1,R} \\ \psi^{R+1} \\ \vdots \end{array} \right\} \frac{\partial \theta}{\partial z} \tag{3.165}$$

The values of the area term vector are defined as follows:

$$\psi^R = \frac{H^R}{hG_{sz}}, \quad \psi^{R-1,R} = \frac{H^{R-1,R}}{hG_{sz}}, \quad \psi^{R,R+1} = \frac{H^{R,R+1}}{hG_{sz}}. \tag{3.166}$$

The values of the matrix $\mathbf{H}$ are calculated in equation 3.167.

$$\mathbf{H} = \mathbf{S}_A^{-1}\mathbf{I} \tag{3.167}$$

The elements of the matrix $\mathbf{S}_A$ are calculated using the following expressions:

$$S_A^R = \frac{\delta_R}{2\Omega_R G_{sz}}, \quad S_A^{R-1,R} = \frac{\delta_{R-1,R}}{2\Omega_R G_{sz}}, \quad S_A^{R,R+1} = \frac{\delta_{R,R+1}}{2\Omega_R G_{sz}}, \tag{3.168}$$

being the δ vector defined as:

$$\delta_R = \oint_R \frac{ds}{h} \approx \sum_{e \in R} \frac{\Delta s_e}{h_e} \tag{3.169}$$

for the walls that only belong to one cell, and:

$$\delta_{R-1,R} = \oint_{R-1,R} \frac{ds}{h} \approx \sum_{e \in \{R-1,R\}} \frac{\Delta s_e}{h_e}, \quad \delta_{R,R+1} = \oint_{R,R+1} \frac{ds}{h} \approx \sum_{e \in \{R,R+1\}} \frac{\Delta s_e}{h_e} \tag{3.170}$$

for the walls shared with the adjacent cells.

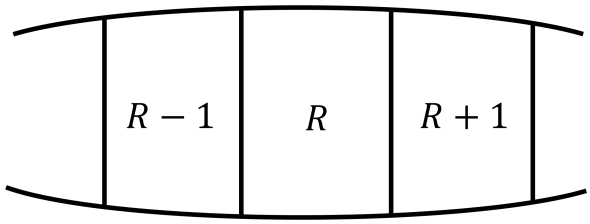

Fig. 3.32 **Diagram of a multi-cell cross-section.** The cell R and the adjacent cells are presented.

Concerning the warping, the cross-sections are allowed to deform out of the plane due to the twisting loads. The warping function integration algorithm is complex and depends on the typology of the section. Different functions are required for calculating the open and the closed cross-sections. For the open cross-section, the algorithm for calculating the warping function of a thin-walled open section is summarized in Figure 3.33.

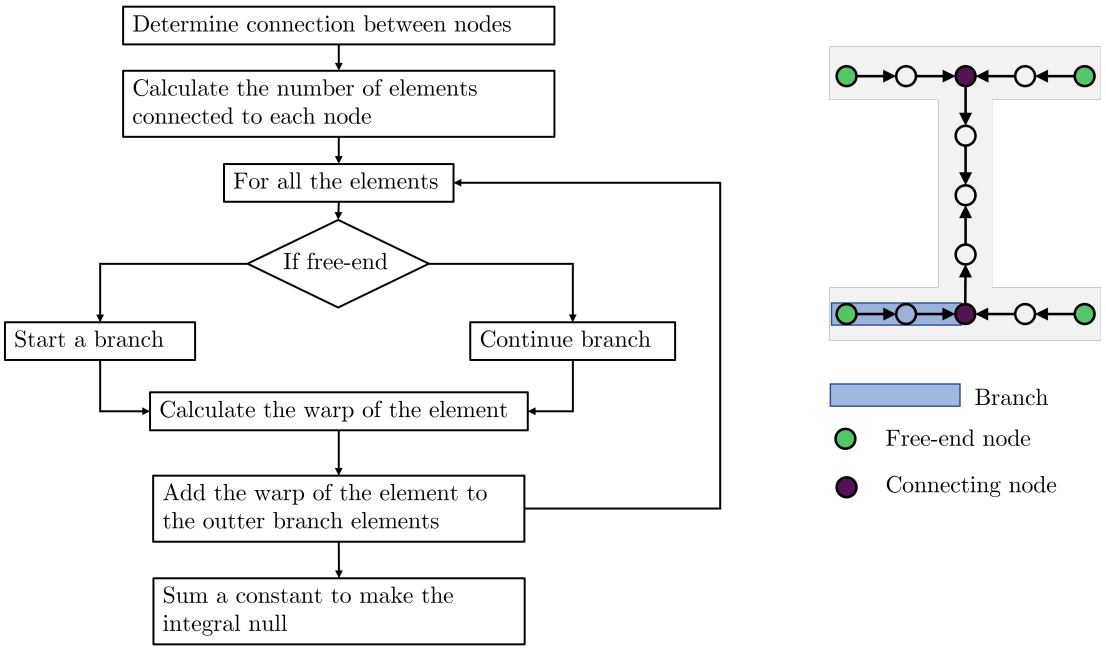

Fig. 3.33 **Algorithm for calculating the open section warping function.** The warping value along the section is accumulated to the free ends. Therefore, the algorithm requires to account for the elements inside each branch.

This algorithm starts by identifying the connections between the nodes and the elements. The number of elements connected to each node is used for sorting the nodes, starting the calculation from the free-end nodes. A branch (blue shading of the cross-section of Figure 3.33) is used for adding the values of the increase in the warping function backward. In other words, the free-end points are required to start the calculation, but the value in these nodes

depends on the following value. Using the branches, the information is transported. Then, for the internal points of the branch, the loop is repeated, adding more nodes in each iteration. Finally, in some cases, the branches may collapse into a single grid point, called connecting node. This node provides the information to the previous branches. Two examples of warping function in open cross-section are provided in Figure 3.34. The example shows warping in an I-shape and C-shape cross-sections. Note that the higher warping function is presented in the free ends of the section. In the figure, the warping function is provided with a color scale. The lighter colors mean positive movement out of its plane, and the darker ones mean negative movement out of the plane.

Fig. 3.34 **Warping function for open cross-section beams.** (Left) I-shape cross-section, (right) C-shape cross-section.

A slightly different code is used for the general multicell closed section. In this case, the algorithm starts associating the elements with the corresponding cells and calculating their connectivity. Some elements may belong to a single cell, while others to a pair of cells. A positive rotation direction is defined for each cell, defining if the rotation is in the same direction as the element or counter-wise. Then, terms of the integrand of Equation (3.113) are calculated for the cross-section elements. The first term, $(r_n)_i \Delta s$, is directly calculated, whereas the procedure presented previously, Equation (3.165), is followed for the calculation of the vector Ψ for every cell. Finally, the integration is started from the initial point, storing the increase of the warping in the initial point of the next element. Multiple inputs or outputs might appear in multicell structures. The schematic algorithm is presented in Figure 3.35.

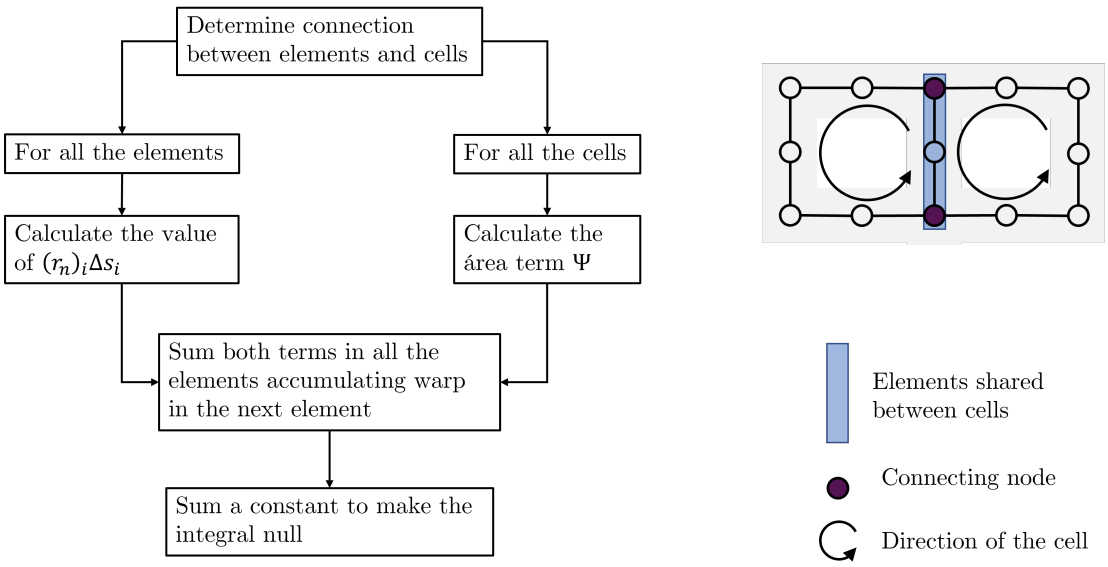

Fig. 3.35 **Algorithm for calculating the closed section warping function.** The warping value along the section is accumulated from the initial element of the first cell. Then a constant term is added to make the integral null. The reference point of the section is the black circle.

The algorithm is tested, and the results on two box-shape closed section beams are calculated. These results are obtained for a single-cell section and a multicell section. The warping functions are presented in Figure 3.36. Note that the corners of the box are the zones where the warping is higher, while their center presents the lower influence. As previously stated, the light colors are related to positive warping, while the darker ones are negative out-of-the-plane displacements.

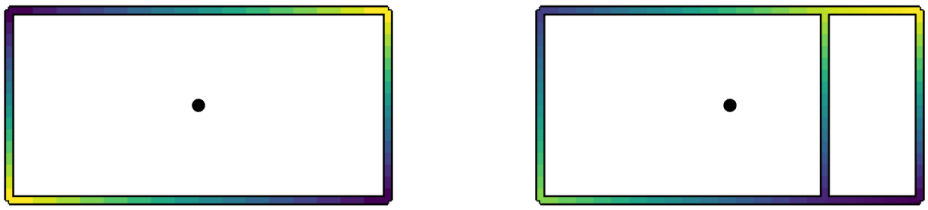

Fig. 3.36 **Warping function for closed cross-section beams.** (Left) Box-shape cross-section, (right) multicell box-shape cross-section. The reference point of the section is the black circle.

Note that the warping function is highly dependent on the reference point of the calculation. In Figures 3.34 and 3.36, the reference point was indicated by a black dot.

Initialization block: structural model, integration of the beam elements

Once the cross-section properties are obtained, they must be integrated along the beam elements. This integration is used to calculate the local stiffness and mass matrices in the local coordinate frame of the element, Equations (3.156) and (3.162). Figure 3.37 presents an example of a beam element.

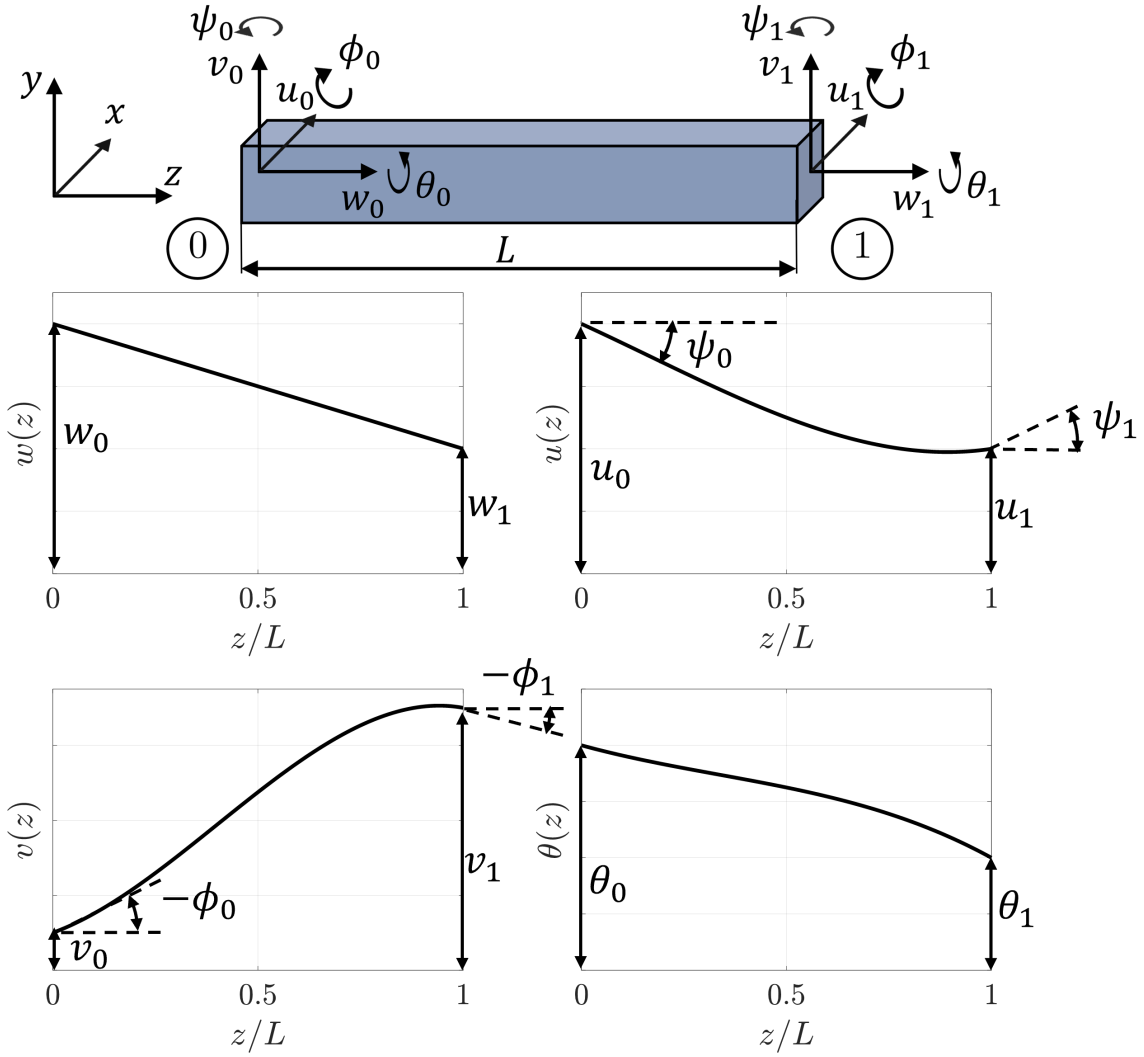

Fig. 3.37 **Beam element diagram.** Note that the beam element solver calculates the displacements on the nodes 0 and 1.

In order to calculate these matrices, the shape functions of the independent variables must be defined. Figure 3.37 shows an example of these shape functions. For the nonshearable beam, four independent variables are taken into account in the solution:

- Axial displacement of the beam. This displacement is assumed to be linear along the beam element.

$$w(z) = \frac{z}{L} w_1 + \left(1 - \frac{z}{L}\right) w_0 \tag{3.171}$$

- Transverse displacement in the x direction. A cubic function is used for defining the displacement inside the element.

$$\begin{aligned} u(z) = &\left(\frac{3z^2}{L^2} - \frac{2z^3}{L^3}\right) u_1 + \left(1 - \frac{3z^2}{L^2} + \frac{2z^3}{L^3}\right) u_0 \\ &+ \left(z - \frac{2z^2}{L} + \frac{z^3}{L^2}\right) \psi_0 + \left(-\frac{z^2}{L} + \frac{z^3}{L^2}\right) \psi_1 \end{aligned} \tag{3.172}$$

- Transverse displacement in the y direction. A cubic function is assumed inside the element.

$$\begin{aligned} v(z) = &\left(\frac{3z^2}{L^2} - \frac{2z^3}{L^3}\right) v_1 + \left(1 - \frac{3z^2}{L^2} + \frac{2z^3}{L^3}\right) v_0 \\ &+ \left(-z + \frac{2z^2}{L} - \frac{z^3}{L^2}\right) \phi_0 + \left(\frac{z^2}{L} - \frac{z^3}{L^2}\right) \phi_1 \end{aligned} \tag{3.173}$$

- Twist in the beam element. A cubic function is used:

$$\begin{aligned} \theta(z) = &\left(\frac{3z^2}{L^2} - \frac{2z^3}{L^3}\right) \theta_1 + \left(1 - \frac{3z^2}{L^2} + \frac{2z^3}{L^3}\right) \theta_0 \\ &+ \left(z - \frac{2z^2}{L} + \frac{z^3}{L^2}\right) \frac{\partial \theta_0}{\partial z} + \left(-\frac{z^2}{L} + \frac{z^3}{L^2}\right) \frac{\partial \theta_1}{\partial z} \end{aligned} \tag{3.174}$$

Once the deformation energy is calculated for the whole beam element, the stiffness matrix is obtained by deriving the matrix with respect to the node displacements and rotations. The vector of the node parameters is presented in the following expression:

$$\mathbf{q}_N^e = \left[u_0, v_0, w_0, \phi_0, \psi_0, \theta_0, \frac{\partial \phi_0}{\partial z}, \frac{\partial \psi_0}{\partial z}, \frac{\partial \theta_0}{\partial z}, u_1, v_1, w_1, \phi_1, \psi_1, \theta_1, \frac{\partial \phi_1}{\partial z}, \frac{\partial \psi_1}{\partial z}, \frac{\partial \theta_1}{\partial z} \right]^T \tag{3.175}$$

Therefore, the deformation energy is calculated from Equation (3.156) and then derived with respect to the $\mathbf{q}_N^e$ vector to calculate the element stiffness matrix $\mathbf{K}^e$.

$$(K^e)_{ij} = \frac{\partial^2 U}{\partial \left(q_N^e\right)_i \partial \left(q_N^e\right)_j} \tag{3.176}$$

The elements of the matrix are presented in Table 3.6. These parameters are the results of Equation (3.176) after integrating the cross-section stiffness along the length of the element.

Table 3.6 **Coefficients of the beam element stiffness matrix.** The coefficients are calculated in their local reference frame.

$K^e_{1,1} = \frac{12a_{22}}{L^3}$	$K^e_{1,2} = K^e_{2,1} = \frac{12a_{23}}{L^3}$	$K^e_{1,3} = K^e_{3,1} = 0$
$K^e_{1,4} = K^e_{4,1} = -\frac{6a_{23}}{L^2}$	$K^e_{1,5} = K^e_{5,1} = \frac{6a_{22}}{L^2}$	$K^e_{1,6} = K^e_{6,1} = \frac{12a_{24}}{L^3}$
$K^e_{1,7} = K^e_{7,1} = 0$	$K^e_{1,8} = K^e_{8,1} = 0$	$K^e_{1,9} = K^e_{9,1} = \frac{6a_{24}+a_{25}L}{L^2}$
$K^e_{1,10} = K^e_{10,1} = -\frac{12a_{22}}{L^3}$	$K^e_{1,11} = K^e_{11,1} = -\frac{12a_{23}}{L^3}$	$K^e_{1,12} = K^e_{12,1} = 0$
$K^e_{1,13} = K^e_{13,1} = -\frac{6a_{23}}{L^2}$	$K^e_{1,14} = K^e_{14,1} = \frac{6a_{22}}{L^2}$	$K^e_{1,15} = K^e_{15,1} = -\frac{12a_{24}}{L^3}$
$K^e_{1,16} = K^e_{16,1} = 0$	$K^e_{1,17} = K^e_{17,1} = 0$	$K^e_{1,18} = K^e_{18,1} = \frac{6a_{24}-a_{25}L}{L^2}$
$K^e_{2,2} = \frac{12a_{33}}{L^3}$	$K^e_{2,3} = K^e_{3,2} = 0$	$K^e_{2,4} = K^e_{4,2} = -\frac{6a_{33}}{L^2}$
$K^e_{2,5} = K^e_{5,2} = \frac{6a_{23}}{L^2}$	$K^e_{2,6} = K^e_{6,2} = \frac{12a_{34}}{L^3}$	$K^e_{2,7} = K^e_{7,2} = 0$
$K^e_{2,8} = K^e_{8,2} = 0$	$K^e_{2,9} = K^e_{9,2} = \frac{6a_{34}+a_{35}L}{L^2}$	$K^e_{2,10} = K^e_{10,2} = -\frac{12a_{23}}{L^3}$
$K^e_{2,11} = K^e_{11,2} = -\frac{12a_{33}}{L^3}$	$K^e_{2,12} = K^e_{12,2} = 0$	$K^e_{2,13} = K^e_{13,2} = -\frac{6a_{33}}{L^3}$
$K^e_{2,14} = K^e_{14,2} = \frac{6a_{23}}{L^2}$	$K^e_{2,15} = K^e_{15,2} = -\frac{12a_{34}}{L^3}$	$K^e_{2,16} = K^e_{16,2} = 0$
$K^e_{2,17} = K^e_{17,2} = 0$	$K^e_{2,18} = K^e_{18,2} = \frac{6a_{34}-a_{35}L}{L^2}$	$K^e_{3,3} = \frac{a_{11}}{L}$
$K^e_{3,4} = K^e_{4,3} = \frac{a_{13}}{L}$	$K^e_{3,5} = K^e_{5,3} = -\frac{a_{12}}{L}$	$K^e_{3,6} = K^e_{6,3} = \frac{a_{15}}{L}$
$K^e_{3,7} = K^e_{7,3} = 0$	$K^e_{3,8} = K^e_{8,3} = 0$	$K^e_{3,9} = K^e_{9,3} = -\frac{a_{14}}{L}$
$K^e_{3,10} = K^e_{10,3} = 0$	$K^e_{3,11} = K^e_{11,3} = 0$	$K^e_{3,12} = K^e_{12,3} = -\frac{a_{11}}{L}$
$K^e_{3,13} = K^e_{13,3} = -\frac{a_{13}}{L}$	$K^e_{3,14} = K^e_{14,3} = \frac{a_{12}}{L}$	$K^e_{3,15} = K^e_{15,3} = -\frac{a_{15}}{L}$
$K^e_{3,16} = K^e_{16,3} = 0$	$K^e_{3,17} = K^e_{17,3} = 0$	$K^e_{3,18} = K^e_{18,3} = \frac{a_{14}}{L}$
$K^e_{4,4} = \frac{4a_{33}}{L}$	$K^e_{4,5} = K^e_{5,4} = -\frac{4a_{23}}{L}$	$K^e_{4,6} = K^e_{6,4} = -\frac{-6a_{34}+a_{35}L}{L^2}$
$K^e_{4,7} = K^e_{7,4} = 0$	$K^e_{4,8} = K^e_{8,4} = 0$	$K^e_{4,9} = K^e_{9,4} = -\frac{a_{35}}{2} - \frac{4a_{34}}{L}$
$K^e_{4,10} = K^e_{10,4} = \frac{6a_{23}}{L^2}$	$K^e_{4,11} = K^e_{11,4} = \frac{6a_{33}}{L^2}$	$K^e_{4,12} = K^e_{12,4} = -\frac{a_{13}}{L}$
$K^e_{4,13} = K^e_{13,4} = \frac{2a_{33}}{L}$	$K^e_{4,14} = K^e_{14,4} = -\frac{2a_{23}}{L}$	$K^e_{4,15} = K^e_{15,4} = \frac{6a_{34}-a_{35}L}{L^2}$

$K^e_{4,16} = K^e_{16,4} = 0$	$K^e_{4,17} = K^e_{17,4} = 0$	$K^e_{4,18} = K^e_{18,4} = \frac{a_{35}}{2} - \frac{2a_{34}}{L}$
$K^e_{5,5} = \frac{4a_{22}}{L}$	$K^e_{5,6} = K^e_{6,5} = \frac{6a_{24} - a_{25}L}{L^2}$	$K^e_{5,7} = K^e_{7,5} = 0$
$K^e_{5,8} = K^e_{8,5} = 0$	$K^e_{5,9} = K^e_{9,5} = \frac{a_{25}}{2} - \frac{4a_{24}}{L}$	$K^e_{5,10} = K^e_{10,5} = -\frac{6a_{22}}{L^2}$
$K^e_{5,11} = K^e_{11,5} = -\frac{6a_{23}}{L^2}$	$K^e_{5,12} = K^e_{12,5} = \frac{a_{12}}{L}$	$K^e_{5,13} = K^e_{13,5} = \frac{-2a_{23}}{L}$
$K^e_{5,14} = K^e_{14,5} = \frac{2a_{22}}{L}$	$K^e_{5,15} = K^e_{15,5} = \frac{-6a_{24} + a_{25}L}{L^2}$	$K^e_{5,16} = K^e_{16,5} = 0$
$K^e_{5,17} = K^e_{17,5} = 0$	$K^e_{5,18} = K^e_{18,5} = -\frac{a_{25}}{2} + \frac{2a_{24}}{L}$	$K^e_{6,6} = \frac{6\left(10a_{44} + a_{55}L^2\right)}{5L^3}$
$K^e_{6,7} = K^e_{7,6} = 0$	$K^e_{6,8} = K^e_{8,6} = 0$	$K^e_{6,9} = K^e_{9,6} = \frac{a_{77}}{10} + \frac{6a_{66}}{L^2}$
$K^e_{6,10} = K^e_{10,6} = -\frac{12a_{24}}{L^3}$	$K^e_{6,11} = K^e_{11,6} = -\frac{12a_{34}}{L^3}$	$K^e_{6,12} = K^e_{12,6} = -\frac{a_{17}}{L}$
$K^e_{6,13} = K^e_{13,6} = -\frac{6a_{34} + a_{35}L}{L^2}$	$K^e_{6,14} = K^e_{14,6} = -\frac{6a_{24} + a_{25}L}{L^2}$	$K^e_{6,15} = K^e_{15,6} = -\frac{12a_{44}}{L^3} - \frac{6a_{55}}{5L}$
$K^e_{6,16} = K^e_{16,6} = 0$	$K^e_{6,17} = K^e_{17,6} = 0$	$K^e_{6,18} = K^e_{18,6} = \frac{a_{55}}{10} + \frac{6a_{44}}{L^2}$
$K^e_{7,7} = 0$	$K^e_{7,8} = K^e_{8,7} = 0$	$K^e_{7,9} = K^e_{9,7} = 0$
$K^e_{7,10} = K^e_{10,7} = 0$	$K^e_{7,11} = K^e_{11,7} = 0$	$K^e_{7,12} = K^e_{12,7} = 0$
$K^e_{7,13} = K^e_{13,7} = 0$	$K^e_{7,14} = K^e_{14,7} = 0$	$K^e_{7,15} = K^e_{15,7} = 0$
$K^e_{7,16} = K^e_{16,7} = 0$	$K^e_{7,17} = K^e_{17,7} = 0$	$K^e_{7,18} = K^e_{18,7} = 0$
$K^e_{8,8} = 0$	$K^e_{8,9} = K^e_{9,8} = 0$	$K^e_{8,10} = K^e_{10,8} = 0$
$K^e_{8,11} = K^e_{11,8} = 0$	$K^e_{8,12} = K^e_{12,8} = 0$	$K^e_{8,13} = K^e_{13,8} = 0$
$K^e_{8,14} = K^e_{14,8} = 0$	$K^e_{8,15} = K^e_{15,8} = 0$	$K^e_{8,16} = K^e_{16,8} = 0$
$K^e_{8,17} = K^e_{17,8} = 0$	$K^e_{8,18} = K^e_{18,8} = 0$	$K^e_{9,9} == a_{45} + \frac{4a_{44}}{L} + \frac{2a_{55}L}{15}$
$K^e_{9,10} = K^e_{10,9} = -\frac{6a_{24} + a_{25}L}{L^2}$	$K^e_{9,11} = K^e_{11,9} = -\frac{6a_{34} + a_{35}L}{L^2}$	$K^e_{9,12} = K^e_{12,9} = \frac{a_{14}}{L}$
$K^e_{9,13} = K^e_{13,9} = -\frac{a_{35}}{2} - \frac{2a_{34}}{L}$	$K^e_{9,14} = K^e_{14,9} = \frac{a_{25}}{2} + \frac{2a_{26}}{L}$	$K^e_{9,15} = K^e_{15,9} = -\frac{a_{55}}{10} - \frac{6a_{44}}{L^2}$
$K^e_{9,16} = K^e_{16,9} = 0$	$K^e_{9,17} = K^e_{17,9} = 0$	$K^e_{9,18} = K^e_{18,9} = \frac{2a_{44}}{L} - \frac{a_{55}L}{30}$
$K^e_{10,10} = \frac{12a_{22}}{L^3}$	$K^e_{10,11} = K^e_{11,10} = \frac{12a_{23}}{L^3}$	$K^e_{10,12} = K^e_{12,10} = 0$
$K^e_{10,13} = K^e_{13,10} = \frac{6a_{23}}{L^2}$	$K^e_{10,14} = K^e_{14,10} = -\frac{6a_{23}}{L^2}$	$K^e_{10,15} = K^e_{15,10} = \frac{12a_{24}}{L^3}$
$K^e_{10,16} = K^e_{16,10} = 0$	$K^e_{10,17} = K^e_{17,10} = 0$	$K^e_{10,18} = K^e_{18,10} = \frac{-6a_{24} + a_{25}L}{L^2}$
$K^e_{11,11} = \frac{12a_{33}}{L^3}$	$K^e_{11,12} = K^e_{12,11} = 0$	$K^e_{11,13} = K^e_{13,11} = \frac{6a_{33}}{L^2}$
$K^e_{11,14} = K^e_{14,11} = -\frac{6a_{23}}{L^2}$	$K^e_{11,15} = K^e_{15,11} = \frac{12a_{36}}{L^3}$	$K^e_{11,16} = K^e_{16,11} = 0$
$K^e_{11,17} = K^e_{17,11} = 0$	$K^e_{11,18} = K^e_{18,11} = \frac{-6a_{36} + a_{37}L}{L^2}$	$K^e_{12,12} = \frac{a_{11}}{L}$
$K^e_{12,13} = K^e_{13,12} = \frac{a_{13}}{L}$	$K^e_{12,14} = K^e_{14,12} = -\frac{a_{12}}{L}$	$K^e_{12,15} = K^e_{15,12} = \frac{a_{15}}{L}$
$K^e_{12,16} = K^e_{16,12} = 0$	$K^e_{12,17} = K^e_{17,12} = 0$	$K^e_{12,18} = K^e_{18,12} = -\frac{a_{14}}{L}$
$K^e_{13,13} = \frac{4a_{33}}{L}$	$K^e_{13,14} = K^e_{14,13} = -\frac{4a_{23}}{L}$	$K^e_{13,15} = K^e_{15,13} = \frac{6a_{34} + a_{35}L}{L^2}$
$K^e_{13,16} = K^e_{16,13} = 0$	$K^e_{13,17} = K^e_{17,13} = 0$	$K^e_{13,18} = K^e_{18,13} = \frac{a_{35}}{2} - \frac{4a_{34}}{L}$
$K^e_{14,14} = \frac{4a_{22}}{L}$	$K^e_{14,15} = K^e_{15,14} = -\frac{6a_{24} + a_{25}L}{L^2}$	$K^e_{14,16} = K^e_{16,14} = 0$
$K^e_{14,17} = K^e_{17,14} = 0$	$K^e_{14,18} = K^e_{18,14} = -\frac{a_{25}}{2} + \frac{4a_{24}}{L}$	$K^e_{15,15} = \frac{12a_{44}}{L^3} + \frac{6a_{55}}{5L}$
$K^e_{15,16} = K^e_{16,15} = 0$	$K^e_{15,17} = K^e_{17,15} = 0$	$K^e_{15,18} = K^e_{18,15} = -\frac{a_{55}}{10} - \frac{6a_{44}}{L^2}$

$K^e_{16,16} = 0$	$K^e_{16,17} = K^e_{17,16} = 0$	$K^e_{16,18} = K^e_{18,16} = 0$
$K^e_{17,17} = 0$	$K^e_{17,18} = K^e_{18,17} = 0$	$K^e_{18,18} = -a_{45} + \frac{4a_{44}}{L} + \frac{2a_{55}L}{15}$

A similar procedure is followed to calculate the beam element mass matrix. In this case, the kinetic energy, Equation (3.162), is used. Then, the mass matrix is obtained by deriving the energy concerning the elements of $\ddot{\mathbf{D}}^e_N$ vector, Equation (3.177). The coefficients of the matrix are presented in Table 3.7.

$$(M^e)_{ij} = \frac{\partial^2 T}{\partial \left(\ddot{q}^e_N\right)_i \partial \left(\ddot{q}^e_N\right)_j} \tag{3.177}$$

Once the beam element stiffness and mass matrices are calculated in the local reference frame, they must be rotated to the global reference frame. After the rotation, the resulting element matrices must be assembled in the global stiffness, $\mathbf{K}^G$, and mass, $\mathbf{M}^G$, matrices. The global system integrates the degrees of freedom of all the nodes. The vector containing all the displacements is called $\mathbf{u}^G$. The loads used during the calculation are concentrated on the nodes. The vector $\mathbf{F}^G$ contains all the loads on the structure.

Table 3.7 **Coefficients of the beam element mass matrix.** The coefficients are calculated in their local reference frame.

$M^e_{1,1} = \frac{13Lm_{11}}{35} + \frac{6m_{55}}{5L}$	$M^e_{1,2} = M^e_{2,1} = \frac{6m_{45}}{5L}$
$M^e_{1,3} = M^e_{3,1} = \frac{m_{35}}{2}$	$M^e_{1,4} = M^e_{4,1} = -\frac{m_{45}}{10}$
$M^e_{1,5} = K^e_{5,1} = \frac{11L^2m_{11}}{210} + \frac{m_{55}}{10}$	$M^e_{1,6} = M^e_{6,1} = \frac{13Lm_{16}}{35} - \frac{6m_{57}}{5L}$
$M^e_{1,7} = M^e_{7,1} = 0$	$M^e_{1,8} = M^e_{8,1} = 0$
$M^e_{1,9} = M^e_{9,1} = \frac{11L^2m_{16}}{210} - \frac{m_{57}}{10}$	$M^e_{1,10} = M^e_{10,1} = \frac{9Lm_{11}}{70} - \frac{6m_{55}}{5L}$
$M^e_{1,11} = M^e_{11,1} = -\frac{6m_{45}}{5L}$	$M^e_{1,12} = M^e_{12,1} = \frac{m_{35}}{2}$
$M^e_{1,13} = M^e_{13,1} = -\frac{m_{45}}{10}$	$M^e_{1,14} = M^e_{14,1} = -\frac{13L^2m_{11}}{420} + \frac{m_{55}}{10}$
$M^e_{1,15} = M^e_{15,1} = \frac{9Lm_{16}}{70} + \frac{6m_{57}}{5L}$	$M^e_{1,16} = M^e_{16,1} = 0$
$M^e_{1,17} = M^e_{17,1} = 0$	$M^e_{1,18} = M^e_{18,1} = -\frac{13L^2m_{16}}{420} - \frac{m_{57}}{10}$
$M^e_{2,2} = \frac{13Lm_{11}}{35} + \frac{6m_{55}}{5L}$	$M^e_{2,3} = M^e_{3,2} = \frac{m_{34}}{2}$
$M^e_{2,4} = M^e_{4,2} = -\frac{11L^2m_{22}}{210} - \frac{m_{44}}{10}$	$M^e_{2,5} = M^e_{5,2} = \frac{m_{45}}{10}$
$M^e_{2,6} = M^e_{6,2} = \frac{13Lm_{26}}{35} - \frac{6m_{47}}{5L}$	$M^e_{2,7} = M^e_{7,2} = 0$
$M^e_{2,8} = M^e_{8,2} = 0$	$M^e_{2,9} = M^e_{9,2} = \frac{11Lm_{26}}{210} - \frac{m_{47}}{10}$
$M^e_{2,10} = M^e_{10,2} = -\frac{6m_{45}}{5L}$	$M^e_{2,11} = M^e_{11,2} = \frac{9Lm_{22}}{70} - \frac{6m_{44}}{5L}$

$M^e_{2,12} = M^e_{12,2} = \frac{m_{34}}{2}$	$M^e_{2,13} = M^e_{13,2} = \frac{13L^2 m_{22}}{420} - \frac{m_{44}}{420}$
$M^e_{2,14} = M^e_{14,2} = \frac{m_{45}}{10}$	$M^e_{2,15} = M^e_{15,2} = \frac{9Lm_{26}}{70} + \frac{6m_{47}}{5L}$
$M^e_{2,16} = M^e_{16,2} = 0$	$M^e_{2,17} = M^e_{17,2} = 0$
$M^e_{2,18} = M^e_{18,2} = -\frac{13L^2 m_{26}}{420} - \frac{m_{47}}{10}$	$M^e_{3,3} = \frac{m_{33}L}{3}$
$M^e_{3,4} = M^e_{4,3} = \frac{m_{34}L}{12}$	$M^e_{3,5} = M^e_{5,3} = -\frac{m_{35}L}{12}$
$M^e_{3,6} = M^e_{6,3} = \frac{-m_{37}}{2}$	$M^e_{3,7} = M^e_{7,3} = 0$
$M^e_{3,8} = M^e_{8,3} = 0$	$M^e_{3,9} = M^e_{9,3} = -\frac{m_{37}L}{12}$
$M^e_{3,10} = M^e_{10,3} = -\frac{m_{35}}{2}$	$M^e_{3,11} = M^e_{11,3} = -\frac{m_{34}}{2}$
$M^e_{3,12} = M^e_{12,3} = -\frac{m_{33}L}{6}$	$M^e_{3,13} = M^e_{13,3} = -\frac{m_{34}L}{12}$
$M^e_{3,14} = M^e_{14,3} = \frac{m_{35}L}{12}$	$M^e_{3,15} = M^e_{15,3} = -\frac{m_{37}}{2}$
$M^e_{3,16} = M^e_{16,3} = 0$	$M^e_{3,17} = M^e_{17,3} = 0$
$M^e_{3,18} = M^e_{18,3} = -\frac{m_{37}L}{12}$	$M^e_{4,4} = \frac{m_{22}L^3}{105} + \frac{2Lm_{44}}{15}$
$M^e_{4,5} = M^e_{5,4} = -\frac{2Lm_{45}}{15}$	$M^e_{4,6} = M^e_{6,4} = -\frac{11L^2 m_{26}}{210} + \frac{m_{47}}{10}$
$M^e_{4,7} = M^e_{7,4} = 0$	$M^e_{4,8} = M^e_{8,4} = 0$
$M^e_{4,9} = M^e_{9,4} = -\frac{L^3 m_{26}}{105} + \frac{2Lm_{47}}{15}$	$M^e_{4,10} = M^e_{10,4} = \frac{m_{45}}{10}$
$M^e_{4,11} = M^e_{11,4} = -\frac{13L^2 m_{22}}{420} + \frac{m_{44}}{10}$	$M^e_{4,12} = M^e_{12,4} = -\frac{m_{34}L}{12}$
$M^e_{4,13} = M^e_{13,4} = -\frac{L^3 m_{22}}{140} + \frac{m_{44}}{30}$	$M^e_{4,14} = M^e_{14,4} = \frac{m_{45}L}{30}$
$M^e_{4,15} = M^e_{15,4} = -\frac{13L^2 m_{26}}{420} - \frac{m_{47}}{10}$	$M^e_{4,16} = M^e_{16,4} = 0$
$M^e_{4,17} = M^e_{17,4} = 0$	$M^e_{4,18} = M^e_{18,4} = \frac{L^3 m_{26}}{140} - \frac{m_{47}L}{30}$
$M^e_{5,5} = \frac{L^3 m_{11}}{105} + \frac{Lm_{55}}{15}$	$M^e_{5,6} = M^e_{6,5} = \frac{11L^2 m_{16}}{210} - \frac{m_{57}}{10}$
$M^e_{5,7} = M^e_{7,5} = 0$	$M^e_{5,8} = M^e_{8,5} = 0$
$M^e_{5,9} = M^e_{9,5} = \frac{L^3 m_{16}}{105} - \frac{Lm_{57}}{15}$	$M^e_{5,10} = M^e_{10,5} = \frac{13L^2 m_{11}}{420} - \frac{m_{55}}{10}$
$M^e_{5,11} = M^e_{11,5} = -\frac{m_{45}}{10}$	$M^e_{5,12} = M^e_{12,5} = \frac{m_{35}L}{12}$
$M^e_{5,13} = M^e_{13,5} = \frac{m_{45}L}{30}$	$M^e_{5,14} = M^e_{14,5} = -\frac{L^3 m_{11}}{140} - \frac{m_{55}}{30}$
$M^e_{5,15} = M^e_{15,5} = -\frac{13L^2 m_{26}}{420} + \frac{m_{57}}{10}$	$M^e_{5,16} = M^e_{16,5} = 0$
$M^e_{5,17} = M^e_{17,5} = 0$	$M^e_{5,18} = M^e_{18,5} = -\frac{L^3 m_{16}}{140} + \frac{m_{57}L}{30}$
$M^e_{6,6} = \frac{13Lm_{66}}{35} + \frac{6m_{77}}{5L}$	$M^e_{6,7} = M^e_{7,6} = 0$
$M^e_{6,8} = M^e_{8,6} = 0$	$M^e_{6,9} = M^e_{9,6} = \frac{11L^2 m_{66}}{210} + \frac{m_{77}}{10}$
$M^e_{6,10} = M^e_{10,6} = \frac{9Lm_{16}}{70} + \frac{6m_{57}}{5L}$	$M^e_{6,11} = M^e_{11,6} = \frac{9Lm_{26}}{70} + \frac{6m_{47}}{5L}$
$M^e_{6,12} = M^e_{12,6} = -\frac{m_{37}}{2}$	$M^e_{6,13} = M^e_{13,6} = \frac{13L^2 m_{26}}{420} + \frac{m_{47}}{10}$
$M^e_{6,14} = M^e_{14,6} = -\frac{13L^2 m_{16}}{420} - \frac{m_{57}}{10}$	$M^e_{6,15} = M^e_{15,6} = -\frac{9Lm_{66}}{70} - \frac{6m_{77}}{5L}$
$M^e_{6,16} = M^e_{16,6} = 0$	$M^e_{6,17} = M^e_{17,6} = 0$
$M^e_{6,18} = M^e_{18,6} = -\frac{13L^2 m_{66}}{420} + \frac{m_{77}}{10}$	$M^e_{7,7} = 0$

$M^e_{7,8} = M^e_{8,7} = 0$	$M^e_{7,9} = M^e_{9,7} = 0$
$M^e_{7,10} = M^e_{10,7} = 0$	$M^e_{7,11} = M^e_{11,7} = 0$
$M^e_{7,12} = M^e_{12,7} = 0$	$M^e_{7,13} = M^e_{13,7} = 0$
$M^e_{7,14} = M^e_{14,7} = 0$	$M^e_{7,15} = M^e_{15,7} = 0$
$M^e_{7,16} = M^e_{16,7} = 0$	$M^e_{7,17} = M^e_{17,7} = 0$
$M^e_{7,18} = M^e_{18,7} = 0$	$M^e_{8,8} = 0$
$M^e_{8,9} = M^e_{9,8} = 0$	$M^e_{8,10} = M^e_{10,8} = 0$
$M^e_{8,11} = M^e_{11,8} = 0$	$M^e_{8,12} = M^e_{12,8} = 0$
$M^e_{8,13} = M^e_{13,8} = 0$	$M^e_{8,14} = M^e_{14,8} = 0$
$M^e_{8,15} = M^e_{15,8} = 0$	$M^e_{8,16} = M^e_{16,8} = 0$
$M^e_{8,17} = M^e_{17,8} = 0$	$M^e_{8,18} = M^e_{18,8} = 0$
$M^e_{9,9} == \frac{L^3 m_{66}}{105} + \frac{2m_{77}L}{15}$	$M^e_{9,10} = M^e_{10,9} = \frac{13L^2 m_{16}}{420} + \frac{m_{57}}{10}$
$M^e_{9,11} = M^e_{11,9} = \frac{13L^2 m_{26}}{420} + \frac{m_{47}}{10}$	$M^e_{9,12} = M^e_{12,9} = -\frac{Lm_{37}}{12}$
$M^e_{9,13} = M^e_{13,9} = \frac{L^3 m_{26}}{140} - \frac{Lm_{47}}{30}$	$M^e_{9,14} = M^e_{14,9} = -\frac{L^3 m_{16}}{140} + \frac{Lm_{57}}{30}$
$M^e_{9,15} = M^e_{15,9} = -\frac{13L^2 m_{66}}{420} - \frac{m_{77}}{10}$	$M^e_{9,16} = M^e_{16,9} = 0$
$M^e_{9,17} = M^e_{17,9} = 0$	$M^e_{9,18} = M^e_{18,9} = -\frac{L^3 m_{66}}{140} - \frac{m_{77}L}{30}$
$M^e_{10,10} = \frac{13Lm_{11}}{35} + \frac{6m_{55}}{5L}$	$M^e_{10,11} = M^e_{11,10} = \frac{6m_{45}}{5L}$
$M^e_{10,12} = M^e_{12,10} = -\frac{m_{35}}{2}$	$M^e_{10,13} = M^e_{13,10} = \frac{m_{45}}{10}$
$M^e_{10,14} = M^e_{14,10} = -\frac{11L^2 m_{11}}{210} - \frac{m_{55}}{10}$	$M^e_{10,15} = M^e_{15,10} = \frac{13Lm_{16}}{35} - \frac{6m_{57}}{5L}$
$M^e_{10,16} = M^e_{16,10} = 0$	$M^e_{10,17} = M^e_{17,10} = 0$
$M^e_{10,18} = M^e_{18,10} = -\frac{11L^2 m_{16}}{210} + \frac{m_{57}}{10}$	$M^e_{11,11} = \frac{13Lm_{22}}{35} + \frac{6m_{44}}{5L}$
$M^e_{11,12} = M^e_{12,11} = -\frac{m_{34}}{2}$	$M^e_{11,13} = M^e_{13,11} = \frac{11L^2 m_{22}}{210} + \frac{m_{44}}{10}$
$M^e_{11,14} = M^e_{14,11} = -\frac{m_{45}}{10}$	$M^e_{11,15} = M^e_{15,11} = \frac{13Lm_{26}}{35} - \frac{6m_{47}}{5L}$
$M^e_{11,16} = M^e_{16,11} = 0$	$M^e_{11,17} = M^e_{17,11} = 0$
$M^e_{11,18} = M^e_{18,11} = -\frac{11L^2 m_{26}}{210} + \frac{a_{47}}{10}$	$M^e_{12,12} = \frac{Lm_{33}}{3}$
$M^e_{12,13} = M^e_{13,12} = \frac{Lm_{34}}{12}$	$M^e_{12,14} = M^e_{14,12} = -\frac{Lm_{35}}{12}$
$M^e_{12,15} = M^e_{15,12} = \frac{m_{37}}{2}$	$M^e_{12,16} = M^e_{16,12} = 0$
$M^e_{12,17} = M^e_{17,12} = 0$	$M^e_{12,18} = M^e_{18,12} = \frac{Lm_{37}}{12}$
$M^e_{13,13} = \frac{L^3 m_{22}}{105} + \frac{2Lm_{44}}{15}$	$M^e_{13,14} = M^e_{14,13} = -\frac{2Lm_{45}}{15}$
$M^e_{13,15} = M^e_{15,13} = \frac{11L^2 m_{26}}{210} - \frac{m_{47}}{30}$	$M^e_{13,16} = M^e_{16,13} = 0$
$M^e_{13,17} = M^e_{17,13} = 0$	$M^e_{13,18} = M^e_{18,13} = -\frac{L^3 m_{26}}{105} + \frac{2Lm_{47}}{15}$
$M^e_{14,14} = \frac{L^3 m_{11}}{105} + \frac{2Lm_{55}}{15}$	$M^e_{14,15} = M^e_{15,14} = -\frac{11L^2 m_{16}}{210} + \frac{m_{57}}{10}$
$M^e_{14,16} = M^e_{16,14} = 0$	$M^e_{14,17} = M^e_{17,14} = 0$

$M^e_{14,18} = M^e_{18,14} = -\frac{L^3 m_{16}}{105} - \frac{2Lm_{57}}{15}$	$M^e_{15,15} = \frac{13Lm_{66}}{35} + \frac{6m_{77}}{5L}$
$M^e_{15,16} = M^e_{16,15} = 0$	$M^e_{15,17} = M^e_{17,15} = 0$
$M^e_{15,18} = M^e_{18,15} = -\frac{11L^2 m_{66}}{210} - \frac{m_{77}}{10}$	$M^e_{16,16} = 0$
$M^e_{16,17} = M^e_{17,16} = 0$	$M^e_{16,18} = M^e_{18,16} = 0$
$M^e_{17,17} = 0$	$M^e_{17,18} = M^e_{18,17} = 0$
$M^e_{18,18} = \frac{L^3 m_{66}}{105} + \frac{2Lm_{77}}{15}$	

Load calculation

The solver is allowed to include structural, aerodynamic, and centrifugal loads. The input of the loads depends on their typology. The structural loads are included in the calculation as a vector of forces, moments, and bi-moments on the beam nodes. Concerning the aerodynamic loads, different models are allowed. Figure 3.38 shows the decision diagram in the load algorithm.

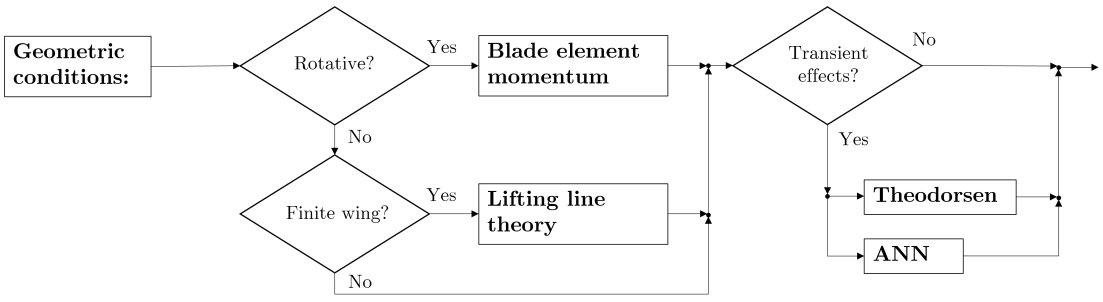

Fig. 3.38 **Algorithm for the calculation of the aerodynamic loads.** The decision algorithm chooses between blade or wing models and includes if required, transient effects.

Different aerodynamic models are allowed for the solver. The models can be classified depending on the physical problem.

- Infinite wing: the aerodynamic surface is considered infinite. Thus, the tip vortex effects are neglected. This model is useful for problems in which the surface is constrained into walls.
- Finite wing: the surface presents a free end. Therefore, a tip vortex is generated, and the induced velocity distribution must be considered. The solver is based on the Prandtl lifting line theory (LLT). The derivation of the model and its equations were presented

in Section 3.3.1. The algorithm for calculating the finite wing-induced velocity and the aerodynamic coefficients are presented in Figure 3.39. The calculation starts by defining a set of control nodes in the beam. These nodes are used for calculating the A_n terms of Equation (3.57). Then, the induced velocity is calculated from the A_n coefficients as previously presented in Equation (3.51). As the nonlinear LLT algorithm is calculated in the code, the workflow of Figure 3.39 presents similar steps compared with Figure 3.10.

- Rotating blade: the surface is rotating in a free stream. The rotation effects generate an induced velocity distribution calculated by the blade element momentum theory (BEM). This model was previously explained in Section 3.3.1. In addition, the tip losses are considered by a correction function. The centrifugal force acting on the blade is also added to the problem. Figure 3.40 presents the diagram showing the BEM algorithm. The control nodes are defined. The initial induced velocity is set for these points, and the aerodynamic coefficients are calculated. The blade element and the momentum theory thrust are calculated. If the results do not match, the normal-induced velocity is iterated, and the thrust is recalculated. The same procedure is used for the tangential-induced velocity and the power. Finally, the results are interpolated or extrapolated to the rest of the blade.

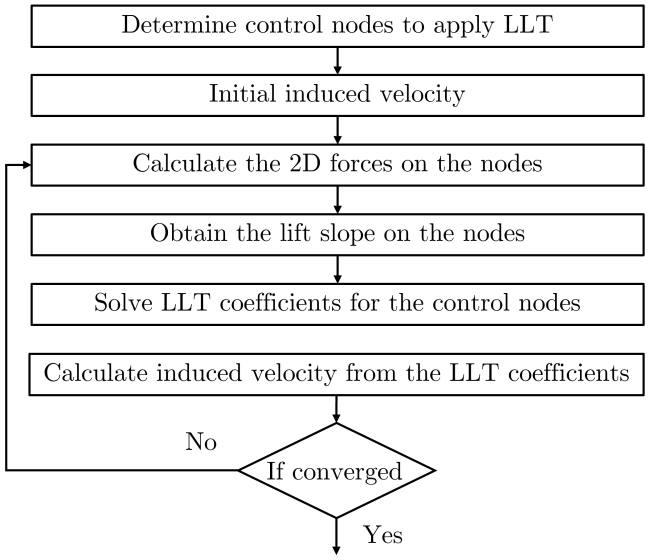

Fig. 3.39 **Algorithm for calculating the lifting line theory.** The induced velocity is iterated on the control points to calculate the aerodynamic coefficients.

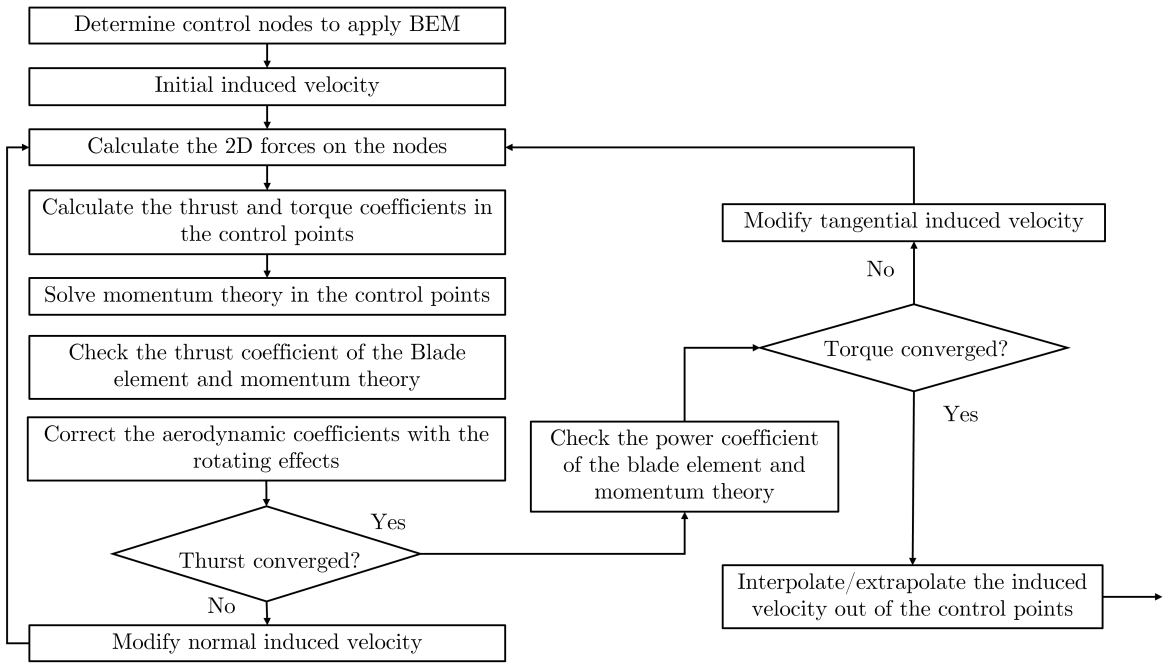

Fig. 3.40 **Algorithm for calculating the blade element momentum theory.** The normal and tangential-induced velocities are iterated on the control points to calculate the aerodynamic coefficients.

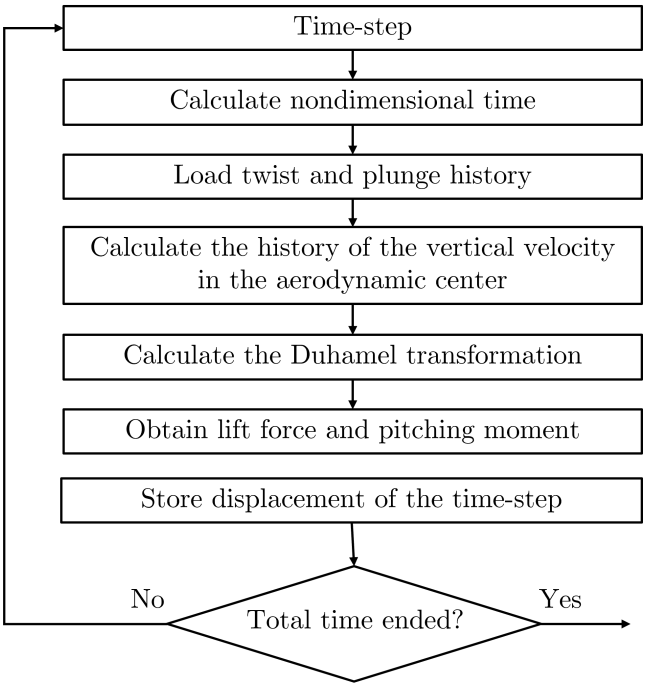

Fig. 3.41 **Algorithm of the Theodorsen transient aerodynamic forces.** Note that the code generates a temporal solution from the frequency-domain loads.

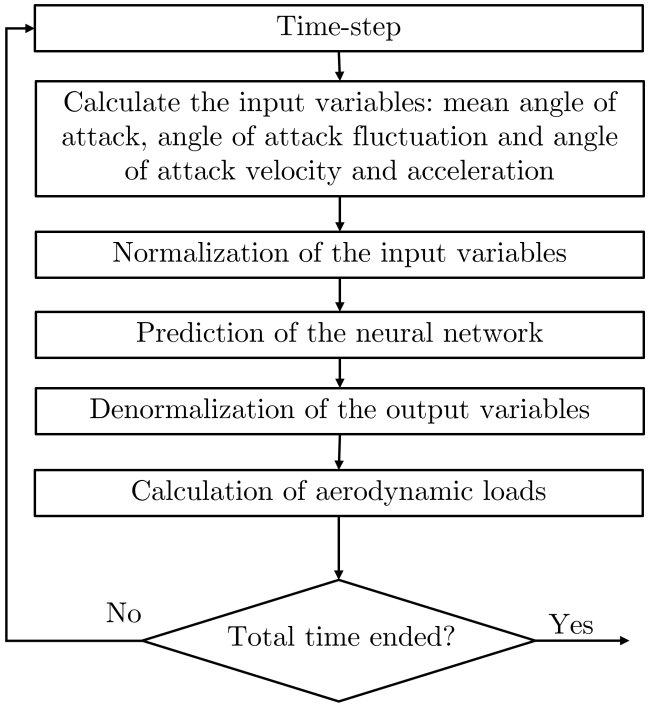

Fig. 3.42 **Algorithm of the surrogated model based on artificial neural networks for calculating transient aerodynamic forces.** This algorithm shows the steps to calculate the dynamic aerodynamic loads once the ANN is trained.

In addition, depending on the transient effects included in the problem, the models can be classified into the following classes:

- Steady or quasi-steady loads: the transient effects are neglected.
- Transient loads based on potential aerodynamics: the transient effects are included based on the effects of the potential wake generated by a moving airfoil. This model, based on Theodorsen coefficients, was presented in Section 3.3.1. Figure 3.41 shows the stages of the algorithm. The calculation starts calculating the nondimensional time of the time step and the historical evolution of the plunge, twist, and vertical velocity of the aerodynamic center. Then, the Duhamel transformation is obtained, Equation (3.72). Finally, the aerodynamic loads are calculated, and the resulting displacement is stored.
- Transient loads based on artificial neural networks: the transient loads acting on the airfoil are predicted using a pre-trained surrogate model. This model takes the variation on the angle of attack and its derivatives to calculate the dynamic effects of the aerodynamic loads, as previously presented in Section 3.3.2. The procedure is

presented in Figure 3.42. The code starts calculating the input variables of the network: mean angle of attack and its deviation, velocity, and acceleration. Then, the input variables are normalized between 0 and 1. The normalized aerodynamic coefficients are predicted using the ANN. Finally, the coefficients are denormalized, and the forces are calculated.

Finally, the three-dimensional physical problems previously described require using the cross-section (airfoil) aerodynamic coefficients. The calculation of these coefficients is allowed via two models:

- Theoretic lift slope: the aerodynamic coefficient is calculated as:

$$c_l = c_{l\alpha}\alpha, \qquad \text{being} \qquad c_{l\alpha} = 2\pi \tag{3.178}$$

  The lift slope of the airfoil, locating the lift force in the theoretical aerodynamic center, a quarter of the chord backward from the leading edge. This aerodynamic model cannot include the stall effects and aerodynamic nonlinearities. It is helpful for initial calculations when the airfoil data is unknown or in case of low incidence.

- Aerodynamic coefficients interpolated from a polar file. This model allows including the stall and nonlinear effects in the calculation. It requires an external calculation or experimental test to determine the value of the aerodynamic coefficients. The file containing these coefficients was previously explained in Table 3.4.

Solver: steady

The solution of the aeroelastic system is obtained for different problems. Some of them are stationary, while others are transient or modal. The steady problems do not require the integration of the solution in time. The dynamic system of the steady numerical problem is defined by the following:

$$\mathbf{K}^G\mathbf{q}^G = \mathbf{F}^G \tag{3.179}$$

A direct resolution of the system of equations obtains the solution. The system matrix is decomposed using LU. The stiffness matrix is factored using partial pivoting and row interchanges:

$$\mathbf{K}^G = \mathbf{K}_p^G\mathbf{L}_{LU}\mathbf{U}_{LU}, \tag{3.180}$$

where $\mathbf{K}_p^G$ is the permutation matrix, $\mathbf{L}_{LU}$ is the unit lower triangular and $\mathbf{U}_{LU}$ is the upper triangular matrix.

In the case of the steady aeroelastic solution, in addition to the previous solver, the results must be converged until the displacement stops oscillating. An initial displacement is calculated. Then the force is reevaluated, and the process continues until convergence, Figure 3.43.

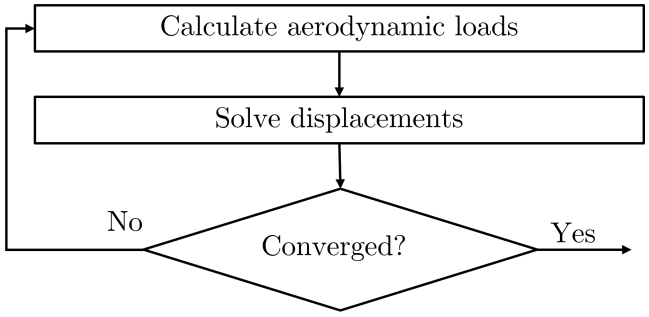

Fig. 3.43 **Algorithm of the steady aeroelastic solver.** The solution of the steady problem is iterated until convergence.

Solver: modal

The modal analysis is required for problems in which the frequency response is the interest solution. This analysis is based on the eigensystem solution. In order to obtain this solution, the dynamic equation is normalized to the mass to obtain the modal functions of the beam. For the most simple case, the natural vibration problem, the dynamic system is expressed as:

$$\mathbf{I}\ddot{\mathbf{y}} + \mathbf{M}^{-1/2}\mathbf{K}\mathbf{M}^{-1/2}\mathbf{y} = \mathbf{0}, \text{ where the vector } \mathbf{y} \text{ is defined as: } \mathbf{q} = \mathbf{M}^{-1/2}\mathbf{y} \tag{3.181}$$

Then, the vibration frequencies are obtained by calculating the eigenvalues of the problem (λ), whereas the modal shapes are obtained from the eigenvectors ($\mathbf{y}_{\text{eig}}$). Thus, Equation 3.181 may be written as:

$$\left(\mathbf{I}\lambda - \mathbf{M}^{-1/2}\mathbf{K}\mathbf{M}^{-1/2}\right)\mathbf{y}_{\text{eig}} = \mathbf{0} \tag{3.182}$$

The vibration frequency vector is calculated from the previous expression as:

$$\mathbf{f}_{\text{mod}} = \frac{\sqrt{\lambda}}{2\pi} \tag{3.183}$$

Note that the eigenvectors must be converted to the global coordinate system using the relations of Equation (3.181):

$$\mathbf{q}_{\text{eig}} = \mathbf{M}^{-1/2}\mathbf{y}_{\text{eig}} \tag{3.184}$$

A similar approach is used when the aeroelastic modal response is required. In this case, the aerodynamic forces are defined using the Theodorsen theory, Equations (3.67) and (3.68). Aerodynamic loads are expressed in a matrix system:

$$\mathbf{F} = \mathbf{A}_{\text{aero}}\mathbf{q} + \mathbf{B}_{\text{aero}}\dot{\mathbf{q}} + \mathbf{D}_{\text{aero}}\ddot{\mathbf{q}} \tag{3.185}$$

The forces are substituted in the dynamic global system, and Equation (2.12) is expressed as:

$$(\mathbf{M} - \mathbf{D}_{\text{aero}})\,\ddot{\mathbf{q}} - \mathbf{B}_{\text{aero}}\dot{\mathbf{q}} + (\mathbf{K} - \mathbf{A}_{\text{aero}})\,\mathbf{q} = \mathbf{0} \rightarrow \mathbf{M}_{\text{aero}}\ddot{\mathbf{q}} + \mathbf{C}_{\text{aero}}\dot{\mathbf{q}} + \mathbf{K}_{\text{aero}}\mathbf{q} = \mathbf{0} \tag{3.186}$$

As in the natural vibration problem, in this case, the equation must be normalized by the mass function:

$$\mathbf{I}\ddot{\mathbf{y}} + \mathbf{M}_{\text{aero}}^{-1/2}\mathbf{C}_{\text{aero}}\mathbf{M}_{\text{aero}}^{-1/2}\dot{\mathbf{y}} + \mathbf{M}_{\text{aero}}^{-1/2}\mathbf{K}_{\text{aero}}\mathbf{M}_{\text{aero}}^{-1/2}\mathbf{y} = \mathbf{0} \tag{3.187}$$

Finally, as the eigenvalue problem requires a first-order ODE system, the dynamic equations must be transformed:

$$\begin{bmatrix} \dot{\mathbf{y}} \\ \ddot{\mathbf{y}} \end{bmatrix} = \begin{bmatrix} \mathbf{0} & \mathbf{I} \\ -\mathbf{M}_{\text{aero}}^{-1/2}\mathbf{K}_{\text{aero}}\mathbf{M}_{\text{aero}}^{-1/2} & -\mathbf{M}_{\text{aero}}^{-1/2}\mathbf{C}_{\text{aero}}\mathbf{M}_{\text{aero}}^{-1/2} \end{bmatrix} \begin{bmatrix} \mathbf{y} \\ \dot{\mathbf{y}} \end{bmatrix} \rightarrow \dot{\mathbf{z}} = \mathbf{A}_{\text{sys}}\mathbf{z} \tag{3.188}$$

Therefore, the solution of the aeroelastic modal system is solved as in Equation (3.182). The solution is obtained as follows:

$$\left(\mathbf{I}\lambda - \mathbf{A}_{\text{sys}}\right)\mathbf{z}_{\text{eig}} = \mathbf{0}, \tag{3.189}$$

the results providing the vibration frequency and the system eigenvector. In order to calculate the modal shape functions, the eigenvector must be converted to the global coordinates:

$$\mathbf{f}_{\text{mod}} = \frac{\lambda}{2\pi}, \qquad \begin{bmatrix} \mathbf{q}_{\text{eig}} \\ \dot{\mathbf{q}}_{\text{eig}} \end{bmatrix} = \mathbf{M}_{\text{aero}}^{-1/2}\mathbf{z}_{\text{eig}} \tag{3.190}$$

Solver: transient

The solution to the transient problem requires the integration of the solution in time. For this reason, a mathematical scheme is required. In this problem, the solution is integrated using an adaptive 4^{th} order Runge-Kutta algorithm. The second-order ordinary derivative equation is reduced to the first-order. The procedure followed is similar to that used for the modal solution. First of all, the equation is expressed in modal coordinates:

$$\mathbf{q}_{\text{eig}}^T\mathbf{M}\mathbf{q}_{\text{eig}}\ddot{\mathbf{y}} + \mathbf{q}_{\text{eig}}^T\mathbf{K}\mathbf{q}_{\text{eig}}\mathbf{y} = \mathbf{q}_{\text{eig}}\mathbf{F} \rightarrow \mathbf{M}_{\text{eig}}\ddot{\mathbf{y}} + \mathbf{K}_{\text{eig}}\mathbf{y} = \mathbf{F}_{\text{eig}}, \text{ where } \mathbf{q} = \mathbf{q}_{\text{eig}}\mathbf{y}, \tag{3.191}$$

and the equation is transformed into a first-order ODE:

$$\begin{bmatrix} \dot{\mathbf{y}} \\ \ddot{\mathbf{y}} \end{bmatrix} = \begin{bmatrix} \mathbf{0} & \mathbf{I} \\ -\mathbf{M}^{-1}\mathbf{K} & 0 \end{bmatrix} \begin{bmatrix} \mathbf{y} \\ \dot{\mathbf{y}} \end{bmatrix} + \begin{bmatrix} \mathbf{0} \\ \mathbf{M}^{-1}\mathbf{F} \end{bmatrix} \rightarrow \dot{\mathbf{z}} = \mathbf{A}_{\text{sys}}\mathbf{z} + \mathbf{F}_{\text{sys}} \tag{3.192}$$

Vector $\mathbf{z}$ is integrated over time. The current value of the displacement is denoted by subscript t while the next step, Δt, is $t+1$. The displacements in the next time-step are obtained following Equations (3.193) and (3.194).

$$\begin{aligned} \mathbf{f}_1 &= \mathbf{A}_{\text{sys}}\mathbf{z}_t + \mathbf{F}_{\text{sys}} & \mathbf{f}_2 &= \mathbf{A}_{\text{sys}}\left(\mathbf{z}_t + \tfrac{1}{2}\mathbf{f}_1\Delta t\right) + \mathbf{F}_{\text{sys}} \\ \mathbf{f}_3 &= \mathbf{A}_{\text{sys}}\left(\mathbf{z}_t + \tfrac{1}{2}\mathbf{f}_2\Delta t\right) + \mathbf{F}_{\text{sys}} & \mathbf{f}_4 &= \mathbf{A}_{\text{sys}}\left(\mathbf{z}_t + \mathbf{f}_3\Delta t\right) + \mathbf{F}_{\text{sys}} \end{aligned} \tag{3.193}$$

$$\mathbf{z}_{t+1} = \mathbf{x}_t + \frac{1}{6}\left(\mathbf{f}_1 + 2\mathbf{f}_2 + 2\mathbf{f}_3 + \mathbf{f}_4\right)\Delta t \tag{3.194}$$

The value of Δt is iterated for each time step to ensure the convergence of the problem, as explicit solvers may diverge if its value exceeds the stability limit. These iterations reduce the value of the time step if the final results of the displacements are modified when taking half its value. In the internal iterations, the aerodynamic forces are calculated only for the initial instant and updated through the Taylor series, Equation (3.195).

$$\begin{aligned} d_{i,0} = f_i;\ d_{i,1} = \frac{f_i - f_{i-1}}{\Delta t};\ d_{i,2} = \frac{d_{i,1} - d_{i-1,1}}{\Delta t} \\ d_{i,3} = \frac{d_{i,2} - d_{i-1,2}}{\Delta t};\ d_{i,4} = \frac{d_{i,3} - d_{i-1,3}}{\Delta t};\ f_{i+1} = \sum_{j=0}^{4} \frac{d_{i,j}\left(\Delta t\right)^j}{j!} \end{aligned} \tag{3.195}$$

The system results are calculated in the modal domain $\mathbf{y}$. Therefore, the displacements must be returned to the original coordinates, Equation (3.191). Note that the original system

of equations was presented in the previous equations. However, to reduce the computational cost, the eigenvectors matrix could be truncated to reduce the number of modes considered for the problem, reducing the cost and speeding up the calculation without relevant accuracy penalties. Figure 3.44 presents the transient solver procedure diagram.

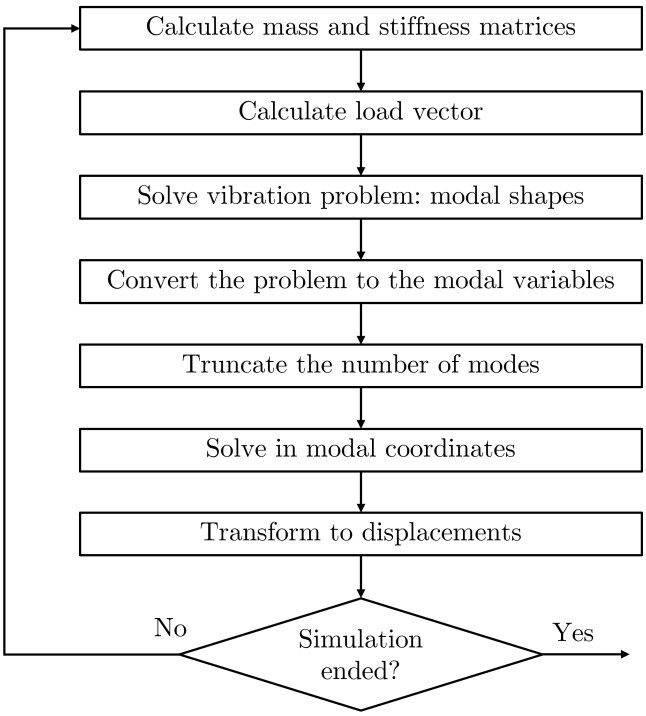

Fig. 3.44 **Algorithm of the transient solver.** The system is calculated in modal coordinates and then transformed to displacements.

References

[1] Barna Szabó and Ivo Babuška. Finite element analysis: Method, verification and validation. 2021.

[2] Shyama Kumari and PK Sinha. Finite element analysis of composite wing t-joints. *Journal of reinforced plastics and composites*, 21(17):1561–1585, 2002.

[3] Antonia B Kesel, Ute Philippi, and Werner Nachtigall. Biomechanical aspects of the insect wing: an analysis using the finite element method. *Computers in biology and medicine*, 28(4):423–437, 1998.

[4] Yuwei Li, Kwang-Jun Paik, Tao Xing, and Pablo M Carrica. Dynamic overset cfd simulations of wind turbine aerodynamics. *Renewable Energy*, 37(1):285–298, 2012.

[5] Rafael Palacios, H Climent, A Karlsson, and B Winzell. Assessment of strategies for correcting linear unsteady aerodynamics using cfd or experimental results. 2001.

[6] JG Marshall and M Imregun. A review of aeroelasticity methods with emphasis on turbomachinery applications. *Journal of fluids and structures*, 10(3):237–267, 1996.

[7] Cécile Münch, Philippe Ausoni, Olivier Braun, Mohamed Farhat, and Francois Avellan. Fluid–structure coupling for an oscillating hydrofoil. *Journal of Fluids and Structures*, 26(6):1018–1033, 2010.

[8] Volker Carstens, Ralf Kemme, and Stefan Schmitt. Coupled simulation of flow-structure interaction in turbomachinery. *Aerospace Science and Technology*, 7(4):298–306, 2003.

[9] S Moffatt and L He. On decoupled and fully-coupled methods for blade forced response prediction. *Journal of fluids and structures*, 20(2):217–234, 2005.

[10] Hamid R. Kaviani and Amir Nejat. Investigating the aeroelasticity effects on aeroacoustics and aerodynamics of a MW-class HAWT. *Journal of Wind Engineering & Industrial Aerodynamics*, 213:104617, 2021.

[11] Liping Dai, Qiang Zhou, Yuwen Zhang, Shigang Yao, Shun Kang, and Xiaodong Wang. Analysis of wind turbine blades aeroelastic performance under yaw conditions. *Journal of Wind Engineering & Industrial Aerodynamics*, 171:273–287, 2017.

[12] Toshiyuki Nakata and Hao Liu. A fluid–structure interaction model of insect flight with flexible wings. *Journal of Computational Physics*, 231(4):1822–1847, 2012.

[13] Roland Feil, Tobias Pflumm, Pietro Bortolotti, and Marco Morandini. A cross-sectional aeroelastic analysis and structural optimization tool for slender composite strictures. *Composite structures*, 253: 112755, 2020.

[14] AT Sarawit, Y Kim, MCM Bakker, and Teoman Peköz. The finite element method for thin-walled members-applications. *Thin-walled structures*, 41(2-3):191–206, 2003.

[15] Diego Cárdenas, Alejandro A Escárpita, Hugo Elizalde, Juan José Aguirre, Horacio Ahuett, Piergiovanni Marzocca, and Oliver Probst. Numerical validation of a finite element thin-walled beam model of a composite wind turbine blade. *Wind Energy*, 15(2):203–223, 2012.

[16] E. Carrera, M. Filippi, and E. Zappino. Free vibration analysis of rotating composite blades via carrera unified formulation. *Composite structures*, 106:317–325, 2013.

[17] Touraj Farsadi, Davood Asadi, and Hasan Kurtaran. Flutter improvement of a thin walled wing engine system by applying curvilinear fiber path. *Aerospace Science and Technology*, 93:105353, 2019.

[18] L. Librescu and S. Thangjitham. Analytical studies on static aeroelastic behavior of forward-swept composite wing structures. *Journal of Aircraft*, 28:151–157, 1991.

[19] C.A. Baxevanou, P.K. Chaviaropoulos, S.G. Voutsinas, and N.S. Vlachos. Evaluation study of a Navier-Stokes cfd aeroelastic model of wind turbine airfoils in classical flutter. *Journal of Wind Engineering & Industrial Aerodynamics*, 96:1425–1443, 2008.

[20] A. Gil, A. Tiseira, P. Quintero, and A. Cremades. Prediction of the non-linear aeroelastic behavior of a cantilever flat plate and equivalent 2d model. *Aerospace Science and Technology*, 113:106685, 2021.

[21] Earl H Dowell, RH Scanlan, F Sisto, HC Curtiss Jr, and H Saunders. A modern course in aeroelasticity. 1981.

[22] J. Kim, P. Moin, and R. Moser. Turbulence statistics in fully developed channels flows at low Reynolds numbers. *Journal of Fluid Mechanics*, 177:133–166, 1987.

[23] F. Alcántara-Ávila, S. Hoyas, and M. Pérez-Quiles. DNS of thermal channel flow up to $Re_\tau = 2000$ for medium to low Prandtl numbers. *Int. J. Heat Mass Transf.*, 127:349–361, 2018.

[24] Sergio Hoyas, Martin Oberlack, Francisco Alcántara-Ávila, Stefanie V. Kraheberger, and Jonathan Laux. Wall turbulence at high friction Reynolds numbers. *Physical Review Fluids*, 7:014602, Jan 2022. doi: 10.1103/PhysRevFluids.7.014602.

[25] Praveen Kumar and Krishnan Mahesh. Large eddy simulation of propeller wake instabilities. *Journal of Fluid Mechanics*, 814:361–396, 2017.

[26] Jacob Keller, Praveen Kumar, and Krishnan Mahesh. Examination of propeller sound production using large eddy simulation. *Physical Review Fluids*, 3(6):064601, 2018.

[27] Silvio Tschisgale, Bastian Löhrer, Richard Meller, and Jochen Fröhlich. Large eddy simulation of the fluid–structure interaction in an abstracted aquatic canopy consisting of flexible blades. *Journal of Fluid Mechanics*, 916:A43, 2021.

[28] Lixiang Zhang, Yakun Guo, and Wenquan Wang. Large eddy simulation of turbulent flow in a true 3d francis hydro turbine passage with dynamical fluid–structure interaction. *International Journal for Numerical Methods in Fluids*, 54(5):517–541, 2007.

[29] William C Lasher and James R Sonnenmeier. An analysis of practical rans simulations for spinnaker aerodynamics. *Journal of Wind Engineering and Industrial Aerodynamics*, 96(2):143–165, 2008.

[30] Md Naimul Haque, Hiroshi Katsuchi, Hitoshi Yamada, and Mayuko Nishio. Investigation of edge fairing shaping effects on aerodynamic response of long-span bridge deck by unsteady rans. *Archives of Civil and Mechanical Engineering*, 16:888–900, 2016.

[31] Cui Peng and Han Jinglong. Prediction of flutter characteristics for a transport wing with wingtip device. *Aerospace Science and Technology*, 23:461–468, 2012.

[32] Jeffrey W Banks, William D Henshaw, and Björn Sjögreen. A stable fsi algorithm for light rigid bodies in compressible flow. *Journal of Computational Physics*, 245:399–430, 2013.

[33] Warren F Phillips and Nicholas R Alley. Predicting maximum lift coefficient for twisted wings using lifting-line theory. *Journal of aircraft*, 44(3):898–910, 2007.

[34] Minu Jeon, Seungmin Lee, and Soogab Lee. Unsteady aerodynamics of offshore floating wind turbines in platform pitching motion using vortex lattice method. *Renewable Energy*, 65:207–212, 2014.

[35] Joseba Murua, Rafael Palacios, J. Michael, and R. Graham. Applications of the unsteady vortex-lattice method in aircraft aeroelasticity and flight dynamics. *Progress in Aeroespace Sciences*, 55:46–72, 2012.

[36] Robert E Spall, Warren F Phillips, and Brian B Pincock. Numerical analysis of multiple, thin-sail geometries based on prandtl's lifting-line theory. *Computers & Fluids*, 82:29–37, 2013.

[37] Faisal Mahmuddin. Rotor blade performance analysis with blade element momentum theory. *Energy Procedia*, 105:1123–1129, 2017.

[38] Manelisi Kagame Rwigema. Propeller blade element momentum theory with vortex wake deflection. In *27th International congress of the aeronautical sciences*, volume 1, pages 727–735, 2010.

[39] Lin Wang, Xiongwei Liu, Nathalie Renevier, Matthew Stables, and George M Hall. Nonlinear aeroelastic modelling for wind turbine blades based on blade element momentum theory and geometrically exact beam theory. *Energy*, 76:487–501, 2014.

[40] James Tangler and David Kocurek. Wind turbine post-stall airfoil performance characteristics guidelines for blade-element momentum methods. In *43rd AIAA Aerospace Sciences Meeting and Exhibit*, page 591, 2005.

[41] T. Theodorsen. General theory of aerodynamic instability and the mechanism of flutter. *NACA*, 496, 1935.

[42] David G Crighton. The kutta condition in unsteady flow. *Annual Review of Fluid Mechanics*, 17(1): 411–445, 1985.

[43] Frank Bowman. *Introduction to Bessel functions*. Courier Corporation, 2012.

[44] Werner J Rauchenstein Jr. A 3d theodorsen-based rotor blade flutter model using normal modes. Technical report, NAVAL POSTGRADUATE SCHOOL MONTEREY CA, 2002.

[45] H Kobayashi and H Nagaoka. Active control of flutter of a suspension bridge. *Journal of Wind Engineering and Industrial Aerodynamics*, 41(1-3):143–151, 1992.

[46] Dan Borglund and Jakob Kuttenkeuler. Active wing flutter suppression using a trailing edge flap. *Journal of Fluids and Structures*, 16(3):271–294, 2002.

[47] JG Leishman and TS Beddoes. A generalized method for unsteady airfoil behaviour and dynamic stall using the indicial method 42nd annual forum of the ahs. 1986.

[48] Sandeep Gupta and J Gordon Leishman. Dynamic stall modelling of the s809 aerofoil and comparison with experiments. *Wind Energy: An International Journal for Progress and Applications in Wind Power Conversion Technology*, 9(6):521–547, 2006.

[49] Morten Hartvig Hansen, Mac Gaunaa, and Helge Aagaard Madsen. *A Beddoes-Leishman type dynamic stall model in state-space and indicial formulations*. 2004.

[50] Dongfeng Li, Andrea Da Ronch, Gang chen, and Yueming Li. Aeroelastic global structural optimization using an efficient cfd-based reduced order model. *Aerospace Science and Technology*, 94:105354, 2019.

[51] Jiaqi Luo. Design optimization of the last stage of a 4.5-stage compressor using a pod-based hybrid model. *Aerospace Science and Technology*, 76:303–314, 2018.

[52] Gang Chen, Dongfeng Li, Qiang Zhou, Andrea Da Ronch, and Yueming Li. Efficient aeroelastic reduced order model with global structural modifications. *Aerospace Science and Technology*, 76:1–13, 2018.

[53] Ricardo Vinuesa and Steven L Brunton. Enhancing computational fluid dynamics with machine learning. *Nature Computational Science*, 2(6):358–366, 2022.

[54] J. Peng, C.T. Luo, Z.J. Han, Z.M. Hu, G.L. Han, and Z.L. Jiang. Parameter-correlation study on shock-shock interaction using a machine learning method. *Aerospace Science and Technology*, 107:106247, 2020.

[55] Teng Wu and Ahsan Kareem. Modeling hysteretic nonlinear behavior of bridge aerodynamics via cellular automata nested neural network. *Journal of Wind Engineering & Industrial Aerodynamics*, 99:378–388, 2011.

[56] Chern-Hwa Chen, Jong-Cheng Wu, and Jow-Hua Chen. Prediction of flutter derivatives by artificial neural networks. *Journal of Wind Engineering & Industrial Aerodynamics*, 96:1926–1937, 2008.

[57] Tajammal Abbas, Igor Kavrakov, Guido Morgenthal, and Tom Lahmer. Prediction of aeroelastic response of bridge decks using artificial neural networks. *Computers and Structures*, 231:106198, 2020.

[58] Tao Li, Teng Wu, and Zhao Liu. Nonlinear unsteady bridge aerodynamics: Reduced-order modeling based on deep lstm networks. *Journal of Wind Engineering & Industrial Aerodynamics*, 198:104116, 2020.

[59] Javier Jiménez. Coherent structures in wall-bounded turbulence. *Journal of Fluid Mechanics*, 842:P1, 2018.

[60] Adrián Lozano-Durán, Oscar Flores, and Javier Jiménez. The three-dimensional structure of momentum transfer in turbulent channels. *Journal of Fluid Mechanics*, 694:100–130, 2012.

[61] David C Wilcox et al. *Turbulence modeling for CFD*, volume 2. DCW industries La Canada, CA, 1998.

[62] Florian R Menter. Two-equation eddy-viscosity turbulence models for engineering applications. *AIAA journal*, 32(8):1598–1605, 1994.

[63] Venkat Venkatakrishnan. On the accuracy of limiters and convergence to steady state solutions. In *31st Aerospace Sciences Meeting*, page 880, 1993.

[64] P Chow, Mark Cross, and K Pericleous. A natural extension of the conventional finite volume method into polygonal unstructured meshes for cfd application. *Applied Mathematical Modelling*, 20(2):170–183, 1996.

[65] Emre Sozer, Christoph Brehm, and Cetin C Kiris. Gradient calculation methods on arbitrary polyhedral unstructured meshes for cell-centered cfd solvers. In *52nd Aerospace Sciences Meeting*, page 1440, 2014.

[66] P.J. Roache. *Verification and Validation in Computational Science and Engineering*. Hermosa Publishers, 1998.

[67] M Ahamed, Sharmin Atique, M Munshi, and Tuomas Koiranen. A concise description of one way and two way coupling methods for fluid-structure interaction problems. *Imperial Journal of Interdisciplinary Research*, 3(3), 2017.

[68] Jr. John D. Anderson. *Fundamentals of Aerodynamics*. McGraw-Hill, 1991.

[69] Gordon J Leishman. *Principles of helicopter aerodynamics with CD extra*. Cambridge university press, 2006.

[70] James F Manwell, Jon G McGowan, and Anthony L Rogers. *Wind energy explained: theory, design and application*. John Wiley & Sons, 2010.

[71] Jerson Rogério Pinheiro Vaz, João Tavares Pinho, and André Luiz Amarante Mesquita. An extension of bem method applied to horizontal-axis wind turbine design. *Renewable Energy*, 36(6):1734–1740, 2011.

[72] P.K. Chaviaropoulos and M. O. L. Hansen. Investigating three-dimensional and rotational effects on wind turbine blades by means of a quasi3d navier-stokes solver. *Journal of Fluids Engineering*, 122:130–136, 2000.

[73] Ben Kröse and Patrick van der Smagt. *An introduction to Neural Networks*. University of Amsterdam, 1996.

[74] Viet-Ha Nhu, Nhat-Duc Hoang, Hieu Nguyen, Phuong Thao Thi Ngo, Tinh Thanh Bui, Pham Viet Hoa, Pijush Samui, and Dieu Tien Bui. Effectiveness assessment of keras based deep learning with different robust optimization algorithms for shallow landslide susceptibility mapping at tropical area. *Catena*, 188: 104458, 2020.

[75] S. Hochreiter and J. Schmidhuber. Long short-term memory. *Neural Computation*, 9:1735–1780, 1997.

[76] Jichao Hong, Zhenpo Wang, Wen Chen, Le-Yi Wang, and Changhui Qu. Online joint-prediction of multi-forward-step battery soc using lstm neural networks and multiple linear regression for real-world electric vehicles. *Journal of Energy Storage*, 30:1001459, 2020.

[77] Liviu Librescu and Ohseop Song. *Thin-Walled Composite Beams. Theory and Application*. Springer, 2006.

[78] Robert D. Blevins. *Formulas for natural frequency and mode shape*. Van Nostrand Reinhold Company, 1979.

Chapter 4

Results

4.1 Introduction to the results

The previous chapter presented the different methodologies for calculating the aeroelastic problems. This chapter focuses on showing the results of the reduced-order models previously introduced.

The chapter is divided into two main sections. The first focuses on the dimensional reduction of the structure into a mass-spring system. In this section, a clamped beam with a squared cross-section is analyzed. The equivalent structure aeroelastic behavior is initially calculated by simulating the aerodynamics with a CFD solver. The deformation of the structure is included in the calculation using a rigid body motion [1]. The solutions of the dimensional reduction are compared to the complete three-dimensional simulation, ensuring their validity. Then, a surrogated model based on artificial neural networks is introduced. This model presents a lower computational cost and allows fast calculations without losing accuracy compared with the CFD simulations [2]. The objective of this section is the validation of the equivalent section models, showing their capabilities for calculating three-dimensional structures. The solution is applied for an isotropic material beam with a simple structure, so the model does not limit the calculation of the mechanical characteristics.

The second section centers on using a beam element solver for general orthotropic materials. This solver allows considering the effects of the fiber orientations and the higher-order vibration modes. Therefore, it has been used for calculating orthotropic material beams and structures where the higher-order modes are critical for the problem. The section is structured as follows. Firstly, the aerodynamic and structural models are validated. Then the application cases are presented. The first application problem is a flat foam plate reinforced with a carbon fiber ply [3]. The solution is compared with the three-dimensional FSI simulation of the problem. Then, the ROM is used in order to evaluate the optimal orientation

of the fibers. The second case of application is the use of the ROM to calculate the aeroelastic coupling of a wind turbine blade. Two structures, one isotropic and the other with oblique fibers, are studied [4]. The third case uses the ROM for calculating the aeroelastic response of a membrane wing.

4.2 Dimensional reduction of a clamped squared-section beam to a mass-spring system

The initial simulations are performed on a simple structural problem, a squared cross-section beam. The mechanical properties of the section are well-known. In addition, the sharp edges of the beam generate nonlinear aerodynamic effects, which require complex models or CFD calculations for a correct analysis.

This geometry is a simplification of common interest problems. For instance, the flat plate cross-section geometry is a simplification of the aerodynamics of many engineering problems: solar panel arrays [5], bridge decks [6], and low Reynolds number flapping wings [7]. Moreover, although an aircraft flights most of its operational life in cruise conditions, the wing may present nonlinear effects when exigent maneuvers are required. Therefore, the flat plate cross-section beam is a valuable benchmark for reproducing complex aerodynamic effects presented in various engineering applications.

4.2.1 Problem description

The simulations of this section are performed on a cantilevered flexible flat plate immersed in a wind tunnel. The beam is fixed on one of its ends and free at the other. The fluid domain dimensions were selected in order to represent the CMT-*Motores Térmicos* (at Universitat Politècnica de València) low Reynolds 400x400mm wind tunnel.

Figure 4.1 presents the principal dimensions defining the domain. This figure provides a schematic representation of the three-dimensional and equivalent bi-dimensional problem. The main dimensions are the chord of the plate ($c =$ 100mm), its length ($L = 3.7\ c$) and its thickness ($h = 0.04\ c$). The plate has an aspect ratio $AR = 2L/c = 7.4$. The wind channel cross-section is a square of side $H = 4\ c$. In addition, the channel has a length of $L_u = 5\ c$ upstream and $L_d = 15\ c$ downstream. Both distances are taken so that the boundary conditions do not affect the computed fluid flow ([8]). Finally, the plate is located at the center of the cross-section of the tunnel with an incidence of $\theta_0 = 2.5$ deg.

Note that if the walls of the tunnel are supposed to be far enough, their boundary layer does not affect the aerodynamics of the plate. A similar distance to the used in Torregrosa et al.

[9] was chosen. In their work, the authors proposed using a slipping boundary condition on the walls. This assumption allows us to reduce the computational cost without jeopardizing the accuracy of the results. A similar strategy is followed in the current work. Although the closeness of the horizontal walls to the beam could produce blockage effects, the three-dimensional and bi-dimensional domains represent the same geometry. Therefore, these effects are similar in both cases.

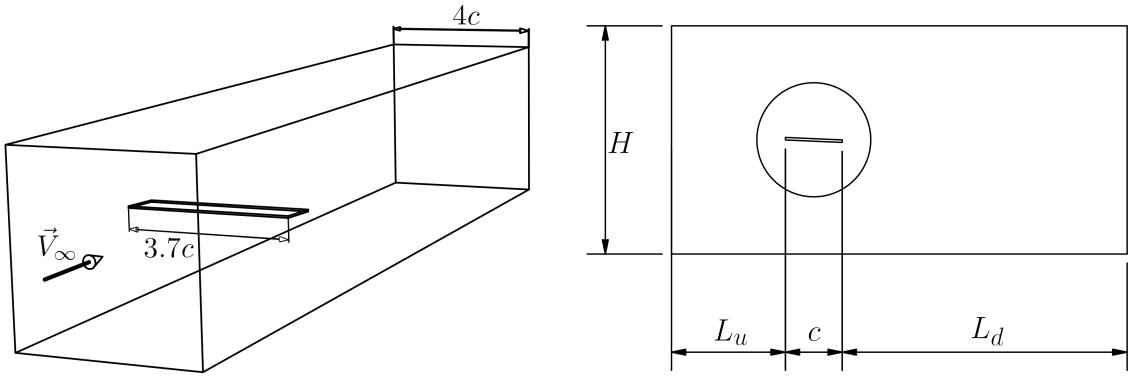

Fig. 4.1 **Sketch of the flat plate structure and computational domain.** (Left) 3D plate simulation and (right) 2D simplification of the problem. The domain is not scaled.

In this problem, the free stream is perpendicular to the inlet section, with a constant velocity of $V_\infty = 20\ \mathrm{m\,s^{-1}}$, which is maintained for all the simulations, being the torsional stiffness of the parameter that is modified. The fluid is air with inlet conditions of density $\rho_\infty = 1.18\ \mathrm{kg\ m^{-3}}$, viscosity $\mu_\infty = 1.86 \cdot 10^{-5}$ Pa s and sound speed $a_\infty = 340\ \mathrm{m\ s^{-1}}$. For the structure, the material is polymethyl methacrylate, whose mechanical properties are given by its Young Modulus, $E = 3300$ MPa; a Poisson coefficient of $\nu = 0.35$ and a density of $\rho_s = 1180\ \mathrm{kgm^{-3}}$. With these parameters, the flow conditions are given by a Reynolds number of $\mathrm{Re} = \rho_\infty V_\infty c/\mu_\infty \approx 1.5 \cdot 10^5$ and a Mach number of $\mathrm{Ma} = V_\infty/a_\infty \approx 0.06$. Thus, the flow can be assumed to be incompressible.

It is essential to point out that the previous values reference the problem. As it will later show, the stiffness parameter which governs the problem is proportional to $E/(\rho_\infty V_\infty^2)$. Therefore, to analyze the influence of this parameter while maintaining the value of Re and Ma, Young's modulus will be varied during the different simulations. The characteristic parameters of the problem are thus:

$$k^* = \frac{k_\theta}{\frac{1}{2}\rho_\infty v_\infty^2 c^2} \qquad k_w^* = \frac{k_f}{\frac{1}{2}\rho_\infty v_\infty^2 c} \tag{4.1}$$

$$I^* = \frac{I_{2\mathrm{D}}}{\frac{1}{2}\rho_\infty c^4} \qquad m^* = \frac{m_{2\mathrm{D}}}{\frac{1}{2}\rho_\infty c^2} \tag{4.2}$$

4.2.2 Bi-dimensional simulated aerodynamics

As a first approach to the problem, the equivalent mass-spring model of Section 3.3.3 is applied to the structure presented in Figure 4.1. Then the methodology of Figure 4.2 is applied to the problem. This methodology allows us to reduce the computational cost of the complete three-dimensional FSI simulation using standard CFD software.

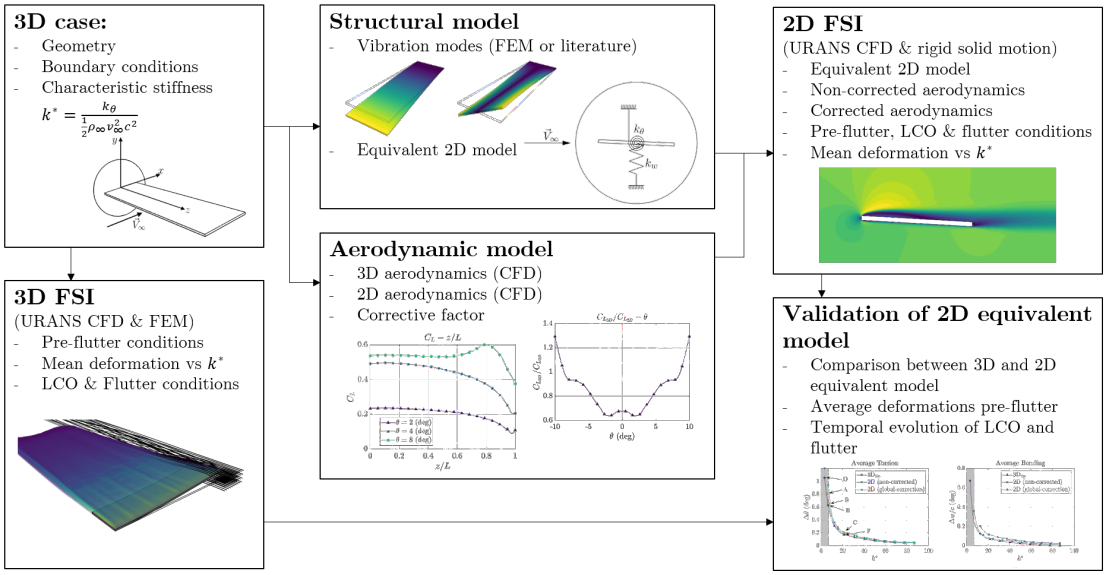

Fig. 4.2 **Block diagram of the procedure followed during the research.** The figure shows the methodology for calculating the equivalent section, validated against the 3D simulation.

The stages of Figure 4.2 are followed along the section. First of all, the three-dimensional structure is defined. From this structure, on the first hand, the complete FSI simulation is calculated. On the other hand, the mass-stiffness structure is calculated by using the information on the vibration modes. In addition, to improve the accuracy of the bi-dimensional model, the aerodynamic coefficients of the complete 3D simulation and the 2D calculation are compared. This reduced order model is used for calculating a bi-dimensional FSI simulation which will be validated against the three-dimensional FSI calculation.

Numerical resolution of the three-dimensional FSI problem

The three-dimensional simulation is calculated using a CFD solver based on the finite volume method for solving the URANS equations [10], using commercial software Simcenter STAR-CCM+®. This methodology previously presented in Section 3.2.1 is used for solving the aerodynamics around the structure. In order to calculate flow separation under adverse pressure gradients ([11], [12]) $k-\omega$ with shear stress transport (SST) turbulence model [13]

is chosen. The solid is calculated using the finite element method derived in Section 3.2.2. An overset region is set in the fluid around its structure to simulate the motion of the solid. The overset methodology [14] ensures the overall quality of the mesh is maintained, even under large displacements [15–19]. The structure is modeled as a linear elastic body and deformed due to the aerodynamic pressure. The overset interface can be freely deformed following the plate motion, and the rest of the cells of the region are interpolated using radial basis functions (RBF) from the solid boundary displacement [20].

A polyhedral mesh is used to discretize the simulation domain. The advection term is computed using a coupled solver with second order upwind ROE FDS scheme [21, 22]. The gradients are calculated with a hybrid Gauss-Least Squares Method with Venkatakrishnan limiter [23]. For transient simulations, second-order time discretization is assumed.

The cell size is chosen based on a mesh independence analysis. In this sense, it was chosen to perform a spatial grid independence study based on calculating the stationary fluid field around the 3D plate. The error of the coefficients for the different meshes is shown in Table 4.1. Observe how the discrepancies between the different simulations are minimal, ensuring grid independence of the fluid solution. The force and moment coefficients around the center of the clamped plate section are calculated under Equation 4.3:

$$c_D = \frac{F_D}{\frac{1}{2}\rho_\infty V_\infty^2 S_w} \qquad c_L = \frac{F_L}{\frac{1}{2}\rho_\infty V_\infty^2 S_w} \qquad c_M = \frac{M}{\frac{1}{2}\rho_\infty V_\infty^2 S_w c} \tag{4.3}$$

Here, $S_w = L\,c$ is the reference surface of the plate and F_D, F_L, and M the aerodynamic drag, lift, and moment, respectively, exerted over the plate.

Table 4.1 **Mesh independence analysis of the three-dimensional beam.** Comparison of the 3D force coefficients at different values of the angle of attack for three different discretizations. Errors measured with respect to the mesh with $N = 15 \cdot 10^6$ elements.

	Mesh $N = 4.7 \cdot 10^6$			Mesh $N = 7.0 \cdot 10^6$			Mesh $N = 15 \cdot 10^6$		
α(deg)	c_d (%)	c_l (%)	c_m (%)	c_d (%)	c_l (%)	c_m (%)	c_d (%)	c_l (%)	c_m (%)
0.0	7.99	0.00	0.00	2.74	0.0000	0.0000	-	-	-
2.5	2.59	2.26	2.82	2.40	2.26	2.82	-	-	-
5.0	1.63	2.47	15.35	1.05	0.73	2.01	-	-	-
10	1.04	0.76	4.25	0.98	0.72	2.73	-	-	-

The cell size at the walls of the plate was set to $\frac{\Delta x_{wall}}{c} \approx 0.010$. This size grows to a value of $\frac{\Delta x_{overset}}{c} \approx 0.020$ at the overset. The cell size at the wake was set to $\frac{\Delta x_{wake}}{c} \approx 0.040$, and the maximum value at the furthest surfaces was $\frac{\Delta x_{domain}}{c} \approx 0.400$. The mesh comprises

$N \approx 5 \cdot 10^6$ elements with this configuration. Figure 4.3 provides a representation of the final mesh.

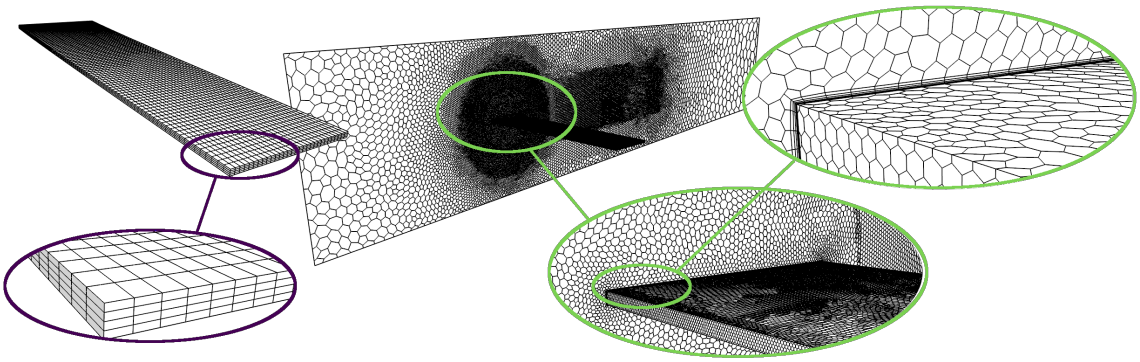

Fig. 4.3 **Flat plate beam mesh of the 3D simulation.** Solid mesh (left) and fluid mesh (right) of the 3D simulation. Detail on the plate and the boundary layer

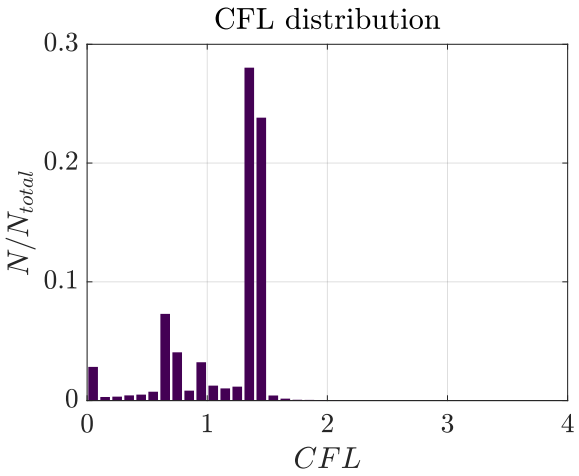

Fig. 4.4 **CFL distribution of the three-dimensional case.** The figure evidences a low CFL for all the domain.

For the time discretization a temporal step of $\Delta t \cdot c/V_\infty = 5.00 \cdot 10^{-7}$ s is used. The time step is to ensure not to critically affect the solution. Additionally, the time step follows the criteria for the Courant-Lewis-Federich (CFL) number $\left(\text{CFL} = \frac{\Delta t V}{\Delta x}\right)$ (Figure 4.4) which is lower than 1 for a 92% of the volume.

Concerning the structure, although the vibration modes of a clamped flat plate can be obtained theoretically [24], the Finite Element Method is used to generalize the procedures to any possible geometry and boundary conditions. The fluid is eliminated from the analysis, and the plate is discretized with elements of uniform size $\frac{\Delta x_{plate}}{c} \approx 0.035$ at the surface and a total

of 4 elements through the thickness. With these values, the eigenfrequencies and eigenvectors of the plate are calculated. When the location value of the first 8 eigenfrequencies is not substantially modified, the discretization is assumed to be independent of the element size. Note that if the resonance frequency, f_i, was expressed in terms of the Strouhal number, $\mathrm{St_i} = \frac{f_i c}{V_\infty}$, the i^{th} Strouhal resonance frequency could always be expressed as a function of the nondimensional stiffness (k^*) and mass ($I^* = \frac{I_{2D}}{\frac{1}{2}\rho_\infty c^4}$), following Equation 4.4:

$$\mathrm{St}_i = C_i \frac{L}{h} \sqrt{\frac{k^*}{I^*}} \tag{4.4}$$

If the constant C_i is known, the vacuum resonance frequency can be calculated at any working condition. Table 4.2 shows the value of each of these constants for different solid mesh discretizations. It can be observed how the result of the eigenfrequency is not noticeably affected by the number of elements chosen in each case. Consequently, the spatial resolution of the structure for $N = 8.5 \cdot 10^3$ elements can be considered accurate enough from this point of view.

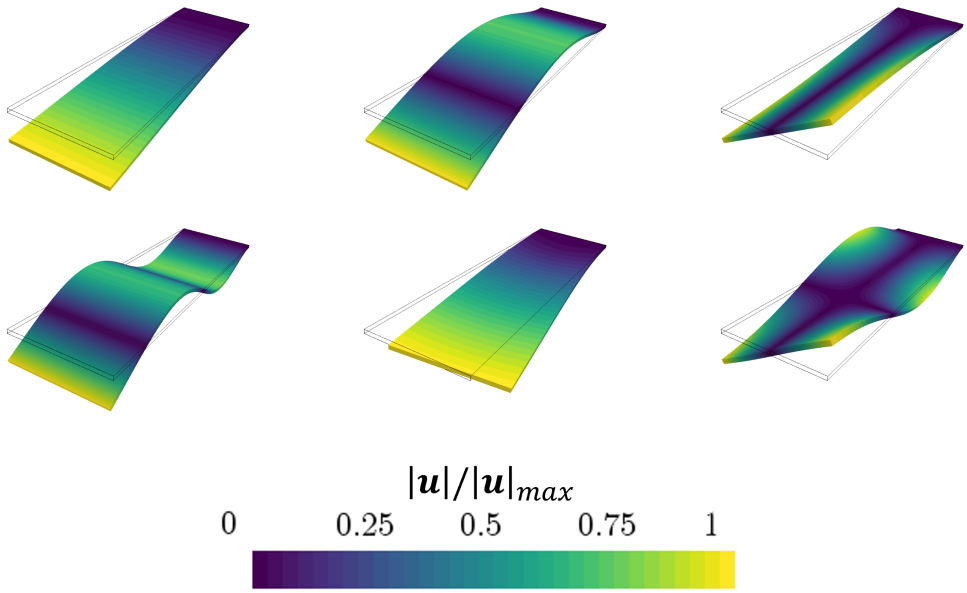

Fig. 4.5 **Modal forms of the flat plate structure.** Representation of the first six eigenmodes. (Top-left) 1^{st} mode, vertical bending; (top-center) 2^{nd} mode, vertical bending; (right-center) 3^{rd} mode, twisting; (bottom-left) 4^{th} mode, vertical bending; (bottom-center) 5^{th} mode, horizontal bending and (bottom-right) 6^{th} mode, twisting.

Additionally, Figure 4.5 shows the modal form corresponding with each one of these eigenfrequencies. It can be observed how 1^{st}, 2^{nd} and 4^{th} modes correspond to the bending modes, while 3^{rd} and 6^{th} represent the first and second torsion modes, respectively. Finally,

the 5^{th} represents a horizontal bending mode which is not expected to be observed at any usual working condition. Although the equivalent section is only including the first bending and first torsion modes, the complete three-dimensional simulation includes all the modes, which are also used for the modal contribution analysis.

Table 4.2 **Mesh independence of the structure of the flat plate.** Comparison of the vacuum resonance frequency for two different discretizations.

N	C_1	C_2	C_3	C_4	C_5	C_6
$8.5 \cdot 10^3$	$2.33 \cdot 10^{-4}$	$1.45 \cdot 10^{-3}$	$1.69 \cdot 10^{-3}$	$4.08 \cdot 10^{-3}$	$5.24 \cdot 10^{-3}$	$5.41 \cdot 10^{-3}$
$5.0 \cdot 10^4$	$2.31 \cdot 10^{-4}$	$1.44 \cdot 10^{-3}$	$1.68 \cdot 10^{-3}$	$4.06 \cdot 10^{-3}$	$5.22 \cdot 10^{-3}$	$5.40 \cdot 10^{-3}$

Numerical resolution of the bi-dimensional FSI problem

As was previously explained, a three-dimensional flat plate can be calculated as a 2D equivalent section whose structural motion is governed by a torsional and a linear spring with stiffness k_θ and k_w, respectively, inertia, I_{2D}, and mass, m_{2D}. Figure 4.6 illustrates this transformation. The left image represents the original three-dimensional model, while the right shows its 2D simplification.

Equations 3.106 and 3.107 have been solved using the finite volume method and the unsteady Reynolds averaged Navier–Stokes (URANS) equations for the fluid, and the rigid solid motion for the plate. The configuration of the solvers is similar to the three-dimensional simulation.

In order to check the spatial discretization, a grid independence study was performed using different cell resolutions. The mesh independence analysis is based on Richardson's extrapolation (RE) [25]. In this study, the aerodynamic forces and moments are studied as a function of the steady angle of attack, as shown in Figure 4.8 where lift (left) and moment (right) coefficients are measured at the center of the plate, are shown as a function of the angle of attack for different levels of grid resolution. In addition, the error of the discretizations with respect to the finest mesh is presented for different angles of attack in Table 4.3. A fair agreement between all meshes for these parameters can be observed, even at angles near to stall. Similar trends are observed at the drag coefficient, but it is not shown as this parameter should not be dominant on the plate motion. The 2D aerodynamic coefficients are defined from the 2D drag, F_D, lift, F_L, and moment, M, measured at the center of the section, as stated by Equation (4.5):

$$c_d = \frac{F_D}{\frac{1}{2}\rho_\infty V_\infty^2 c} \qquad c_l = \frac{F_L}{\frac{1}{2}\rho_\infty V_\infty^2 c} \qquad c_m = \frac{M}{\frac{1}{2}\rho_\infty V_\infty^2 c^2} \tag{4.5}$$

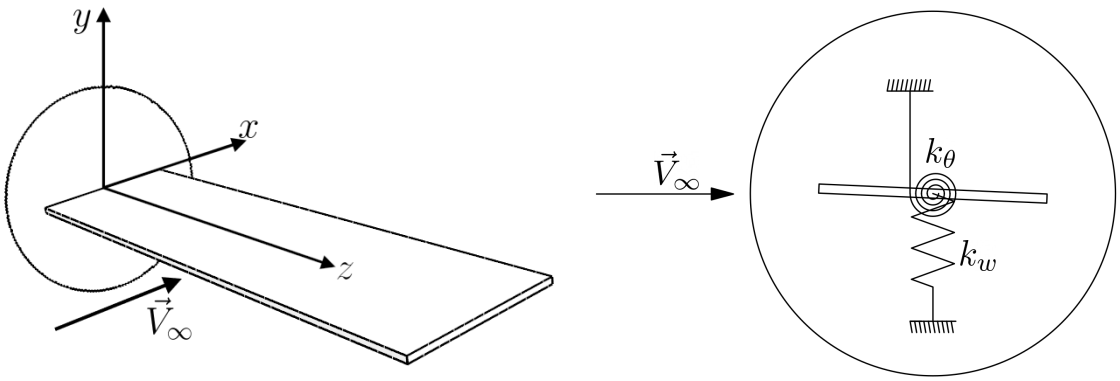

Fig. 4.6 **Tranformation of the dimensional reduction.** Scheme of the three-dimensional lifting flat plate (left) and its equivalent two-dimensional model (right).

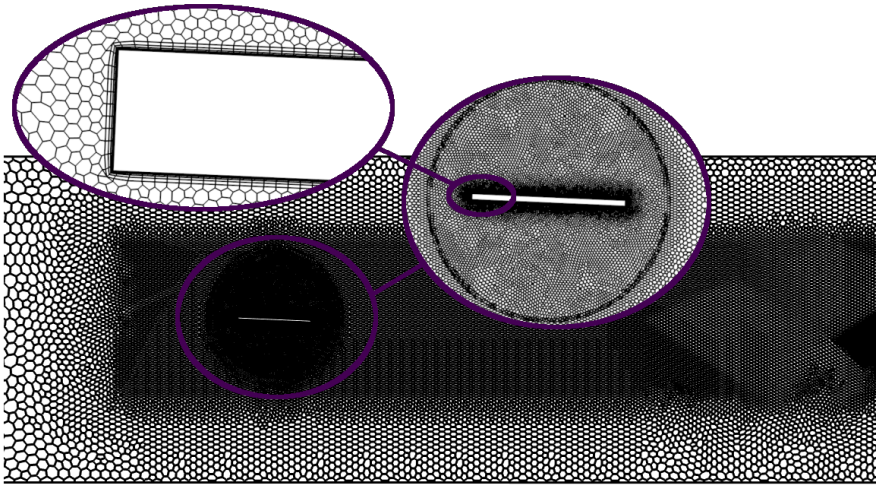

Fig. 4.7 **Mesh of the bi-dimensional simulation.** The figure shows the different zones of refinement.

The previous figures are in agreement with the geometrical features of the case. As the boundary layer tends to become highly turbulent at the edge of the plate, the prediction of a laminar-turbulent transition is not essential. Furthermore, the fluid flow is entirely detached at the suction side, even for very low values of the angle of attack, as can be observed in Figure 4.9, where the contours of velocity are sketched over the plate for different values of

the angle of attack. The previous fact reinforces the almost independence from the Reynolds number, as stated by Pfahl and Uhlemann [26].

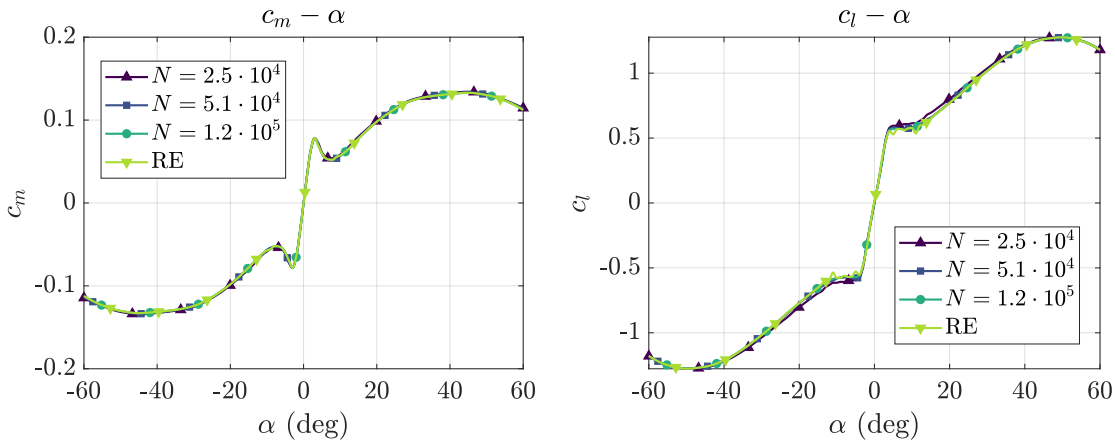

Fig. 4.8 **Computation of aerodynamic lift and moment coefficient for different meshes.** Comparison with RE. N is the number of elements of the mesh.

Table 4.3 **Mesh independence analysis of the two-dimensional beam.** Comparison of the errors of the 2D force coefficients at different values of the angle of attack for three different discretizations. Errors measured with respect to the mesh with $N = 1.2 \cdot 10^5$ elements.

	Mesh $N = 2.5 \cdot 10^4$			Mesh $N = 5.1 \cdot 10^4$			Mesh $N = 1.2 \cdot 10^5$		
α(deg)	c_d (%)	c_l (%)	c_m (%)	c_d (%)	c_l (%)	c_m (%)	c_d (%)	c_l (%)	c_m (%)
0.0	1.58	0.00	0.00	0.44	0.0000	0.0000	-	-	-
2	0.71	0.11	0.45	0.29	0.94	0.71	-	-	-
5.0	2.67	2.42	4.24	1.15	0.04	1.88	-	-	-
10	4.41	6.17	2.12	0.46	0.59	1.27	-	-	-

In order to properly apply the turbulence model, a minimum resolution of the boundary layer is required. In order to do this, it is necessary to ensure that the wall y^+ is kept in the viscous sublayer $(y^+ < 5)$ for the significant part of the wall. The left image of Figure 4.10 shows the evolution of the wall-distance parameter at the suction and pressure side for different angles of attack values. Note how $y^+ < 1$ for the whole plate. Moreover, this parameter allows us to recognize how, even for the low angle of $\theta = 1$ deg, the recirculation bubble appears at the suction side, extending for almost 50 % of the length. For $\theta = 5$ deg, the recirculation is found for the whole length. These trends are confirmed by Figure 4.10 (right), where the distribution of the pressure coefficient ($c_p = \frac{p - p_\infty}{\frac{1}{2}\rho_\infty V_\infty^2}$) is presented for different

values of the angle of attack. Note how the effects of the recirculation bubble can be inferred from observing the almost flat values of the curves at the suction side of the plate.

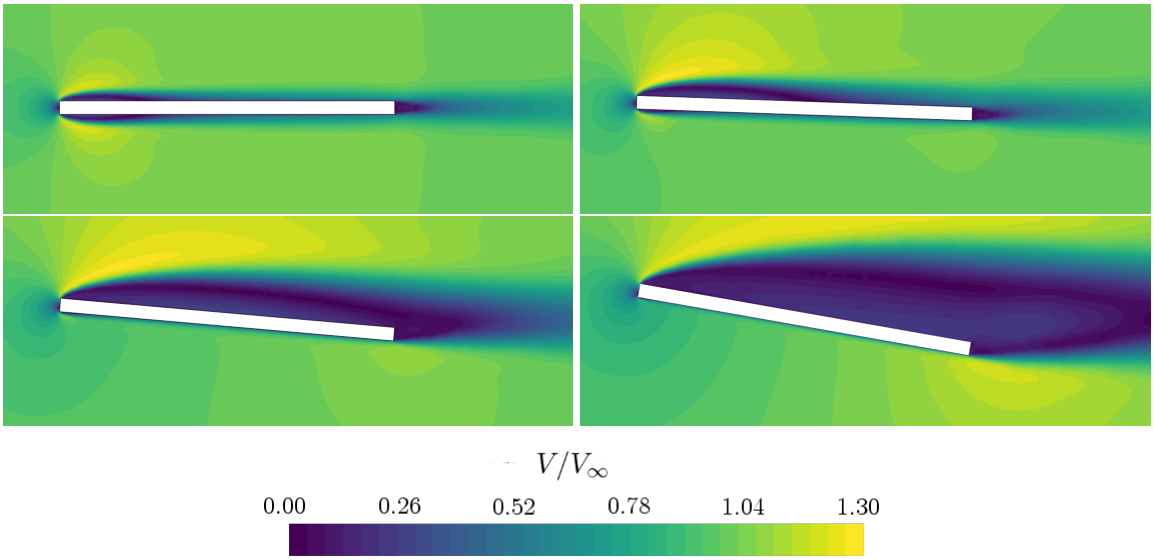

Fig. 4.9 **Velocity contour of the 2D flat plate for different angles of attack.** Results corresponding to the mesh of $N = 5.1 \cdot 10^4$ elements and an incidence of 0 deg (left-top), 2 deg (right-top), 5 deg (left-bottom) and 10 deg (right-bottom).

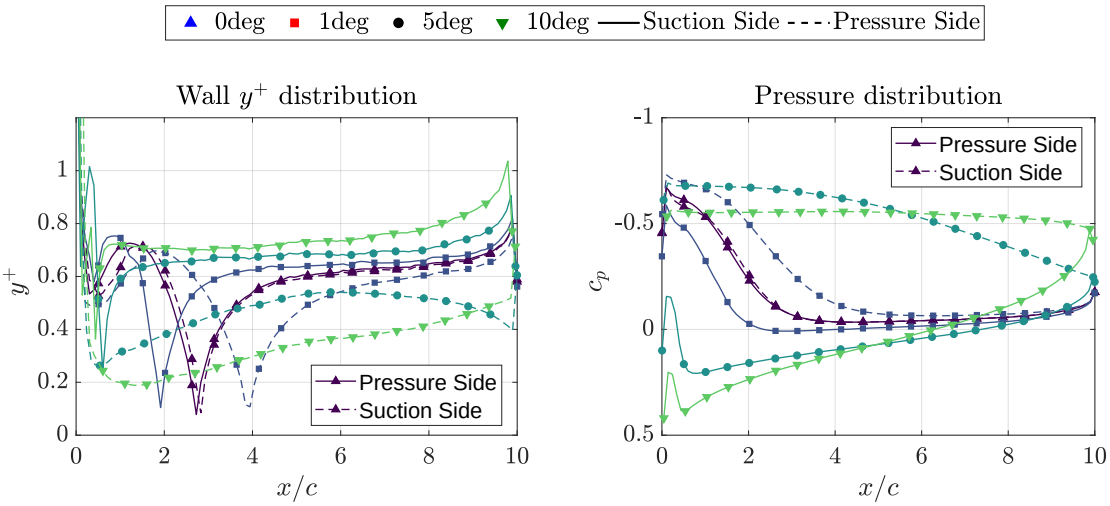

Fig. 4.10 **Wall distance and pressure on the bi-dimensional cross-section.** Distribution of wall y^+ (left) and pressure coefficient, c_p (right) over the plate at different angles of the angle of attack.

In order to correctly model unsteady effects, the CFL number should be maintained as low as possible for most of the computational domain. For the current mesh with $N = 3.5 \cdot 10^4$ a

time step of $\Delta t \cdot c/V_\infty = 1.25 \cdot 10^{-6}$ was chosen. Figure 4.11 shows the distribution of CFL at an arbitrary instant, for a rigid angle of attack of $\theta_0 = 2.5$ deg at conditions of $\frac{k_\theta}{\frac{1}{2}\rho_\infty V_\infty^2 c^2} = 6.44$ and Re $\approx 10^5$. For the mentioned conditions, most cells present a CFL lower than 2, and 90% of the volume has a CFL lower than 1.5.

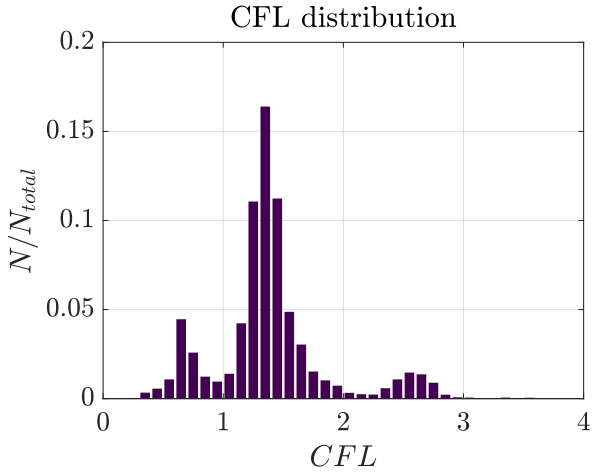

Fig. 4.11 .**CFL distribution of the bi-dimensional case.** The CFL number is kept in low values for all the domain.

For each value of stiffness or velocity, the case is first initialized with a steady-rigid flow field. This steady field is used as the initial condition for the unsteady flexible simulations, which are iterated until steady or statistically steady conditions are reached. The initialization from this rigid solid state excites the structure producing the instability in case the conditions are unstable and the stabilization for the stable conditions.

Aerodynamic correction of the three-dimensional effect

The aerodynamic coefficients of the structure are affected by three-dimensional effects such as the vortex generated in the wing tip. A critical drawback of the reduction of dimensions is that, for three-dimensional geometry, the aerodynamic loads are expected to vary as a function of the position in the span direction. These steady effects affect the aerodynamics even for the low angle of attack values due to the wing-tip vortex. Distribution of loads is generated span-wise, producing a difference between the three-dimensional aerodynamic coefficients and the bi-dimensional values. Moreover, the center of pressure is moved, and the aerodynamic moment is modified. To visualize these effects, in Figure 4.12, the evolution of the force coefficients of the 3D plate with the depth coordinate is presented for two low and one moderate angle of attack. Note how integration about the z axis would allow us to obtain the global aerodynamic coefficient of the plate. The left image of Figure 4.12

shows the distribution of the lift coefficient. Observe how near the clamping ($z/L = 0$), the lift coefficient can be considered to be approximately constant and decreases near the tip ($z/L \approx 1$). For moderate-high incidence, θ, the three-dimensional effects of the plate and the influence of the channel's walls produce an increase in lift close to the tip. Similar effects can be observed for the pitching moment, shown in the right image of Figure 4.12.

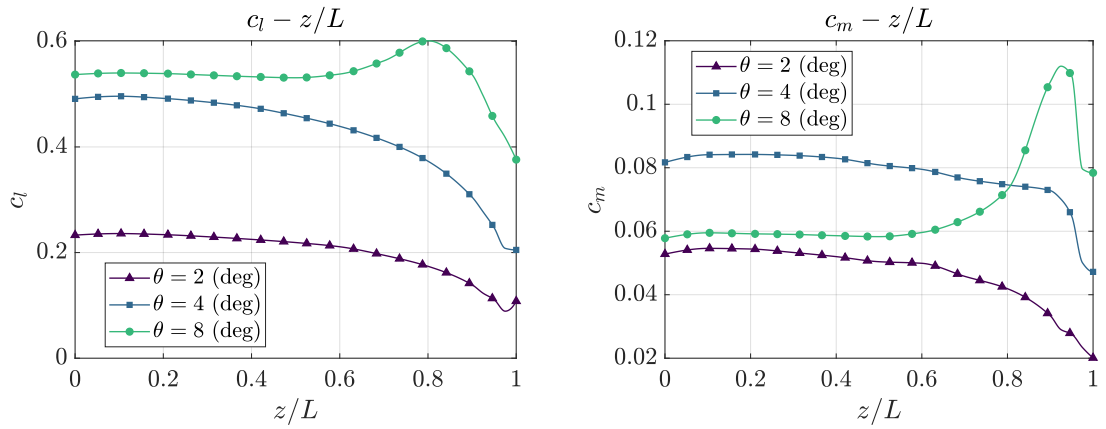

Fig. 4.12 **Distribution of aerodynamic loads along the span of the structures.** Distribution of lift force (left) and pitching (right) moment along the span measured at the center of the chord for a steady simulation.

Three-dimensional effects can also be illustrated using Figure 4.13, which shows the streamlines of the wall shear stress over the plate, colored by the pressure coefficient value, for different incidence angles. These lines indicate the direction of the air over the plate and can be easily used for identifying different flow patterns. Note the existence of a recirculation bubble beginning at the leading edge of the suction side, even for very low incidence. For the case of $\theta = 2\,\text{deg}$, this bubble is shorter at the tip, and its size tends to increase when reaching the $z/L = 0$ position, where it occupies approximately the 25% of the chord. The recirculation bubble grows when increasing the angle of attack (for instance, at $\theta = 4\,\text{deg}$, it occupies almost 80 % of the chord) until its length corresponds to the whole chord for high angles of attack.

Figure 4.14 might also be helpful for visualization of these effects. Here, streamlines passing near the tip of the plate are shown in the perfectly rigid configuration (left) and at an arbitrary time step of the statistically stationary fully coupled solution, corresponding to a nondimensional stiffness parameter of $k^* = 6.44$. As expected, similar fluid patterns can be inferred from the streamlines of both figures. Additionally, turbulence kinetic energy, k, is visualized and non-dimensionalized with the free stream velocity. Streamlines show the vortex produced at the tip of the plate. A high turbulence kinetic energy zone starts after the sharp edge of the plate and continues downwards. The turbulent kinetic energy is higher

in the areas with high vorticity: the recirculation bubble of the suction side near the shear layer. Then, the kinetic energy is diffused downwards, and its value is decreased until it is dissipated. In addition, these high turbulent kinetic energy regions are related to the presence of stall cells along the wingspan.

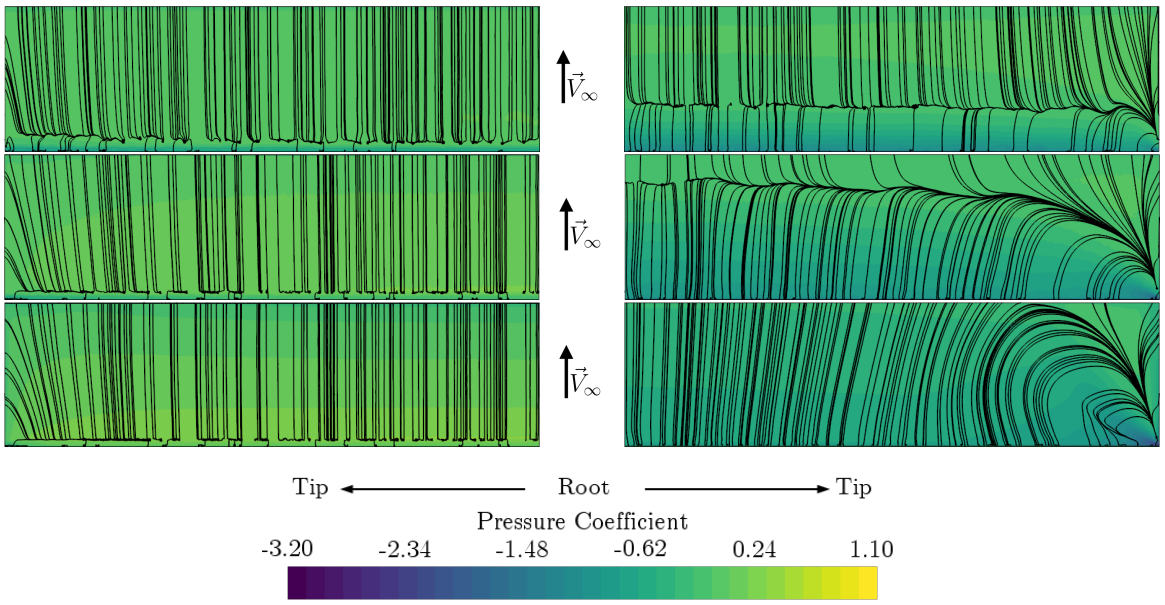

Fig. 4.13 **Pressure coefficient and shear structures on the beam.** Representation of the pressure side (left) and suction side (right) for different values of angle of attack 2 deg (top), 4 deg (middle) and 8 deg bottom for the steady simulation.

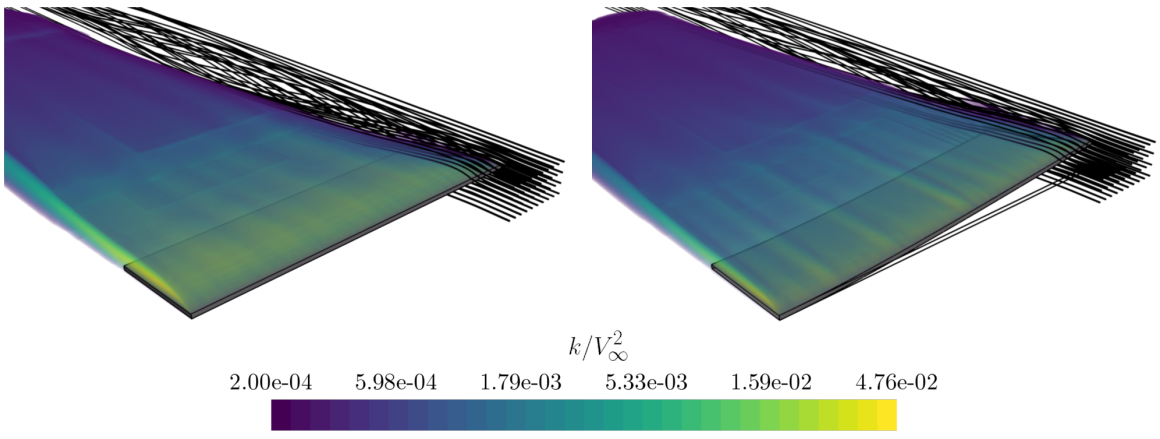

Fig. 4.14 **Three-dimensional effects on the beam aerodynamics.** Flow pattern of a flat plate with $\theta_0 = 2.5$ deg. The figure shows the solution for a rigid plate of $k^* \to \infty$ (left) and for an arbitrary time step corresponding with the simulations of a flexible plate of $k^* = 6.44$ (right)

The previous results evidence the importance of the three-dimensional aerodynamic effects. A correction is proposed to include this three-dimensional behavior. This correction is based on the ratio between 3D and 2D coefficients.

The steady CFD analysis is performed both for the 2D and 3D problems. Then, a corrective factor multiplies the section aerodynamic coefficients. However, the inspection of Equation 4.6, which shows the equation governing the torsion of the corrected 2D system, leads to the conclusion that multiplying the aerodynamic coefficients by the corrective factor is entirely analogous to dividing both the 2D masses and stiffness by the same factor.

$$I_{2D_{corr}}\ddot{\theta}_{2D} + k_{\theta_{corr}}\theta_{2D} = \frac{1}{2}\rho_\infty V_\infty^2 c^2 \left(c_{m_0} + \sum_{n=0}^{\infty} \frac{c_{m_w^{(n)}} V_\infty^n}{c^{n-1}} {w_{2D}}^{(n)} + \sum_{n=0}^{\infty} \frac{c_{m_w^{(n)}} V_\infty^n}{c^n} {\theta_{2D}}^{(n)} \right) \tag{4.6}$$

In this equation, $I_{2D_{corr}}$, $k_{\theta_{corr}}$ are the corrected inertia and stiffness respectively. A similar analysis can be applied to the flexural degree of freedom to obtain the corrected mass and inertia as a function of the angle of attack.

$$I_{2D_{corr}} = \frac{c_m(\theta)}{c_M(\theta)} I_{2D} \qquad m_{2D_{corr}} = \frac{c_l(\theta)}{c_L(\theta)} m_{2D} \qquad k_{\theta_{corr}} = \frac{c_m(\theta)}{c_M(\theta)} k_\theta \qquad k_{w_{corr}} = \frac{c_l(\theta)}{c_L(\theta)} k_w \tag{4.7}$$

Here, c_l and c_m are the 2D lift and pitching moment coefficients of the equivalent section, and c_L and c_M are the lift and moment coefficients of the 3D plate.

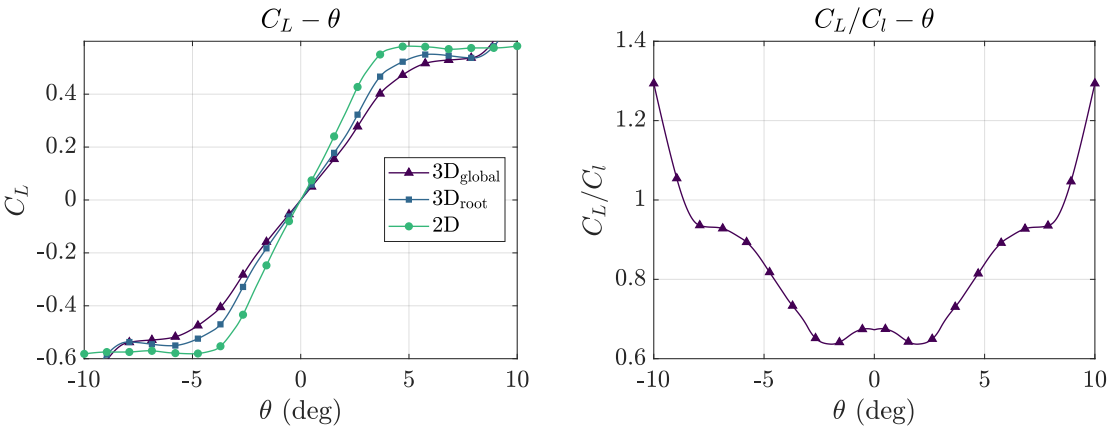

Fig. 4.15 **Lift coefficient comparison for the flat plate.** Lift coefficient for the 2D section and tip section of the 3D plate (left) and scaling coefficient for the lift force (right).

Figure 4.15 illustrates the variation of the lift coefficient. Values of the coefficient calculated at the root ($z/L = 0; 3\text{D}_{\text{root}}$) and the tip ($z/L = 0.98; 3\text{D}_{\text{tip}}$) sections are provided.

The global lift coefficient ($3D_{global}$) is also shown. Note how, as expected, the aerodynamic force coefficient near the root is similar to the two-dimensional calculation, although slightly minored. However, the value near the tip differs greatly from the 2D case. The correction uses the global value of the 3D simulation to correct 2D results. Similar effects are observed for the pitching moment, shown in Figure 4.16.

In Figures 4.15 and 4.16, it is possible to appreciate how for low θ, the lift and moment in the 2D problem are higher than in the 3D simulation. For moderate to high values of the angle of attack, the two-dimensional plate stalls while the value of c_M continues increasing. Therefore, the correction applied to the 2D problem must decrease the value of the coefficients in the first zone, and after a stall angle of attack, the coefficient must be amplified.

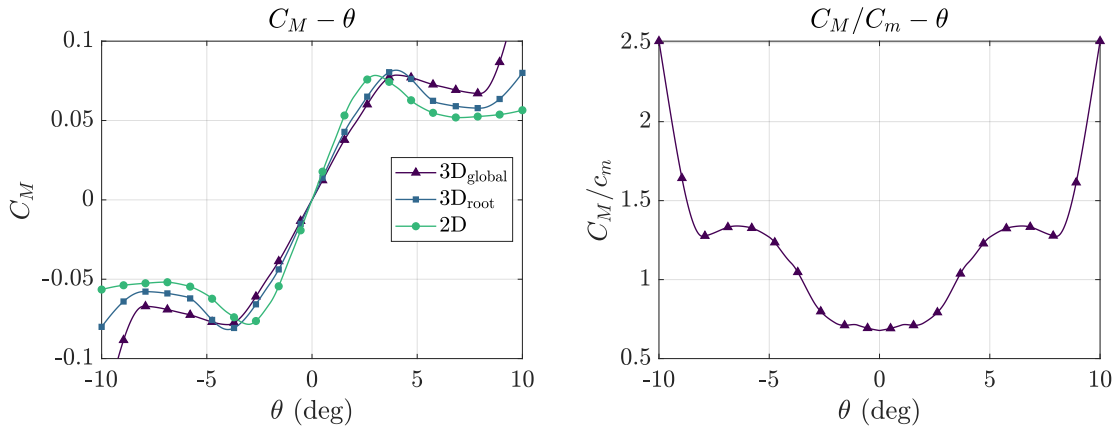

Fig. 4.16 **Moment coefficient comparison for the flat plate.** moment coefficient for the 2D section and tip section of the 3D plate (left) and scaling coefficient for the pitch moment (right).

Structural deformation of the system

In order to derive the mass-spring system theory, the displacement of the structure must be dominated by the first modes of torsion and bending. The shape of the deformed structure is compared with the modal deformation shapes, similarly as performed at [9], to examine the accuracy of neglecting the high-order modes. Figure 4.17 shows the modal contribution for bending (left) and torsion (right) for the four first modes. From this figure, it can be inferred that the first mode is dominant in bending and torsion, with a modal factor contribution of at least two orders of magnitude greater than the participation of higher-order modes. Slight differences are observed between the first mode and the actual deformed shape. Consequently, for practical purposes, and given the substantial simplification in terms of computational cost, the hypothesis of neglecting high-order modes can be considered accurate enough.

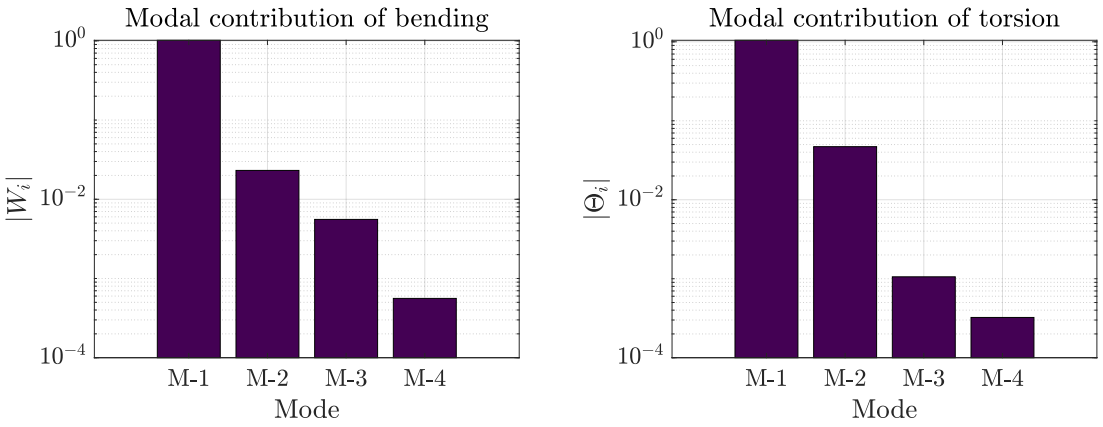

Fig. 4.17 **Modal contribution in the deformation shapes.** Bending modes (left) and the torsion modes (right) for a reference plate with $k^* = 21$

The structural equivalence between the 2D and the 3D models can be applied to the problem as the contribution of the high-order modes has been analyzed, resulting from being negligible. Next, the capabilities of both models will be analyzed. Figure 4.18 show the time average torsion and bending, respectively, predicted by the 3D and 2D (with aerodynamic corrections) models when a statistically stationary state is reached. Some points of this curve are highlighted, as their time history will be discussed later. The operation points in which the slope of the curves becomes significantly high are marked inside the gray zone. This zone, then, indicates the limits of the aeroelastic instabilities. Note the high capability of the 2D model for predicting similar results compared with the 3D simulation for the average torsion, even when not considering any three-dimensional effect corrections for the 2D aerodynamic evaluation (red lines). However, this non-corrected model tends to overestimate the value of the average bending, which is in accordance with the already mentioned overestimation of the force coefficient of the 2D model.

The accuracy of the bi-dimensional models can be improved by applying a three-dimensional aerodynamic correction. This corrective factor is used and proved to increase the accuracy of the simulations. Note that the corrected simulations (black lines) better agree with the three-dimensional results. While the non-corrected model maintains the error lower than the 3% of the initial angle of attack of the plate for the stable operations, the corrected model reduces the error to a lower value than 0.7%.

Finally, note how the beginning of an aeroelastic instability could be identified by observing a zone of the curves at which the average torsion and bending slope is abruptly increased, approximately for the same value of $k^* \approx 5.5$. The instabilities are characterized by an oscillatory motion that amplifies the twist with time. This instability can be attributed to the stall flutter phenomenon. This phenomenon should not be confused with the classical linear

flutter, as their mechanisms are entirely different. The classical linear flutter is the coupling between torsional and bending modes, which can be predicted by ignoring aerodynamic nonlinearities. Moreover, flutter is not expected to occur when the center of gravity and the elastic axis coincide, being in these cases, the divergence is the expected instability.

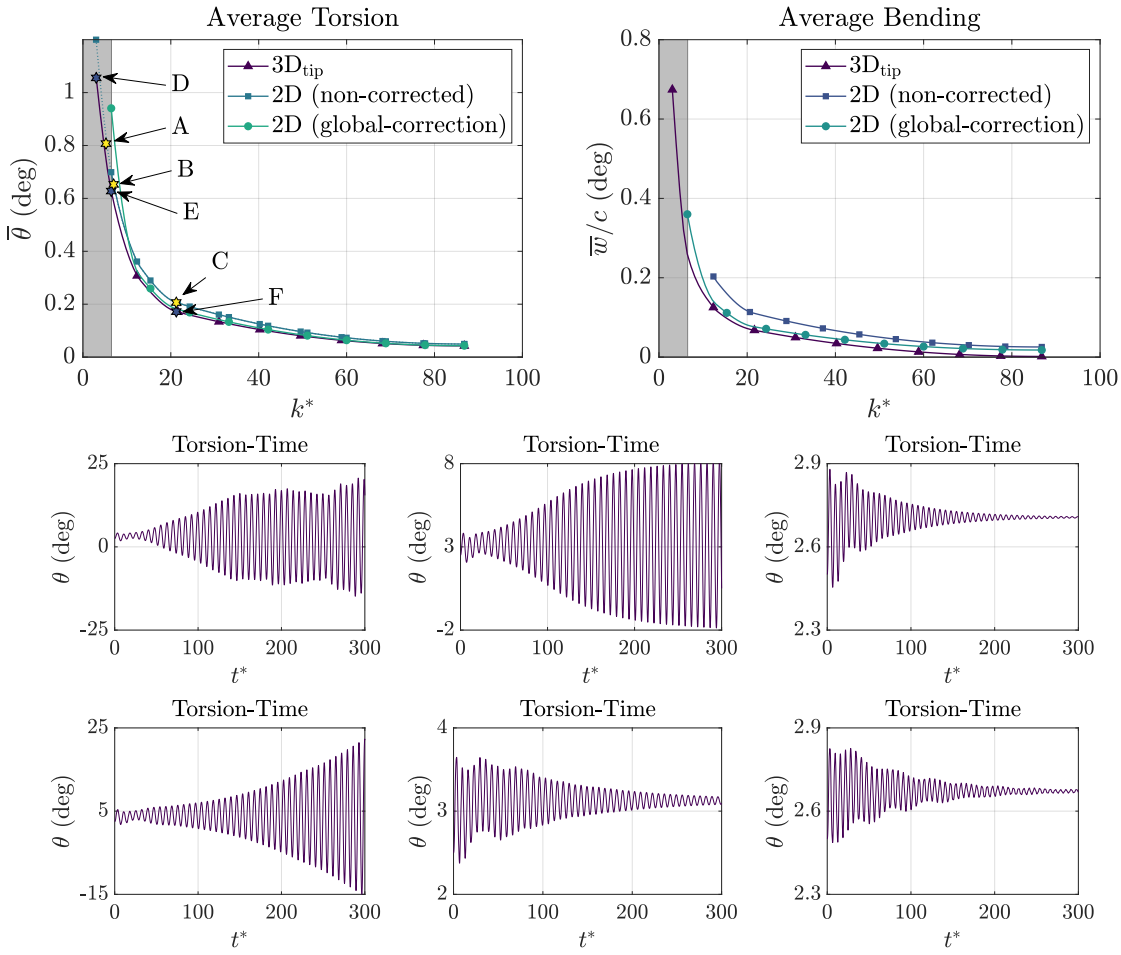

Fig. 4.18 **Mean deformation of the structure and temporal evolution of the main operation points.** Average deformation for the nondimensional stiffness: twist (top-left) and plunge (top-right). The shaded area shows the uncertainty limit of the 2D-derived section. Temporal evolution of the pitch respect a non-dimensional time $\left(t^* = \frac{tv_\infty}{c}\sqrt{\frac{k^*}{I^*}}\right)$ for 2D simulation cases A, B and C [*] and 3D simulations D, E and F [*] (bottom). Note that $t^* = 0$ corresponds to the transition from the rigid and steady to the elastic and transient simulations.

The analysis of the time evolution of 2D and 3D models is also presented and discussed next, using the unsteady responses shown in Figure 4.18. In order to compare the time evolu-

tion of the different operating phenomena, the time is nondimensionalized: $\left(t^* = \frac{tv_\infty}{c}\sqrt{\frac{k^*}{I^*}}\right)$. In the figure, the cases C and F correspond to the evolution of the bi-dimensional and three-dimensional computations for low free stream velocities and high values of k^*. In these cases, the aerodynamic damping is high enough to decrease the amplitude of the oscillations until a steady state.

When the nondimensional stiffness is decreased, the aerodynamic damping is also reduced. Therefore, the oscillations of the structure are not suppressed so quickly. In fact, the stability limits are represented by Case B for the bi-dimensional section. This simulation observes a stable limit cycle oscillation (LCO). For this value of k^*, LCO is not already reached for the 3D simulation, case E.

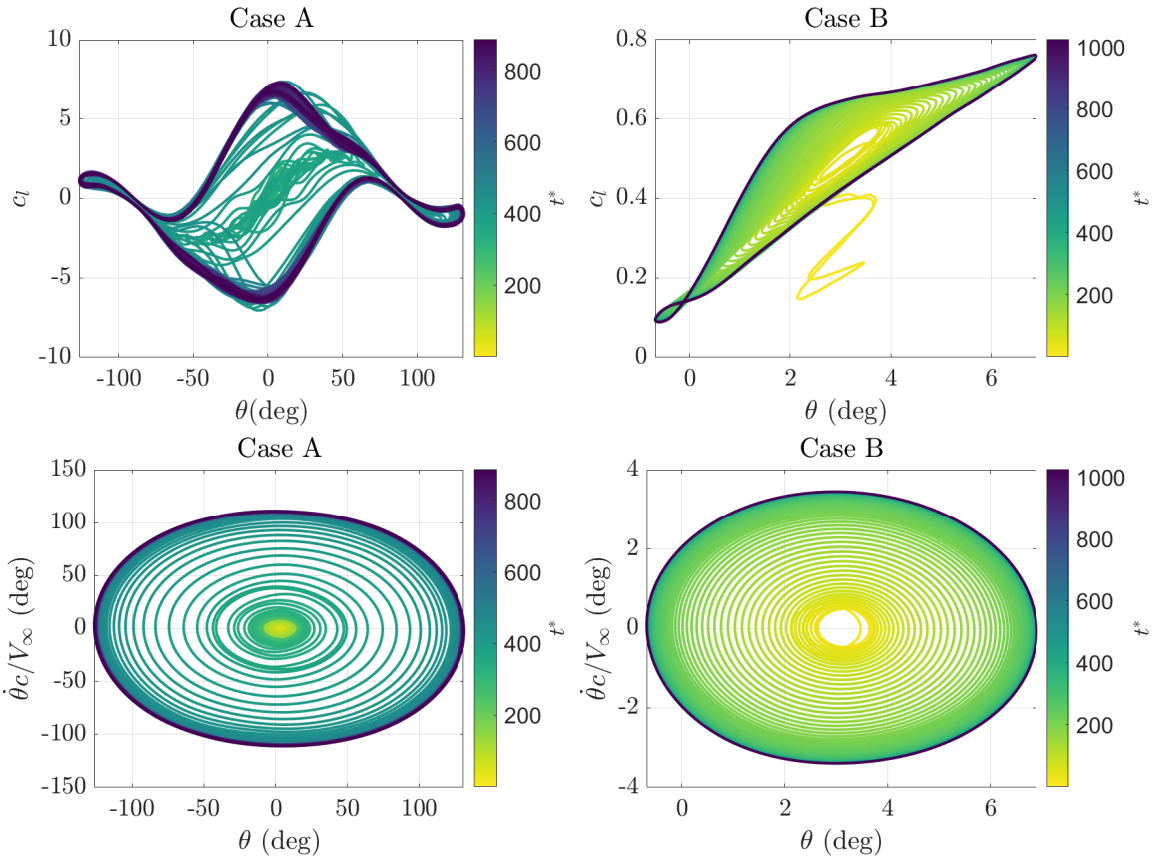

Fig. 4.19 **Aerodynamic hysteresis loop of the aeroelastic 2D simulation.** (Top) lift coefficient as a function of the incidence, (bottom) velocity of the twist as a function of the twist. (left) Flutter conditions and (right) LCO.

In the case of the unstable simulations, Cases A and D, similar trends are observed. In these cases, the aerodynamic damping is reduced, becoming zero or negative, resulting in an unstable oscillation. The bi-dimensional simulations also present an abrupt response

compared with the three-dimensional case. The unstable oscillations of both methodologies present a similar evolution as a stall flutter phenomenon generates them.

The Limit Cycle Oscillation can be further discussed in Figure 4.19. Here, the curves of c_l vs. θ and the phase diagram are shown for the 2D calculation for a case just after (Case A) and just before (Case B) the instability region. The stable cycle (right image) can be identified in the figure for high-time values. However, the amplitude is monotonically increasing for the unstable cycle (left image). In the figure, the nonlinearities of the calculations can also be observed. The shape of the loops is significantly different from the results of traditional flutter in the linear aerodynamic regime [27, 28].

Discussion

Along the section, the methodology of Section 3.3.3 has been presented for obtaining an equivalent cross-section for an arbitrary three-dimensional structure. The mechanical properties of the cross-section have been integrated along the beam span using the modal shapes. This integration might be more complicated for structures with variable cross-sections and materials and might reach, depending on the case, the limitations of the model. In addition, the structural bending-twisting coupling is not straightforward, and more complex models are required.

The procedure models the main aeroelastic features of the three-dimensional system, being able to account for the aerodynamic nonlinearities at arbitrary sections. The equivalent airfoil is shown not to be of straightforward derivation, as presented in the literature. The main advantage of the equivalent structure is the computational cost reduction with a similar accuracy level compared to the three-dimensional simulations.

The equivalent section methodology has been applied to a cantilever cross-section beam inside a wind tunnel. The simplified methodology is compared with the complete three-dimensional simulation. Low differences are obtained between the bi-dimensional and the three-dimensional cases. The equivalent section is demonstrated to represent a three-dimensional structure for a significant part of the operation range. The procedure allows the simulation of arbitrary beam sections accounting for nonlinear aerodynamic effects.

Regarding the flow perspective, the wind loads calculated in the bi-dimensional simulations do not consider three-dimensional effects, such as the tip-vortex. In addition, a corrective factor for these three-dimensional effects is proposed in the work, improving the mean values of deformation obtained in the simulations. The corrective factor requires a three-dimensional simulation and might be opposite to the computational cost reduction. As previously presented, this factor reduces the error in the prediction of the mean deformation of the beam. Nevertheless, the instability and the structure dynamics were correctly predicted

by the non-corrected model, evidencing that the corrective factor might be avoided. In the case of requiring the improvement produced by the corrective factor, the computational cost of the model is still lower than the FSI complete analysis, as only steady three-dimensional calculations are required.

The results have evidenced that the non-corrected simulations have provided accurate results for calculating the pitching angle and the vertical displacement. However, the bending displacement shows a slight overprediction compared with the complete simulation. Moreover, introducing a three-dimensional correction has improved the prediction accuracy of the mean deformations.

The main essential advantages of this simplified methodology can be listed next:

- Although important simplifications have been assumed during the derivation of the equivalent model, it allows us to obtain accurate deformation results, implying a reduction in the computational cost by orders of magnitude concerning the 3D simulation.
- The aerodynamics of the reduced bi-dimensional model can be considered fully nonlinear, given that the hypothesis listed during its derivation could be assumed to be valid.
- Therefore, the model should be useful for relatively quick estimations of aeroelastic linear instabilities, such as flutter or divergence. Also, it could be used to estimate nonlinear instabilities/phenomena such as stall flutter.

The equivalent 2D derivation lies in the hypothesis of neglecting the high-order modes of the structures. This hypothesis has been discussed, showing its applicability. The equivalent section has provided similar results to the complete simulations. Therefore, the capabilities of the methodology for simulating general aeroelastic problems are demonstrated, allowing the computational cost reduction of the simulations.

4.2.3 Bi-dimensional ANN surrogate aerodynamics

The methodology previously presented requires the discretization of the domain, the motion of a rigid solid inside the grid mesh, and the deformation of the mesh to adapt to the new conditions. The bi-dimensional simulations may require too many computational resources for the initial design of a structure. In order to reduce the computational cost of the simulation, the equivalent cross-section is combined with an aerodynamic surrogate model. In other words, the equivalent flat plate of the previous section is joined with the aerodynamic model of Section 3.3.2.

The workflow of the surrogate model is shown in Figure 4.20. First, the database of the simulations is generated by calculating the aerodynamics of oscillating cross-sections. This data is used to train the surrogate model and validate the training results. Finally, the aerodynamic model is coupled to the equivalent section.

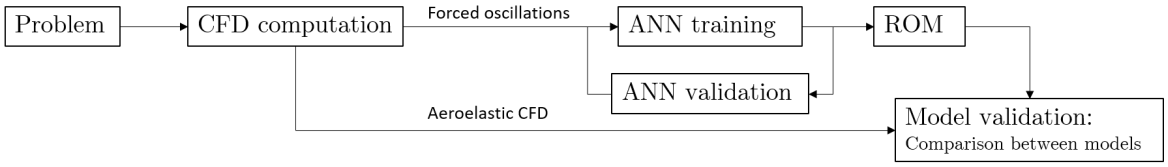

Fig. 4.20 **Scheme of the workflow of the aeroelastic ROM based on surrogate models.** The procedure includes training, validation, and application of the ANN.

Data base construction from CFD simulations

The database is generated with a matrix of 324 CFD bi-dimensional simulations of forced oscillations. The conditions of the simulations are selected to represent a wide range of operating points, Figure 4.21. The database is limited to the range of conditions in which the initial angle of attack and the amplitude of the movement produce negligible vortex shedding. These conditions are similar to many engineering problems, such as solar panels in stow position [29]. The cases with intense vortex shedding produce significant random oscillations of the aerodynamic coefficients. These cases reduce the accuracy of the network under the interest conditions. Finally, the aeroelastic simulations are calculated through a strongly coupled algorithm [30].

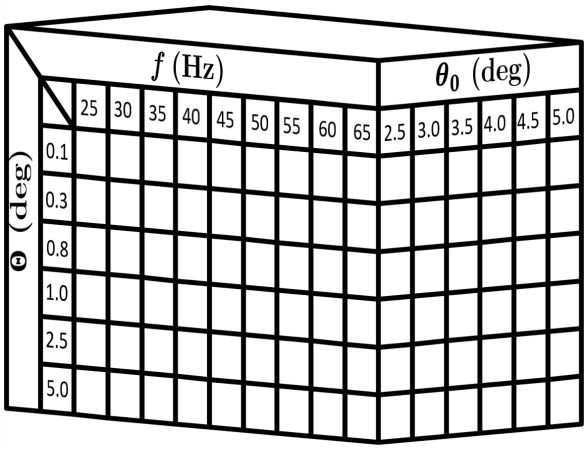

Fig. 4.21 **Training simulation data set matrix.** The data set requires enough information on the angle of attack and frequency of the motion.

The training simulations represent a forced oscillatory pitching motion with the formulation of equation 4.8:

$$\theta = \theta_0 + \Theta \sin(2\pi f t) \tag{4.8}$$

being θ_0 the initial pitch angle, Θ the amplitude of the motion and f the frequency of the motion. The matrix of simulations contains the training cases shown in Figure 4.21. The forced oscillations only take into account the twisting of the airfoil. The angle of attack is extracted from the database, and after training the network, a quasi-steady angle of attack is used for feeding the surrogate model.

In these simulations, the oscillating motion of the plate produces cycles that modify the value of the linear aerodynamic derivatives (Equation 4.9). Note that the aerodynamic coefficients might be expressed as the sum of the stationary and the dynamic terms.

$$c_l = c_{l0} + c_{l\alpha}\alpha + c_{l\dot{\alpha}}\frac{c\dot{\alpha}}{V_\infty} + c_{l\ddot{\alpha}}\frac{c^2\ddot{\alpha}}{V_\infty^2} + \ldots \tag{4.9}$$

As the aerodynamics of the section are nonlinear, the CFD has been used to calculate the aerodynamic coefficients. The stationary coefficients interpolation curves and the forced oscillations results are shown.

In Figure 4.22, the static coefficients are shown as a function of the angle of attack and the plunge. The coefficients exhibit a nonlinear behavior for higher angles of attack than 4 deg. In addition, the moment is significantly affected by the vertical position of the plate.

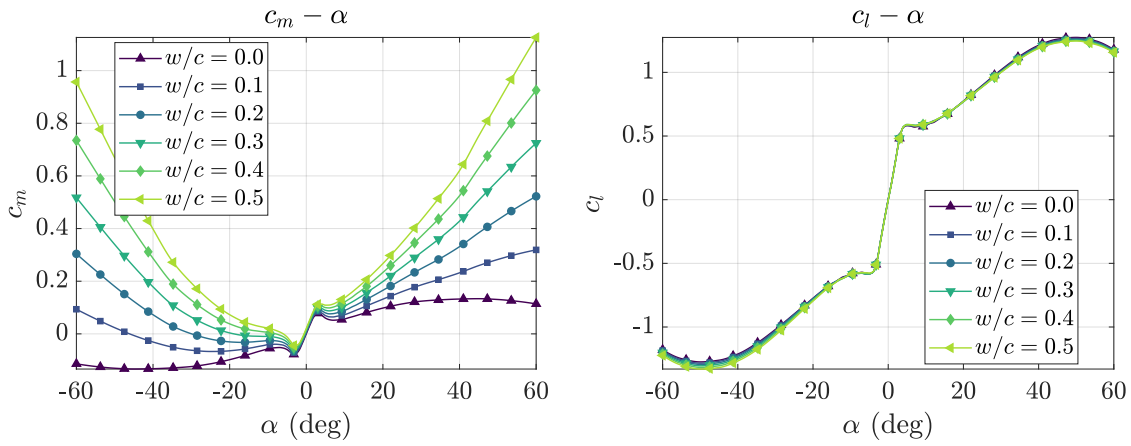

Fig. 4.22 **Stationary aerodynamic coefficients of a flat plate.** The coefficients are presented as a function of the angle of attack and the plate plunge.

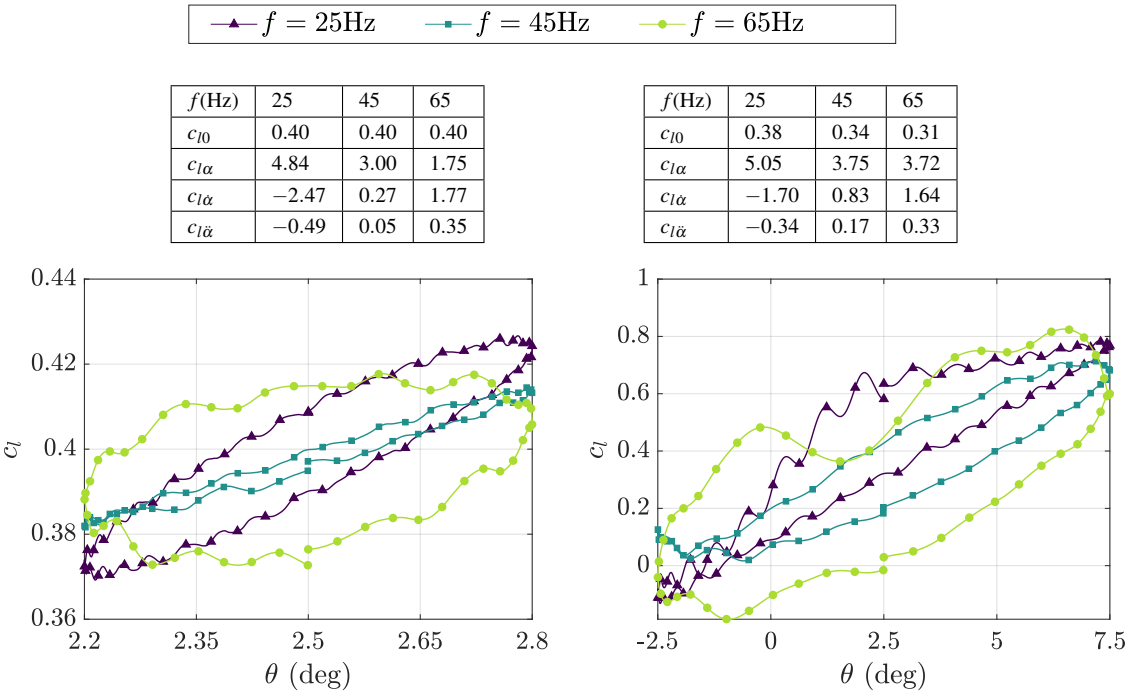

f(Hz)	25	45	65
c_{l0}	0.40	0.40	0.40
$c_{l\alpha}$	4.84	3.00	1.75
$c_{l\dot{\alpha}}$	−2.47	0.27	1.77
$c_{l\ddot{\alpha}}$	−0.49	0.05	0.35

f(Hz)	25	45	65
c_{l0}	0.38	0.34	0.31
$c_{l\alpha}$	5.05	3.75	3.72
$c_{l\dot{\alpha}}$	−1.70	0.83	1.64
$c_{l\ddot{\alpha}}$	−0.34	0.17	0.33

Fig. 4.23 **Aerodynamic cycles for low angle of attack.** (Left) $\Theta = 0.3$ deg & $\theta_0 = 2.5$ deg and (right) $\Theta = 5$ deg & $\theta_0 = 2.5$ deg.

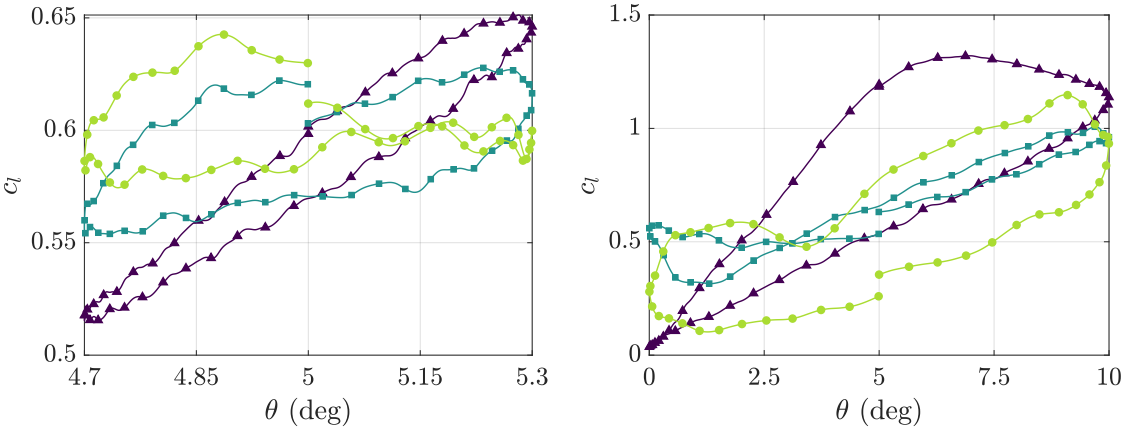

f(Hz)	25	45	65
c_{l0}	0.58	0.59	0.60
$c_{l\alpha}$	12.56	4.35	−0.22
$c_{l\dot{\alpha}}$	−3.54	−3.46	−1.42
$c_{l\ddot{\alpha}}$	−0.71	−0.69	−0.28

f(Hz)	25	45	65
c_{l0}	0.70	0.68	0.57
$c_{l\alpha}$	6.36	3.13	3.88
$c_{l\dot{\alpha}}$	−3.71	0.10	1.51
$c_{l\ddot{\alpha}}$	−0.74	0.02	0.30

Fig. 4.24 **Aerodynamic cycles for low angle of attack.** (Left) $\Theta = 0.3$ deg & $\theta_0 = 5$ deg and (right) $\Theta = 5$ deg & $\theta_0 = 5$ deg.

Figures 4.23 and 4.24 show the cyclic behavior of the aerodynamic coefficients due to the forced oscillation motion. In the figure, the initial angle of attack of the plate, the amplitude, and the frequency of the movement condition the aerodynamic loops. In the case of the airfoils operating in the linear aerodynamic range, Figure 4.23, the coefficient $c_{l\alpha}$ decreases with the frequency. Moreover, the second derivative of the lift coefficient increases, producing a higher curvature in the loop.

For post-stall conditions, Figure 4.24, the section presents a nonlinear behavior. In these operation points, the effects of the nonlinearities increase with the frequency.

The aerodynamic coefficients present an oscillating cycle with the vortex shedding frequency. Therefore, for the post-stall simulations, an increase in the lift slope is noticed as an effect of the nonlinearities. In these cases, the coefficient $c_{l\alpha}$ grows for the highest angles of attack, becoming higher than the potential lift slope of 2π, as shown in Figure 4.24.

Note that the aerodynamic coefficients present oscillations in the curves. These oscillations are a consequence of the cross-section geometry. The squared airfoil produces a detached flow from the leading edge, even for low angles of attack. Consequently, the effects of the wake produce the variation in the aerodynamic coefficient during the hysteresis cycle.

Surrogate model based on artificial neural networks

This section presents the procedure to fit the artificial neural network with the nonlinear phenomena of the aerodynamic forced oscillations. The sensitivity analysis of the number of neurons is performed, and the energetic global error of the cycle prediction is determined. The number of epochs of the training process is adjusted to minimize the training and validation errors of the ANN. The networks are trained using the RMSprop algorithm. Moreover, the database is segmented arbitrarily, using 90% of the simulations for the training and the remaining 10% for the validation.

The aerodynamic coefficient is divided into a steady and a dynamic term. The former provides a quasi-steady model, while the second is calculated by applying a neural network. The quasi-steady aerodynamic model is interpolated linearly from the coefficients of the CFD results. These coefficients are provided in Figure 4.22 as a function of the angle of attack and the vertical position inside the wind tunnel. Four different models are shown in the section. The first is the CFD, the equivalent section structure coupled with bi-dimensional CFD simulations. The methodology of this method was presented in the previous section. The quasi-steady model combines the equivalent section structures with interpolating the steady CFD coefficients. The last models combine the sum of the quasi-steady terms with calculating the dynamic terms based on neural networks. These models employ feed-forward (FFN) and long short-term memory (LSTM) networks.

The number of neurons in the network defines the total number of weights and variables required to adjust the ANN. Determining the appropriate number of neurons is conditioning the accuracy and computational cost of the training process [31]. However, an excessive number of neurons can also produce overfitting, the capacity of the network to adapt to an out-of-training situation is reduced by an excessive number of parameters or epochs in training. This analysis is applied to the different configurations: FFN and LSTM. The different ANN present a similar architecture. An input layer, a hidden layer with N_1 neurons, and an output layer with $N_2 = 2$ neurons, as presented in the work methodology.

The energetic error of the aerodynamic cycle, εE_{c_m}, is calculated as the difference of the power coefficient ($c_w = c_m \frac{\dot{\theta} c}{V_\infty}$) integrated in time for CFD and ANN, as stated by Equation (4.10), to perform the neuron independence analysis.

$$\varepsilon E_{c_m} = \frac{\int_t^{t+T} (c_{w_{ANN}}) dt - \int_t^{t+T} (c_{w_{CFD}}) dt}{\int_t^{t+T} (c_{w_{CFD}}) dt} \tag{4.10}$$

Figure 4.25 presents the power coefficient comparison between CFD and ANN for a network of 2 and 50 neurons. In the figure, an improvement in accuracy compared with the steady solution is observed.

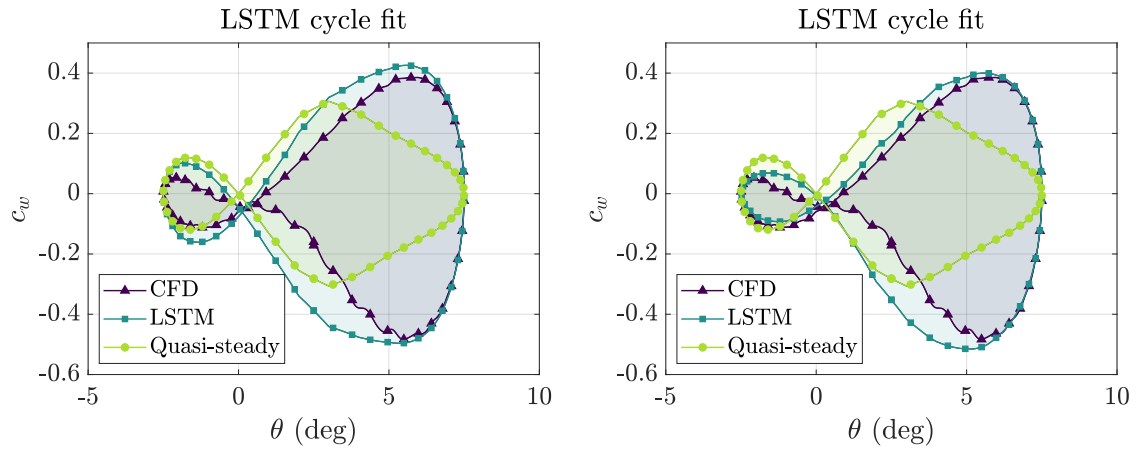

Fig. 4.25 **Power coefficient comparison between the ANNs and the CFD simulations for two representative numbers of neurons on the hidden layer.** (Left) 2 neurons in the hidden layer and (right) 50 neurons in the hidden layer. The cycle is shown for an initial incidence of 2.5 deg, an amplitude of 5 deg, and a nondimensional frequency of $\frac{fc}{V_\infty} = 0.1250$.

The cycle energetic error density function is shown for the FNN and the LSTM in Figure 4.26 for different numbers of neurons of the first layer. The energetic error becomes approximately constant from $N_1 = 50$, making this number of neurons the optimal choice regarding the accuracy and computational cost.

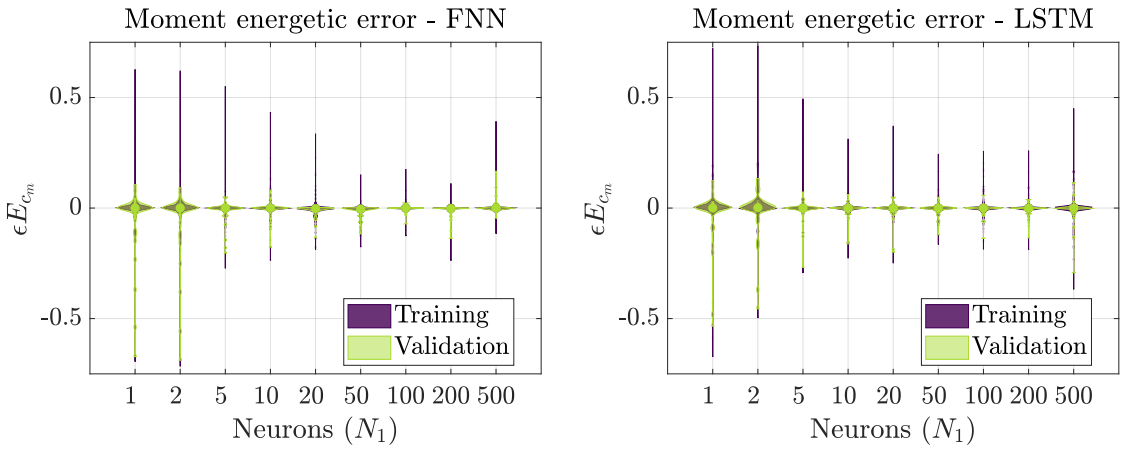

Fig. 4.26 **Distribution of the energy error for the different number of neurons.** (Left) results for the FNN network and (right) results for the LSTM network.

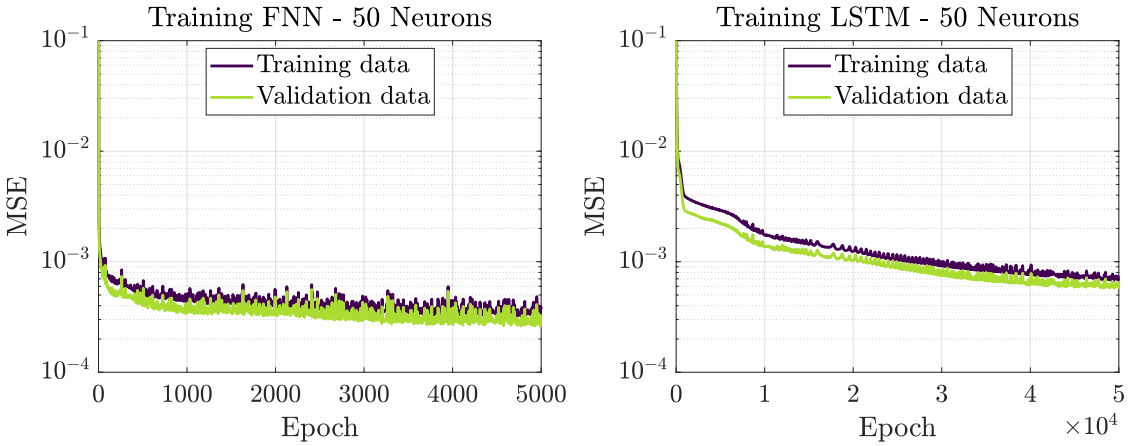

Fig. 4.27 **Evolution of the MSE as a function of the epoch of training.** The results are presented for FNN (left) and LSTM networks (right).

In addition, the network accuracy is also dependent on the number of epochs of the training [32]. This number is selected to ensure that the logarithmic validation error has either reached an asymptotic limit or started to increase (overfitting). The validation mean squared error (MSE) is shown to flatten for a number of $5 \cdot 10^3$ and $5 \cdot 10^4$ epochs for the FNN and LSTM networks, respectively. In addition, a k-fold cross-validation analysis [33] is performed. A mean prediction error of $5.34 \cdot 10^{-4}$ for 10-folds using the FNN model.

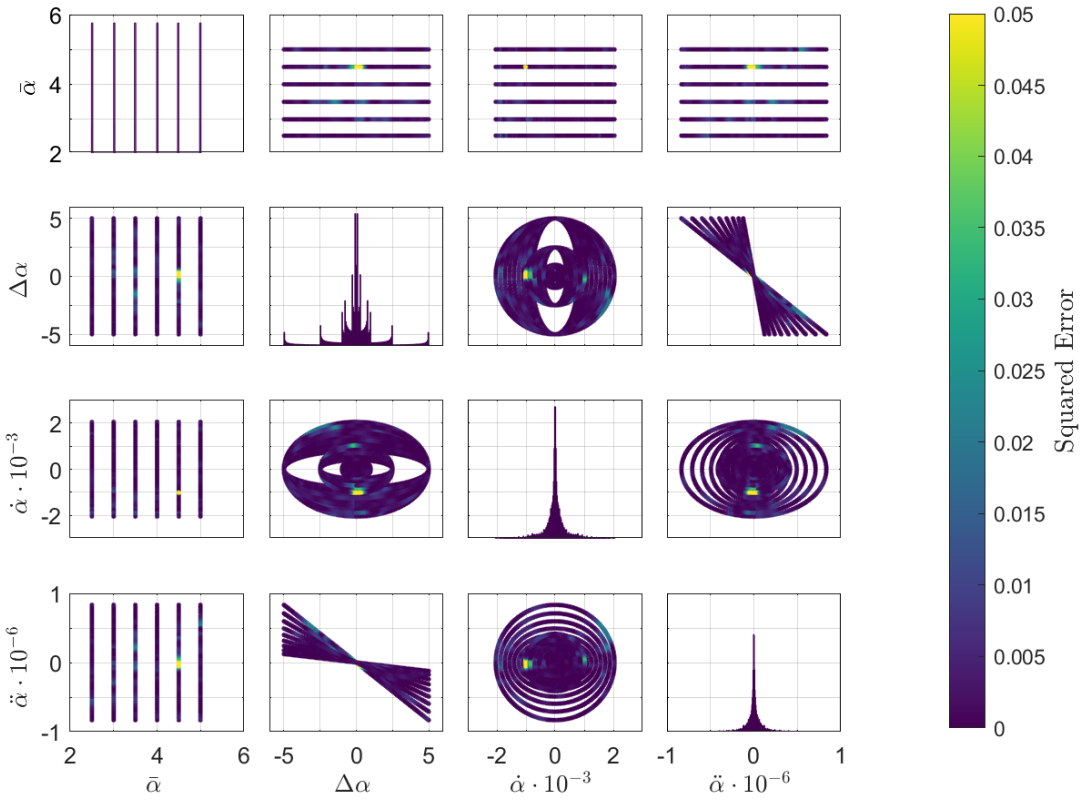

Fig. 4.28 **Squared error distribution for the input variables.** The plots on the diagonal show the distribution of the training variables, while the subfigures out of the diagonal show the squared error distribution for each pair of input variables.

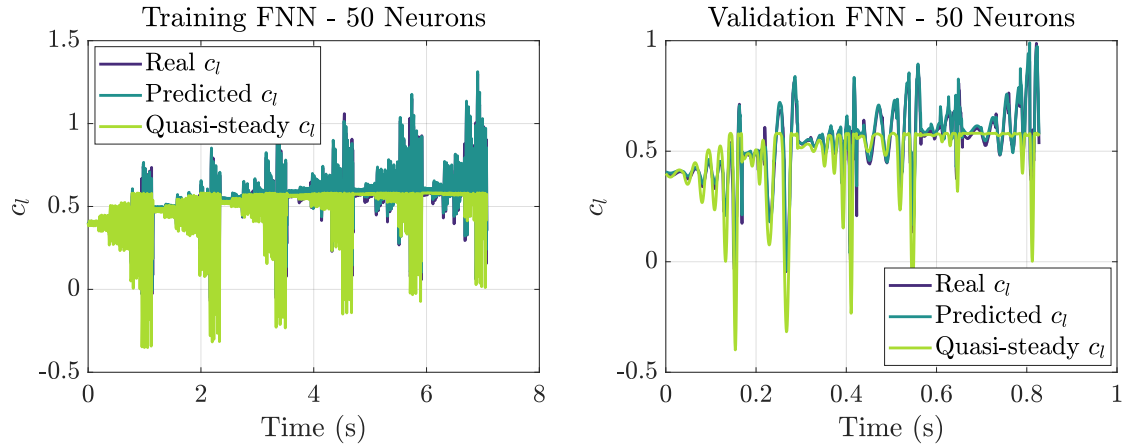

Fig. 4.29 **Lift coefficient of the training and validation of the FNN neural network.** (Left) training and (right) validation.

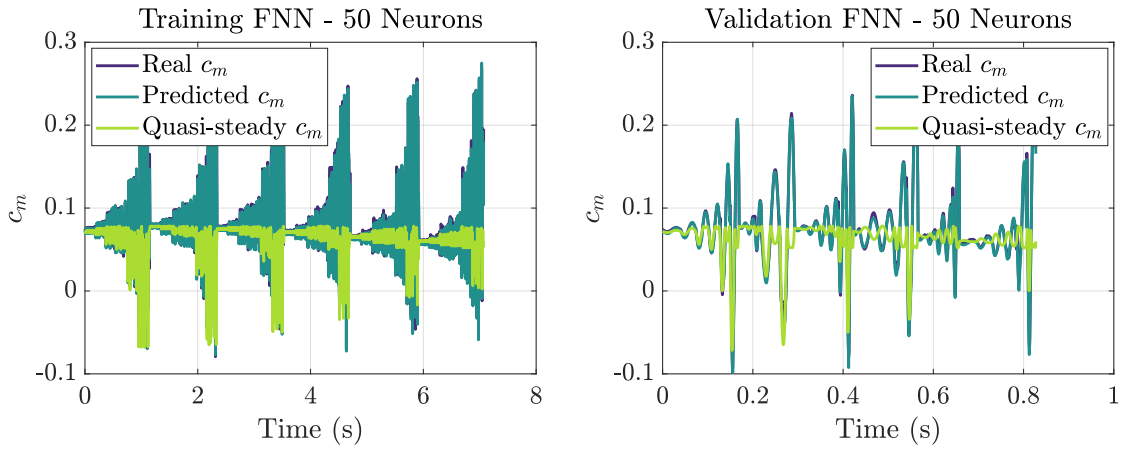

Fig. 4.30 **Moment coefficient of the training and validation of the FNN neural network.** (Left) training and (right) validation.

Figure 4.28 shows the error distribution in the whole data set. The figure shows the distribution of values of the input variables where the neural networks were evaluated. Note that the squared error is demonstrated to be low for the analysis domain, locating the higher errors near the stall point of the plate: incidence of 4.5 deg and null increment of the angle of attack.

Figures 4.29, 4.30, 4.31 and 4.32 show the performance of the ANN for the training and validation data. An accurate behavior is presented for both typologies of networks in the simulation of nonlinear aerodynamics compared with the quasi-steady approach. The CFD and the predicted values overlap in the significant part of the cycles. Similar behavior is evidenced in training and testing, although the large amount of data in the figure complicates the visualization of the training curves.

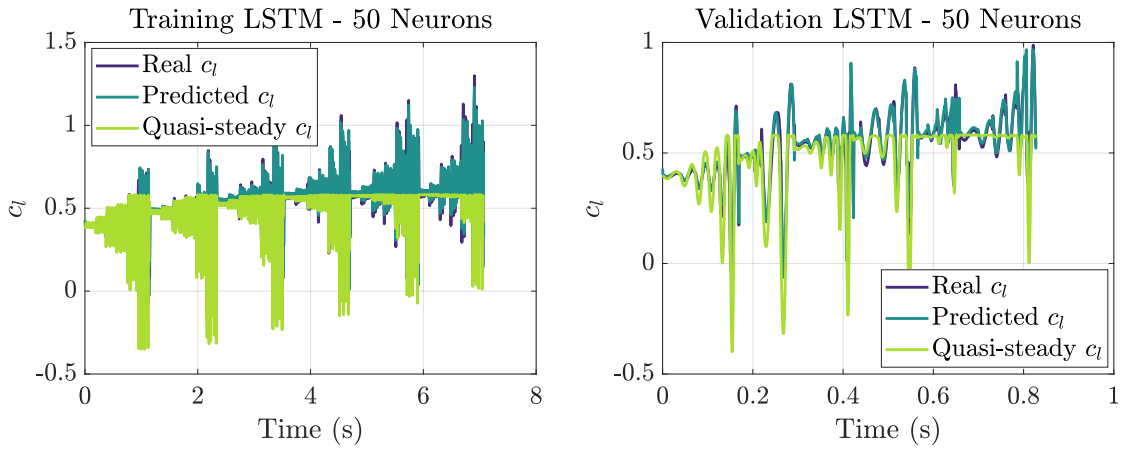

Fig. 4.31 **Lift coefficient of the training and validation of the LSTM neural network.** (Left) training and (right) validation.

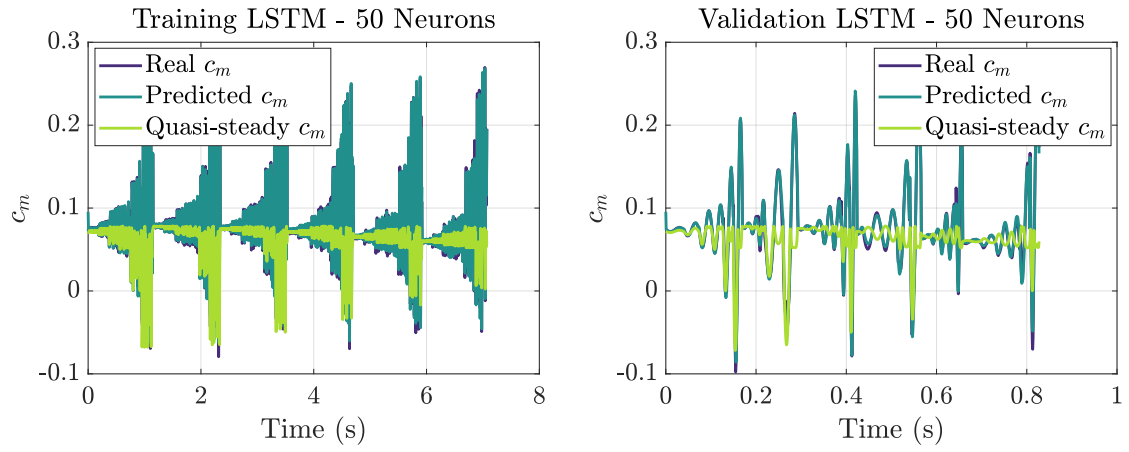

Fig. 4.32 **Moment coefficient of the training and validation of the LSTM neural network.** (Left) training and (right) validation.

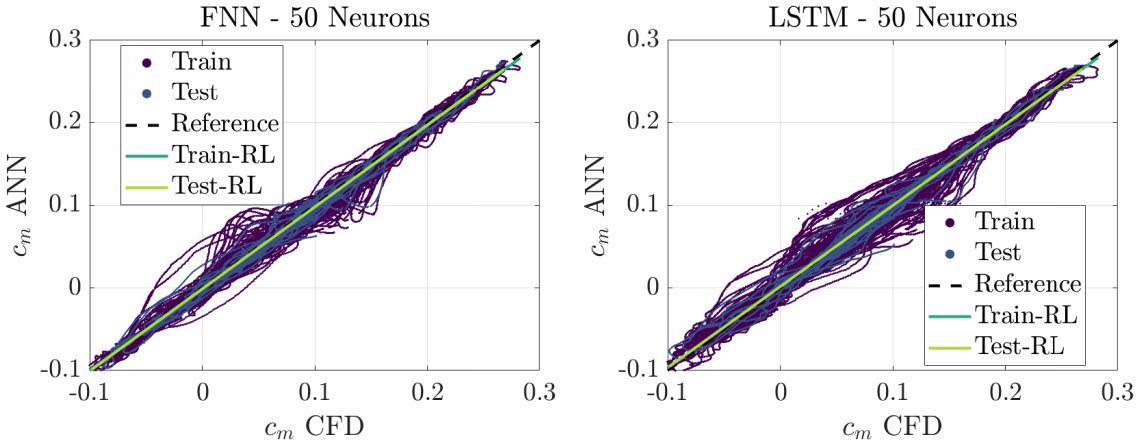

Fig. 4.33 **Regression plots for the moment coefficient.** (Left) FNN and (Rigth) LSTM.

Figure 4.33 clarify the results of Figures 4.30 and 4.32 by showing the linear regression between the real and the predicted value of the coefficient, comparing it with the ideal non-error solution. In the figure, a fair agreement can be observed between ANN and CFD.

In addition, for showing a temporal evolution of the aerodynamic coefficients, a prescribed aeroelastic motion is imposed on the neural network, comparing the results of the aerodynamic coefficients. The results of the surrogate models are presented in Figure 4.34. The figures show the high accuracy of the aerodynamic coefficients with respect to the CFD simulations.

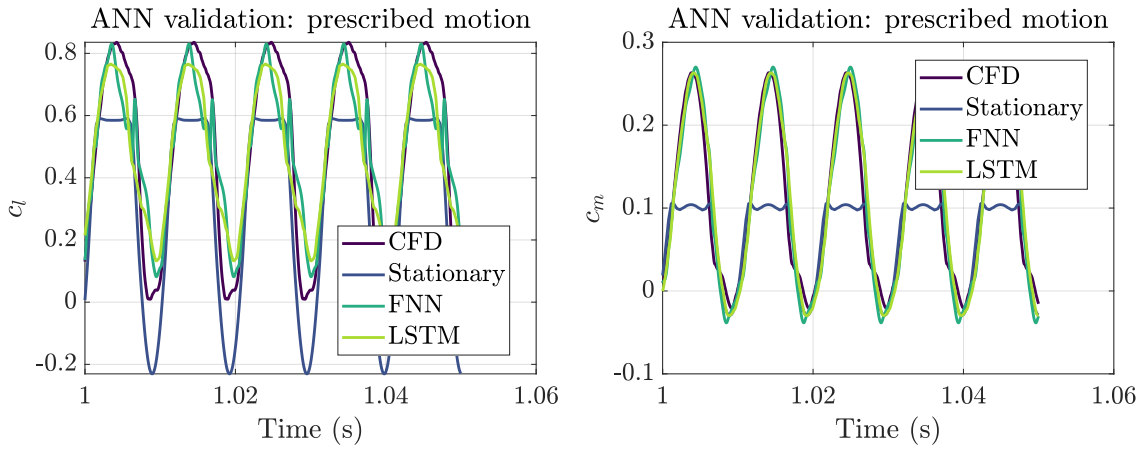

Fig. 4.34 **Prediction of the aerodynamic coefficients by the surrogate model for a prescribed motion.** (Left) lift coefficient and (right) pitching moment coefficient.

Aeroelastic surrogate model

The ROM is then tested on the equivalent rigid cross-section of Figure 4.6. Different working conditions are calculated, varying the nondimensional stiffness k^* along the stability range, the LCO, and the post-flutter.

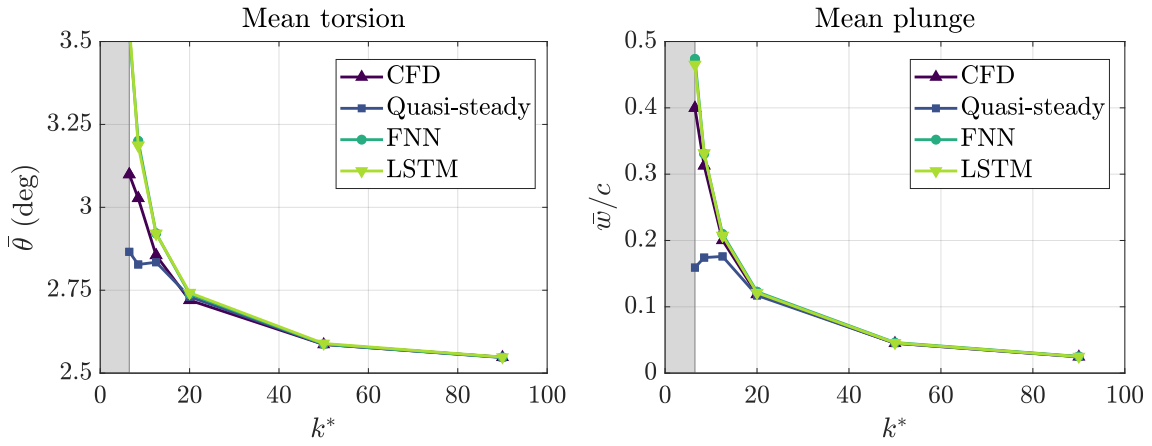

Fig. 4.35 **Comparison of the mean deformation of the ROM and CFD simulation for the different aerodynamic models.** (Left) mean twist and (right) mean plunge.

As observed in Figure 4.35, the ROM accurately reproduces the aeroelastic deformation of the plate. The error remains lower than 5% until the instability where the model is not reliable. The ANN improves the prediction of the nonlinear oscillatory aerodynamics with respect to the steady coefficients. This model captures the dynamic effect on the flow and can damp the oscillations or prevent the aerodynamic stall.

The instability zone may be identified as the value of nonlinear stiffness in which there is an abrupt change in slope, as can be observed in Figure 4.35. A shaded area represents this instability zone. The deformation of the structure inside the unstable area is amplified with time. The use of an artificial neural network predicts the LCO accurately. The amplitude and the frequency of the predicted motion are analyzed to evaluate the LCO prediction and the limitations of the ROM transient results.

The motion amplitude is presented in Figure 4.36. A fair similitude is presented between the FNN and the LSTM with respect to the CFD simulation. Nevertheless, quasi-steady aerodynamics tend to overpredict the deformation value for higher values of the nondimensional stiffness. The identification of the stall flutter corresponds to the point at which the amplitude of the motion abruptly increases. These unstable conditions are reached when the nondimensional stiffness is decreased below the flutter value k_f^* or when the velocity rises above the flutter value V_f.

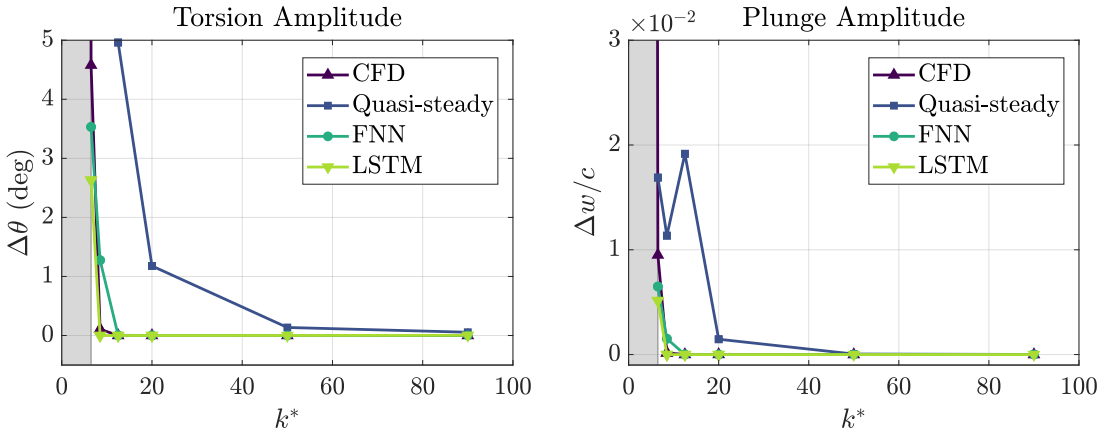

Fig. 4.36 **Comparison of the amplitude of the motion of the ROM and CFD simulation using different aerodynamic models.** (Left) twist amplitude and (right) plunge amplitude.

However, although both typologies of neural networks show similar behaviors, slightly different results might be observed in the amplitude of the motion. FNN is more sensitive to changes in stiffness. Therefore, the amplitude starts to increase before the stall flutter. Note also that the LSTM raises the aerodynamic damping. The motion is damped to a steady value and only grows when after the stall flutter condition. The CFD aeroelastic simulation presents an intermediate situation. The motion increases amplitude in the same conditions as the FNN. Nevertheless, for low values, near the damped aerodynamics, the CFD is closer to the LSTM (Figure 4.37). In addition, the amplitude of the ANNs increases the amplitude slower than the CFD when the stall flutter is reached, Figure 4.38.

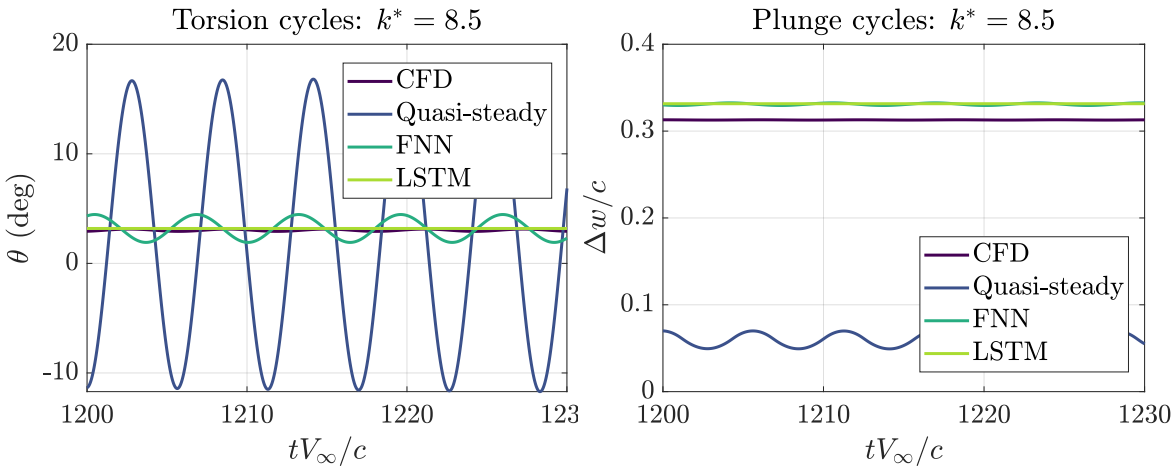

Fig. 4.37 **Time cycles for a nondimesional stiffness of k* = 8.5**. (Left) torsion and (right) plunge.

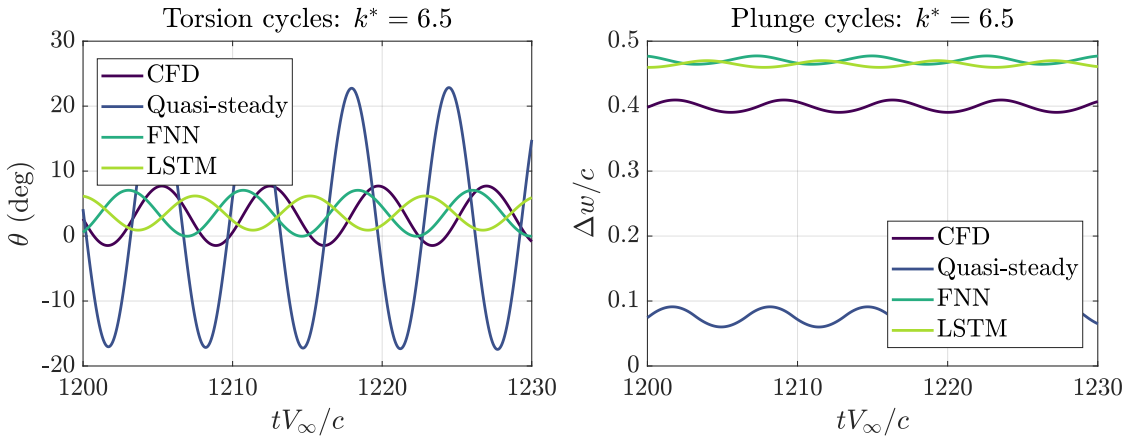

Fig. 4.38 **Time cycles for a nondimesional stiffness of k* = 6.5**. (Left) torsion and (right) plunge.

The time evolution of the previous models is presented in Figures 4.37 and 4.38 for two different working conditions. Small differences may be observed in the oscillation frequency, which accumulated during the evolution of the motion results in a phase error. The motion frequency is also analyzed in Figure 4.39. The error in the twist frequency was found to be lower than 5%. The differences in frequency are slightly more noticeable, 10%, when the plunge nondimensional frequency is analyzed far from the aeroelastic instability. However, the influence of this frequency is of second order when estimating nonlinear aeroelastic instabilities, as observed in Figures 4.35 and 4.36.

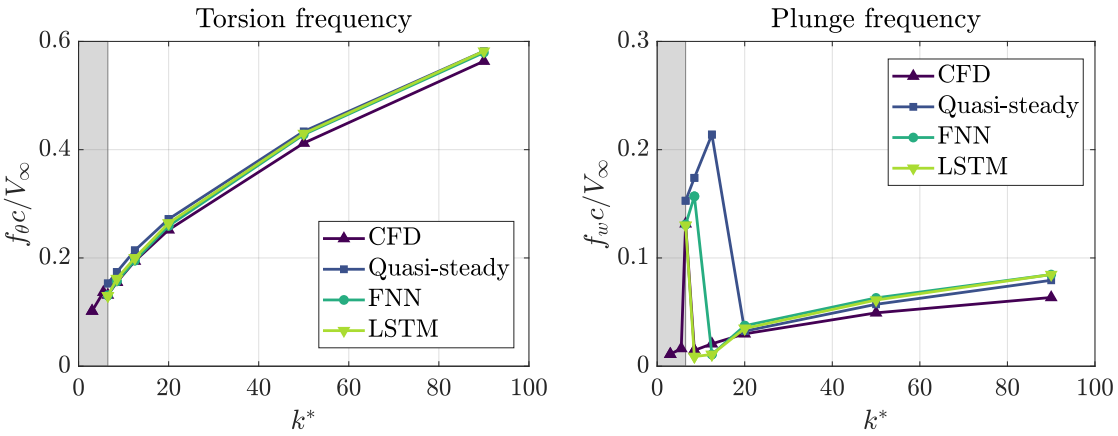

Fig. 4.39 **Comparison of the frequency of the motion of the ROM and CFD simulation for the different aerodynamic models.** (Left) twist and (right) plunge.

An essential point of the analysis is comparing the computational cost of the different models. Both simulations, CFD and ANN surrogated model, were performed on an Intel® Xeon® CPU ES-2630 v2. The simulations were run using five parallel processes. In the case of the CFD calculations, an average computational time of ten hours per simulation was required. The computational cost of the surrogated models was much lower, requiring between three and five minutes for the FNN and the LSTM architectures, respectively.

Discussion

This section compares a reduced order model (ROM), which combines the equivalent aeroelastic cross-section with artificial neural networks (ANN), with the aeroelastic bi-dimensional simulations calculated using CFD. The main objective of the section is to test the accuracy of the surrogated model in predicting aeroelastic instabilities. Nonlinear effects such as stall flutter and aerodynamic stall were successfully predicted, obtaining accurate results in the aeroelastic calculations.

The simulations have been performed in a flat plate cross-section. This geometry presents many benefits, as the mechanical properties of the structure are well-known, and its aerodynamic behavior is highly nonlinear, requiring nonlinear models. The aerodynamic coefficients are demonstrated to depend on the initial angle of attack, the amplitude of the motion, and its frequency. In order to reproduce the different aerodynamic conditions of the test bench, a set of CFD simulations have been calculated for generating the database for training the ANN. Nevertheless, the data required for training the network might be obtained from a different source, for instance, experimental tests. The ANN is trained in order to reduce the error. The network accuracy and training and validation data are evaluated, ensuring its

correct performance in a general case. The procedure is applied to two different architectures, feed-forward neural networks (FFN) and long short-term memory (LSTM) neural networks. Both typologies of ANN are tested and compared with higher-order models. Note the impact that the training process has on the predictions of the neural network. The database must represent the whole operation range to ensure the accurate performance of the neural network. In addition, training the network presents an associated computational cost which might be excessive if the number of simulations in which the surrogate model is used does not compensate for it. Therefore, the applicability of the procedure is totally conditioned by the expected use of the trained model.

Different conditions have been tested. The networks show high accuracy in reproducing the aerodynamic coefficients of the flat plate cross-section and use its motion as input. These models suppose a gain of accuracy compared with the quasi-steady models calculated by interpolating the nonlinear steady polar. However, some of the aerodynamic effects, such as the variations of the aerodynamic coefficients due to the wake fluctuations, are lost. The ANNs tend to reproduce a sinusoidal oscillation of the aerodynamic coefficients. Other effects, like vortex shedding, limit the range of application of the surrogate model. Therefore, the methodology works for the nonlinear aerodynamics of the flat plate in a specific range of applications where the oscillations due to turbulence are small or negligible. The models can be applied to an oscillating plate for low angles of attack (between -6 and 6 deg), low amplitudes of the oscillation (between 0 and 5 deg), and low or moderate frequencies (approximately a maximum of $\frac{fc}{V_\infty} = 0.3$). Higher frequencies present strong vortex-shedding effects, which can reduce in a significant way the accuracy of the network.

No significant difference was obtained for the different architectures (FFN and LSTM) in the validation of the networks. This fact, added to the more straightforward definition of the FFN models, makes this architecture more efficient in obtaining the transient aerodynamic coefficients of the plate for the working conditions.

The aerodynamic ANN surrogated model was coupled with a simplified structural solver. The results show an accurate prediction in determining the mean plunge and twist of the motion. The model can accurately predict the instabilities. An abrupt slope on the mean deformation curve is detected around the instability. Different behaviors were also obtained by comparing the aerodynamic models. The quasi-steady aerodynamics present a lack of accuracy when predicting the dynamic phenomenon. The different ANN architectures show similar results. Nevertheless, the LSTM solutions damp the oscillations faster than the CFD, while the FNN increases the amplitude and predicts the instabilities for slightly lower free stream velocities.

In a summary, the previous facts lead to the following main conclusions:

- The mean angle of attack, the amplitude, and the frequency of the oscillation strongly condition the aerodynamic loads in a dynamic problem. Thus, the stationary polar cannot be used to obtain accurate solutions.
- The utilization of artificial neural networks (ANN) may reduce both the time of simulation (compared with CFD simulations) and the error (compared with linear or steady models) in aeroelastic nonlinear problems.
- Different typologies of the neural networks obtained similar results. However, recursive structures such as LSTM networks damp the oscillations faster for similar training conditions. FNNs are faster and reduce the calculation cost, but they may be too conservative in predicting aeroelastic instabilities.

Finally, this section shows the applicability of the ANN to the aeroelastic problem. Different types of ANN are compared, coupling the aerodynamics with the structure of the section. This procedure has been demonstrated to reduce in a significant way the computational cost and to preserve the accuracy of the solution for arbitrary sections and nonlinear aerodynamics.

4.3 Application of beam theory to elastic structures

The following section provides the results of the previously presented beam element solver. Firstly, the model is validated against the literature results. Then the algorithm is applied to the interest cases. The reduced order model is, thus, applied to a set of complex problems involving advanced orthotropic materials and shell-resistant structures.

4.3.1 Validation of the beam element solver

The structural solver must be validated before applying the ROM to any engineering problem. This validation compares the structural deformation with the experimental and numerical results of the literature. The beam of Chadra et al. [34] is used as a validation test bench. The schematic representation of this beam can be observed in Figure 4.40. This structure is a six-carbon fiber ply laminated box cross-section beam.

The structure is studied for different layup configurations. The initial configuration is an oblique laminate with six plies. The main direction of the fibers is deviated 30 deg from the longitudinal axis of the beam, forcing a bending-twisting coupling. The deformation of the beam is due to a load of 4.45 N applied on the free end.

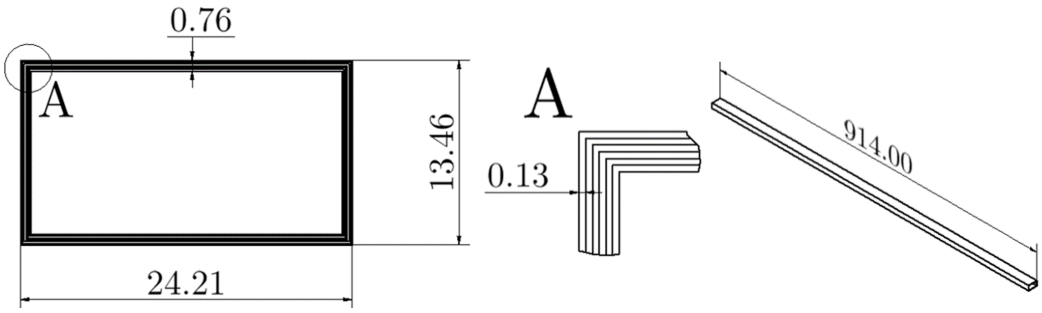

Fig. 4.40 **Chandra test bench for the structural model.** The test bench is a carbon fiber laminated box section clamped on one end.

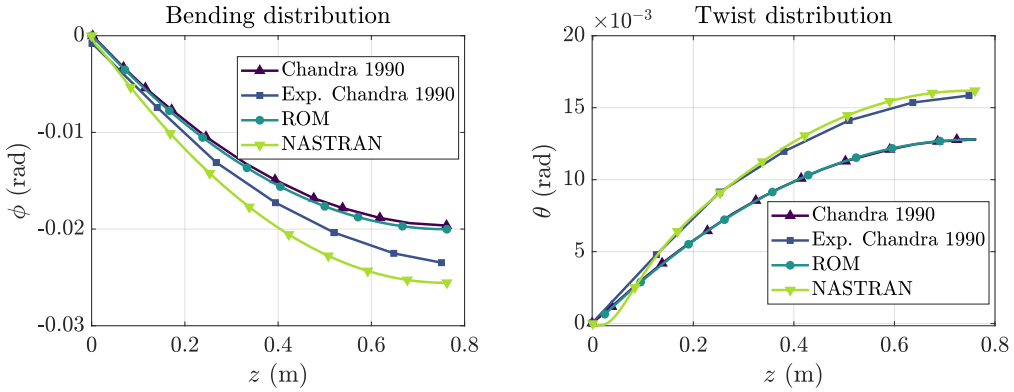

Fig. 4.41 **Structural validation of the Chandra 30 deg oriented fiber beam.** (Left) bending angle of the structure and (right) twist angle of the structure.

Similar results are obtained when the fibers are rotated 15 deg from the longitudinal axis of the beam, Figure 4.42.

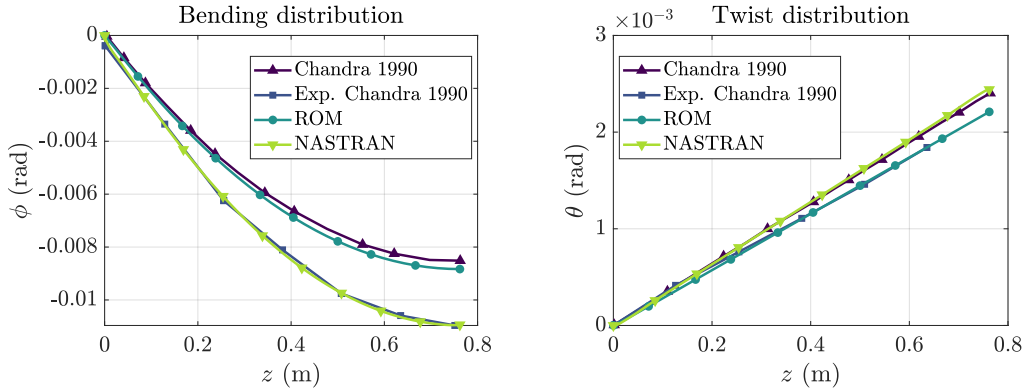

Fig. 4.42 **Structural validation of the Chandra 15 deg oriented fiber beam.** (Left) bending angle of the structure and (right) twist angle of the structure.

The previous figures show the accuracy between the present beam element model and Chandra's model. Nevertheless, the beam models cannot accurately simulate the bending-torsion couplings, as could be inferred from Chandra's work. In addition, the structural model is tested to validate the vibration modes of the structure using the work of Chandra and Chopra [35]. Table 4.9 show the results of the modal analysis.

Table 4.4 **Validation of the vibration modes.** The table provides the first three vibration frequencies of the reference structure.

Mode	Frequency ROM(Hz)	Frequency Chandra et al.(Hz)	Error (%)	Movement
1	22.50	21.03	6.99	Flap 1
2	35.69	36.92	3.33	Lag 1
3	140.87	128.36	9.75	Flap 2

Concerning the dynamic behavior of the beam element solver, the results show a reduced error in the first vibration modes. Observing the results of Table 4.9, these modes have been shown to properly reproduce the stiffness and mass properties that determine the dynamical motion of the structure. Therefore, observing the previous results, although the structural model is demonstrated to predict the characteristics of the orthotropic beam structures accurately, the algorithm is restrained to modeling limitations in the beam deformation prediction. For this reason, the structure itself must be checked to be correctly modeled for a particular application.

4.3.2 Orthotropic 1D squared cross-section beam clamped by one edge.

Case of study

Along this section, a carbon fiber laminated foam squared-section beam is used. The external geometry of these structures was used in the previous sections. This fact allows us to use the ANN-based surrogate model presented in the previous sections. However, in this section, the material is modified using a layup of a carbon fiber shell and a foam core. Table 4.5 presents the properties of the laminate materials.

The dimensions of the beam are presented in Figure 4.1. In addition, the fluid flow is constrained inside the same wind channel as the previous sections. The laminate material presents a $\left[\theta_f/-\right]$ configuration where θ_f is the orientation of the fiber, which is varied from -90 to 90 deg. The thickness of the carbon-fiber-reinforced polymer (CFRP) ply is 0.13

mm, and the foam ply completes the total thickness of 4 mm. The cross-section geometry is illustrated in Figure 4.43.

Table 4.5 **Material properties of CFRP and foam.** These properties are based on the works of Qin and Librescu [36] and Koohi et al. [37] respectively. E_l and E_t are the longitudinal and transverse elastic modulus respectively, G_{lt} and G_{tt} the longitudinal-transverse and transverse-transverse shear modulus, ν_{lt} and ν_{tt} the longitudinal-transverse and transverse-transverse Poisson ratios, h_{ply} is the ply thickness and ρ_s is the material density.

	AS4/3501-6	Foam		AS4/3501-6	Foam
E_l (MPa)	141960	15	ν_{lt} (-)	0.42	0.28
E_t (MPa)	9780	15	ν_{tt} (-)	0.50	0.28
G_{lt} (MPa)	6000	8	h_{ply} (mm)	0.13	3.87
G_{tt} (MPa)	4830	8	ρ_s (kg/m^3)	1445	35

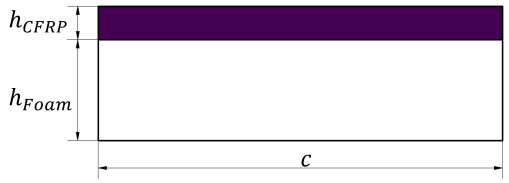

Fig. 4.43 **Cross-section of the beam.** The dimensions of the cross-section are not-scaled.

Note that the aeroelastic three-dimensional simulations were performed using the same methodology as explained in Section 4.2.2 with the corresponding modifications on the structure.

Validation of the structure

The correct structure simulation must be ensured before calculating the aeroelastic behavior of the different layups configuration. Firstly, the models (structural, aerodynamic, and aeroelastic) are validated. The computational cost of the ROM is compared against the full CSD/CFD simulation to measure the computational savings, demonstrating the capabilities of the reduced order model in the structural optimization process. Therefore, after validating the mathematical and physical background, the influence of fiber orientation is analyzed for different working conditions.

The initial validation of the structure was performed by comparing the results of the flat plate cross-section against the literature. The natural frequencies of a carbon fiber laminated

beam taken from Minguet [38] were compared with the results of the ROM for the same structure. Table 4.6 presents the previous comparison, showing an accurate agreement for the 1D models of the literature. However, the experimental data obtained a tip deflection of 137 mm due to the nonlinear structural effects that appeared in the structure. This fact explains the differences in mode 4. Figure 4.44 shows the structure's mode shapes. Structural coupling is evidenced in all the mode shapes, as the beam twists and bends in the same vibration mode. For instance, the first mode presents an increase in the twist and plunge with the longitudinal coordinate. This mode is dominant in the aeroelastic motion. The second and third modes present zeros in the torsion when the plunge amplitude derivative is null. In the fourth mode, torsion increases along the longitudinal coordinate while the vertical displacement has two relative maxima and two relative minima. The aeroelastic dynamic motion of the beam is expected to reproduce the first mode with small vibrations of the higher-order modes.

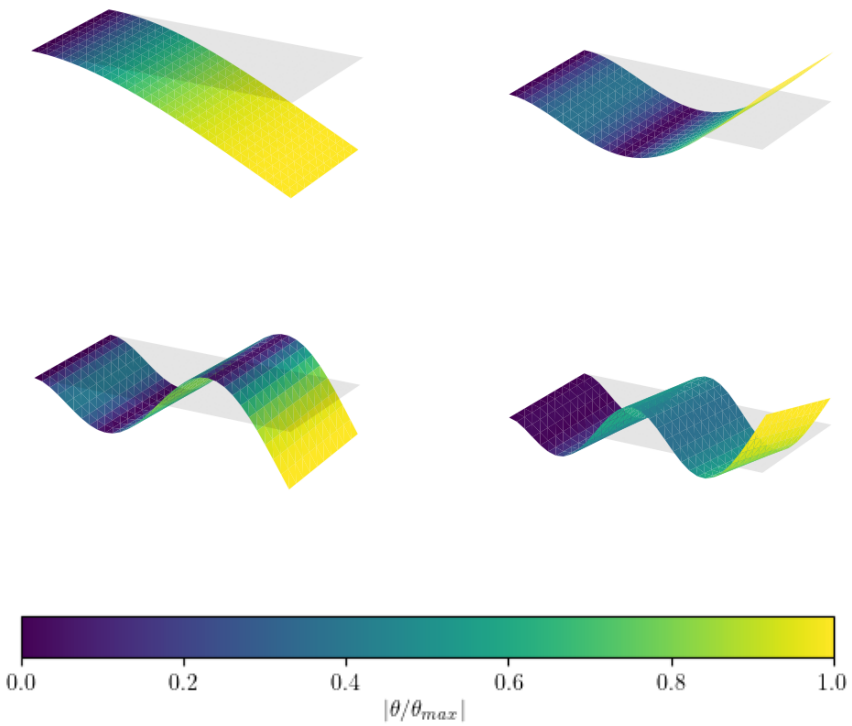

Fig. 4.44 **Modes of vibration of the reference flat plate beam.** Mode shapes (not-scaled) of the beam structure based on Minguet [38].

Table 4.6 **Validation of the structural model.** Natural frequency comparison with the literature.

Mode	Shaat [39]	Banerjee [40]	Minguet [41]		Current
			Analytical	Experimental	
1	1.278 Hz	1.280 Hz	1.280 Hz	1.400 Hz	1.285 Hz
2	8.012 Hz	8.020 Hz	8.010 Hz	8.000 Hz	8.053 Hz
3	22.433 Hz	22.441 Hz	22.500 Hz	20.000 Hz	22.544 Hz
4	43.960 Hz	43.927 Hz	44.400 Hz	68.000 Hz	44.045 Hz
5	-	48.431 Hz	48.700 Hz	-	47.748 Hz

Aerodynamic model results and limitations

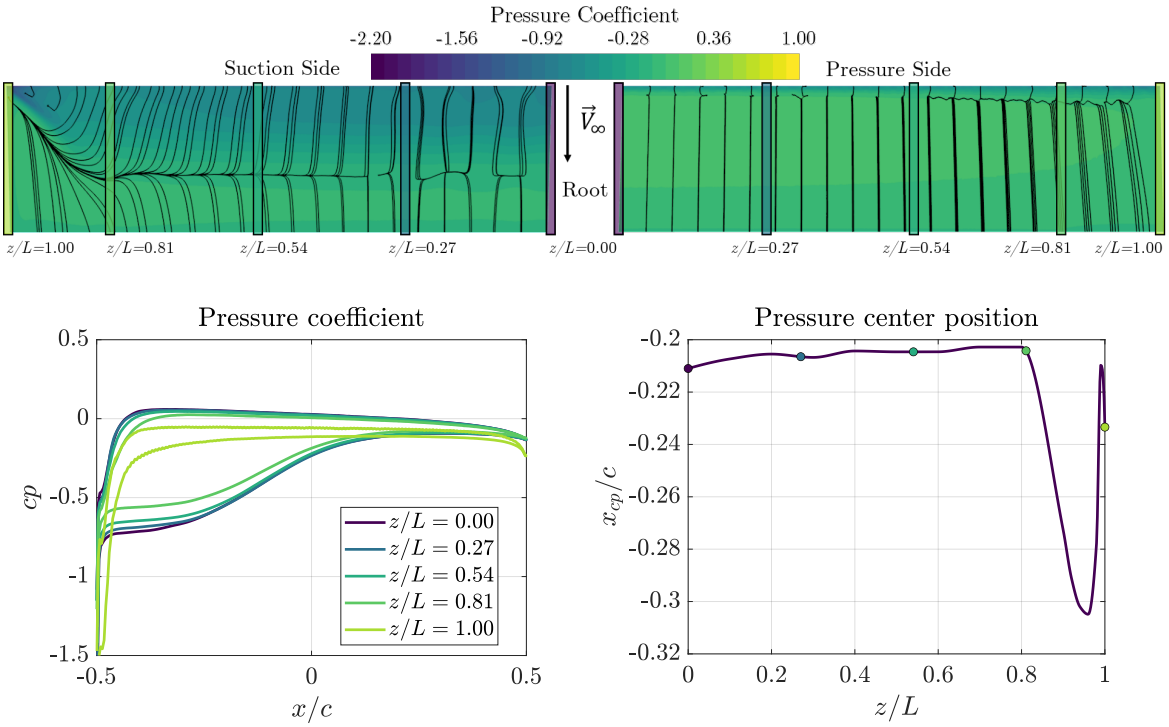

Fig. 4.45 **Three-dimensional aerodynamic effects of the structure.** Tip vortex effects, pressure distribution and pressure center position over the structure surface.

A finite wing immersed in a wind flow generates a pattern of three-dimensional vortexes. These patterns can be calculated and observed in the CFD three-dimensional simulations. The recirculation of the flow couples with the tip vortex effects near the free tip of the beam producing a flow pattern that displaces the pressure center of the sections near the tip. Thus,

the previous effects modify the moment coefficient with respect to the value estimated with the Lifting Line Theory. In fact, Figure 4.45 presents the aerodynamic effects of the tip vortex. The figure shows the distribution of the pressure coefficient along the span of the beam, evidencing that the nonlinearities of the aerodynamic loads are induced in the first term by a recirculation area near the leading edge. Near the tip, the recirculation area is diminished due to the homogenized pressure resulting from the vortex. In the figure, the wing span is marked with five color rectangles indicating the measured cross-sections. In these sections, the pressure coefficient has been measured and presented at the bottom of the figure using the same color code. In addition, the wall shear loads acting on the wall are included in the image. These lines show the limit of the recirculation area and its reduction in the suction side near the tip. Finally, the center of pressure is evidenced to move near the tip vortex, indicating with the color points the reference cross-sections used for visualizing the pressure coefficient.

Although the Lifting Line Theory fails when estimating three-dimensional effects near the tip (due to the movement of the center of pressure), as shown in Figure 4.46, the error remains below 4%, being acceptable for the aeroelastic simulations.

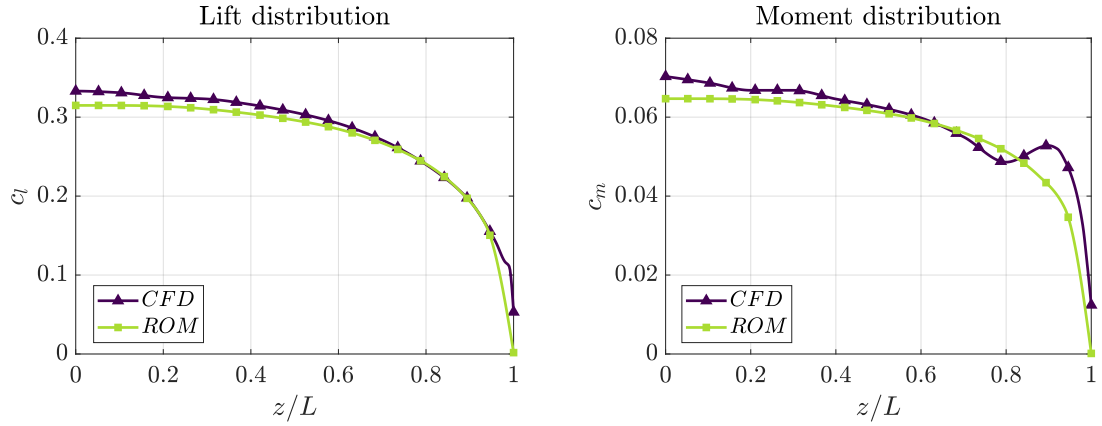

Fig. 4.46 Aerodynamic load distribution along the span. Steady aerodynamic load distribution along the span for 3D CFD simulations and 3D ROM analysis.

Aeroelastic validation against CSD/CFD

In order to determine the accuracy of the procedure, the solution of the complete CSD/CFD simulation was compared with the results of the ROM. Firstly, the deviation between the mean deformation of the ROM and the aeroelastic CFD/CSD simulations was evaluated, and the results are presented in Figure 4.47. The continuous line represents a perfect agreement between both methodologies. The points located below this line indicate an underestimation of the plunge motion, Figure 4.47 (left), and a higher twist in absolute value, Figure 4.47

(right). Therefore, according to the results presented in the figure, the ROM is able to obtain similar mean deformation results to those of the high-cost solution but in a computationally speaking more efficient way. However, the error of the ROM simulation increases as the deformations grow.

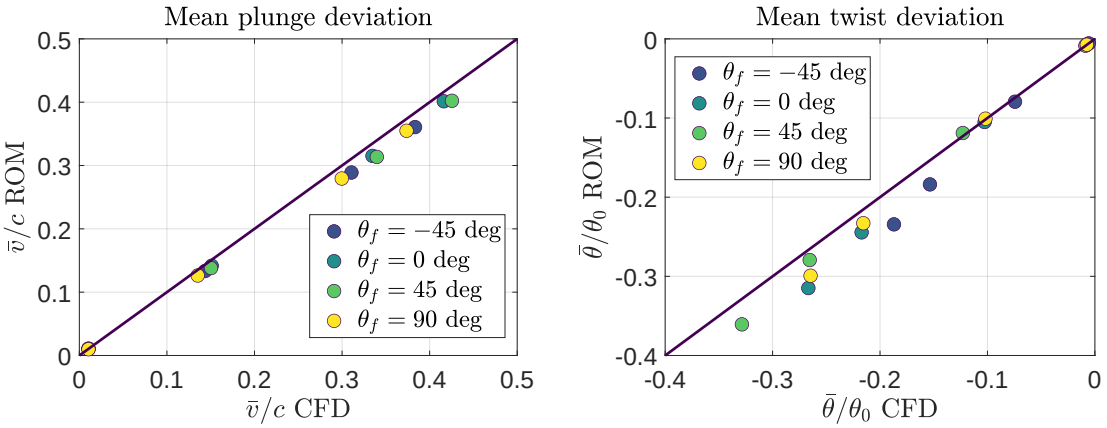

Fig. 4.47 **Deviation of the ROM solution with respect to CFD/CSD simulations.** (Left) plunge and (right) twist comparison.

A comparison of the evolution of the mean deformation values is also provided in Figure 4.48. This evolution is shown as a function of the nondimensional carbon fiber stiffness, $E^* = \frac{E_l^c}{\frac{1}{2}\rho_\infty v_\infty^2}\left(\frac{h}{c}\right)^3$ for four layup configurations. In this figure, the effects of fiber orientation are evidenced. Those fibers oriented longitudinally present a lower displacement in the bending direction. This effect is a consequence of the orthotropy of the material, which presents a higher elastic modulus in the normal stress direction, where the bending loads act. In addition, asymptotic behavior can be appreciated in the system. The coupling between the air and the structure reduces the global nondimensional stiffness. Therefore, as the flow velocity increases, the asymptotic limit appears for lower nondimensional stiffness.

Figure 4.49 shows the mean twist of the structures for four different configurations. Both models agree on the longitudinal and oblique orientation of the fibers. In fact, similar effects to the plunge can be observed. As the elastic axis of the structure, leaving apart bending-torsion couplings coincides with its center of gravity, no dynamic instabilities are expected. Therefore, nonoscillatory infinite displacements are expected near the instability limitations, called divergence velocity. However, when the structure reaches these limits, the angle of attack will increase dramatically, and the structure will stall and oscillate (stall flutter).

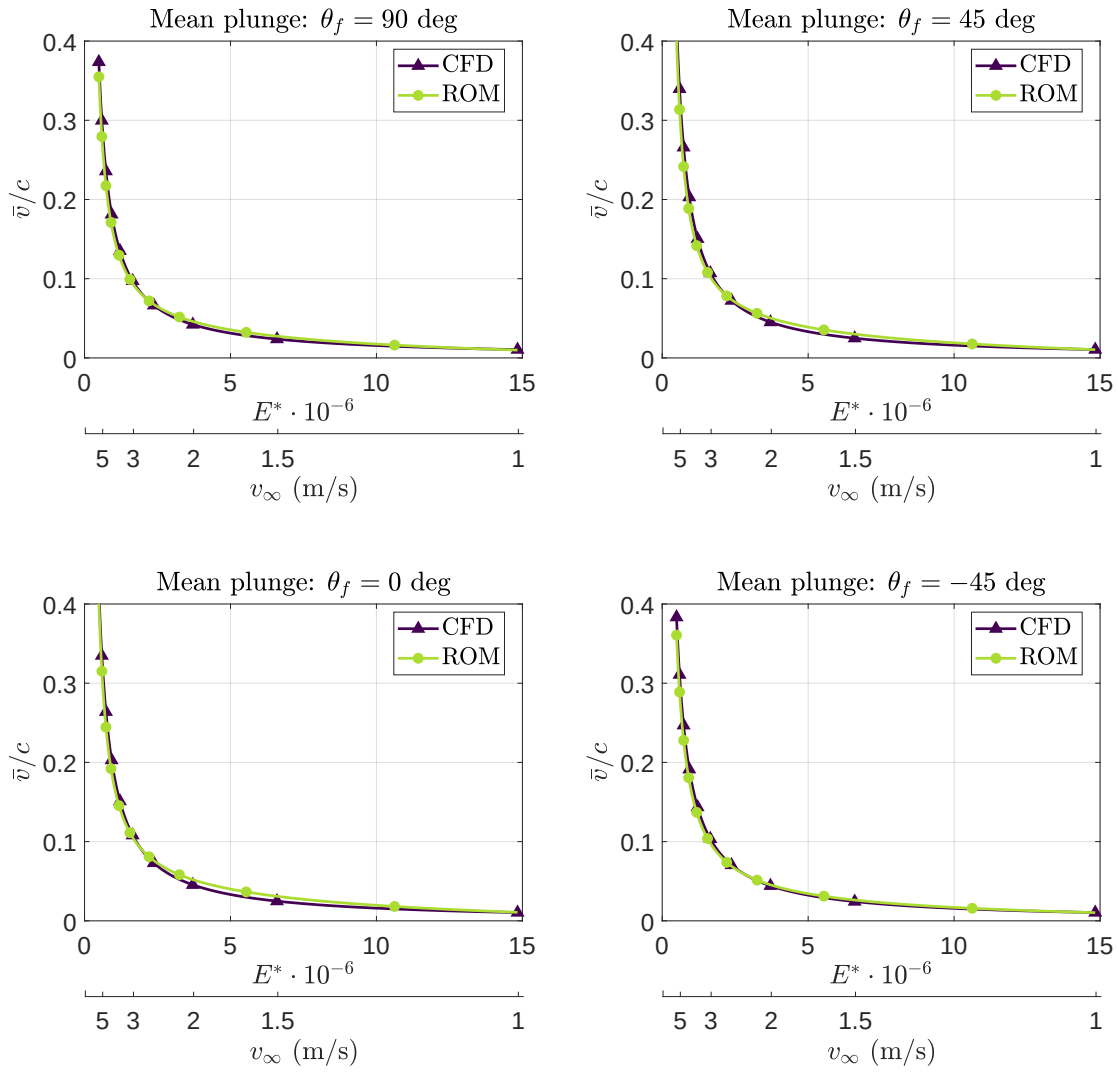

Fig. 4.48 **Plunge evolution of CFD and ROM calculations for different fiber orientations.** Note that the velocity measurements correspond to a structure of the properties listed in Table 4.5. (Top-left) $\theta_f = 90$ deg, (top-right) $\theta_f = 45$ deg, (bottom-left) $\theta_f = 0$ deg and (bottom-right) $\theta_f = -45$ deg.

According to the previous figures, plunge and twist are demonstrated to be accurately captured by the reduced order model. Therefore, the methodology can predict the influence of fiber orientation, allowing more efficient structural designs. The predictions of the ROM are evidenced to be more accurate for highly enhanced nondimensional stiffness. However, a progressive increase in the error near the instability conditions was detected. Moreover, the asymptotic values of the CFD/CSD solution are shifted; see Figure 4.47.

Nevertheless, the accuracy remains sufficiently high to predict aeroelastic phenomena such as flutter, divergence, or limit cycle oscillations (LCO). In addition, the ROM supposes a reduction of orders of magnitude in the computational cost of the calculations. Note that the aerodynamic model provides the nonlinearities leading to the LCO, as the structure remains linear in the present work.

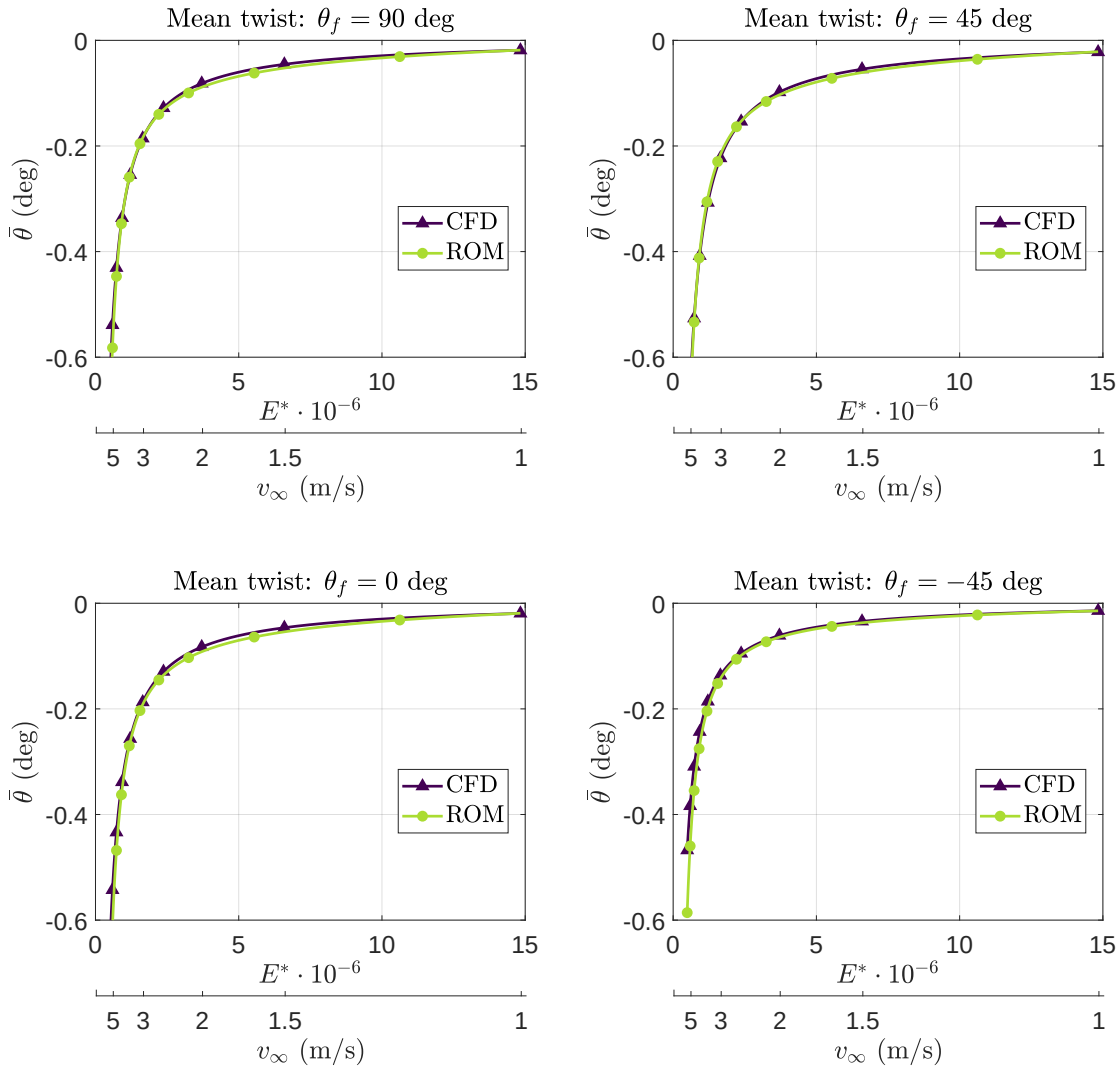

Fig. 4.49 **Twist evolution of CFD and ROM calculations for different fiber orientations.** Note that the velocity measurements correspond to a structure of the properties listed in Table 4.5. (Top-left) $\theta_f = 90$ deg, (top-right) $\theta_f = 45$ deg, (bottom-left) $\theta_f = 0$ deg and (bottom-right) $\theta_f = -45$ deg.

The computational cost of the different computing tools was measured to determine the benefits of the ROM. The CSD/CFD simulations were performed on a 15 Intel® Xeon® Gold

6154 CPUs multiuser cluster, whereas ROM simulations were run on an Intel® Xeon® CPU ES-2630 v2. The CSD/CFD simulations required a CPU computing time for a time step slightly above $2 \cdot 10^4$ s, and the complete simulation required 430 h. For the ROM, the CPU time per time step is around 2.2 s, being the simulation 3 h long. This fact implies a decrease of more than two orders of magnitude and four orders of magnitude in the total simulation and CPU computational cost, respectively.

Influence of fiber orientation

The fiber orientation strongly conditions the aeroelastic behavior of the beam. Therefore, the ROM was applied to a range of orientations from -90 to 90 deg to find an effective layup configuration. The variations of the mean deformation are presented in Figure 4.50 as a function of the nondimensional stiffness and the fiber orientation. A reduction in the mean twist is observed for negative orientations of the fiber. The structure reduces the angle of attack as it bends. This fact matches the results found in the literature [42]. The wash-out effect is applied to the beam, resulting in an alleviation of the aerodynamic loads. A passive aeroelastic control has been generated, as the plunge of the beam generates a reduction in the angle of attack. Moreover, the reduction of the twist has also decreased the aerodynamic force resulting in a lower plunge. Inverse effects are obtained for positive orientations, generating higher deformations and, consequently, reducing the unstable free stream velocity.

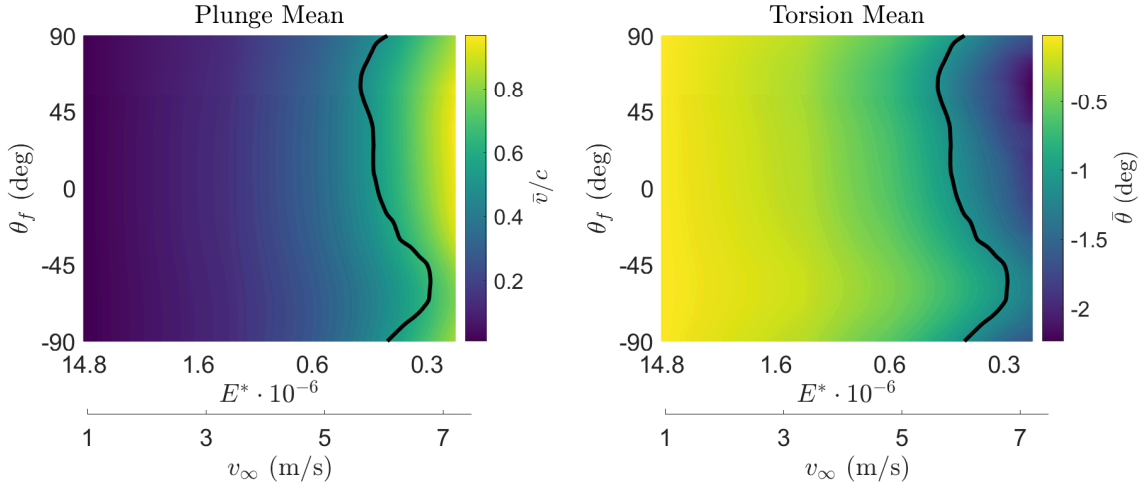

Fig. 4.50 **Mean deformation of the tip section as a function of the velocity and fiber orientation.** (Left) mean plunge of the tip section and (right) mean twist of the tip section. The solid line limits the stable region.

Additionally to the structural couplings described in the literature, the current methodology includes the simulation of non-linear aerodynamic effects, improving the results near the instability with respect to the linear potential aerodynamic model [43].

The damping of the solution signal estimated the stability limit of the system, and it is presented by the solid line in Figures 4.50 and 4.51. Figure 4.51(left) illustrates the torsion damping of the system. The aerodynamic damping increases with the velocity in the stable region for the negative values of the orientation. This effect was previously noted by the works of Chadra et al. [34] and Chandra and Chopra [35]. As previously stated, the negative orientation of the fiber (fiber rotated to the leading edge) produces wash-out: the twist of the tip is reduced when its plunge increases.

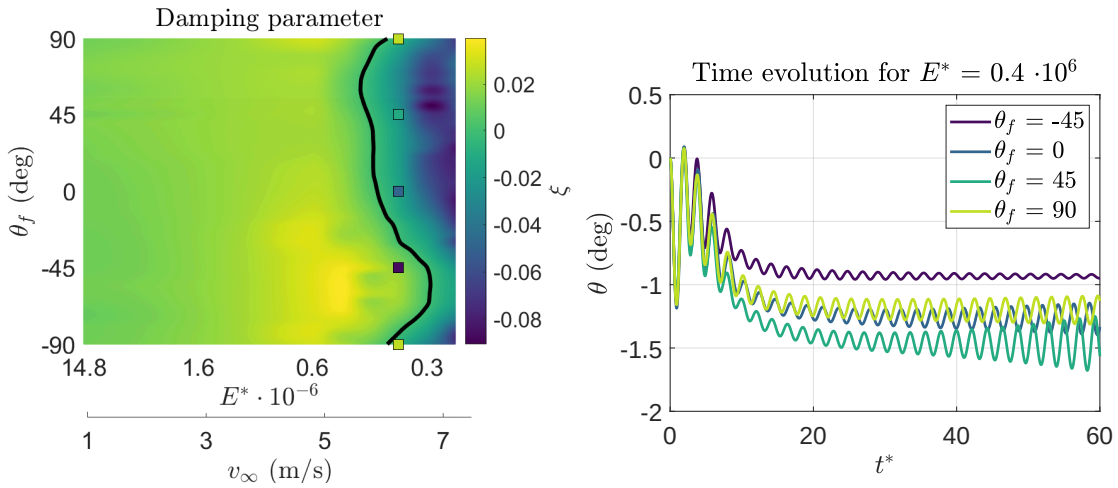

Fig. 4.51 **Torsional evolution of the system for different conditions.** (Left) torsional damping and (right) evolution of the torsion of the system for different flow and structural conditions. The damping map shows the time evolution for the highlighted color squares. The solid line limits the stable region, and $t^* = \frac{tv_\infty}{c}$ is the value of the nondimensional time.

Due to the structural couplings, the mean torsion is lower than for positive and longitudinal orientations. Therefore, the configuration of the material is preventing against stall. For a squared-section beam, stall initializes flutter, creating a phenomenon known as stall flutter. This oscillatory instability is dominated by torsion and produced by aerodynamic nonlinearities. The time evolution of the system is presented in Figure 4.51 (right) for the indicated design points. The figure shows that the most efficient fiber orientation for protecting against instability is the -45 deg orientation. This configuration remains stable while the rest are under stall flutter. Therefore, according to Figure 4.51 (left), for an optimum design, the fiber should be in the range $[-44, -68]$ deg for maximizing the stall flutter velocity and protect the structure.

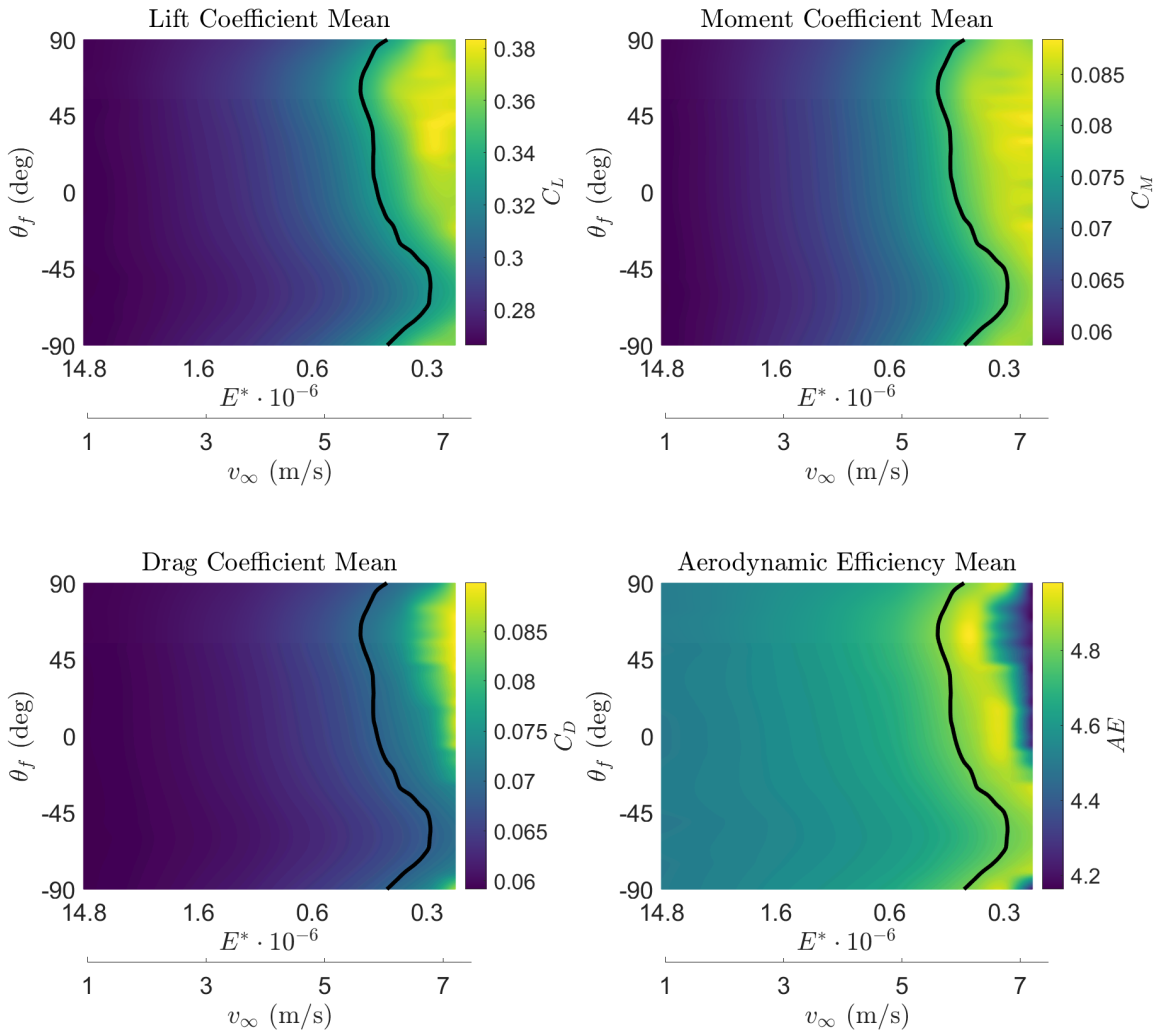

Fig. 4.52 **Aerodynamic coefficients of the beam for different flow and structural conditions.** (Top-left) lift coefficient, (top-right) right coefficient, (bottom-left) moment coefficient and (bottom-right) aerodynamic efficiency. The solid lines limit the stable regions.

The aerodynamic coefficients show similar results. Figure 4.52 illustrates the Lift and moment coefficients. The aerodynamic coefficients are directly related to the angle of attack, in other words, the twist of the beam. Thus, the increase in the mean twist generates higher lift and moment coefficients. It produces an augmentation on the aerodynamic loads.

Moreover, when the aerodynamic coefficients rise approximately 20% off the rigid beam value, instability appears. The aerodynamic coefficient growth is equivalent to an increment of 1 deg of the mean twist in the tip section. Similar effects are noticed in the drag coefficient. These effects generate a constant aerodynamic efficiency for the stability domain. When

the instability begins, the coefficients increase, raising the aerodynamic efficiency until the cross-section stalls.

Finally, the modal contribution on the deformed shape is presented in Figure 4.53 for the highlighted operational points of Figure 4.51. A similar contribution is observed for all the fiber orientations. The displacement of the nodes is mainly affected by the first mode. This means that the phenomenon could be simulated by using an equivalent section. However, as the velocity of the nodes is affected by the first three modes, in the case of studying the aeroelastic behavior of the equivalent section, the contribution of the velocity of vibration would be omitted.

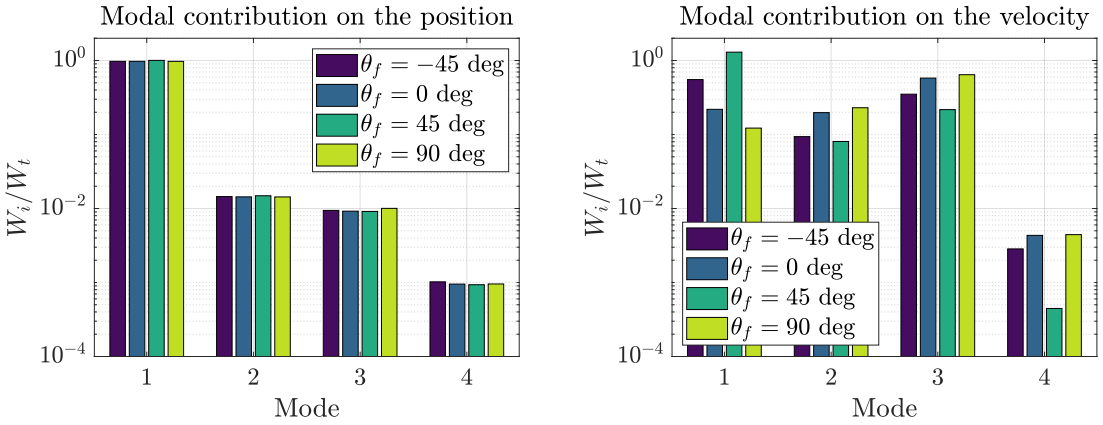

Fig. 4.53 **Modal contribution in the simulations.** Squared mean modal contribution of the last 0.2 s of simulation for the position (left) and velocity (right) for $E^* = 0.4 \cdot 10^6$.

Discussion

A Reduced Order Model enhanced by Artificial Neural Networks has been used for the aeroelastic calculations of a carbon fiber laminated beam. Adding the surrogate aerodynamic model based on Neural Network to the existing Lisbrescu's thin-walled beam model has allowed the reproduction of nonlinear aerodynamic effects. Thus, nonlinear oscillatory phenomena have been simulated. The resolution of the carbon fiber-reinforced foam squared-section beam has been validated against the literature, and the results have been compared with three-dimensional CSD/CFD simulations. Finally, the behavior of the beam has been analyzed for different fiber orientations, showing the influence of the fiber direction on the solution and the applicability of ROMs in the structural design process.

Concerning the methodology, ROMs have been demonstrated to be an efficient low-fidelity tool for calculating the aeroelastic behavior of the structure. Compared with the complete three-dimensional calculations, a reduction of four orders of magnitude of CPU cost has been noticed in the ROM. In addition, the error in the mean deformation remains

under 2% far from the instability and increases near the asymptote up to 15% when compared with complex CSD/CFD simulations. However, the increase in the error is not a limitation of using the methodology. The nondimensional curves have been demonstrated to fit both methodologies. The increase in the error is due to a slight deviation of approximately 5% on the asymptote.

In addition, in order to test the structural optimization capabilities of the model, a batch of operational points has been simulated, forcing different bending-torsion coupling effects. The wash-out effects presented in the literature have been evidenced to prevent stall flutter. Rotating the fibers, upwash reduces the angle of attack when the plunge is increased. For the geometry studied, a range of $[-44, -68]$ deg has been obtained as the more effective structure protection.

Regarding the modal contribution, the first mode dominates the displacement. Plunge and twist are contained in the same mode in contraposition to the isotropic material simulations. In addition, the second and third modes contribute to the velocity of the sections and, thus, to the aerodynamic damping. Therefore, only the first bending and the first torsion mode are required if the problem is reduced to an equivalent section. In the case of oblique fibers, both modes (plunge and twist) are contained in the first vibration mode, being only this mode necessary for reproducing the aeroelastic behavior of the beam. However, the effects of the velocity (secondary modes) would be canceled.

Summarizing, the benefits and limitations of the ANN-enhanced beam element ROM have been analyzed while solving the flat plate beam test bench. The methodology has proved to be a powerful tool in the predesign process. It allows us to determine an optimum structure and reduce the high-fidelity simulations required in the optimization process. Therefore, using the ROM helps decrease computational costs and speed up the design by orders of magnitude.

4.3.3 Orthotropic wind turbine blade.

The reduced order models have been tested for simple cases regarding squared beam structure deformation presented in Section 4.2.1. Nevertheless, the algorithm must be tested in a real engineering problem with complex geometry and structural properties. Due to the increasing importance of wind energy production and the large size and aspect ratio of the novel blade designs of wind turbines, a wind turbine geometry is selected to evaluate the solver.

This section focuses on presenting the aeroelastic behavior of the blade of the NREL Phase VI Rotor [44] using two different structural composite material layups. The comparison between a quasi-isotropic material and a purely orthotropic configuration is presented.

The section shows the capabilities of the ROM for predicting the nonlinear aeroelastic dynamic evolution of rotating lifting surfaces. In addition, the benefits of using an appropriate bending-torsion coupling are demonstrated.

Case of study

The NREL Phase VI Rotor blade geometry was selected due to the extensive data available in the literature. The geometrical characteristics of the rotor are presented in Table 4.7. The blade cross-section uses an S809 airfoil. From the structural perspective, the airfoil is divided into two cells internal cells divided by a vertical spar located in the mean chord, Figure 4.54.

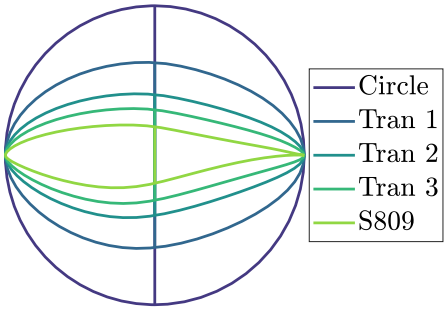

Fig. 4.54 **Transition of the unitary chord cross-section of the blade.** The figure shows the blade airfoil S809, the root circular cross-section and the transition airfoils.

Two different structural configurations are presented in the section. In both cases, the cross-section wall is a laminated layup of 8 plies, the six internal plies of unidirectional carbon fiber [36] and the external of quasi-isotropic glass fiber fabric [45]. For the first layup (Structure 1), a quasi-isotropic structure is created using orientations $(90/45/-45)_s$, while the external present a configuration $90/0$. For the second structure (Structure 2), the skin layup after the transition sections are modified, using a $(60)_6$ lamination for the internal carbon fiber plies, except for the spar, which maintains the previous layup. The composite material fibers are rotated backward on both blade surfaces in this configuration.

Table 4.7 **Geometrical distribution of the NREL Phase VI rotor blade.** r is the radial position of the section, c is the chord of the section, θ_g geometric torsion of the section, ξ nondimensional position of the geometric torsion axis (percentage of the chord).

r (m)	c (m)	θ_g (deg)	ξ (%)	Airfoil	r (m)	c (m)	θ_g (deg)	ξ (%)	Airfoil
0.00	0.22	0.0	50.0	Circ	2.56	0.61	-3.4	30.0	S809
0.51	0.22	0.0	50.0	Circ	2.87	0.57	-2.1	30.0	S809
0.66	0.22	0.0	50.0	Circ	3.17	0.54	-1.2	30.0	S809
0.88	0.18	0.0	50.0	Circ	3.19	0.54	-1.1	30.0	S809
1.01	0.35	-6.7	35.9	Tr1	3.48	0.51	-0.5	30.0	S809
1.07	0.44	-9.9	33.5	Tr2	3.78	0.48	0.0	30.0	S809
1.13	0.54	-13.4	31.9	Tr3	4.02	0.46	0.4	30.0	S809
1.26	0.74	-20.0	30.0	S809	4.09	0.45	0.5	30.0	S809
1.34	0.73	-18.1	30.0	S809	4.39	0.42	0.9	30.0	S809
1.51	0.71	-14.3	30.0	S809	4.70	0.39	1.4	30.0	S809
1.65	0.70	-11.9	30.0	S809	4.78	0.38	1.5	30.0	S809
1.95	0.67	-8.0	30.0	S809	5.00	0.36	1.8	30.0	S809
2.26	0.64	-5.3	30.0	S809	5.31	0.33	2.2	30.0	S809
2.34	0.63	-4.7	30.0	S809	5.53	0.31	2.5	30.0	S809

Table 4.8 **Composite material properties for the wind turbine blade.** Material properties of the carbon-fiber and the glass-fiber-reinforced polymer: E_l longitudinal elastic modulus, E_t transverse elastic modulus, G_{lt} longitudinal-transverse shear modulus, G_{tt} transverse-transverse shear modulus, ν_{lt} longitudinal-transverse Poisson's ratio, ν_{tt} transverse-transverse Poisson's ratio, h_{ply} ply thickness, ρ material density.

Material	E_l	E_t	G_{lt}	G_{tt}	ν_{lt}	ν_{tt}	h_{ply}	ρ
Units	(GPa)	(GPa)	(GPa)	(GPa)	(-)	(-)	(mm)	(kg/m^3)
CFRP	141.96	9.78	6.0	4.83	0.42	0.5	0.13	1445
GFRP	20.0	19.0	4.2	4.2	0.13	0.13	0.53	2540

Material properties are presented in Table 4.8. The previous material properties would correspond to a glass and carbon fiber volume fraction of approximately 27% and 63%, respectively, according to Vijcic and Dimic [46] and Singh et al. [47].

In addition, shell cross-section distortion is prevented by adding dense aluminum ribs at the root, the transitions and the tip and thin-walled ribs being located every 2% of the span, Figure 4.55.

The reference system of the wind turbine blade is presented in Figure 4.56. The figure defines the main displacements of the section: horizontal displacement u, vertical displacement v, and twist θ. Note that the directions of the angle of attack α and the twist θ are inverted. In the figure, the variables a and a' are the induced velocities, and r is the radial position.

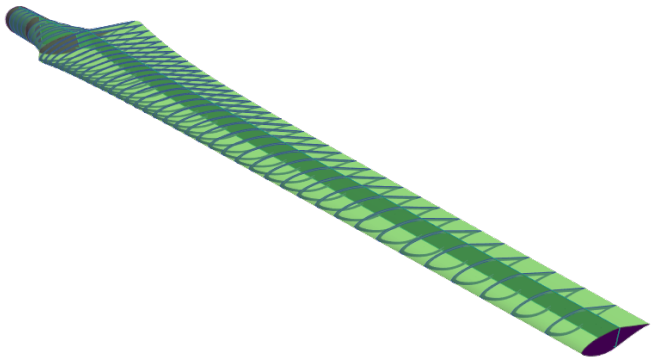

Fig. 4.55 **Geometry of the NREL Phase VI blade.** The figure shows the external geometry of the blade, and the internal elements, such as the main spar and the dense and thin-walled ribs

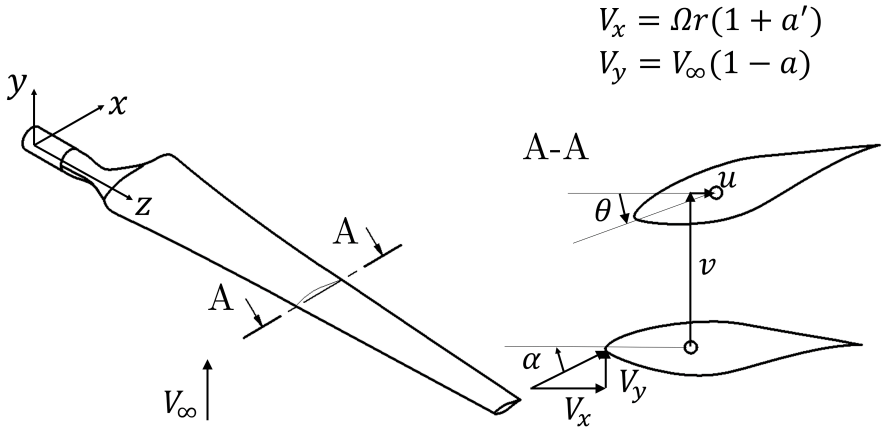

Fig. 4.56 **Blade reference system.** The global reference frame and the main displacements of the section are shown.

Computational solid dynamics

In order to validate the results of the ROM, an FEA of the blade is calculated. The FEM simulation was calculated using NASTRAN for a composite laminate shell mesh. The mesh was created using a final grid of $1.2 \cdot 10^4$ quadrilateral parabolic elements, which keeps the

discretization error below the acceptable accuracy value, Figure 4.57. The finite element mesh of the blade is shown in the figure. The details on the external shell, the ribs, and the spar are visualized in the figure. This mesh is used for simulating linear elastic analysis of the structure. The FEA is resolved for both steady deformation and vibration modes simulations.

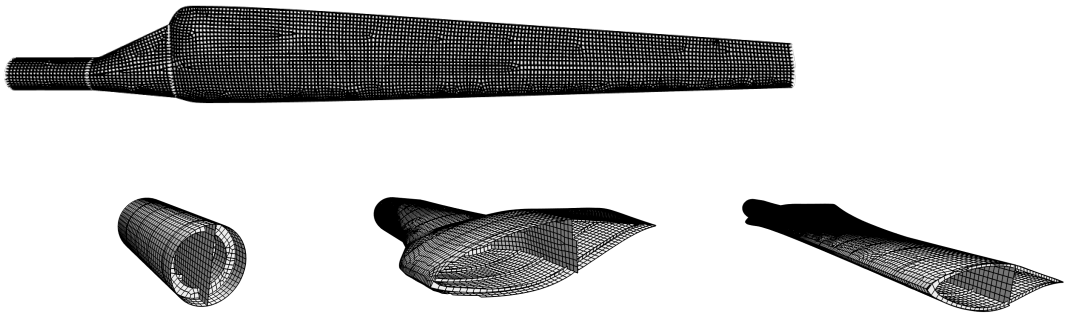

Fig. 4.57 **Mesh of the blade.** Detail of the cross-section for the cylindrical, transition, and S809 zones. Skin, spar, and dense and thin-walled ribs are included.

Computational fluid dynamics

A CFD simulation is run to validate the results of the Theodorsen transient aerodynamic coefficients. This simulation has been performed by calculating a pitching and plunging airfoil with the proprietary software Simcenter Star-CCM+. The mesh of the domain is made using an overset strategy and polygonal elements, Figure 4.58. The conservative equations of the fluid are computed by means of a coupled solver. The advection terms are solved with second order upwind ROE FDS scheme for the advection terms [21, 22]. A Gauss-Least Squares Method with the Venkatakrishnan limiter [23] is employed for computing the gradients.

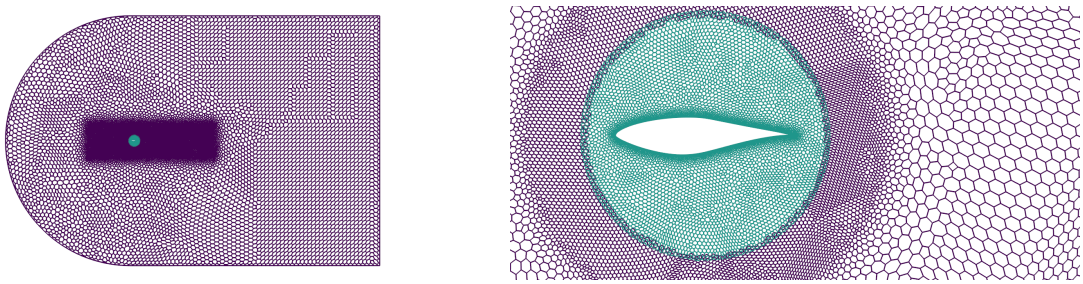

Fig. 4.58 **CFD mesh of the blade.** (Left) global mesh and (right) detail of the overset region.

Structure validation

As previously mentioned, the NASTRAN FEA simulation has been used to validate the ROM accuracy. The blade stiffness was compared to the FEM solution by analyzing the simulation results. Then, a modal analysis was employed to validate the vibration modes and the modal shapes.

The steady simulation was configured for testing the blade structural stiffness. A combination of forces and moments was applied to the blade tip, locating their center in the geometrical rotation axis. A vertical (F_y) and horizontal (F_x) forces of 100 N and a twisting moment (M_z) of 100 N m were applied to the structure. The deformation of the blade is visualized in Figure 4.59. The results evidence the high accuracy of the ROM with respect to the FEA model, been the displacement error of around 3% in the blade tip. Nevertheless, the FEA twist presents higher errors, such as the sawtooth behavior near the root.

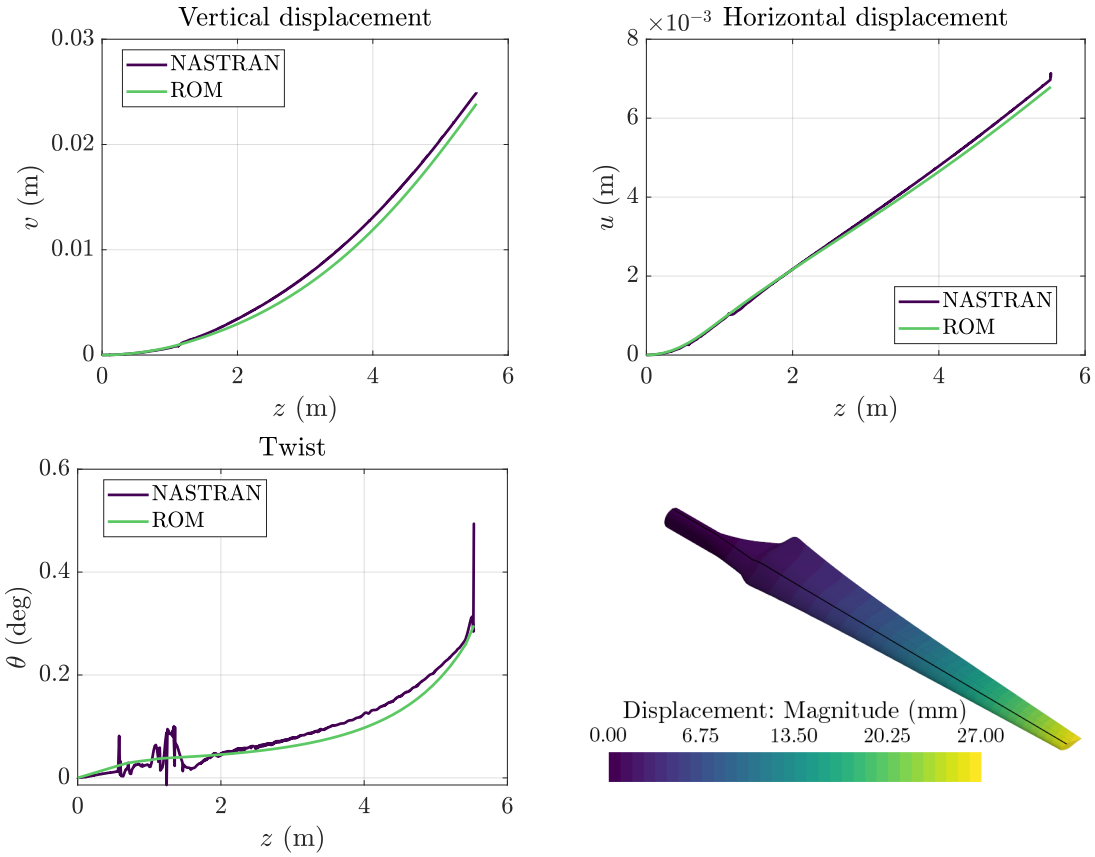

Fig. 4.59 **Deformation of the blade under static loads.** The external loads are: $F_y = 100$ N, $F_x = 100$ N, $M_z = 100$ N m. The longitudinal black line on the bottom-right image presents the geometrical center of rotation where the displacements are measured. In the Figure, v is the vertical displacement (top-left), u the horizontal displacement (top-right) and θ the twist (bottom-left) and the three-dimensional (bottom-right).

In addition, the validity of the ROM requires the one-dimensional beam behavior of the blade. The cross-section distortion of the blade is analyzed in Figure 4.60 by determining the rotation of the sell elements in the three axes. These shell effects are conditioning the rotation of the blade cross-section. The contours of the figure evidence the contribution of the internal ribs, which are restraining the rotation of the shell over them. Their presence allows them to maintain the 1D beam behavior, which is crucial for applying the beam element solver.

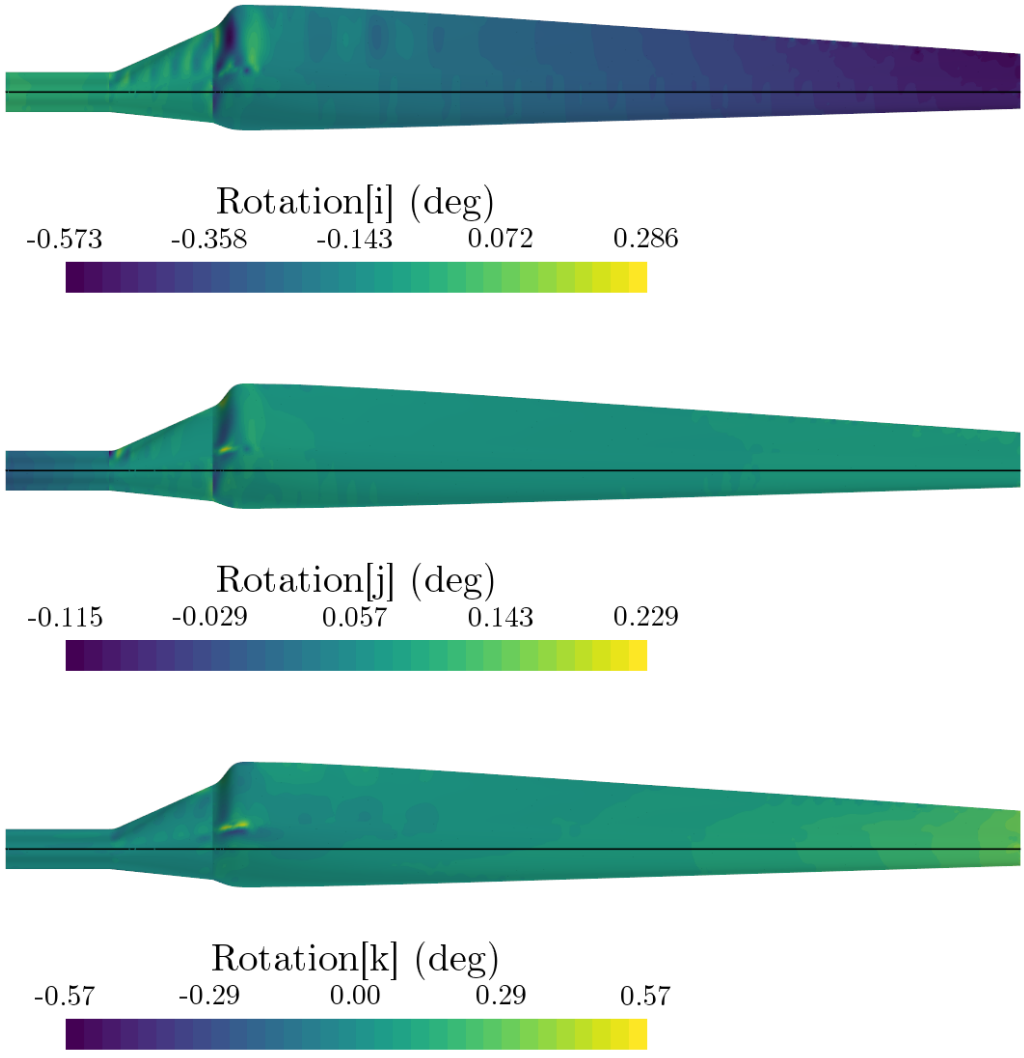

Fig. 4.60 **Rotation of the shell elements of the blade.** The geometrical rotation axis is marked over the surface. (Top) rotation in the x direction, (middle) rotation in the y direction and (bottom) rotation in the z direction.

Moreover, the vibration modes were analyzed in order to ensure the accurate dynamic modeling of the structure. The first four vibration modes of the blade are compared in Table 4.9. These modes are expected to be the most influential for the dynamic behavior of the blade. Both models agree with a maximum error of 9%. Therefore, the structural ROM can accurately reproduce both stiffness and mass properties and be used in the elastic analysis of the structure. The possibility of predicting the motion of the blade using a ROM also allows us to reduce the computational cost compared with a 3D finite element analysis.

Table 4.9 **Natural frequencies of the first four vibration modes.** The results show the comparison between the reduced order model and the finite elements analysis.

Solver	Mode 1 (Hz)	Mode 2 (Hz)	Mode 3 (Hz)	Mode 4 (Hz)
NASTRAN	4.647	6.504	21.494	48.951
ROM	4.456	6.430	19.794	48.067
Deviation (%)	4.11	1.15	8.82	1.81

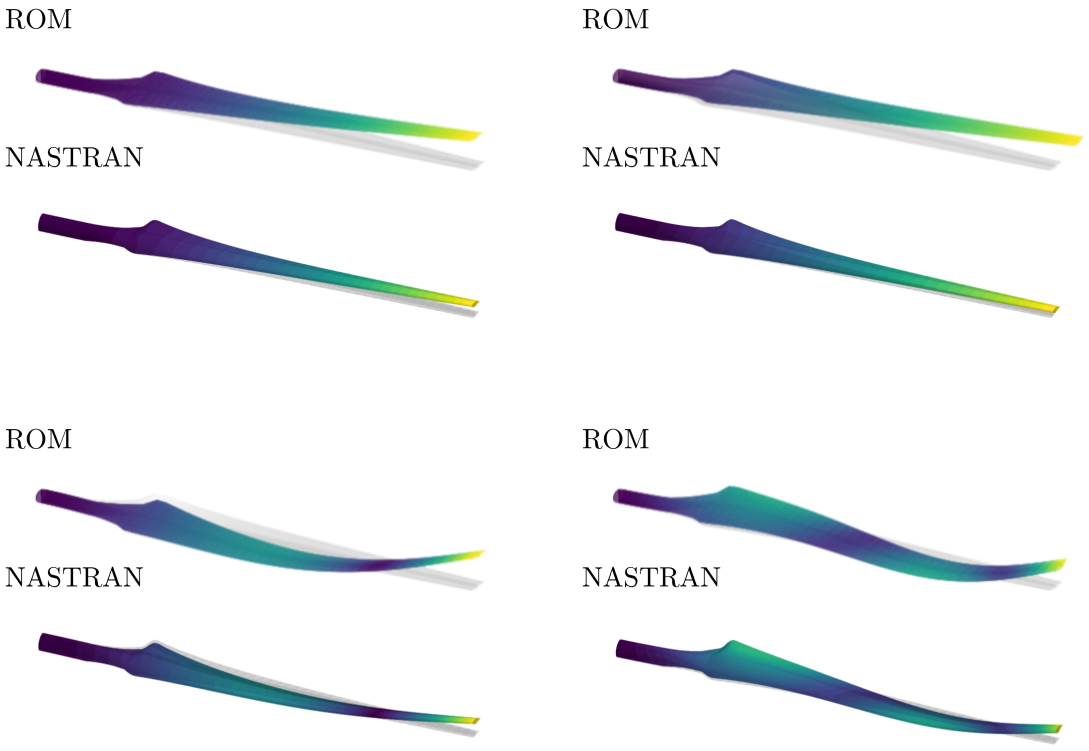

Fig. 4.61 **Vibration modes obtained from the 1D reduced order model.** (Top-left) mode 1, (top-right) mode 2, (bottom-left) mode 3 and (bottom-right) mode 4.

Additionally, Figure 4.61 displays the modal shape of the blade. Similar modal shapes are obtained for both methodologies: the ROM and NASTRAN models. This fact can be tested in the Modal Assurance Criterion (MAC) of Figure 4.62 [9]. In the figure, a higher correlation is presented for the darker colors, having the diagonal of the matrix values closer to the unity. Thus, both models correlate. Note that the problem is dominated by bending modes due to the high torsional stiffness of the multicell cross-sections. Nevertheless, modes 3 and 4 include bending-torsion couplings.

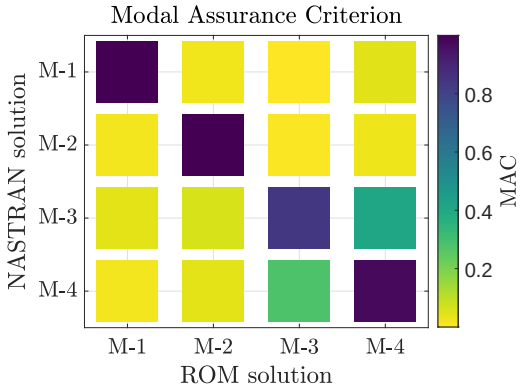

Fig. 4.62 **Modal Assurance Criterion.** Note that the darker colors are related to a higher correlation between the ROM and NASTRAN.

Validation of the wind turbine aerodynamic characteristics

The steady aerodynamic blade element momentum model for the wind turbine lifting surface was validated against the experimental data of Lee et al. [48] for a tip speed ratio of $\lambda = 6$, Figure 4.64 (left). The predicted force coefficient is slightly higher for the BEM model than for the literature data. Indeed, the power coefficient curves are compared in the right image of Figure 4.64 with the simulated and experimental data of Torregrosa et al. [49]. The figure shows a difference in the maximum power peak between the CFD results and the BEM calculations. According to Plaza et al. [50], the maximum power peak is obtained for lower values of the tip speed ratio in the BEM. In the figure, the BEM was demonstrated to overpredict the loads; this fact is consistent with the higher power obtained. Although there is a lack of accuracy when obtaining the power peak, the methodology reduces by orders of magnitude the computational cost. Therefore, it speeds up the initial stages of the aerodynamic design with acceptable accuracy in predicting the loads.

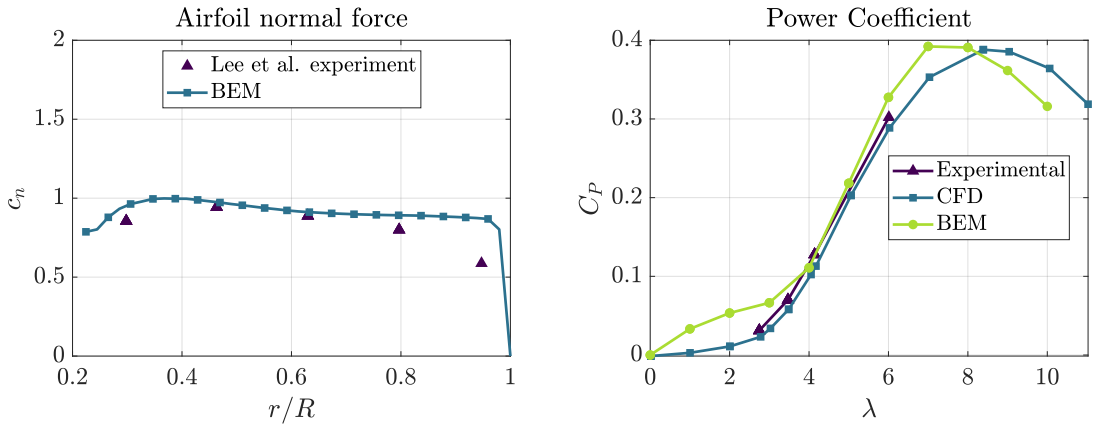

Fig. 4.63 **Aerodynamic validation of the BEM.** (Left) Normal force coefficient distribution for a wind velocity of 7 m/s and a rotation velocity of 73 rpm and (right) Validation of the blade element momentum theory with CFD and experimental data.

In addition, the transient loads calculated with Theodorsen's theory are compared to a pitching and plunging airfoil whose movement is described by Equation (4.11).

$$\theta(t) = \bar{\theta} + 2.5sin(20\pi t); \;\; v(t) = 0.01sin(8\pi t) \tag{4.11}$$

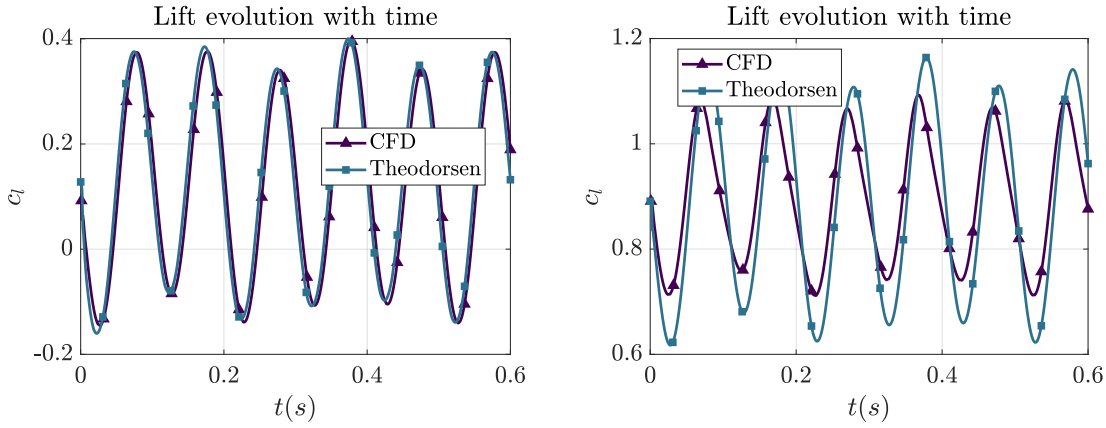

Fig. 4.64 **Aerodynamic validation of Theodorsen model.** (Left) Validation for mean incidence of 0 deg and (right) validation for mean incidence of 8 deg.

Figure 4.64 presents the lift coefficient calculated by the ROM and the CFD simulations. In the figure, two validation cases are visualized. The first simulation is performed for a low mean incidence, $\bar{\theta} = 0$ deg, while the second is calculated near the stall phenomena, $\bar{\theta} = 8$ deg. Note that the transient Theodorsen's model supposes an attached flow; for this reason, the accuracy of the solution is higher for low incidence angles, reducing its accuracy in the

point of maximum efficiency of the blade, approximately 8 deg of incidence. However, the models exhibit an efficient computational cost and low deviations from CFD simulations in the operating points. Thus, it is applied for calculating the transient effects of this work.

Elastic wind turbine solution: prediction of flutter speed

In order to calculate the aeroelastic dynamics of the blade, the structural beam momentum and the aerodynamic blade element method with Theodorsen's transient coefficients models were coupled. The structure deformation and the transient displacements were obtained for different operation points. The free stream and rotation velocities were modified in terms of the characteristic parameters of the simulations: tip speed ratio $\left(\lambda = \frac{\Omega R}{V_\infty}\right)$ and nondimensional elastic modulus $\left(E^* = \frac{E_l}{\frac{1}{2}\rho_\infty V_\infty^2\left(1+\lambda^2\right)}\right)$. The mean twist of the tip section is analyzed in the aeroelastically speaking stable operations. The stability of the simulations is limited by defining two consecutive intervals in the time evolution curve, Figure 4.65. Then the evolution of its amplitude is measured and analyzed. The range of the time intervals has been chosen to contain twice the first natural frequency, in other words, the main oscillation of the structure. In this figure, three different conditions are presented: damped, Figure 4.65 (left), limit cycle (middle), and unstable (right).

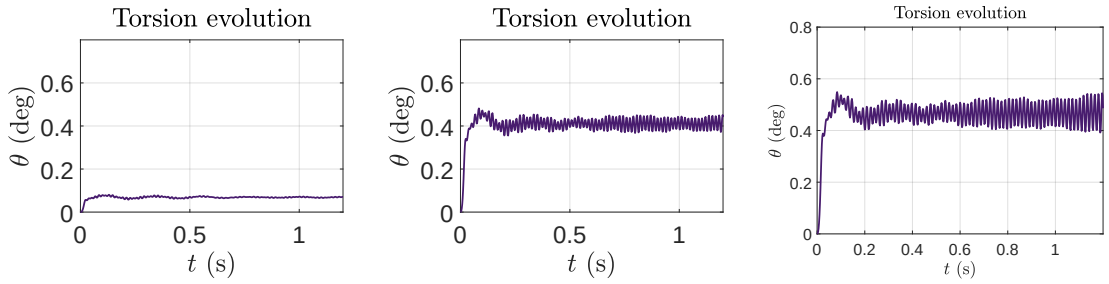

Fig. 4.65 **Torsion evolution for structure 1 under different operation points.** (Left) $\lambda = 7$, $E^* = 500$, (middle) $\lambda = 7$, $E^* = 80$ and (right) $\lambda = 7$, $E^* = 62$.

When the amplitude of the oscillations tends to increase with time, negative damping is detected, and the unstable condition is reached in the computed time signals. Figure 4.66 shows these limits for both layup configurations. In the figure, the aeroelastic limitations are improved for structure 2 in the range between $\lambda = 2$ and $\lambda = 7$ due to the bending-twisting coupling effect, which compensates for the unsteady aerodynamic loads.

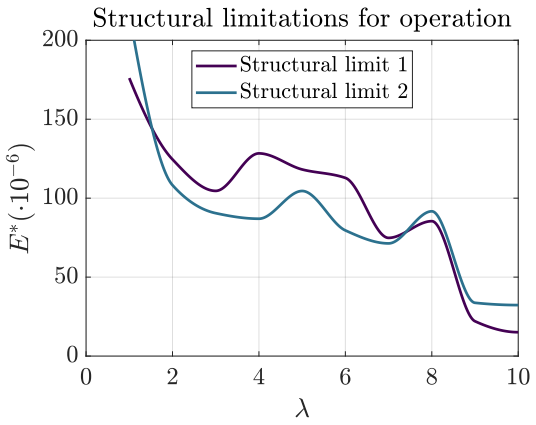

Fig. 4.66 **Limitations of the structure for nondimensional variables.** The limitations are presented for a quasi-isotropic material (structure 1) and an oblique fiber distribution (structure 2).

Wind turbine range of operation

In this subsection, the previous deformation results of Figure 4.66 are used for setting the limits in the operation curves of the turbine. Inside the stability limits, The mean values of the power coefficient are evaluated inside the stability limits of the structure. In the previous results, the reduction of nondimensional stiffness is not producing noticeable effects on the power generation, which is a function of the tip speed ratio, Figure 4.67. For this reason, in the operational analysis of the turbines, the generation of power is evaluated using the rigid rotor data using the elastic blade information for determining the operation limits of each structure.

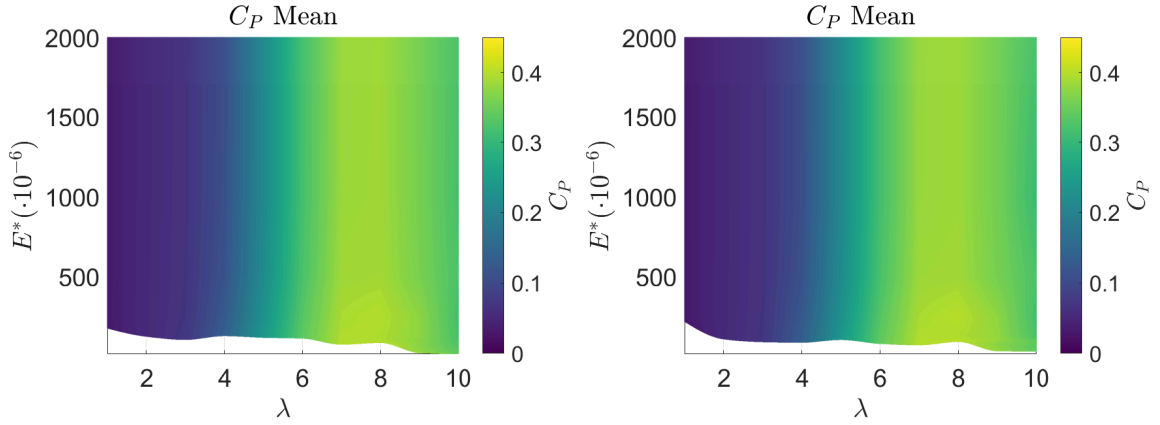

Fig. 4.67 **Mean value of the power coefficient of the structures for the different operation conditions.** (Left) structure 1 and (right) structure 2.

The following control law determines the operation of the wind turbines:

- The turbine can rotate at optimum tip speed ratio ($\lambda \approx 7$) until the maximum rotation velocity is reached. This maximum angular velocity is limited to generate the maximum power for the values of the wind velocity in which the power derivative remains low or null. Higher values of power could damage the electrical system. Accordingly, with the literature [44], the rated power of the turbine is 19.8 kW.

- Then, a maximum rotation velocity is maintained, forcing the rotor to operate out of the optimum performance point.

The power and rotational velocity curves are presented in Figure 4.68 together with the structural and electrical limitations.

The increased range of operation produced by the modified structure can be observed in Figure 4.68. Figure 4.68 (top-left) visualizes the control law in terms of the nondimensional variables. In this figure, the solid dark line represents the value of the dimensionless parameters. The direction of the arrowheads indicates the direction of increasing the wind velocity, following the control law of Figure 4.68 (top-right). The dashed lines mark the physical limitations established by the structure and the electrical generator of the wind turbine. The intersection between the solid and the dashed lines supposes the collapse of the structure. After these points, the deformation of the blade will be amplified with time.

According to the results, it is evidenced that rotating the fibers backward protects against the instabilities. The analysis of the capabilities of the system may be performed in dimensional terms. Figure 4.68 (bottom-left) presents the power generated by the rotor as a function of the wind velocity. This figure shows the benefits of a correct bending-torsion coupling. This coupling acts as a passive aeroelastic control, increasing the wind velocity of the structural limit with respect to the original structure. This oblique fiber structure is demonstrated to produce an improvement of approximately 10% in the maximum wind velocity of the system. The rotation of the fiber generates the phenomenon called wash-in, which is related to delaying the flutter effects of a lifting surface. In the present analysis, the wash-in provides better blade performance for the same structural weight (29.6 kg). In addition, the modified structure may be loaded with higher axial forces, Figure 4.68 (bottom-right); therefore, the tower and blades should also be calculated under these loads to prevent static failure.

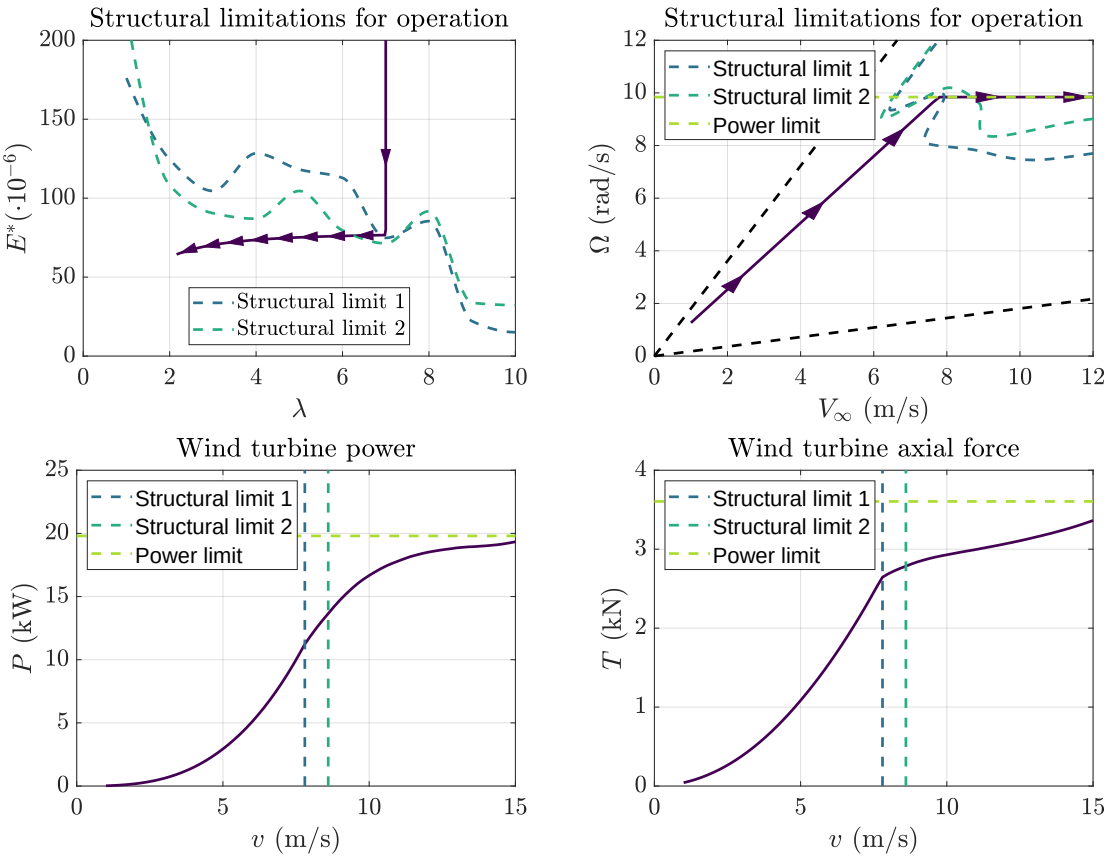

Fig. 4.68 **Operation curves of the wind turbine.** (Top-left) operation limits, (top-right) rotational velocity in the operations, (bottom-left) power in the operations and (bottom-right) axial force in the operations. The dashed lines represent the structural and electrical limitations of the system, whereas the solid curves represent the operation of the turbine.

Discussion

The current section analyzed the aeroelastic behavior of a carbon-fiber-reinforced polymer wind turbine blade. The results provided a general idea of the effects of fiber orientation influence and tested the calculation capabilities of the ROM in rotating aerodynamic problems. The structural integrity of the blade has been evaluated for two different layup configurations. The first configuration presented a quasi-isotropic layup. Then, the layup was modified, proposing a different fiber orientation for the second layup. In this case, a negative bending-torsion structural coupling was created by rotating the unidirectional fibers backward. This rotation is related to load alleviation as stated by Stanford et al. [42]. These results open the possibility of future work to evaluate the optimum layup configuration for a general wind turbine operation and validate the elastic results with high computational cost simulations or

experimental data. The main findings of the work are summarized in the following bullet points:

- The steady blade deformation of the blade was proven to predict with an error lower than 5% the steady deformation of the blades and with less than 9% the dynamic behavior through the vibration modes.
- Blade element momentum methodology and Theodorsen's theory provide accurate results with a low computational cost compared with experimental data and CFD simulations.
- The power coefficient has been demonstrated to depend exclusively on the tip speed ratio in the stable region.
- Flutter velocity has been calculated for two different layup configurations, showing the oblique fibers better limitations for the operating conditions. Indeed, the modified structure has been demonstrated to improve the maximum allowable wind velocity by 10% as a consequence of the structural coupling.

4.3.4 Flexible membrane semi-monocoque wing.

The interest in resistant membrane wings has been increasing in the last decades. This growth of interest is strongly connected with the development of civil and military micro air vehicles (MAVs) due to their capability of carrying video cameras and sensors in hazardous locations while being lightweight and easy to transport [51]. These aircraft operate in low Reynolds numbers, between 10^4 and 10^5. In these conditions, the airflow around the wing may detach and produce nonlinearities or stall for low angles of attack. Therefore, the MAV application requires using bio-inspired structures [52–54]. Flying animals, such as bats and insects, can maneuver in the air by morphing their wings to adapt to the flying conditions [55, 56]. These capabilities have attracted the attention of the MAV industry for the membrane wing [57–59].

Additionally, to the previous benefits of the membrane structures, their lightweight and safe operation in proximity to a human have spread their application in sailing and sports to manufacture aerodynamic surfaces or flexible kites [60, 61]. For instance, the yachts of America's Cup have replaced the traditional sails with membrane-resistant wings, achieving a higher lift-to-drag ratio [62]. As a drawback, the membrane-resistant wings present a higher weight than the traditional sails. Therefore, a semi-monocoque structure composed of a main spar, a set of battens, and a resistant membrane is widely used, similarly to the MAV industry [63]. The resistant membrane wings are lightweight compared to traditional wings

and are significantly susceptible to aerodynamic loads. The aeroelastic effects are critical, and the control of the yacht is dependent on the deformation of the structure [64].

Many researchers have extensively analyzed membrane-resistant wings. The study can be conducted employing experimental campaigns or fluid-structure interaction simulations. Regarding the former, Stanford et al. [65] performed a set of experiments to investigate the aeroelastic behavior of a MAV wing. Similar studies have been applied to sails and yacht wings [66, 67]. Concerning the numerical simulations, authors like Scott et al. [68] have used the FEA to calculate a flexible membrane's structural response. Furthermore, the coupled fluid-structure simulation has also been calculated for the resistant membrane [69]. This section focuses on applying the beam element-based ROM to the resistant membrane wing problem. The results are compared with the three-dimensional fully coupled simulations, accurately predicting the aeroelastic instabilities while reducing the computational cost by orders of magnitude.

Case of study

In this section, a semi-monocoque wing is analyzed. The internal structure of the wing is composed of a C-shape cross-section main spar, a set of nine internal battens, and the external membrane skin. Figure 4.69 presents the layout of the wing structure. Regarding the structure dimensions, the wing presents a chord, c, of 100 mm and a span, $b = 3.98c$. The batten thickness, $t_b = 0.03c$ and the distance between them $d_b = 0.464c$, the spar external diameter $d_s = 0.06c$ and its thickness $t_s = 0.005c$. Concerning the cross-section of the wing, a triangular airfoil is used.

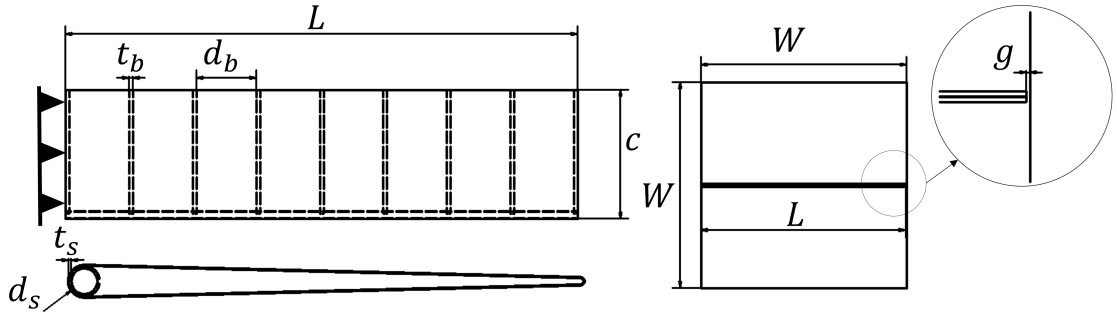

Fig. 4.69 **Membrane resistant structure.** Wing (left-up) and cross-section (left-down) layout composed of the C-shaped spar, the battens, and the membrane. Wind tunnel cross-section (right).

The wing is fixed by one of its ends, as Figure 4.69 indicates. The fixed end restricts the displacements and rotations of the structure, while the other end is allowed to move freely. In addition, a perfect rigid contact is assumed for the connections between the internal elements. The elements are bonded, and no relative displacement between them is allowed.

In addition, the case study is a benchmark for validating the capabilities of the ROM. Therefore, the simulations are calculated for a wing immersed in a wind tunnel, Figure 4.69, so the results could be compared with experimental data in the future. The wind tunnel cross-section presents a square shape of side $W = 4c$. Due to the small size of the wind tunnel with respect to the wing, a gap $g = 0.02c$ is generated in the wing tip. This gap could be observed in the detail of Figure 4.69.

The airflow is modeled incompressible due to the low free stream velocity. A density of $1.225\ \mathrm{kg/m^3}$ and dynamic viscosity $1.74 \cdot 10^{-5}\ \mathrm{Ns/m^2}$ are assumed. The velocity of the free stream is modified in the range from 5 to 25 $\mathrm{m/s}$. Finally, the solid mechanical properties are presented in Table 4.10 for the different materials.

Table 4.10 **Material properties of the membrane wing structure.** The table shows the materials of the different elements of the wing.

Element	Material	Elastic modulus (MPa)	Shear modulus (MPa)	Density ($\mathrm{kg/m^3}$)
Spar	Aluminum	71000	27000	2770
Membrane	Latex rubber	2	0.75	1000
Battens	PMMA	2690	964	1180

Coupling simulation of the resistant membrane wing

The coupled aeroelastic simulations were calculated using a procedure similar to the previous sections. The proprietary software Simcenter STAR-CCM+ version 17.06.007-R8 was employed for the three-dimensional simulations. A polyhedral mesh of 10.9M cells was created to discretize the domain. The numerical accuracy of the previous grid was determined by a mesh independence analysis, ensuring that the computational deviation was lower than 5% compared to a finer mesh. The details of the mesh refinements on the fluid and the solid are visualized in Figure 4.70.

The flow was solved using the Unsteady Reynolds Average Navier-Stokes equations with a $k-\omega$ SST turbulence model. This model was selected due to its applicability under adverse pressure gradients and high incidences. The advection terms are resolved with SIMPLE and

PISO segregated schemes for the steady and transient simulations, Figure 3.5. The gradients are computed using a Gauss-Least Squares Method with Venkatakrishnan limiter.

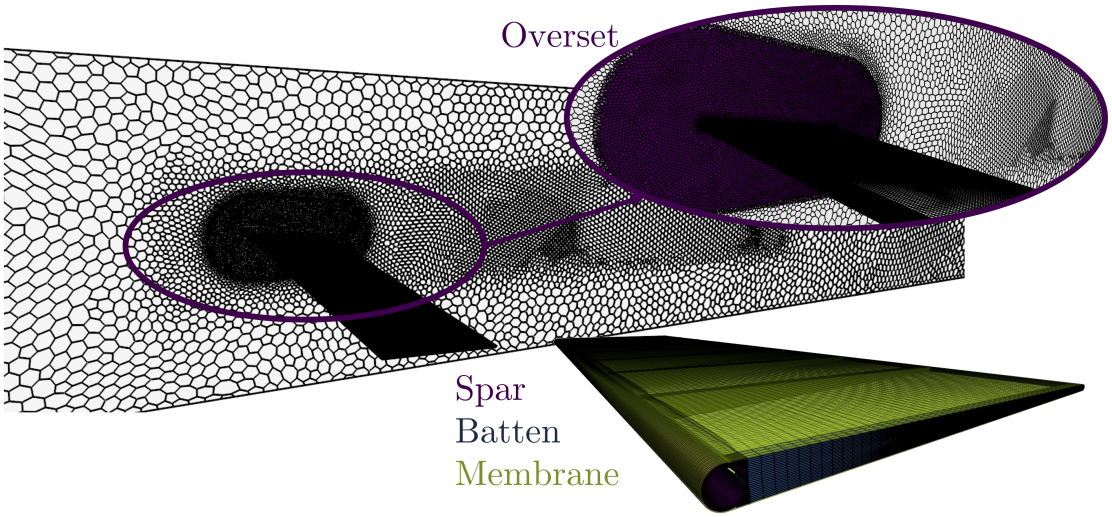

Fig. 4.70 **Mesh of the membrane resistant wing simulation.** Fluid mesh (left), detail of the overset mesh (right-top) and structure mesh (right-bottom).

The structural mesh is composed of a total of 560,000 hexahedral elements, Figure 4.70. The number of grid points is determined to limit the error to 3.6% in a twist. The elastic equations are also solved using Simcenter STAR-CCM+ version 17.06.007-R8. A MUMPS sparse solver was used for calculating the solid [70]. The contact between the elements is a surface-to-surface contact interface with bonded restriction. The spar and batten material is considered an elastic solid. Nevertheless, the membrane is modeled using nonlinear geometric properties. The stiffness and mass matrices of the membrane must be recomputed at every time step due to its low thickness and elastic modulus. Considering the membrane, a linear elastic solid results in unrealistic deformations. Finally, in order to stiffen the skin of the wing, an analysis of adding prestress on the membrane was also performed. The structure includes the prestress by applying a thermal deformation (contraction) in the membrane. Therefore, a thermal displacement model was also included in the simulation.

The solid and the fluid are coupled through a mapped contact interface. The aerodynamic loads are interpolated in the membrane surface. The pressure and viscous stresses are applied to the wing surface, generating a displacement of the structure and then morphing the fluid domain. The overset methodology, Figure 4.70, was applied to the problem to reduce the computational cost of morphing the whole mesh at high deformations. The mesh is morphed from the initial position in each iteration, allowing repeatable meshes in oscillatory

movements. The interfaces of the contact are recomputed at every time step. A time step sensibility analysis determines the maximum time step and the minimum number of internal iterations that maximize the computational accuracy. A resulting time step of $5 \cdot 10^{-4}$ s with a second order implicit solver was used in the time integration in combination with three internal iterations, which ensure similar results than five or ten with a high reduction of the computational cost.

Aeroelastic reduced order model

The main objective of the section is to prove the accuracy of the reduced-order model for predicting the aeroelastic phenomena of a membrane-resistant wing. The simplified solver based on the beam element model was applied to the problem to reduce its computational costs.

The membrane-resistant structure is configured in the ROM by defining a single beam that contains the spar and the membrane. Then, the effect of the battens is taken into account in the simulation by applying a rib boundary condition. The boundary condition limits the twist derivative to null values in the positions of the battens.

For the aerodynamic forces, the nonlinear steady model interpolated from a CFD bi-dimensional polar and the transient aerodynamic coefficients calculated by Theodorsen's theory are applied to the problem. Figure 4.71 presents the steady bi-dimensional aerodynamic CFD polar. The tip vortex and three-dimensional effects were considered using an infinite wing model and a nonlinear lifting line theory.

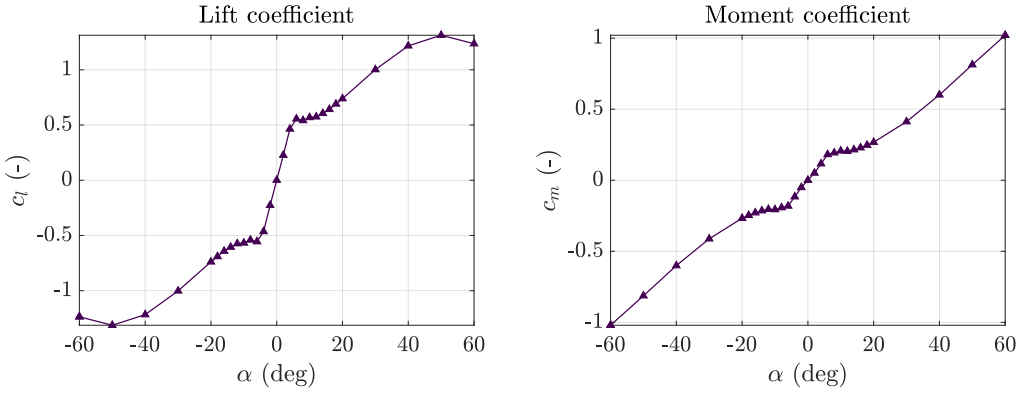

Fig. 4.71 **Bi-dimensional polar of the triangular cross-section.** Lift coefficient (left) and pitching moment coefficient (right).

Note that although the ROM can provide a computationally efficient alternative for calculating the aeroelastic behavior of the whole structure, it cannot predict the distortion of the membrane.

Validation of the aeroelastic ROM

Verifying the accuracy of the reduced order model requires ensuring the precision of the models isolatedly. Firstly, the structural model was validated. In order to perform the validation, the results are compared with the FEM simulations calculated with SimCenter STAR-CCM+. A vertical load of 1 N is applied in the trailing edge of the wing tip. Plunge and twist were calculated along the beam. Figure 4.72 presents the distribution of the previous displacements. The structural model shows high accuracy for the bending and torsion effects with an error of approximately 1% and 2%, respectively. Note that higher deviations are obtained for the twist while the bending solution is perfectly reproduced. The effect of the battens is also reproduced in the ROM; see the waves on the twisting curves. These waves result from the boundary conditions, which limit the twist of the beam, as calculated in the FEA simulations.

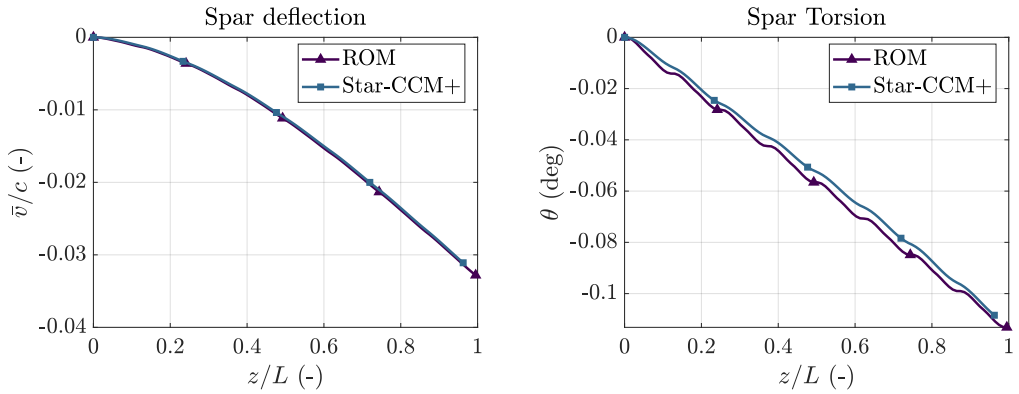

Fig. 4.72 **Comparison of ROM and FSI simulations for the resistant membrane wing.** The results are calculated for a vertical load of 1 N located in the trailing edge tip section. The vertical displacement is shown in the left image, while the twist is exhibited in the right.

In addition, the aerodynamic forces of the rigid beam are compared with the CFD steady simulations of the wing to validate the aerodynamic model. The results of the analysis are presented in Table 4.11. The comparison between the models evidences that the infinite wing model tends to overpredict the aerodynamic loads with an approximate error of 10% while the LLT tends to underpredict them with an error of around 20%. A small gap between the wing and the tunnel walls generates three-dimensional effects. However, the tip vortex presents lower intensity than the finite wing calculated by LLT and only affects the last sections of the wing, remaining almost constant in the load distribution. Figure 4.73 shows the lift and moment distribution for the CFD and the ROM models. The curves show the necessity of determining an aerodynamic model to address the small-gap effects. Moreover, modifying the models needs to correct the lift and moment differently, as the moment is

more affected by the previous tip effects. In order to address the previous problems, the aerodynamic coefficients were corrected by reducing the moment coefficient and the lift coefficient value by 10%, as illustrated in Figure 4.73. These results were obtained using the last correction for the three-dimensional aerodynamic effects and present an error of around 5% of the simulated three-dimensional wing.

Table 4.11 **Aerodynamic coefficients of the different models.** The table compares the global coefficients of the lift and moment for the CFD and ROM models.

Model	C_L	C_M	ε_{C_L} (%)	ε_{C_M} (%)
CFD	0.4307	0.1002	-	-
Infinite Wing	0.4651	0.1166	8.0	16.4
LLT	0.3860	0.090	10.4	10.2

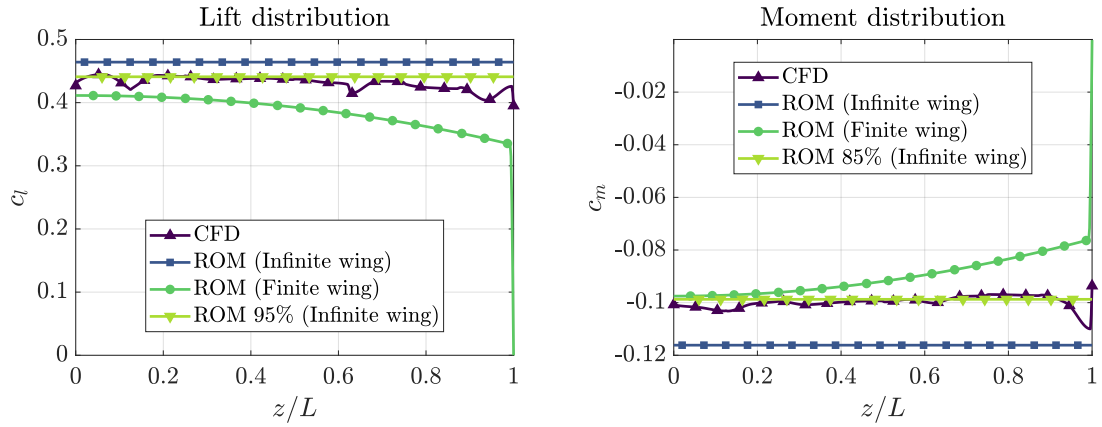

Fig. 4.73 **Load distribution on the wing.** Lift coefficient (left) and pitching moment coefficient (right).

Aeroelastic coupling validation of the ROM

The dynamic aeroelastic simulations are performed using the CSD/CFD solvers and the reduced-order models. Initially, the aeroelastic behavior of the system is estimated by determining the eigenvalues of the linear system. The results of the aeroelastic eigenvalues calculated by the ROM are presented in Figure 4.74. This figure presents the evolution of the first six vibration modes as a function of the free stream velocity. The instability is determined to appear around 15 m/s when the real part of mode six becomes positive. In addition, modes three and four present a low damping in the whole velocity range and are

minimally influenced by the aerodynamic loads. However, as the magnitude of their real part is negligible, the modes are expected to be damped in the transient simulations.

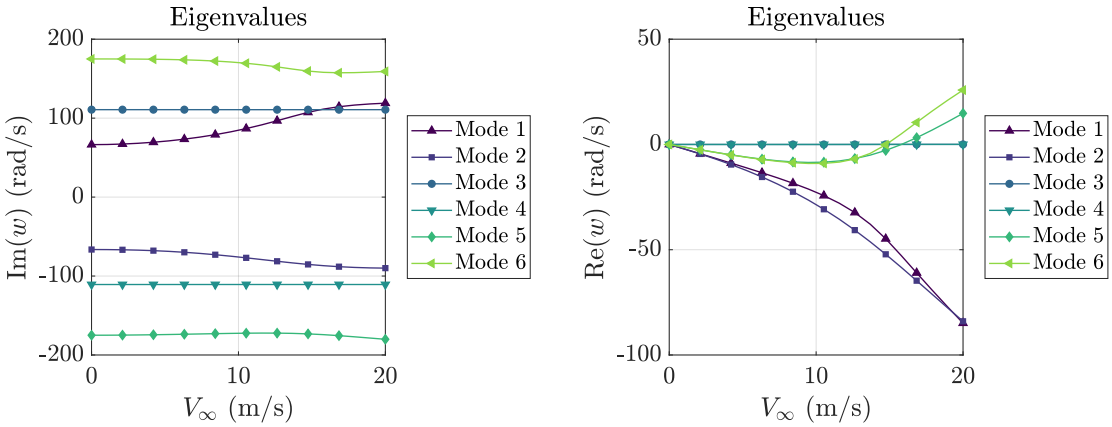

Fig. 4.74 **Aeroelastic eigenvalues of the ROM for the membrane-resistant wing.** (Left) imaginary part of the modes and (right) real part of the modes

The modal information of the last figure is complemented in Figure 4.75, where the modal shape of the first six modes after the instability are shown, for a velocity of 19 m/s. Note that modes five and six exhibit a combination of bending and torsion deformations. These modes generate instability. Regarding the critical stability modes, the shapes can clearly be related to bending, modes three and four, while a mixture between bending and torsion dominates the first two modes. Although the first modes are expected to dominate the problem, the instability is produced for higher-order modes, evidencing the necessity of taking them into account. This fact evidences the limitations of the equivalent section models, which can only take into account a mode per degree of freedom.

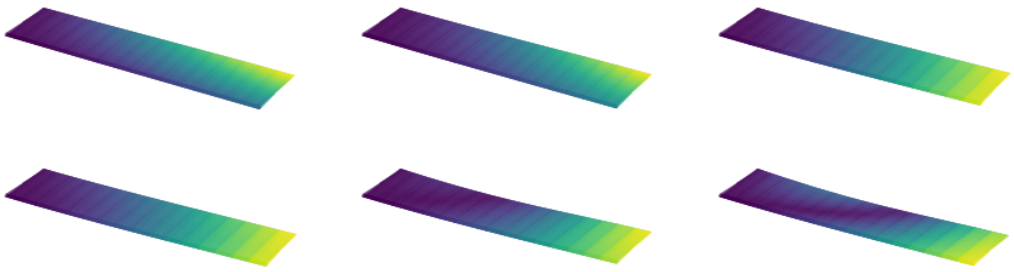

Fig. 4.75 **Modal shape of the modes after instability.** The figure shows the first six vibration modes for a velocity of $V_\infty = 19$ m/s. (Top-left) mode 1, (top-center) mode 2, (top-right) mode 3, (bottom-left) mode 4, (bottom-center) mode 5 and (bottom-right) mode 6.

After the eigenvalues were used for estimating the instability velocities, the ROM and FSI solvers were used for calculating the dynamic behavior of the wing without prestress for a range of velocities between 0 and 25 m/s. Initially, the ROM solver was evaluated to obtain a low-cost estimation of the dynamic aeroelastic behavior of the wing. The deformation of the wing was calculated with the transient ROM. The transient evolution of the plunge and the twist of the tip cross-section of the wing is shown in Figure 4.76. An important fact extracted from the figure is the higher value of the instability velocity compared with the linear eigensystem, around 18 m/s. The difference is a consequence of the nonlinearities in the aerodynamic model included in the transient simulations.

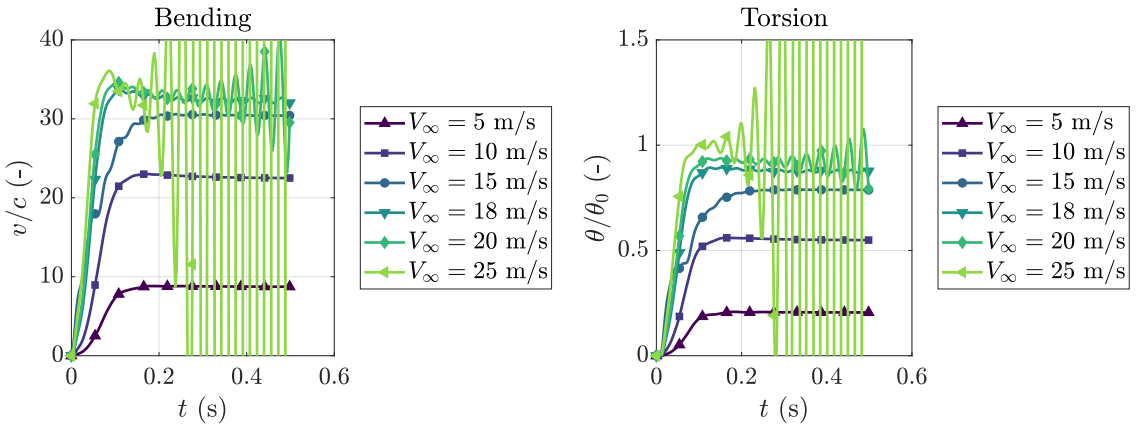

Fig. 4.76 **ROM deformation evolution of the sail.** (Left) bending evolution and (right) torsion evolution of the membrane wing.

Then, the coupled FSI simulation was calculated using the CSD/CFD solver. The results of bending and twisting are presented in Figure 4.77. This model can include the three-dimensional aerodynamic effects and the shell deformation of the membrane. The deformation of the external membrane of the wing can be observed in Figure 4.78 for a stable condition and the LCO. The membrane visualization shows more significant deformations far from the battens in both cases, presenting a nonlinear behavior. In addition, higher deformations are presented near the wing tips. In this simulation, as in the transient ROM calculations, the LCO is reached for a velocity of approximately 18 m/s, Figure 4.77. The structures start to flutter for higher free stream velocities due to the instability; the coupled bending and torsion deformations increase their amplitude as the motion evolves. Both models agree, predicting a flutter velocity higher than the eigensystem. In this case, similar reasons produce the deviation in the unstable velocity. Indeed, neglecting nonlinearities is the principal source of error in the eigensystem.

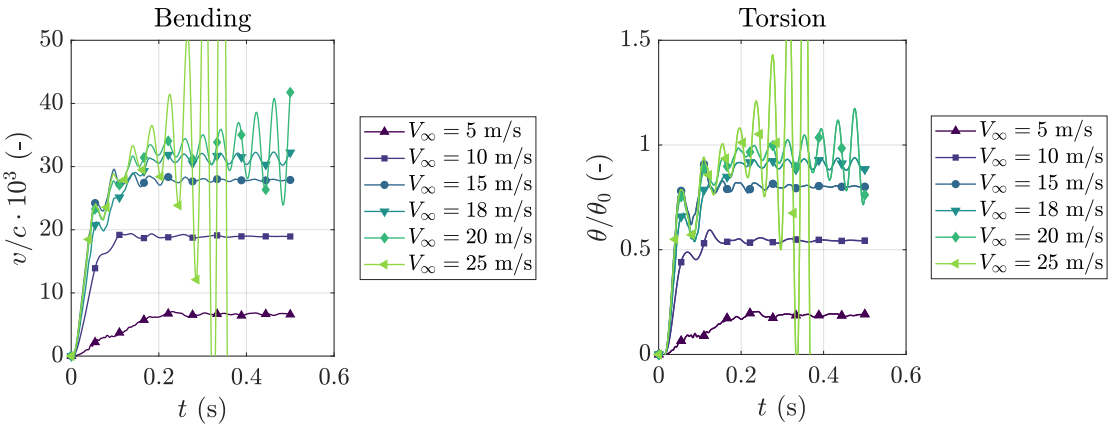

Fig. 4.77 **FSI deformation evolution of the wing.** (Left) vertical displacement and (right) torsion of the beam.

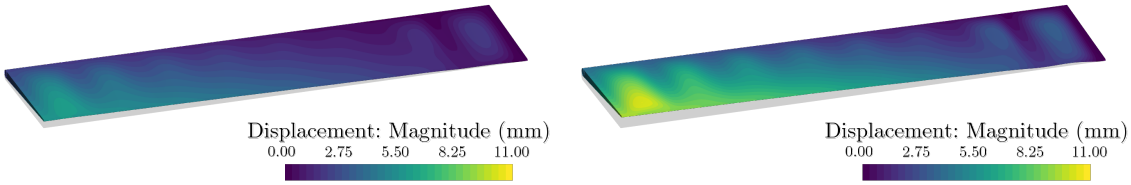

Fig. 4.78 **FSI displacement of the wing.**(Left) preflutter, $V_\infty = 10$ m/s, and (right) LCO conditions, $V_\infty = 18$ m/s.

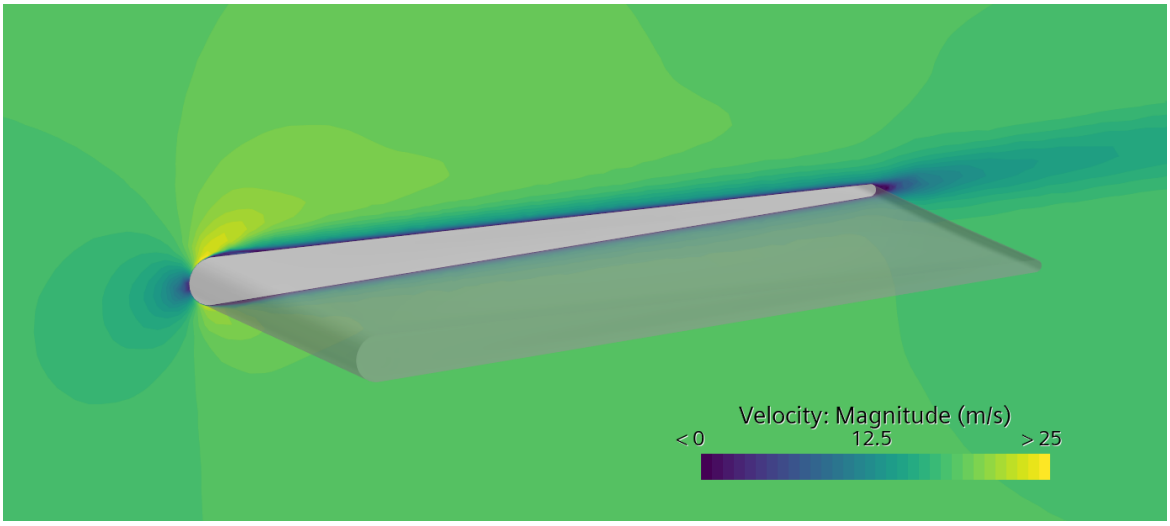

Fig. 4.79 **Detail of the flow around the deformed structure.** Note the increase in the boundary layer after the circular surface.

As previously stated, the discrepancy between the flutter velocity obtained by the eigenvalue identification and the transient simulations can be attributed to the use of linear aerodynamic coefficients in the eigensystem. This assumption is inaccurate for the triangular cross-section of the membrane, as shown in Figure 4.79. This figure illustrates the velocity field around the deformed membrane wing. Note the increase in the thickness of the boundary layer after the circular surface. This effect lowers the stall velocity and, thus, contributes to the onset of nonlinearities in the aerodynamic coefficients.

A nonlinear behavior is presented on the membrane as it stiffens at the same time that it is deforming. As a consequence of this deformation, the cross-section shape is modified. The ROM cannot account for this effect. Therefore, the membrane had to be simplified as a linear shell that strains coupled to the spar. The membrane distortion is shown in Figure 4.80. A maximum deformation of approximately 3% of the cross-section chord can be obtained between the battens.

Moreover, the aerodynamic effects derived from morphing the external shape of the wing cannot be included in the ROM. Figure 4.81 (left) shows the shear wall stress lines over the wing walls. These lines define the direction of the air over the surface. The membrane distortion produces a modification on the streamlines far from the battens, affecting the aerodynamic loads on these sections. Nevertheless, despite its limitations, the ROM was demonstrated to accurately predict the flutter velocity with a noticeable lowering in the computational cost, being a powerful tool for structural design.

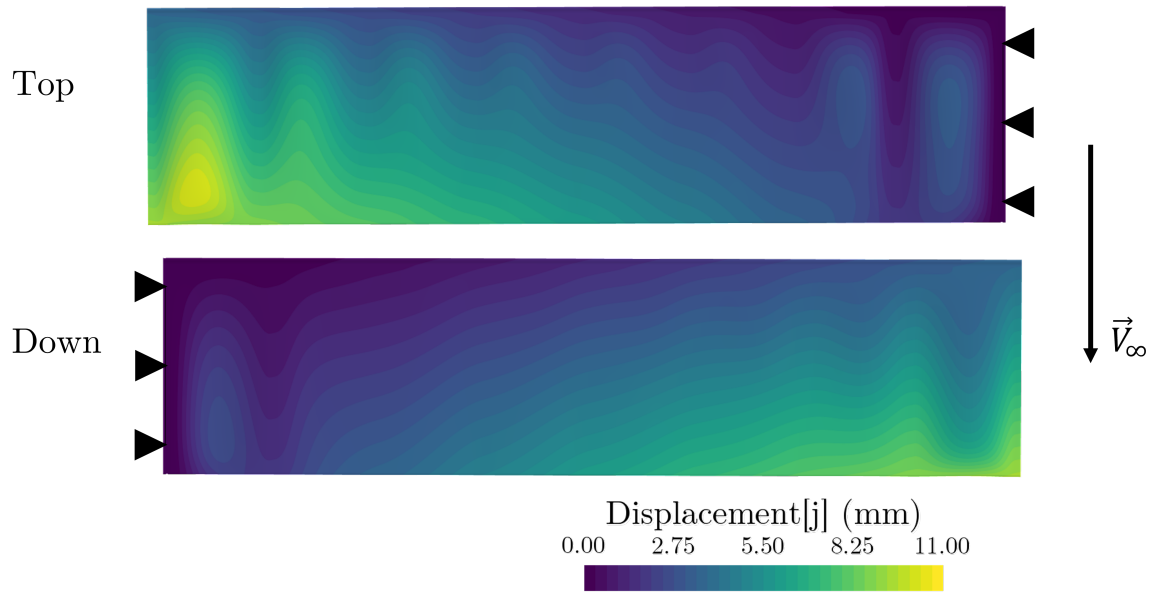

Fig. 4.80 **Vertical displacement of the external membrane.** Displacement calculated for a free stream velocity of 18 m/s.

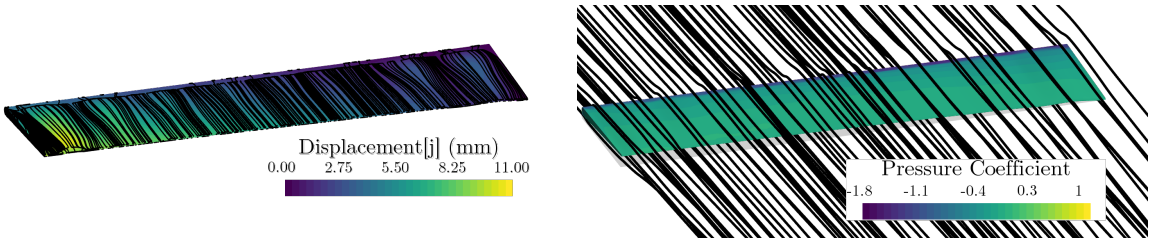

Fig. 4.81 **Visualization of the three-dimensional aerodynamic effects of the flexible membrane wing.** (Left) distortion of the flow over the wing surface due to the membrane deformation and (right) tip vortex effects of the wing.

Finally, the ROM cannot take into account either the tip vortex appearing in the wing or the effects of the walls. As shown in Figure 4.81 (right), a pressure loss is generated in the small gap between the wing and the wall. This pressure loss leads to a reduction in the wing-tip vortex intensity. Due to the previous effect, the aerodynamic coefficient is closer to the infinite wing multiplied by some corrective factor. Although membrane distortion and the tip effects influence the streamlines, the figure reveals that almost infinite wing aerodynamics can still be observed. Therefore, the adequacy of a corrected infinite wing model was demonstrated.

Effects of the prestress

In addition to the previous aeroelastic analysis, the effects of stiffening the membrane by applying prestress loads are presented in this section. Three different prestress configurations are studied in the analysis: 0%, 0.05%, and 0.1% of material deformation. As previously mentioned, the deformation of the membrane is defined as a volumetric thermal contraction. The temperature variation generating the contraction is calculated in Equation (4.12).

$$\Delta T_{\text{ps}} = \frac{\varepsilon_0}{\alpha_{\text{thex}}} \tag{4.12}$$

A homogeneous deformation is obtained on the material using the previous thermal contraction. Figure 4.82 presents the resulting initial deformation of the membrane after applying the previous prestress conditions. In this figure, the distortion increases with the contraction of the membrane. Two effects are observed on the wing external surface. First, the membrane is less sensitive to aerodynamic loads. The prestress adds internal contraction forces that reduce the aeroelastic effects, stiffening the material. Then, the aerodynamic loads are modified due to the initial deformations and the lower distortion generated by the aerodynamic forces.

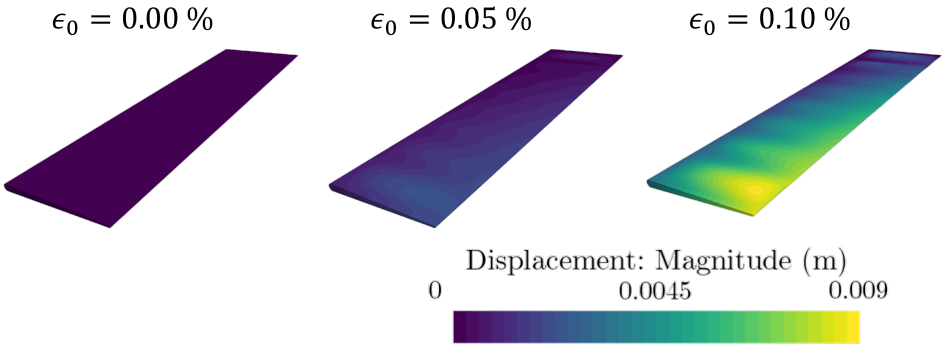

Fig. 4.82 **Residual displacement of the prestress.** Displacement of the structure generated by an initial prestress of 0.00%, 0.05% and 0.10%.

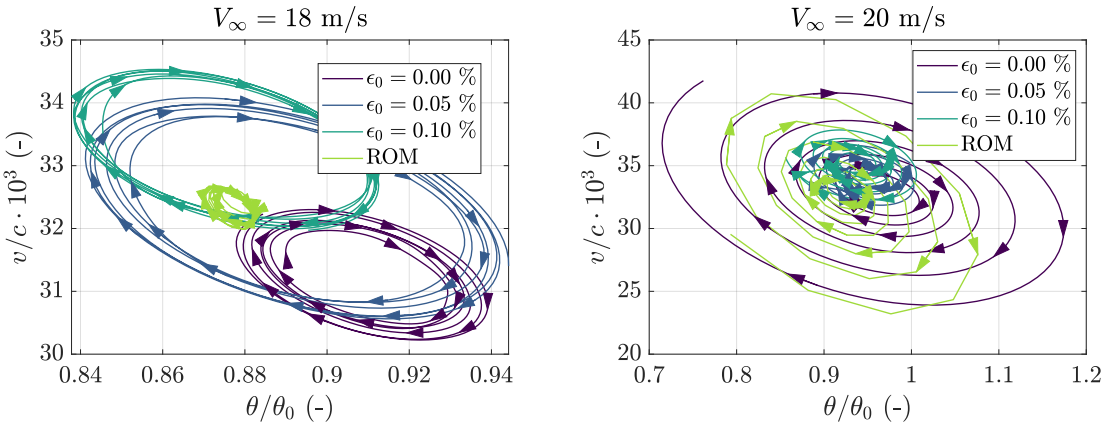

Fig. 4.83 **Evolution of plunge-twits with time for the prestressed membrane.** (Left) LCO conditions, $V_\infty = 18$ m/s, and (right) post-flutter conditions, $V_\infty = 20$ m/s.

The solutions of the different cases of prestressed structures are compared. Figure 4.83 shows the plunge-twist evolution of the structure for the limit cycle oscillation conditions, $V_\infty = 18$ m/s, and post-flutter conditions, $V_\infty = 20$ m/s. The mean torsion of the resistant membrane wing is demonstrated to remain lower for higher prestress conditions. Nevertheless, higher prestress increases the plunge motion. The membrane generates higher lift coefficients in the case of higher prestress due to the membrane distortion and higher stiffness, Figure 4.84. In addition, in the LCO conditions, the motion presents slightly higher amplitudes for a value of prestress of $\varepsilon_0 = 0.05$ %. Furthermore, the amplitude of its lift coefficient is also higher. Moreover, the prestress of the membrane is demonstrated to improve the flutter velocity compared with the non prestressed structure 4.83 (right).

Regarding the applicability of the ROM, the simulation results can reproduce the instability appropriately. In the case of the ROM, the whole membrane cross-section is considered rigid. For this reason, the section acts closer to a prestressed membrane but with a different initial geometry. Nevertheless, in the ROM, the aerodynamic coefficients tend to dampen the amplitude; consequently, the amplitude of the LCO remains lower than for the FSI simulations.

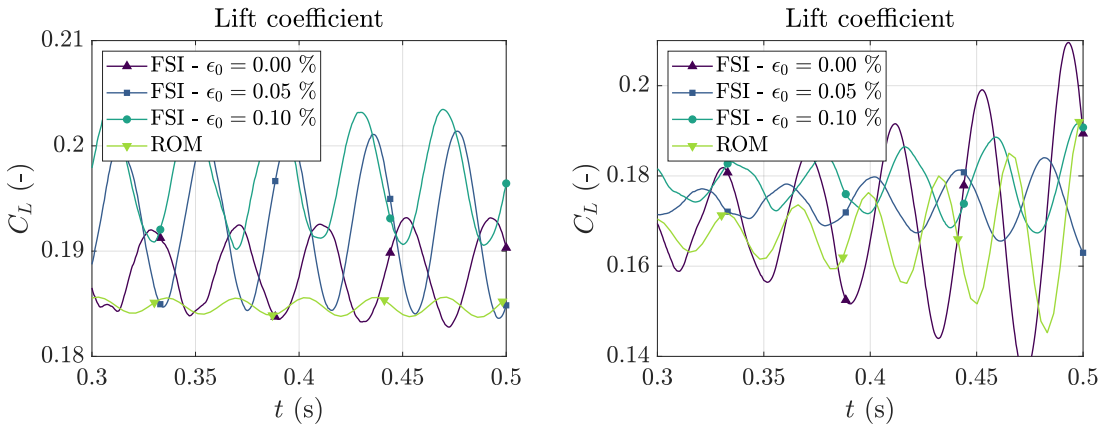

Fig. 4.84 **Transient evolution of the lift coefficient for the prestressed membrane.** (Left) LCO conditions, $V_\infty = 18$ m/s, and (right) post-flutter conditions, $V_\infty = 20$ m/s.

Regarding the mean displacements of the tip section of the structure, Figure 4.85 presents the mean plunge and twist time evolution. A progressive increase of the mean deformation value is observed with the velocity until reaching the instability velocity. The reduced order model yields a satisfactory agreement in the mean structure deformation compared to the three-dimensional simulations of the CSD/CFD methodology. Thus, the ROM is a powerful tool when optimizing the initial designs of the membrane-resistant wing. The instability can be visualized by analyzing the motion amplitude. Figure 4.86 shows the amplitude as a function of the free stream velocity. In the figure, the instability can be determined as the point ins in which the plunge and twist amplitude increase dramatically. The point at which the amplitude remains finite but cannot be damped is the so-called LCO. The results show that ROM accurately captures the instabilities. Therefore, its relevance in the design process, even for prestressed membranes, has been demonstrated in this section.

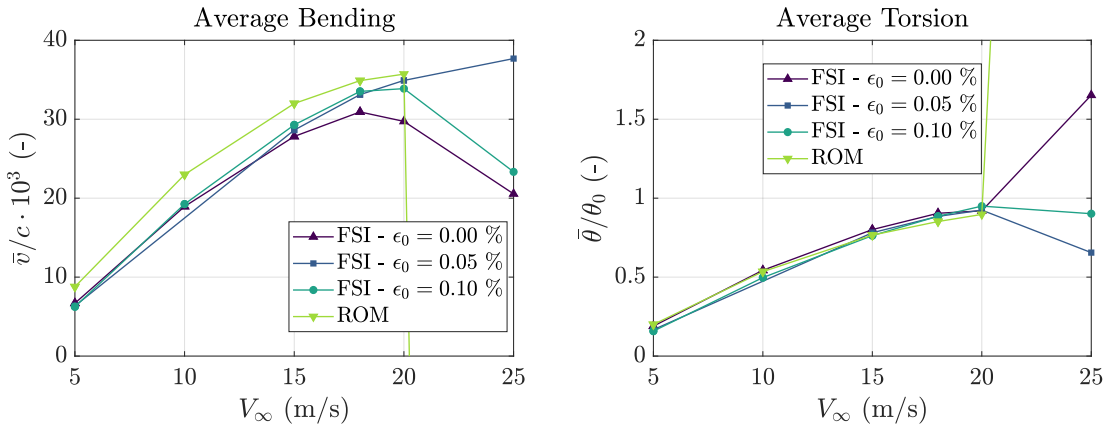

Fig. 4.85 **Mean values of bending and twist of the prestressed membrane wing.** (Left) mean bending and (right) mean twist.

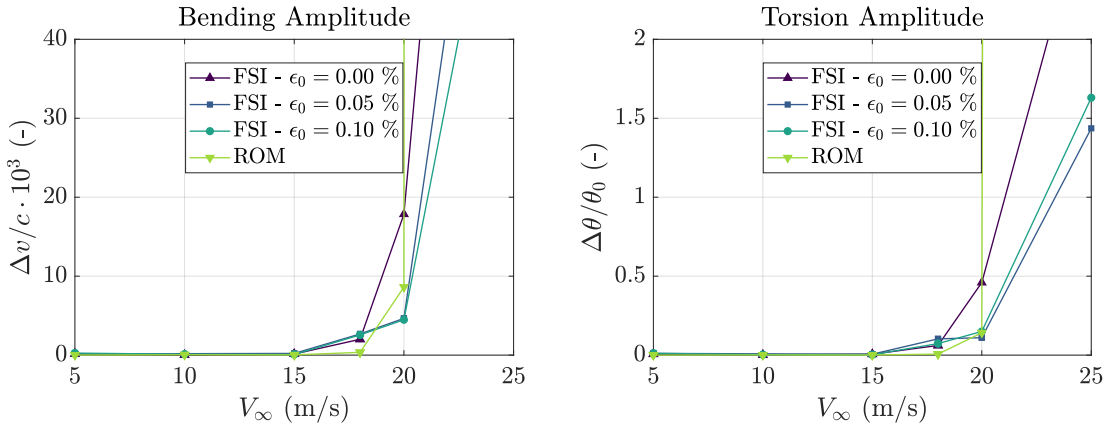

Fig. 4.86 **Amplitude of bending and twist of the prestressed membrane wing.** (Left) bending amplitude and (right) twist amplitude.

Finally, as a consequence of the distortion of the shell structure, a discrepancy is presented between the ROM and the FSI solutions. These differences are due to the modification of the stiffness characteristics and the aerodynamic coefficients of the cross-sections.

Discussion

This section presents a numerical analysis of the structural dynamics and aeroelastic behavior of a resistant membrane wing. The previous FSI analysis has been performed by applying two different and complementary methodologies. Firstly, the CSD/CFD coupled simulation. This calculation can account for the effects of the membrane distortion, aerodynamic evolution due to the external shape modification of the wing, interaction of the walls with the tip wing

vortex, and prestress loads. Then, a ROM based on a beam element solver was used for the calculation. The ROM reduces the computational cost of the simulations by orders of magnitude. The most important outcomes extracted from the section are enumerated below:

- The Reduced Order Model structural solver has been validated against a finite element analysis solution, presenting a high accuracy in the bending and torsion solutions and being able to include the effects of the battens in the twist prediction.
- The Reduced Order Model aerodynamic solution has been compared with a CFD simulation. The influence of the tip gap has been evidenced to deviate the result from the well-known infinite and finite wing solution. The infinite wing model has been selected as the distribution of the coefficients is similar to the CFD simulations. However, the aerodynamic coefficients needed to be reduced by a small percentage of their value to reproduce the effects of the gap correctly. This three-dimensional correction presents a nature similar to the corrective factor of Section 4.2.2. Although the correction improves the deformation results, this correction is not a simulation requirement and could be avoided if the computational cost is lower. Because of brevity, the results without correction are not provided, but the ROM predicts the same flutter velocity of 18 $\mathrm{m/s}$.
- The nonlinear behavior of the membrane has been analyzed. A distortion is presented in the cross-section of the wing, modifying the external shape of the structure far from the battens and altering the aerodynamic loads.
- Initial deformations are produced as a consequence of the prestress of the membrane. Nevertheless, the prestress stiffens the structure and raises the flutter velocity.
- The reduced order model has been proven an efficient tool for predicting aeroelastic instabilities. The reduced order methodology allows calculating the mean deformation values with high accuracy and is a powerful tool for optimizing structural designs.

As previously stated, the ROM is a powerful tool for estimating the aeroelastic instabilities, flutter velocity, and the average deformation of the resistant membrane wing structures. Nevertheless, a higher fidelity tool is required to analyze the intricate details of the flow or the phenomena. CSD/CFD simulations are required to calculate membrane deformations and cross-section distortion, deviation of the streamlines as a consequence of the membrane displacement, aerodynamic interactions with the wind tunnel walls, and prestressing effects.

References

[1] A. Gil, A. Tiseira, P. Quintero, and A. Cremades. Prediction of the non-linear aeroelastic behavior of a cantilever flat plate and equivalent 2d model. *Aerospace Science and Technology*, 113:106685, 2021.

[2] AJ Torregrosa, LM García-Cuevas, P Quintero, and A Cremades. On the application of artificial neural network for the development of a nonlinear aeroelastic model. *Aerospace Science and Technology*, 115: 106845, 2021.

[3] AJ Torregrosa, A Gil, P Quintero, and A Cremades. A reduced order model based on artificial neural networks for nonlinear aeroelastic phenomena and application to composite material beams. *Composite Structures*, 295:115845, 2022.

[4] AJ Torregrosa, A Gil, P Quintero, and A Cremades. On the effects of orthotropic materials in flutter protection of wind turbine flexible blades. *Journal of Wind Engineering and Industrial Aerodynamics*, 227:105055, 2022.

[5] Aly Mousaad Aly, Chanachock Chokwitthaya, and Raymond Poche. Retrofitting building roofs with aerodynamic features and solar panels to reduce hurricane damage and enhance eco-friendly energy production. *Sustainable Cities and Society*, 35:581–593, 2017.

[6] Guy L Larose and Flora M Livesey. Performance of streamlined bridge decks in relation to the aerodynamics of a flat plate. *Journal of Wind Engineering and Industrial Aerodynamics*, 69:851–860, 1997.

[7] Kunihiko Taira and TIM Colonius. Three-dimensional flows around low-aspect-ratio flat-plate wings at low reynolds numbers. *Journal of Fluid Mechanics*, 623:187–207, 2009.

[8] Abdolrahim Rezaeiha, Ivo Kalkman, and Bert Blocken. Cfd simulation of a vertical axis wind turbine operating at a moderatetip speed ratio: Guidelines for minimum domain size and azimuthalincrement. *Renewable Energy*, 107:373–385, 2017.

[9] A. Torregrosa, A. Gil, P. Quintero, A. Ammirati, H. Denayer, and W. Desmet. Prediction of flow induced vibration of a flat plate located after a bluff wall mounted obstacle. *Journal of Wind Engineering & Industrial Aerodynamics*, 190:23–39, 2019.

[10] S. Pope. *Turbulent Flows*. Cambridge University Press, 2009.

[11] R. Gavasane, P. Pai, and V. Kumar. Numerical simulation of pitching and plunging motion of flat plate using oversetmeshes. Symposium on Applied Aerodynamics and Design of Aerospace Vehicle (SAROD 2013), 2013.

[12] J. Morgado, R. Vizinho, M.A.R. Silvestre, and J.C. Páscoa. Xfoil vs cfd performance predictions for high lift low reynolds number airfoils. *Aerospace Science and Technology*, 75:207–214, 2016.

[13] F. Menter. Zonal two-equation $k-\omega$ turbulence model for aerodynamic flows. *AIAA*, 93:93–2906, 1986.

[14] H. Hadzic. Development and application of finite volume method for the computation of flows around moving bodies on unstructure, overlapping grids. 2005.

[15] T. T. Tran and D.H. Kim. The platform pitching motion of floating offshore wind turbine: A preliminary unsteady aerodynamic analysis. *Journal of Wind Engineering & Industrial Aerodynamics*, 142:65–81, 2015.

[16] T. T. Tran and D.H. Kim. A cfd study into the influence of unsteady aerodynamic interference on wind turbine surge motion. *Renewable energy*, 90:204–228, 2016.

[17] T. T. Tran, D.H. Kim, and J. Song. Computational fluid dynamic analysis of a floating offshore wind turbine experiencing platform pitching motion. *Energies*, 7:5011–5026, 2014.

[18] B Dose, H. Rahimi, B. Stoevesandt, and J. Peinke. Fluid-structure coupled investigations of the nrel 5mw wind turbine for two downwind configurations. *Renewable energy*, 146:1113–1123, 2020.

[19] A. Marouf, N. Simiriotis, J.B. To, Y. Bmegaptche, Y. Hoarau, and M. Braza. Ddes and oes simulations of a morphing airbus a320 wing and flap in different scales at high reynolds. *Progress in Hybrid RANS-LES Modelling*, pages 249–258, 2020.

[20] Seungyong Lee, George Wolberg, and Sung Yong Shin. Scattered data interpolation with multilevel b-splines. *IEEE Transactions on Visualization and Computer Graphics*, 3, 1997.

[21] J.M. Weiss, J.P. Maruszewski, and W.A. Smith. Implicit solution of preconditioned navier-stokes equations using algebraic multigrid. *AIAA Journal*, 37:29–36, 1999.

[22] J.M. Weiss and W.A. Smith. Preconditioning applied to variable and constant density flows. *AIAA Journal*, 33:2050–2057, 1995.

[23] V. Venkatakrishnan. On the convergence of limiters and convergence to steady state solutions. *AIAA-93-0880*, 1995.

[24] Robert D. Blevins. *Formulas for natural frequency and mode shape*. Van Nostrand Reinhold Company, 1979.

[25] P.J. Roache. *Verification and Validation in Computational Science and Engineering*. Hermosa Publishers, 1998.

[26] A. Pfahl and H. Uhlemann. Wind loads on heliostats and photovoltaic trackers at various reynolds numbers. *Journal of Wind Engineering & Industrial Aerodynamics*, 99:964–968, 2011.

[27] A. Hassan, S. Mohammad-Reza, and M. Mohammand-Javad. Transitional boundary layer study over an airfoil in combined pitch-plunge motions. *Aerospace Science and Technology*, 98:105694, 2020.

[28] D.R. Williams, F. Reissner, D. Greenblatt, H. Muller-Vahl, and C. Strangfeld. Modeling lift hysteresis with a modified goman-khrabrov model on pitching airfoils. *45th AIAA Fluid Dynamics Conference*, page 2631, 2015.

[29] Matthew J. Emes, Farzin Ghanadi, Maziar Arjomandi, and Richard M. Kelso. Investigation of peak wind loads on tandem heliostats in stow position. *Renewable Energy*, 121:548–558, 2018.

[30] Pedro Manuel Quintero Igeño. *Characterization of Fluid Structure Interaction Mechanisms and its application to the vibroacoustic phenomena*. PhD thesis, June 2019.

[31] Ben Kröse and Patrick van der Smagt. *An introduction to Neural Networks*. University of Amsterdam, 1996.

[32] Igor V. Tetko, David J. Livingstone, and Alexander I. Luik. Neural network studies 1. comparison of overffiting and overtraining. *The Journal for Chemical Information and Computer scientists*, 35:826–833, 1995.

[33] Sanjay Yadav and Sanyam Shukla. Analysis of k-fold cross-validation over hold-out validation on colossal datasets for quality classification. 6th International Advanced Computing Conference, 2016.

[34] Ramesh Chadra, Alan D. Stemple, and Inderjit Chopra. Thin-walled composite beams under bending, torsional, and extensional loads. *Journal of Aircrafts*, 184:872–882, 1990.

[35] Ramesh Chandra and Inderjit Chopra. Experimental-theoretical investigation of the vibration characteristics of rotating composite box beams. *Journal of Aircraft*, 29(4), 1992.

[36] Zhanming Qin and Liviu Librescu. Static/dynamic solutions and validation of a refined anisotropic thin-walled beam model. 43rd AIAA/ASME/ASCE/AHS/ASC Structures, Structural Dynamics and Materials Conference, 2002.

[37] Reza Koohi, Hossein Shahverdi, and Hassan Haddadpour. Nonlinear aeroelastic analysis of a composite wing by finite element method. *Composite Structures*, 113:118–126, 2014.

[38] Pierre J.A. Minguet. *Static and Dynamic Behavior of Composite Helicopter Rotor Blades under Large Deflections.* PhD thesis, Department of Aeronautics and Astronautics, Massachusetts Institute of Technology, 1989.

[39] M. Shaat, B. Aidi, S.W. Case, and A. Abdelkefi. Predictions of the frequencies of bending-torsion coupled laminated composite plates with discontinuities: Novel analytical modeling and experimental validation. *Composite Structures*, 180:334–350, 2017.

[40] J.R. Banerjee. Explicit analytical expressions for frequency equation and mode shapes of composite beams. *International Journal of Solids Structures*, 38:2415–2426, 2001.

[41] Pierre Minguet and John Dugundji. Experiments and analysis for composite blades under large deflections part ii: Dynamic behavior. *AIAA Journal*, pages 1580–1588, 1990.

[42] Bret K. Stanford, Christine V. Jutte, and K. Chauncey Wu. Aeroelastic benefits of tow steering for composite plates. *Composite Structures*, 118:416–422, 2014.

[43] A. Attaran, D.L. Majid, S. Basri, A.S. Mohd Rafie, and E.J. Abdullah. Structural optimization of an aeroelastically tailored composite flat plate made of woven fiberglass/epoxy. *Aerospace Science and Technology*, 15:393–401, 2011.

[44] M.M. Hand, D.A. Simms, L.J. Fingersh, D.W. Jager, J.R. Cotrell, S.Schreck, and S.M. Larwood. Unsteady Aerodynamics Experiment Phase VI: Wind Tunnel Test Configurations and Available Data Campaigns. Technical Report NREL/TP-500-29955, National Renewable Energy Laboratory, 2001.

[45] E. Mahdi, B.S. Almabrouk, A.M.S. Hamouda, A.S. Mokhtar, Robiah Younus, and H. Sultan. Utilization of composite's tensile properties for energy absorbing systems. *Composite Structures*, 75:29–38, 2006.

[46] Ivica T. Vijcic and Ivana D. Dimic. Microstructural characterization of glass-epoxy composites subjected to tensile testing. *Acta Periodica Technologica*, 2013.

[47] Shamsher Singh, Madappa Sivasubramanian, A. Reddy, Chandra Khatri, K. Nagarjuna, and A. Kiran. Performance of NSM-FRP RC beams in flexure and shear using locally developed CFRP rebars. . *Int. J. of Sustainable Materials and Structural Systems*, 1:42–67, 2012.

[48] Kyoungsoo Lee, Ziaul Huque, Raghava Kommalapati, and Sang-Eul Han. Fluid-structure interaction analysis of NREL phase VI wind turbine: Aerodynamic force evaluation and structural analysis using FSI analysis. *Renewable Energy*, 113:512–531, 2017.

[49] A.J. Torregrosa, A. Gil, P. Quintero, and A. Tiseira. Enhanced design methodology of a low power stall regulated wind turbine. BEMT and MRF-RANS combination and comparison with existing designs. *Journal of Wind Engineering & Industrial Aerodynamics*, 190:230–244, 2019.

[50] Borja Plaza, Rafael Bardera, and Sergio Visiedo. Comparison of BEM and CFD results for MEXICO rotor aerodynamics. *Journal of Wind Engineering & Industrial Aerodynamics*, 145:115–122, 2015.

[51] Yongsheng Lian, Wei Shyy, Dragos Viieru, and Baoning Zhang. Membrane wing aerodynamics for micro air vehicles. *Progress in Aerospace Sciences*, 39(6-7):425–465, 2003.

[52] Wei Shyy, Peter Ifju, and Dragos Viieru. Membrane Wing-Based Micro Air Vehicles. *Applied Mechanics Reviews*, 58(4):283–301, 07 2005.

[53] L. Tregidgo, Z. Wang, and I. Gursul. Unsteady fluid–structure interactions of a pitching membrane wing. *Aerospace Science and Technology*, 28(1):79–90, 2013. ISSN 1270-9638. doi: https://doi.org/10.1016/j.ast.2012.10.006.

[54] Benoît Béguin and Christian Breitsamter. Effects of membrane pre-stress on the aerodynamic characteristics of an elasto-flexible morphing wing. *Aerospace Science and Technology*, 37:138–150, 2014. ISSN 1270-9638. doi: https://doi.org/10.1016/j.ast.2014.05.005.

[55] Shuanghou Deng, Jun Wang, and Hanru Liu. Experimental study of a bio-inspired flapping wing mav by means of force and piv measurements. *Aerospace Science and Technology*, 94:105382, 2019. ISSN 1270-9638. doi: https://doi.org/10.1016/j.ast.2019.105382.

[56] Dawei Bie, Daochun Li, Jinwu Xiang, Huadong Li, Zi Kan, and Yi Sun. Design, aerodynamic analysis and test flight of a bat-inspired tailless flapping wing unmanned aerial vehicle. *Aerospace Science and Technology*, 112:106557, 2021. ISSN 1270-9638. doi: https://doi.org/10.1016/j.ast.2021.106557.

[57] Bor-Jang Tsai and Yu-Chun Fu. Design and aerodynamic analysis of a flapping-wing micro aerial vehicle. *Aerospace Science and Technology*, 13(7):383–392, 2009. ISSN 1270-9638. doi: https://doi.org/10.1016/j.ast.2009.07.007.

[58] Sonya Tiomkin and Daniella E Raveh. A review of membrane-wing aeroelasticity. *Progress in Aerospace Sciences*, 126:100738, 2021.

[59] Junhee Lee, Sang-Hoon Yoon, and Chongam Kim. Experimental surrogate-based design optimization of wing geometry and structure for flapping wing micro air vehicles. *Aerospace Science and Technology*, 123:107451, 2022. ISSN 1270-9638. doi: https://doi.org/10.1016/j.ast.2022.107451.

[60] Julien Deparday, Patrick Bot, Frederic Hauville, Benoit Augier, and Marc Rabaud. Full-scale flying shape measurement of offwind yacht sails with photogrammetry. *Ocean Engineering*, 127:135–143, 2016.

[61] D. Trimarchi and C.M. Rizzo. A fem-matlab code for fluid-structure interaction coupling with application to sail aerodynamics of yachts. In Ömer Gören, Barbaros Okan, and Şafak C. Karakaş, editors, *13th International Congress of International Maritime Association of Mediterranean (IMAM2009), Towards the Sustainable Marine Technology. 12-15 October, 2009, Istanbul, Turkey. Proceedings Vol.III*, pages 907–916. ITU Faculty of Naval Architecture and Ocean Engineering, 2009.

[62] Nils Haack. *C-class catamaran wing performance optimisation*. PhD thesis, The University of Manchester (United Kingdom), 2011.

[63] Joseph Banks, Margot Cocard, and Jacobo Jaspe. Assessing the impact of membrane deformations on wing sail performance. *Journal of Sailing Technology*, 6(01):73–90, 2021.

[64] Benoit Augier, Patrick Bot, Frederic Hauville, and Mathieu Durand. Dynamic behaviour of a flexible yacht sail plan. *Ocean Engineering*, 66:32–43, 2013.

[65] Bret Stanford, Peter Ifju, Roberto Albertani, and Wei Shyy. Fixed membrane wings for micro air vehicles: Experimental characterization, numerical modeling, and tailoring. *Progress in Aerospace Sciences*, 44(4): 258–294, 2008.

[66] Fabio Fossati and Sara Muggiasca. Experimental investigation of sail aerodynamic behavior in dynamic conditions. *Journal of Sailboat Technology*, 2(8):1–41, 2011.

[67] Benoit Augier, Patrick Bot, Frederic Hauville, and Mathieu Durand. Experimental validation of unsteady models for fluid structure interaction: Application to yacht sails and rigs. *Journal of Wind Engineering and Industrial Aerodynamics*, 101:53–66, 2012.

[68] Robert Scott, Robert Bartels, and Osama Kandil. An aeroelastic analysis of a thin flexible membrane. In *48th AIAA/ASME/ASCE/AHS/ASC Structures, Structural Dynamics, and Materials Conference*, page 2316, 2007.

[69] Guojun Li, Boo Cheong Khoo, and Rajeev K Jaiman. Computational aeroelasticity of flexible membrane wings at moderate reynolds numbers. In *AIAA Scitech 2020 Forum*, page 2036, 2020.

[70] Multifrontal Massively Parallel Solver (MUMPS 5.0.2) Users' Guide. July 15, 2016.

Chapter 5

Conclusions and future work

5.1 Conclusions

Along the dissertation, different fidelity approaches to the computational resolution of the aeroelastic phenomena were presented. The main objective of the work was the development of new methodologies capable of simulating the aeroelastic dynamics of a general structure of application problem. The methodology was developed to include complex nonlinear aerodynamic effects in the simulations and allow the simulation of orthotropic material structures.

Initially, the mathematical background underlying the algorithms was introduced. The physical equations for fluid dynamics and solid elasticity were introduced. The widely known computational techniques (CFD and FEA) for solving the previous equations were presented. Then, a set of reduced-order models were derived to reduce the computational cost of the previous algorithms.

The simplest model is based on the dimensional reduction of the structural problem. The three-dimensional structure is reduced into an equivalent section. In order to simulate a representative equivalent section that considers the boundary conditions of the beam, its motion is based on the vibration modes of the three-dimensional solid. In addition, to include complex nonlinearities on the aerodynamic coefficients, the flow field is calculated through a two-dimensional CFD simulation. This CFD-based procedure can include the effects of stall and boundary layer detachment. However, the three-dimensional aerodynamic effects cannot be reproduced. For this reason, a corrective factor is proposed to decrease the value of the bi-dimensional coefficients.

However, the computational cost associated with these simulations is still high for the designing process in which iterating mass or stiffness properties results in additional CFD simulations. For this reason, a fast calculation ROM based on ANN is also developed and

presented in the dissertation. This ANN is trained using a database of forced oscillations in a bi-dimensional airfoil and then used for predicting the transient term of the aerodynamic coefficients. The surrogate model was trained and used for predicting the aeroelastic behavior of the structure, showing its accuracy and demonstrating its capabilities for reproducing the aeroelastic problems.

The equivalent section simplifies the structure so that only the main vibration modes are included in the calculation. The example shown in this document only includes the first bending and twisting mode. Therefore, this model needs to be extended to increase the number of modes taken into account and reproduce complex bending-twisting couplings of orthotropic materials. A beam model for generic orthotropic materials is presented in the document. This ROM has been used in different engineering problems proving its applicability for the resolution of the general aeroelastic problem. The model was tested in different types of aeroelastic problems, using wing or blade aerodynamic models depending on the requirements.

Along the work, the aeroelastic instabilities have been demonstrated to be produced by the effect of the stalling process and nonlinear aerodynamics. Thus, the simulation of the nonlinear loads becomes critical for many applications and flow conditions. The resolution of the flow pattern created in these conditions is complex and requires, for the general case, the resolution of conservation equations (CFD).

However, the simulation of the phenomena by solving the complete solid and fluid equations may be computationally requiring. In order to reduce the computational cost of the simulation without losing the nonlinear effects of the stall, the dimensional reduction of the structure is recommended. After obtaining the mass and stiffness terms, the structure can be simulated in a CFD calculation as an equivalent section with a rigid solid motion. In fact, far from the unstable zone, where the dynamic effects are less critical, the results of the equivalent section can be improved by correcting the aerodynamic coefficients of the section with the three-dimensional coefficient.

Even with the previous simplifications, the computational cost of the rigid solid cross-section motion is still restrictive during design stages. For this reason, the ROM based on ANN is recommended for this process. The initial cost of the ROM is higher as it requires training the aerodynamic surrogate model. Nevertheless, the training effort is compensated as the ANN reduces by orders of magnitude the cost of the simulations. Note that training an ANN requires the creation of a data set. This data set can be obtained from a computational or experimental point of view. In this work, a database of CFD-forced oscillations has been used for the process. As the aerodynamic coefficient obtained in the simulations presents a high dependence on the initial angle of attack, its amplitude, and the frequency of the motion,

the database should cover the interest conditions to avoid extrapolation. Feed-forward and long short-term memory neurons were tested. Both typologies showed similar results. Nevertheless, FNN does not require the use of past data, and thus, their computational cost is lower than the LSTM architecture, and they are recommended for predicting aerodynamic coefficients.

As previously stated, the inclusion of higher vibration modes and structural coupling requires the use of a beam model. The beam model is first validated against the literature showing accurate results. Then it is applied to a set of problems of different natures. The beam model is combined with the previously mentioned ANN-based ROM and a lifting line theory aerodynamic model for the three-dimensional effects, showing a high accuracy when predicting the stall flutter effects. In addition, the effects that the fiber orientation has on the results were also analyzed, showing the adequacy of the ROM for determining optimum fiber layups. This structural ROM is also combined with rotating aerodynamics models. In this case, the flutter effects were calculated using Theodorsen's transient coefficients in combination with blade element momentum theory. The ROM was used for predicting the aeroelastic instabilities, showing that a correct fiber orientation could improve the limits of the structure without increasing its weight.

Finally, resistant membrane structures were calculated using the ROM. Theodorsen's coefficients were combined with the lifting line theory in this case. Although the model is too simple to reproduce the deformation of the membrane, it presented accurate results when obtaining its free stream velocity limits. Moreover, the effects of prestressing the external membrane of the structure were analyzed. The initial tension produced initial deformations, but when the aerodynamic loads were applied, the stiffness of the structure was increased.

From the previous ideas, the main conclusion of the dissertation is inferred. The complete three-dimensional aeroelastic simulation requires complex and computationally requiring calculations. The resolution of these simulations is suitable for the final phases of the design process. The use of ROMs is recommended for the initial stages, in which many parameters are still undefined. The selection of the ROM depends on the characteristics of the physical problem. If the motion of the structure is bi-dimensional and it does not present bending-torsion couplings, the equivalent section is preferred. On the contrary, the beam element model ROM should be used if the structure is expected to behave unidimensionally. The use of artificial neural networks should be avoided in the case of a reduced number of simulations due to the cost of the training process.

5.2 Future works

The methodology presented in this dissertation is an initial point for the fluid-structure simulations in CMT institute of Polytechnic University of Valencia. The algorithm developed in the thesis can be applied to complex problems, including propulsion applications which are the traditional field of applications in the so-mentioned institute. Future works will be related to optimizing the code, including additional models and their application to different engineering problems, and including structural damping in the calculations.

With respect to code optimization, the proposed improvements are related to reducing memory usage and simplifying the algorithms. These algorithms could be improved and optimized to optimize the computational cost reduction of the simulation.

In addition, new models can be included. The potential models used for calculating finite wings aerodynamics can be extended between these models to simulate the interaction between different lifting surfaces. This modification would allow the simulation of a complete aircraft and the prediction of aeroelastic problems during flight. Moreover, to improve the calculation of the dynamic stall of the airfoils, Theodorsen's coefficients should be substituted by the Leishman-Beddoes model [1]. Finally, combining the present results with aeroacoustic simplified solutions is another possibility. In this case, the method proposed by Farassat [2] could be included for estimating generated noise in flexible blades. Another possible improvement is creating a flexible neural network that can calculate the dynamic effects of a general airfoil. It applies to a wide range of problems with a wide range of geometries.

The solvers presented in this work could also be used for developing active control techniques in the aeroelastic structure protection or the flexible wing optimization of the structure. Machine learning strategies such as deep reinforced learning can be used to control the deformation of the structure.

Finally, it is essential to mention that the turbulence model strongly conditions the algorithms for simulating the flow field around the structures. These turbulent models are a simplification of the conservation equations. Therefore, the aerodynamic forces generated on the surface of the structure are an approximation of the actual loads. In order to improve the accuracy of the forces, high-fidelity simulations are required, with LES and DNS as the alternative to the RANS and URANS models. However, the drawback of high-fidelity algorithms is their elevated computational cost. Therefore, new approaches are required to improve the accuracy of the flow field prediction.

References

[1] JG Leishman and TS Beddoes. A generalized method for unsteady airfoil behaviour and dynamic stall using the indicial method 42nd annual forum of the ahs. 1986.

[2] Feri Farassat. Linear acoustic formulas for calculation of rotating blade noise. *AIAA journal*, 19(9): 1122–1130, 1981.

References

[1] A. Gil, A. Tiseira, P. Quintero, and A. Cremades. Prediction of the non-linear aeroelastic behavior of a cantilever flat plate and equivalent 2d model. *Aerospace Science and Technology*, 113:106685, 2021.

[2] AJ Torregrosa, LM García-Cuevas, P Quintero, and A Cremades. On the application of artificial neural network for the development of a nonlinear aeroelastic model. *Aerospace Science and Technology*, 115:106845, 2021.

[3] AJ Torregrosa, A Gil, P Quintero, and A Cremades. A reduced order model based on artificial neural networks for nonlinear aeroelastic phenomena and application to composite material beams. *Composite Structures*, 295:115845, 2022.

[4] AJ Torregrosa, A Gil, P Quintero, and A Cremades. On the effects of orthotropic materials in flutter protection of wind turbine flexible blades. *Journal of Wind Engineering and Industrial Aerodynamics*, 227:105055, 2022.

[5] AJ Torregrosa, A Gil, P Quintero, and A Cremades. Multi
delity approach to the numerical aeroelastic simulation of flexible membrane wings. *preprint submited to Aerospace Science and Technology*, 2023.

[6] Andres Cremades, Sergio Hoyas, Pedro Quintero, Martin Lellep, Moritz Linkmann, and Ricardo Vinuesa. Explaining wall-bounded turbulence through deep learning. *arXiv preprint arXiv:2302.01250*, 2023.

[7] International Energy Agency. Key world energy statistics, https://www.iea.org/reports/key-world-energy-statistics-2020, accessed 20-nov-2022. IEA, Paris, 2020.

[8] William Richard Graham, Cesare Alan Hall, and M Vera Morales. The potential of future aircraft technology for noise and pollutant emissions reduction. *Transport policy*, 34:36–51, 2014.

[9] Jason E Hicken and David W Zingg. Induced-drag minimization of nonplanar geometries based on the euler equations. *AIAA journal*, 48(11):2564–2575, 2010.

[10] A Abbas, J De Vicente, and E Valero. Aerodynamic technologies to improve aircraft performance. *Aerospace science and technology*, 28(1):100–132, 2013.

[11] Frederico Afonso, José Vale, Éder Oliveira, Fernando Lau, and Afzal Suleman. A review on non-linear aeroelasticity of high aspect-ratio wings. *Progress in Aerospace Sciences*, 89:40–57, 2017.

[12] Edward M Greitzer, PA Bonnefoy, E DelaRosaBlanco, CS Dorbian, M Drela, DK Hall, RJ Hansman, JI Hileman, RH Liebeck, J Lovegren, et al. N+ 3 aircraft concept designs and trade studies. Technical report, 2010.

[13] R Bombardieri, R Cavallaro, R Castellanos, and F Auricchio. On the dynamic fluid–structure stability response of an innovative airplane configuration. *Journal of Fluids and Structures*, 105:103347, 2021.

[14] Ibrahim Dincer. Renewable energy and sustainable development: a crucial review. *Renewable and sustainable energy reviews*, 4(2):157–175, 2000.

[15] Salvatore Ruggiero and Heikki Lehkonen. Renewable energy growth and the financial performance of electric utilities: A panel data study. *Journal of Cleaner Production*, 142:3676–3688, 2017.

[16] Rehana Perveen, Nand Kishor, and Soumya R Mohanty. Off-shore wind farm development: Present status and challenges. *Renewable and Sustainable Energy Reviews*, 29:780–792, 2014.

[17] S. Yao, M. Chetan, D. T. Griffith, A. S. Escalera Mendoza, M. S. Selig, D. Martin, Sepideh Kianbakh, Kathryn Johnson, and E. Loth. Aero-structural design and optimization of 50 MW wind turbine with over 250-m blades. *Wind Engineering*, 46: 273–295, 2021.

[18] Zhanwei Li, Binrong Wen, Xingjian Dong, Zhike Peng, Yegao Qu, and Wenming Zhang. Aerodynamic and aeroelastic characteristics offlexible wind turbine bladesunder periodic unsteady inflows. *Journal of Wind Engineering & Industrial Aerodynamics*, 197:104057, 2020.

[19] M.H. Hansen. Aeroelastic Instability Problems for Wind Turbines. *Wind Energy*, 10: 551–577, 2007.

[20] Morten H Hansen. Improved modal dynamics of wind turbines to avoid stall-induced vibrations. *Wind Energy: An International Journal for Progress and Applications in Wind Power Conversion Technology*, 6(2):179–195, 2003.

[21] L. Sanches, T. A. Guimaraes, and F. D. Marques. Aeroelastic tailoring of nonlinear typical section using the method of multiple scales to predict post-flutter stable LCOs. *Aerospace Science and Technology*, 90:157–168, 2019.

[22] Andreas Schellenberg, Joe Maffei, Karl Telleen, and Rob Ward. Structural analysis and application of wind loads to solar arrays. *Journal of Wind Engineering and Industrial Aerodynamics*, 123:261–272, 2013. ISSN 0167-6105. doi: https://doi.org/10.1016/j.jweia.2013.06.011.

[23] Matthew T.L. Browne, Zachary J. Taylor, Sihan Li, and Scott Gamble. A wind load design method for ground-mounted multi-row solar arrays based on a compilation of wind tunnel experiments. *Journal of Wind Engineering and Industrial Aerodynamics*, 205:104294, 2020. ISSN 0167-6105. doi: https://doi.org/10.1016/j.jweia.2020.104294.

[24] Onur Yemenici and Muhammed Osman Aksoy. An experimental and numerical study of wind effects on a ground-mounted solar panel at different panel tilt angles and wind directions. *Journal of Wind Engineering and Industrial Aerodynamics*, 213:104630, 2021. ISSN 0167-6105. doi: https://doi.org/10.1016/j.jweia.2021.104630.

[25] Aly Mousaad Aly and Girma Bitsuamlak. Aerodynamics of ground-mounted solar panels: Test model scale effects. *Journal of Wind Engineering and Industrial Aerodynamics*, 123:250–260, 2013. ISSN 0167-6105. doi: https://doi.org/10.1016/j.jweia.2013.07.007.

[26] Robert M Jones. *Mechanics of composite materials*. CRC press, 2018.

[27] Trevor William Clyne and Derek Hull. *An introduction to composite materials*. Cambridge university press, 2019.

[28] Rachid Hsissou, Rajaa Seghiri, Zakaria Benzekri, Miloudi Hilali, Mohamed Rafik, and Ahmed Elharfi. Polymer composite materials: A comprehensive review. *Composite structures*, 262:113640, 2021.

[29] Guo Dong Goh, Vishwesh Dikshit, Arun Prasanth Nagalingam, Guo Liang Goh, Shweta Agarwala, Swee Leong Sing, Jun Wei, and Wai Yee Yeong. Characterization of mechanical properties and fracture mode of additively manufactured carbon fiber and glass fiber reinforced thermoplastics. *Materials & Design*, 137:79–89, 2018.

[30] A. D. Shaw, I. Dayyani, and M. I. Friswell. Optimisation of composite corrugated skins for buckling in morphing aircraft. *Composite Structures*, 119:227–237, 2015.

[31] Trevor Sabiston, Bin LiJidong Kang, David Wilkinson, and Carlos Engler-Pinto. Accounting for the microstructure in the prediction of the fatigue lifeof injection moulded composites for automotive applications. *Composite Structures*, 255:112898, 2021.

[32] A. Gargano, K. Pingkarawat, M. Blacklock, V. Pickerd, and A.P. Mouritz. Comparative assessment of the explosive blast performance of carbonand glass fibre-polymer composites used in naval ship structures. *Composite Structures*, 171:306–316, 2017.

[33] Roham Rafiee, Mojtaba Tahani, and Mohsen Moradi. Simulation of aeroelastic behavior in a composite wind turbine blade. *Journal of Wind Engineering & Industrial Aerodynamics*, 151:60–69, 2016.

[34] Lin Wang, Robin Quant, and Athanasios Kolios. Fluid structure interaction modelling of horizontal-axis wind turbine blades based on cfd and fea. *Journal of Wind Engineering & Industrial Aerodynamics*, 158:11–25, 2016.

[35] Carlos Pascual Agullo. *Translucent load-bearing GFRP envelopes for daylighting and solar cell integration in buliding construction.* PhD thesis, EPFL, Laussane, 2014.

[36] Carlos Pascual, Julia de Castro, Andreas Schueler, and Thomas Keller. Integration of dye solar cells in load-bearing translucent glass fiber-reinforced polymer laminates. *Journal of Composite Materials*, 51:939–953, 2016.

[37] VC Sherrer, TJ Hertz, and MH Shirk. Wind tunnel demonstration of aeroelastic tailoring applied to forward swept wings. *Journal of Aircraft*, 18(11):976–983, 1981.

[38] Terrence Weisshaar, Changho Nam, and Alicia Batista-Rodriguez. Aeroelastic tailoring for improved uav performance. In *39th AIAA/ASME/ASCE/AHS/ASC Structures, Structural Dynamics, and Materials Conference and Exhibit*, page 1757, 1998.

[39] Bret K Stanford and Christine V Jutte. Comparison of curvilinear stiffeners and tow steered composites for aeroelastic tailoring of aircraft wings. *Computers & Structures*, 183:48–60, 2017.

[40] Zhi-Guang Song and Feng-Ming Li. Active aeroelastic flutter analysis and vibration control of supersonic composite laminated plate. *Composite Structures*, 94(2):702–713, 2012.

[41] G.A. Geroghiades and J.R. Banerjee. Flutter modes of composite wings exhibiting wash-in and wash-out. 38th Structures, Structural Dynamics and Materials Conference, 1997.

[42] Bret K. Stanford, Christine V. Jutte, and K. Chauncey Wu. Aeroelastic benefits of tow steering for composite plates. *Composite Structures*, 118:416–422, 2014.

[43] Terrence A Weisshaar and Rosemary J Ryan. Control of aeroelastic instabilities through stiffness cross-coupling. *Journal of Aircraft*, 23(2):148–155, 1986.

[44] Anthony P Ricciardi, Robert A Canfield, Mayuresh J Patil, and Ned Lindsley. Nonlinear aeroelastic scaled-model design. *Journal of Aircraft*, 53(1):20–32, 2016.

[45] Roland Feil, Tobias Pflumm, Pietro Bortolotti, and Marco Morandini. A cross-sectional aeroelastic analysis and structural optimization tool for slender composite strictures. *Composite structures*, 253:112755, 2020.

[46] Earl H Dowell, RH Scanlan, F Sisto, HC Curtiss Jr, and H Saunders. A modern course in aeroelasticity. 1981.

[47] Lin Wang, Xiongwei Liu, and Athanasios Kolios. State of the art in the aeroelasticity of wind turbine blades: Aeroelastic modelling. *Renewable and Sustainable Energy Reviews*, 64:195–210, 2016.

[48] M Vahdati, AI Sayma, JG Marshall, and M Imregun. Mechanisms and prediction methods for fan blade stall flutter. *Journal of Propulsion and Power*, 17(5):1100–1108, 2001.

[49] Norizham Abdul Razak, Thomas Andrianne, and Grigorios Dimitriadis. Flutter and stall flutter of a rectangular wing in a wind tunnel. *AIAA journal*, 49(10):2258–2271, 2011.

[50] Alfonso Del Carre and Rafael Palacios. Efficient time-domain simulations in nonlinear aeroelasticity. In *AIAA Scitech 2019 Forum*, page 2038, 2019.

[51] Liviu Librescu and Ohseop Song. *Thin-Walled Composite Beams. Theory and Application*. Springer, 2006.

[52] Pedro Manuel Quintero Igeño. *Characterization of Fluid Structure Interaction Mechanisms and its application to the vibroacoustic phenomena*. PhD thesis, June 2019.

[53] Olga V. Korotkaya. Substructure method for thermal-stress analysis of liquid-propellant rocket engine combustion chamber. *International Journal of Aerospace and Mechanical Engineering*, 8(4):739–742, 2014.

[54] Vladislav M Anisimov, Ivan A Zubrilin, and Mikhail Y Orlov. Investigation of thermal and stress states of the annular combustion chamber flame tube walls. In *Turbo Expo: Power for Land, Sea, and Air*, volume 49767, page V04BT04A021. American Society of Mechanical Engineers, 2016.

[55] Chaobin Hu and Xiaobing Zhang. A fluid-structure coupling method to obtain parameter distributions in a combustion chamber with moving boundaries. *Applied Thermal Engineering*, 141:1048–1054, 2018. ISSN 1359-4311.

[56] J. Pei, F.-K. Benra, and H. Dohmen. Application of different strategies of partitioned fluid-structure interaction simulation for a single-blade pump impeller. *Proceedings of the Institution of Mechanical Engineers, Part E: Journal of Precess Mechanical Engineering*, 226(4):297–308, 2012.

[57] Hyun-Su Kang and Youn-Jea Kim. Optimal design of impeller for centrifugal compressor under the influence of one-way flid-structure interaction. *Journal of Mechanical Science and Technology*, 30(9):3953–3959, 2016.

[58] S. Huo, H. Huang, D. Huang, Z. Liu, and H. Chen. Modal characteristics and fluid-structure interaction vibration response of submerged impeller. *Journal of Vibration and Control*, 28(15-16):2020–2031, 2022.

[59] K. Wijesooriya, D. Mohotti, A. Amin, and K. Chauhan. An uncouple fluid structures interaction method in the assessment of structureal responses of tall buildings. *Structures*, 25:448–462, 2020.

[60] K. Wijesooriya, D. Mohotti, A. Amin, and K. Chauhan. Comparison between an uncoupled one-way and two-way fluid structure interaction simulation on a super-tall slender structure. *Engineering Structures*, 229:111636, 2021.

[61] H. Mazaheri, A.H. Nambdar, and A. Amiri. Behavior of a smart one-way micro-valve considering fluid-structure interaction. *Journal of Intelligent material Systems and Structures*, 29(20):3960–3971, 2018.

[62] M.J. de C. Henshaw, K.J. Badcock, G.A. Vio, C.B. Allen, J. Chamberlain, I. Kaynes, G. Dimitriadis, J.E. cooper, M.A. Woodgate, A.M. Rampurawala, D. Jones, C. Fenwick, A.L. Gaitonde, N.V. Taylor, D.S. Amor, T.A. Eccles, and C. J. Denley. Non-linear aeroelastic prediction for aircraft applications. *Progress in Aeroespace Sciences*, 43: 65–137, 2007.

[63] Joseba Murua, Rafael Palacios, J. Michael, and R. Graham. Applications of the unsteady vortex-lattice method in aircraft aeroelasticity and flight dynamics. *Progress in Aeroespace Sciences*, 55:46–72, 2012.

[64] Rafic M. Ajaj, Muhammed S. Parancheerivilakkathil, Mohammadreza Amoozgar, Michael I. Friswell, and Wesley J. Cantwell. Recent developments in the aeroelasticity of morphing aircraft. *Progress in Aeroespace Sciences*, 120:100682, 2021.

[65] Martin Otto Laver Hansen, Jens Nørkær Sørensen, S Voutsinas, Niels Sørensen, and H Aa Madsen. State of the art in wind turbine aerodynamics and aeroelasticity. *Progress in aerospace sciences*, 42(4):285–330, 2006.

[66] Pinting Zhang and Shuhong Huang. Review of aeroelasticity for wind turbine: Current status, research forcus and future perspectives. *Frontiers in Energy*, 5:419–434, 2011.

[67] Luca Formaggia, Alexandra Moura, and Fabio Nobile. On the stability of the coupling of 3d and 1d fluid-structure interaction models for blood flow simulations. *ESAIM: Mathematical Modelling and Numerical Analysis*, 41(4):743–769, 2007.

[68] Boyang Su, Liang Zhong, Xi-Kun Wang, Jun-Mei Zhang, Ru San Tan, John Carson Allen, Soon Keat Tan, Sangho Kim, and Hwa Liang Leo. Numerical simulation of patient-specific left ventricular model with both mitral and aortic valves by fsi approach. *Computer Methods and Programs in Biomedicine*, 113:474–482, 2014.

[69] Marco Fedele, Elena Faggiano, Luca Dedè, and Alfio Quarteroni. A patient-specific aortic valve model based on moving resistive immersed implicit surfaces. *Biomech Model Mechanobiol*, 16:1779–1803, 2017.

[70] Nhan T. Nguyen, Kevin Reynlds, Ting Eric, and Natalia Nguyen. Distributed Propulsion Aircraft with Aeroelastic Wing Shaping Control for Improved Aerodynamic Efficiency. *Journal of Aircraft*, pages 1–19, 2018.

[71] Xu-Hui He, Hao Ding, Hai-Quan Jing, Fang Zhang, Xiao-Ping Wu, and Xiao-Jun Weng. Wind-induced vibration and its suppression of photovoltaic modules supported by suspension cables. *Journal of Wind Engineering & Industrial aerodynamics*, page 104275, 2020.

[72] A Chizfahm, E Azadi Yazdi, and M Eghtesad. Dynamic modeling of vortex induced vibration wind turbines. *Renewable Energy*, 121:632–643, 2018.

[73] Chapter 1 - introduction. In Shigehiko Kaneko, Tomomichi Nakamura, Fumio Inada, Minoru Kato, Kunihiko Ishihara, Takashi Nishihara, and Mikael A. Langthjem, editors, *Flow-induced Vibrations (Second Edition)*, pages 1–28. Academic Press, Oxford, second edition edition, 2014. ISBN 978-0-08-098347-9. doi: https://doi.org/10.1016/B978-0-08-098347-9.00001-1.

[74] Masaki Kameyama and Hisao Fukunaga. Optimum design of composite plate wings for aeroelastic characteristics using lamination parameters. *Computers & structures*, 85(3-4):213–224, 2007.

[75] George Platanitis and Thomas W Strganac. Suppression of control reversal using leading-and trailing-edge control surfaces. *Journal of guidance, control, and dynamics*, 28(3):452–460, 2005.

[76] Steven J Hollowell and John Dugundji. Aeroelastic flutter and divergence of stiffness coupled, graphite/epoxy cantilevered plates. *Journal of Aircraft*, 21(1):69–76, 1984.

[77] Peter Dunn and John Dugundji. Nonlinear stall flutter and divergence analysis of cantilevered graphite/epoxy wings. *AIAA journal*, 30(1):153–162, 1992.

[78] Xinzhong Chen, Masaru Matsumoto, and Ahsan Kareem. Time domain flutter and buffeting response analysis of bridges. *Journal of Engineering Mechanics*, 126(1): 7–16, 2000.

[79] S. Timoshenko and J.N. Goodier. *Theory of Elasticity*. Engineering Societies Monographs, 1982.

[80] E.J. HEARN. Mechanics of materials 1 (third edition). Butterworth-Heinemann, Oxford, third edition edition, 1997. ISBN 978-0-7506-3265-2. doi: https://doi.org/10.1016/B978-075063265-2/50000-1.

[81] Jean P. Mercier, Gérald Zambelli, and Wilfried Kurz. *Chapter 6 - Elastic behaviour of solids*. Elsevier, Oxford, 2002. ISBN 978-2-84299-286-6. doi: https://doi.org/10.1016/B978-2-84299-286-6.50012-3.

[82] James R Barber. *Elasticity*. Springer, 2002.

[83] Gerald Wempner. *Mechanics of solids with applications to thin bodies*, volume 2. Springer Science & Business Media, 1982.

[84] Antonio Crespo Martínez. *Mecánica de fluidos*. S.A. Ediciones Paraninfo, 2006.

[85] John F Douglas, Janusz M Gasiorek, John A Swaffield, and Lynne B Jack. *Fluid mechanics*. Pearson education, 2005.

[86] Bruce Roy Munson, Theodore Hisao Okiishi, Wade W Huebsch, and Alric P Rothmayer. *Fluid mechanics*. Wiley Singapore, 2013.

[87] Osborne Reynolds. An experimental investigation of the circumstances which determine whether the motion of water shall be direct or sinuous, and of the law of resistance in parallel channels. *Philosophical Transactions of the Royal society of London*, 174:935–982, 1883.

[88] A. N. Kolmogorov. Local structure of turbulence in an incompressible fluid at very high Reynolds numbers. *Dokl. Akad. Nauk.*, SSSR (30):9–13, 1941.

[89] J. Kim, P. Moin, and R. Moser. Turbulence statistics in fully developed channels flows at low Reynolds numbers. *Journal of Fluid Mechanics*, 177:133–166, 1987.

[90] Osborne Reynolds. Iv. on the dynamical theory of incompressible viscous fluids and the determination of the criterion. *Philosophical transactions of the royal society of london.(a.)*, (186):123–164, 1895.

[91] Joseph Smagorinsky. General circulation experiments with the primitive equations: I. the basic experiment. *Monthly weather review*, 91(3):99–164, 1963.

[92] A Ro Collar. The expanding domain of aeroelasticity. *The Aeronautical Journal*, 50 (428):613–636, 1946.

[93] Weiwei Zhang and Zhengyin Ye. Control law design for transonic aeroservoelasticity. *Aerospace Science and Technology*, 11(2-3):136–145, 2007.

[94] RM Botez. Morphing wing, uav and aircraft multidisciplinary studies at the laboratory of applied research in active controls, avionics and aeroservoelasticity larcase. *Aerospace Lab*, (14):1–11, 2018.

[95] Rauno Cavallaro and Rocco Bombardieri. Studies on lateral-directional coupled flight dynamics and aeroelasticity of a prandtlplane. In *AIAA Scitech 2019 Forum*, page 1118, 2019.

[96] YJ Ge, ZX Lin, FC Cao, JB Pang, and HF Xiang. Investigation and prevention of deck galloping oscillation with computational and experimental techniques. *Journal of Wind Engineering and Industrial Aerodynamics*, 90(12-15):2087–2098, 2002.

[97] John HG Macdonald and Guy L Larose. Two-degree-of-freedom inclined cable galloping—part 1: General formulation and solution for perfectly tuned system. *Journal of Wind Engineering and Industrial Aerodynamics*, 96(3):291–307, 2008.

[98] Barna Szabó and Ivo Babuška. Finite element analysis: Method, verification and validation. 2021.

[99] Shyama Kumari and PK Sinha. Finite element analysis of composite wing t-joints. *Journal of reinforced plastics and composites*, 21(17):1561–1585, 2002.

[100] Antonia B Kesel, Ute Philippi, and Werner Nachtigall. Biomechanical aspects of the insect wing: an analysis using the finite element method. *Computers in biology and medicine*, 28(4):423–437, 1998.

[101] Yuwei Li, Kwang-Jun Paik, Tao Xing, and Pablo M Carrica. Dynamic overset cfd simulations of wind turbine aerodynamics. *Renewable Energy*, 37(1):285–298, 2012.

[102] Rafael Palacios, H Climent, A Karlsson, and B Winzell. Assessment of strategies for correcting linear unsteady aerodynamics using cfd or experimental results. 2001.

[103] JG Marshall and M Imregun. A review of aeroelasticity methods with emphasis on turbomachinery applications. *Journal of fluids and structures*, 10(3):237–267, 1996.

[104] Cécile Münch, Philippe Ausoni, Olivier Braun, Mohamed Farhat, and Francois Avellan. Fluid–structure coupling for an oscillating hydrofoil. *Journal of Fluids and Structures*, 26(6):1018–1033, 2010.

[105] Volker Carstens, Ralf Kemme, and Stefan Schmitt. Coupled simulation of flow-structure interaction in turbomachinery. *Aerospace Science and Technology*, 7(4): 298–306, 2003.

[106] S Moffatt and L He. On decoupled and fully-coupled methods for blade forced response prediction. *Journal of fluids and structures*, 20(2):217–234, 2005.

[107] Hamid R. Kaviani and Amir Nejat. Investigating the aeroelasticity effects on aeroacoustics and aerodynamics of a MW-class HAWT. *Journal of Wind Engineering & Industrial Aerodynamics*, 213:104617, 2021.

[108] Liping Dai, Qiang Zhou, Yuwen Zhang, Shigang Yao, Shun Kang, and Xiaodong Wang. Analysis of wind turbine blades aeroelastic performance under yaw conditions. *Journal of Wind Engineering & Industrial Aerodynamics*, 171:273–287, 2017.

[109] Toshiyuki Nakata and Hao Liu. A fluid–structure interaction model of insect flight with flexible wings. *Journal of Computational Physics*, 231(4):1822–1847, 2012.

[110] AT Sarawit, Y Kim, MCM Bakker, and Teoman Peköz. The finite element method for thin-walled members-applications. *Thin-walled structures*, 41(2-3):191–206, 2003.

[111] Diego Cárdenas, Alejandro A Escárpita, Hugo Elizalde, Juan José Aguirre, Horacio Ahuett, Piergiovanni Marzocca, and Oliver Probst. Numerical validation of a finite element thin-walled beam model of a composite wind turbine blade. *Wind Energy*, 15 (2):203–223, 2012.

[112] E. Carrera, M. Filippi, and E. Zappino. Free vibration analysis of rotating composite blades via carrera unified formulation. *Composite structures*, 106:317–325, 2013.

[113] Touraj Farsadi, Davood Asadi, and Hasan Kurtaran. Flutter improvement of a thin walled wing engine system by applying curvilinear fiber path. *Aerospace Science and Technology*, 93:105353, 2019.

[114] L. Librescu and S. Thangjitham. Analytical studies on static aeroelastic behavior of forward-swept composite wing structures. *Journal of Aircraft*, 28:151–157, 1991.

[115] C.A. Baxevanou, P.K. Chaviaropoulos, S.G. Voutsinas, and N.S. Vlachos. Evaluation study of a Navier-Stokes cfd aeroelastic model of wind turbine airfoils in classical flutter. *Journal of Wind Engineering & Industrial Aerodynamics*, 96:1425–1443, 2008.

[116] F. Alcántara-Ávila, S. Hoyas, and M. Pérez-Quiles. DNS of thermal channel flow up to $Re_\tau = 2000$ for medium to low Prandtl numbers. *Int. J. Heat Mass Transf.*, 127: 349–361, 2018.

[117] Sergio Hoyas, Martin Oberlack, Francisco Alcántara-Ávila, Stefanie V. Kraheberger, and Jonathan Laux. Wall turbulence at high friction Reynolds numbers. *Physical Review Fluids*, 7:014602, Jan 2022. doi: 10.1103/PhysRevFluids.7.014602.

[118] Praveen Kumar and Krishnan Mahesh. Large eddy simulation of propeller wake instabilities. *Journal of Fluid Mechanics*, 814:361–396, 2017.

[119] Jacob Keller, Praveen Kumar, and Krishnan Mahesh. Examination of propeller sound production using large eddy simulation. *Physical Review Fluids*, 3(6):064601, 2018.

[120] Silvio Tschisgale, Bastian Löhrer, Richard Meller, and Jochen Fröhlich. Large eddy simulation of the fluid–structure interaction in an abstracted aquatic canopy consisting of flexible blades. *Journal of Fluid Mechanics*, 916:A43, 2021.

[121] Lixiang Zhang, Yakun Guo, and Wenquan Wang. Large eddy simulation of turbulent flow in a true 3d francis hydro turbine passage with dynamical fluid–structure interaction. *International Journal for Numerical Methods in Fluids*, 54(5):517–541, 2007.

[122] William C Lasher and James R Sonnenmeier. An analysis of practical rans simulations for spinnaker aerodynamics. *Journal of Wind Engineering and Industrial Aerodynamics*, 96(2):143–165, 2008.

[123] Md Naimul Haque, Hiroshi Katsuchi, Hitoshi Yamada, and Mayuko Nishio. Investigation of edge fairing shaping effects on aerodynamic response of long-span bridge deck by unsteady rans. *Archives of Civil and Mechanical Engineering*, 16:888–900, 2016.

[124] Cui Peng and Han Jinglong. Prediction of flutter characteristics for a transport wing with wingtip device. *Aerospace Science and Technology*, 23:461–468, 2012.

[125] Jeffrey W Banks, William D Henshaw, and Björn Sjögreen. A stable fsi algorithm for light rigid bodies in compressible flow. *Journal of Computational Physics*, 245: 399–430, 2013.

[126] Warren F Phillips and Nicholas R Alley. Predicting maximum lift coefficient for twisted wings using lifting-line theory. *Journal of aircraft*, 44(3):898–910, 2007.

[127] Minu Jeon, Seungmin Lee, and Soogab Lee. Unsteady aerodynamics of offshore floating wind turbines in platform pitching motion using vortex lattice method. *Renewable Energy*, 65:207–212, 2014.

[128] Robert E Spall, Warren F Phillips, and Brian B Pincock. Numerical analysis of multiple, thin-sail geometries based on prandtl's lifting-line theory. *Computers & Fluids*, 82:29–37, 2013.

[129] Faisal Mahmuddin. Rotor blade performance analysis with blade element momentum theory. *Energy Procedia*, 105:1123–1129, 2017.

[130] Manelisi Kagame Rwigema. Propeller blade element momentum theory with vortex wake deflection. In *27th International congress of the aeronautical sciences*, volume 1, pages 727–735, 2010.

[131] Lin Wang, Xiongwei Liu, Nathalie Renevier, Matthew Stables, and George M Hall. Nonlinear aeroelastic modelling for wind turbine blades based on blade element momentum theory and geometrically exact beam theory. *Energy*, 76:487–501, 2014.

[132] James Tangler and David Kocurek. Wind turbine post-stall airfoil performance characteristics guidelines for blade-element momentum methods. In *43rd AIAA Aerospace Sciences Meeting and Exhibit*, page 591, 2005.

[133] T. Theodorsen. General theory of aerodynamic instability and the mechanism of flutter. *NACA*, 496, 1935.

[134] David G Crighton. The kutta condition in unsteady flow. *Annual Review of Fluid Mechanics*, 17(1):411–445, 1985.

[135] Frank Bowman. *Introduction to Bessel functions*. Courier Corporation, 2012.

[136] Werner J Rauchenstein Jr. A 3d theodorsen-based rotor blade flutter model using normal modes. Technical report, NAVAL POSTGRADUATE SCHOOL MONTEREY CA, 2002.

[137] H Kobayashi and H Nagaoka. Active control of flutter of a suspension bridge. *Journal of Wind Engineering and Industrial Aerodynamics*, 41(1-3):143–151, 1992.

[138] Dan Borglund and Jakob Kuttenkeuler. Active wing flutter suppression using a trailing edge flap. *Journal of Fluids and Structures*, 16(3):271–294, 2002.

[139] JG Leishman and TS Beddoes. A generalized method for unsteady airfoil behaviour and dynamic stall using the indicial method 42nd annual forum of the ahs. 1986.

[140] Sandeep Gupta and J Gordon Leishman. Dynamic stall modelling of the s809 aerofoil and comparison with experiments. *Wind Energy: An International Journal for Progress and Applications in Wind Power Conversion Technology*, 9(6):521–547, 2006.

[141] Morten Hartvig Hansen, Mac Gaunaa, and Helge Aagaard Madsen. *A Beddoes-Leishman type dynamic stall model in state-space and indicial formulations*. 2004.

[142] Dongfeng Li, Andrea Da Ronch, Gang chen, and Yueming Li. Aeroelastic global structural optimization using an efficient cfd-based reduced order model. *Aerospace Science and Technology*, 94:105354, 2019.

[143] Jiaqi Luo. Design optimization of the last stage of a 4.5-stage compressor using a pod-based hybrid model. *Aerospace Science and Technology*, 76:303–314, 2018.

[144] Gang Chen, Dongfeng Li, Qiang Zhou, Andrea Da Ronch, and Yueming Li. Efficient aeroelastic reduced order model with global structural modifications. *Aerospace Science and Technology*, 76:1–13, 2018.

[145] Ricardo Vinuesa and Steven L Brunton. Enhancing computational fluid dynamics with machine learning. *Nature Computational Science*, 2(6):358–366, 2022.

[146] J. Peng, C.T. Luo, Z.J. Han, Z.M. Hu, G.L. Han, and Z.L. Jiang. Parameter-correlation study on shock-shock interaction using a machine learning method. *Aerospace Science and Technology*, 107:106247, 2020.

[147] Teng Wu and Ahsan Kareem. Modeling hysteretic nonlinear behavior of bridge aerodynamics via cellular automata nested neural network. *Journal of Wind Engineering & Industrial Aerodynamics*, 99:378–388, 2011.

[148] Chern-Hwa Chen, Jong-Cheng Wu, and Jow-Hua Chen. Prediction of flutter derivatives by artificial neural networks. *Journal of Wind Engineering & Industrial Aerodynamics*, 96:1926–1937, 2008.

[149] Tajammal Abbas, Igor Kavrakov, Guido Morgenthal, and Tom Lahmer. Prediction of aeroelastic response of bridge decks using artificial neural networks. *Computers and Structures*, 231:106198, 2020.

[150] Tao Li, Teng Wu, and Zhao Liu. Nonlinear unsteady bridge aerodynamics: Reduced-order modeling based on deep lstm networks. *Journal of Wind Engineering & Industrial Aerodynamics*, 198:104116, 2020.

[151] Javier Jiménez. Coherent structures in wall-bounded turbulence. *Journal of Fluid Mechanics*, 842:P1, 2018.

[152] Adrián Lozano-Durán, Oscar Flores, and Javier Jiménez. The three-dimensional structure of momentum transfer in turbulent channels. *Journal of Fluid Mechanics*, 694:100–130, 2012.

[153] David C Wilcox et al. *Turbulence modeling for CFD*, volume 2. DCW industries La Canada, CA, 1998.

[154] Florian R Menter. Two-equation eddy-viscosity turbulence models for engineering applications. *AIAA journal*, 32(8):1598–1605, 1994.

[155] Venkat Venkatakrishnan. On the accuracy of limiters and convergence to steady state solutions. In *31st Aerospace Sciences Meeting*, page 880, 1993.

[156] P Chow, Mark Cross, and K Pericleous. A natural extension of the conventional finite volume method into polygonal unstructured meshes for cfd application. *Applied Mathematical Modelling*, 20(2):170–183, 1996.

[157] Emre Sozer, Christoph Brehm, and Cetin C Kiris. Gradient calculation methods on arbitrary polyhedral unstructured meshes for cell-centered cfd solvers. In *52nd Aerospace Sciences Meeting*, page 1440, 2014.

[158] P.J. Roache. *Verification and Validation in Computational Science and Engineering*. Hermosa Publishers, 1998.

[159] M Ahamed, Sharmin Atique, M Munshi, and Tuomas Koiranen. A concise description of one way and two way coupling methods for fluid-structure interaction problems. *Imperial Journal of Interdisciplinary Research*, 3(3), 2017.

[160] Jr. John D. Anderson. *Fundamentals of Aerodynamics*. McGraw-Hill, 1991.

[161] Gordon J Leishman. *Principles of helicopter aerodynamics with CD extra*. Cambridge university press, 2006.

[162] James F Manwell, Jon G McGowan, and Anthony L Rogers. *Wind energy explained: theory, design and application*. John Wiley & Sons, 2010.

[163] Jerson Rogério Pinheiro Vaz, João Tavares Pinho, and André Luiz Amarante Mesquita. An extension of bem method applied to horizontal-axis wind turbine design. *Renewable Energy*, 36(6):1734–1740, 2011.

[164] P.K. Chaviaropoulos and M. O. L. Hansen. Investigating three-dimensional and rotational effects on wind turbine blades by means of a quasi3d navier-stokes solver. *Journal of Fluids Engineering*, 122:130–136, 2000.

[165] Ben Kröse and Patrick van der Smagt. *An introduction to Neural Networks*. University of Amsterdam, 1996.

[166] Viet-Ha Nhu, Nhat-Duc Hoang, Hieu Nguyen, Phuong Thao Thi Ngo, Tinh Thanh Bui, Pham Viet Hoa, Pijush Samui, and Dieu Tien Bui. Effectiveness assessment of keras based deep learning with different robust optimization algorithms for shallow landslide susceptibility mapping at tropical area. *Catena*, 188:104458, 2020.

[167] S. Hochreiter and J. Schmidhuber. Long short-term memory. *Neural Computation*, 9: 1735–1780, 1997.

[168] Jichao Hong, Zhenpo Wang, Wen Chen, Le-Yi Wang, and Changhui Qu. Online joint-prediction of multi-forward-step battery soc using lstm neural networks and multiple linear regression for real-world electric vehicles. *Journal of Energy Storage*, 30:1001459, 2020.

[169] Robert D. Blevins. *Formulas for natural frequency and mode shape*. Van Nostrand Reinhold Company, 1979.

[170] Aly Mousaad Aly, Chanachock Chokwitthaya, and Raymond Poche. Retrofitting building roofs with aerodynamic features and solar panels to reduce hurricane damage and enhance eco-friendly energy production. *Sustainable Cities and Society*, 35: 581–593, 2017.

[171] Guy L Larose and Flora M Livesey. Performance of streamlined bridge decks in relation to the aerodynamics of a flat plate. *Journal of Wind Engineering and Industrial Aerodynamics*, 69:851–860, 1997.

[172] Kunihiko Taira and TIM Colonius. Three-dimensional flows around low-aspect-ratio flat-plate wings at low reynolds numbers. *Journal of Fluid Mechanics*, 623:187–207, 2009.

[173] Abdolrahim Rezaeiha, Ivo Kalkman, and Bert Blocken. Cfd simulation of a vertical axis wind turbine operating at a moderatetip speed ratio: Guidelines for minimum domain size and azimuthalincrement. *Renewable Energy*, 107:373–385, 2017.

[174] A. Torregrosa, A. Gil, P. Quintero, A. Ammirati, H. Denayer, and W. Desmet. Prediction of flow induced vibration of a flat plate located after a bluff wall mounted obstacle. *Journal of Wind Engineering & Industrial Aerodynamics*, 190:23–39, 2019.

[175] S. Pope. *Turbulent Flows*. Cambridge University Press, 2009.

[176] R. Gavasane, P. Pai, and V. Kumar. Numerical simulation of pitching and plunging motion of flat plate using oversetmeshes. Symposium on Applied Aerodynamics and Design of Aerospace Vehicle (SAROD 2013), 2013.

[177] J. Morgado, R. Vizinho, M.A.R. Silvestre, and J.C. Páscoa. Xfoil vs cfd performance predictions for high lift low reynolds number airfoils. *Aerospace Science and Technology*, 75:207–214, 2016.

[178] F. Menter. Zonal two-equation $k-\omega$ turbulence model for aerodynamic flows. *AIAA*, 93:93–2906, 1986.

[179] H. Hadzic. Development and application of finite volume method for the computation of flows around moving bodies on unstructure, overlapping grids. 2005.

[180] T. T. Tran and D.H. Kim. The platform pitching motion of floating offshore wind turbine: A preliminary unsteady aerodynamic analysis. *Journal of Wind Engineering & Industrial Aerodynamics*, 142:65–81, 2015.

[181] T. T. Tran and D.H. Kim. A cfd study into the influence of unsteady aerodynamic interference on wind turbine surge motion. *Renewable energy*, 90:204–228, 2016.

[182] T. T. Tran, D.H. Kim, and J. Song. Computational fluid dynamic analysis of a floating offshore wind turbine experiencing platform pitching motion. *Energies*, 7:5011–5026, 2014.

[183] B Dose, H. Rahimi, B. Stoevesandt, and J. Peinke. Fluid-structure coupled investigations of the nrel 5mw wind turbine for two downwind configurations. *Renewable energy*, 146:1113–1123, 2020.

[184] A. Marouf, N. Simiriotis, J.B. To, Y. Bmegaptche, Y. Hoarau, and M. Braza. Ddes and oes simulations of a morphing airbus a320 wing and flap in different scales at high reynolds. *Progress in Hybrid RANS-LES Modelling*, pages 249–258, 2020.

[185] Seungyong Lee, George Wolberg, and Sung Yong Shin. Scattered data interpolation with multilevel b-splines. *IEEE Transactions on Visualization and Computer Graphics*, 3, 1997.

[186] J.M. Weiss, J.P. Maruszewski, and W.A. Smith. Implicit solution of preconditioned navier-stokes equations using algebraic multigrid. *AIAA Journal*, 37:29–36, 1999.

[187] J.M. Weiss and W.A. Smith. Preconditioning applied to variable and constant density flows. *AIAA Journal*, 33:2050–2057, 1995.

[188] V. Venkatakrishnan. On the convergence of limiters and convergence to steady state solutions. *AIAA-93-0880*, 1995.

[189] A. Pfahl and H. Uhlemann. Wind loads on heliostats and photovoltaic trackers at various reynolds numbers. *Journal of Wind Engineering & Industrial Aerodynamics*, 99:964–968, 2011.

[190] A. Hassan, S. Mohammad-Reza, and M. Mohammand-Javad. Transitional boundary layer study over an airfoil in combined pitch-plunge motions. *Aerospace Science and Technology*, 98:105694, 2020.

[191] D.R. Williams, F. Reissner, D. Greenblatt, H. Muller-Vahl, and C. Strangfeld. Modeling lift hysteresis with a modified goman-khrabrov model on pitching airfoils. *45th AIAA Fluid Dynamics Conference*, page 2631, 2015.

[192] Matthew J. Emes, Farzin Ghanadi, Maziar Arjomandi, and Richard M. Kelso. Investigation of peak wind loads on tandem heliostats in stow position. *Renewable Energy*, 121:548–558, 2018.

[193] Igor V. Tetko, David J. Livingstone, and Alexander I. Luik. Neural network studies 1. comparison of overffiting and overtraining. *The Journal for Chemical Information and Computer scientists*, 35:826–833, 1995.

[194] Sanjay Yadav and Sanyam Shukla. Analysis of k-fold cross-validation over hold-out validation on colossal datasets for quality classification. 6th International Advanced Computing Conference, 2016.

[195] Ramesh Chadra, Alan D. Stemple, and Inderjit Chopra. Thin-walled composite beams under bending, torsional, and extensional loads. *Journal of Aircrafts*, 184:872–882, 1990.

[196] Ramesh Chandra and Inderjit Chopra. Experimental-theoretical investigation of the vibration characteristics of rotating composite box beams. *Journal of Aircraft*, 29(4), 1992.

[197] Zhanming Qin and Liviu Librescu. Static/dynamic solutions and validation of a refined anisotropic thin-walled beam model. 43rd AIAA/ASME/ASCE/AHS/ASC Structures, Structural Dynamics and Materials Conference, 2002.

[198] Reza Koohi, Hossein Shahverdi, and Hassan Haddadpour. Nonlinear aeroelastic analysis of a composite wing by finite element method. *Composite Structures*, 113: 118–126, 2014.

[199] Pierre J.A. Minguet. *Static and Dynamic Behavior of Composite Helicopter Rotor Blades under Large Deflections.* PhD thesis, Department of Aeronautics and Astronautics, Massachusetts Institute of Technology, 1989.

[200] M. Shaat, B. Aidi, S.W. Case, and A. Abdelkefi. Predictions of the frequencies of bending-torsion coupled laminated composite plates with discontinuities: Novel analytical modeling and experimental validation. *Composite Structures*, 180:334–350, 2017.

[201] J.R. Banerjee. Explicit analytical expressions for frequency equation and mode shapes of composite beams. *International Journal of Solids Structures*, 38:2415–2426, 2001.

[202] Pierre Minguet and John Dugundji. Experiments and analysis for composite blades under large deflections part ii: Dynamic behavior. *AIAA Journal*, pages 1580–1588, 1990.

[203] A. Attaran, D.L. Majid, S. Basri, A.S. Mohd Rafie, and E.J. Abdullah. Structural optimization of an aeroelastically tailored composite flat plate made of woven fiberglass/epoxy. *Aerospace Science and Technology*, 15:393–401, 2011.

[204] M.M. Hand, D.A. Simms, L.J. Fingersh, D.W. Jager, J.R. Cotrell, S.Schreck, and S.M. Larwood. Unsteady Aerodynamics Experiment Phase VI: Wind Tunnel Test Configurations and Available Data Campaigns. Technical Report NREL/TP-500-29955, National Renewable Energy Laboratory, 2001.

[205] E. Mahdi, B.S. Almabrouk, A.M.S. Hamouda, A.S. Mokhtar, Robiah Younus, and H. Sultan. Utilization of composite's tensile properties for energy absorbing systems. *Composite Structures*, 75:29–38, 2006.

[206] Ivica T. Vijcic and Ivana D. Dimic. Microstructural characterization of glass-epoxy composites subjected to tensile testing. *Acta Periodica Technologica*, 2013.

[207] Shamsher Singh, Madappa Sivasubramanian, A. Reddy, Chandra Khatri, K. Nagarjuna, and A. Kiran. Performance of NSM-FRP RC beams in flexure and shear using locally developed CFRP rebars. . *Int. J. of Sustainable Materials and Structural Systems*, 1: 42–67, 2012.

[208] Kyoungsoo Lee, Ziaul Huque, Raghava Kommalapati, and Sang-Eul Han. Fluid-structure interaction analysis of NREL phase VI wind turbine: Aerodynamic force evaluation and structural analysis using FSI analysis. *Renewable Energy*, 113:512–531, 2017.

[209] A.J. Torregrosa, A. Gil, P. Quintero, and A. Tiseira. Enhanced design methodology of a low power stall regulated wind turbine. BEMT and MRF-RANS combination and comparison with existing designs. *Journal of Wind Engineering & Industrial Aerodynamics*, 190:230–244, 2019.

[210] Borja Plaza, Rafael Bardera, and Sergio Visiedo. Comparison of BEM and CFD results for MEXICO rotor aerodynamics. *Journal of Wind Engineering & Industrial Aerodynamics*, 145:115–122, 2015.

[211] Yongsheng Lian, Wei Shyy, Dragos Viieru, and Baoning Zhang. Membrane wing aerodynamics for micro air vehicles. *Progress in Aerospace Sciences*, 39(6-7):425–465, 2003.

[212] Wei Shyy, Peter Ifju, and Dragos Viieru. Membrane Wing-Based Micro Air Vehicles. *Applied Mechanics Reviews*, 58(4):283–301, 07 2005.

[213] L. Tregidgo, Z. Wang, and I. Gursul. Unsteady fluid–structure interactions of a pitching membrane wing. *Aerospace Science and Technology*, 28(1):79–90, 2013. ISSN 1270-9638. doi: https://doi.org/10.1016/j.ast.2012.10.006.

[214] Benoît Béguin and Christian Breitsamter. Effects of membrane pre-stress on the aerodynamic characteristics of an elasto-flexible morphing wing. *Aerospace Science and Technology*, 37:138–150, 2014. ISSN 1270-9638. doi: https://doi.org/10.1016/j.ast.2014.05.005.

[215] Shuanghou Deng, Jun Wang, and Hanru Liu. Experimental study of a bio-inspired flapping wing mav by means of force and piv measurements. *Aerospace Science and Technology*, 94:105382, 2019. ISSN 1270-9638. doi: https://doi.org/10.1016/j.ast.2019.105382.

[216] Dawei Bie, Daochun Li, Jinwu Xiang, Huadong Li, Zi Kan, and Yi Sun. Design, aerodynamic analysis and test flight of a bat-inspired tailless flapping wing unmanned aerial vehicle. *Aerospace Science and Technology*, 112:106557, 2021. ISSN 1270-9638. doi: https://doi.org/10.1016/j.ast.2021.106557.

[217] Bor-Jang Tsai and Yu-Chun Fu. Design and aerodynamic analysis of a flapping-wing micro aerial vehicle. *Aerospace Science and Technology*, 13(7):383–392, 2009. ISSN 1270-9638. doi: https://doi.org/10.1016/j.ast.2009.07.007.

[218] Sonya Tiomkin and Daniella E Raveh. A review of membrane-wing aeroelasticity. *Progress in Aerospace Sciences*, 126:100738, 2021.

[219] Junhee Lee, Sang-Hoon Yoon, and Chongam Kim. Experimental surrogate-based design optimization of wing geometry and structure for flapping wing micro air vehicles. *Aerospace Science and Technology*, 123:107451, 2022. ISSN 1270-9638. doi: https://doi.org/10.1016/j.ast.2022.107451.

[220] Julien Deparday, Patrick Bot, Frederic Hauville, Benoit Augier, and Marc Rabaud. Full-scale flying shape measurement of offwind yacht sails with photogrammetry. *Ocean Engineering*, 127:135–143, 2016.

[221] D. Trimarchi and C.M. Rizzo. A fem-matlab code for fluid-structure interaction coupling with application to sail aerodynamics of yachts. In Ömer Gören, Barbaros Okan, and Şafak C. Karakaş, editors, *13th International Congress of International Maritime Association of Mediterranean (IMAM2009), Towards the Sustainable Marine Technology. 12-15 October, 2009, Istanbul, Turkey. Proceedings Vol.III*, pages 907–916. ITU Faculty of Naval Architecture and Ocean Engineering, 2009.

[222] Nils Haack. *C-class catamaran wing performance optimisation*. PhD thesis, The University of Manchester (United Kingdom), 2011.

[223] Joseph Banks, Margot Cocard, and Jacobo Jaspe. Assessing the impact of membrane deformations on wing sail performance. *Journal of Sailing Technology*, 6(01):73–90, 2021.

[224] Benoit Augier, Patrick Bot, Frederic Hauville, and Mathieu Durand. Dynamic behaviour of a flexible yacht sail plan. *Ocean Engineering*, 66:32–43, 2013.

[225] Bret Stanford, Peter Ifju, Roberto Albertani, and Wei Shyy. Fixed membrane wings for micro air vehicles: Experimental characterization, numerical modeling, and tailoring. *Progress in Aerospace Sciences*, 44(4):258–294, 2008.

[226] Fabio Fossati and Sara Muggiasca. Experimental investigation of sail aerodynamic behavior in dynamic conditions. *Journal of Sailboat Technology*, 2(8):1–41, 2011.

[227] Benoit Augier, Patrick Bot, Frederic Hauville, and Mathieu Durand. Experimental validation of unsteady models for fluid structure interaction: Application to yacht sails and rigs. *Journal of Wind Engineering and Industrial Aerodynamics*, 101:53–66, 2012.

[228] Robert Scott, Robert Bartels, and Osama Kandil. An aeroelastic analysis of a thin flexible membrane. In *48th AIAA/ASME/ASCE/AHS/ASC Structures, Structural Dynamics, and Materials Conference*, page 2316, 2007.

[229] Guojun Li, Boo Cheong Khoo, and Rajeev K Jaiman. Computational aeroelasticity of flexible membrane wings at moderate reynolds numbers. In *AIAA Scitech 2020 Forum*, page 2036, 2020.

[230] Multifrontal Massively Parallel Solver (MUMPS 5.0.2) Users' Guide. July 15, 2016.

[231] Feri Farassat. Linear acoustic formulas for calculation of rotating blade noise. *AIAA journal*, 19(9):1122–1130, 1981.